BAR CODE

101 381 288 3.

RECOVERY, RECRYSTALLISATION AND FORMABILITY OF FERRITIC STAINLESS STEELS

A thesis submitted to the Council for National Academic Awards for the degree of

DOCTOR OF PHILOSOPHY

AT

SHEFFIELD CITY POLYTECHNIC

BY

DAVID BRIAN LEWIS CEng MIM

OCTOBER 1978

This thesis is based on an investigation carried out during the period December 1972 to November 1975 at Sheffield City Polytechnic. During this period, regular meetings were held to discuss the progress of the work and the following conference was attended :

Textures and the Properties of Materials, Cambridge University, 2 - 4 July 1975

In addition, the following lecture modules, from the part-time MSc in Industrial Metallurgy at Sheffield City Polytechnic, were attended :

1. Mechanical Metallurgy
2. High Strength Alloys
3. Numerical Analysis and Programming

The candidate also attended a course on the use of X-rays and Electron Microscopy in the study of materials.

The results obtained in this investigation and the theories developed are, to the best of my knowledge, original except where reference has been made to other authors. No part of this thesis has been submitted for a degree at any other University or College.

October 1978

ACKNOWLEDGEMENTS

The author is indebted to the Sheffield Education Authority for providing the financial assistance during the period of this investigation. He wishes to express his gratitude to Dr F B Pickering for his help and guidance given so freely during the course of this investigation and to Dr T Gladman of Swinden Laboratories for his help and suggestions. Thanks are also due to the technicians in the Departments of Metallurgy, Applied Physics and Mechanical and Production Engineering for their help, particularly to Mr J Evans, Mr P S Cassy and Mr D Fitzpatrick. Thanks are also due to the British Steel Corporation Special Steels Division and the University of Sheffield Metallurgy Department. Finally, thanks are due to Miss S V Clifford for many hours spent typing the manuscript.

Words cannot express my appreciation for the assistance given, patience and tolerance shown by my wife during the past few years.

SYNOPSIS

The effects of additions of C, N, Mo, Ti and Nb on recovery, recrystallisation and formability have been investigated in 17% and 25% Cr steels after 35%, 50% and 75% reduction.

In general additions of molybdenum retarded recovery at both chromium and interstitial levels, while additions of titanium increased the rate of recovery. Additions of niobium increased the rate of recovery at the lower interstitial level and decreased the rate of recovery at the higher interstitial level.

In the majority of steels a distinct hardness plateau was observed between recovery and recrystallisation, the extent of which depends on composition degree of cold reduction and temperature, and was associated with the pinning of subgrain boundaries by precipitating particles during recovery. The end of the plateau coincided with the incubation period for recrystallisation and was interpreted in terms of the unpinning of subgrain boundaries leading to the formation of recrystallised grains.

Additions of Mo, Nb and increasing the interstitial content in general retarded recrystallisation while additions of Ti and increasing the chromium had relatively little effect.

A comprehensive determination of the cold worked and recrystallisation textures has been made. Alloying elements had little effect on the development of deformation textures but considerably affected the development of recrystallisation textures. Additions of niobium, titanium and molybdenum in general favoured the development of {111} <112> recrystallisation textures because the nucleation of {111} oriented grains was favoured at particle/matrix interfaces.

Swift cupping and Erichsen tests have been used as a measure of formability in these steels. The recrystallisation textures have been related to $\bar{r}$ values and LDR. Good correlations have been obtained between $\bar{r}$ values, LDR and the ratio of the $I_{(111)}:I_{(100)}$ texture and between $\bar{r}$ values and LDR. Both deep drawability and $\bar{r}$ value increased as the ratio of $I_{(111)}:I_{(100)}$ increased. The LDR was increased by increasing the degree of cold reduction, by additions of titanium and niobium at the lower interstitial level and molybdenum because of the increased the $I_{(111)}:I_{(100)}$ texture ratio. The Erichsen value was increased with increasing cold reduction but decreasing the interstitial content did not improve the Erichsen value in the base 17% Cr and 17% Cr molybdenum steels.

A quantitative relationship has been obtained between the yield stress, composition and recrystallised grain size. Additions of molybdenum and chromium increased the yield stress because of their effects on lattice dilation, while titanium additions decreased the yield stress because it removed interstitials from solid solution.

CONTENTS

CHAPTER ONE

INTRODUCTION

The term "ferritic stainless steel" refers to a group of chromium-bearing steels containing chromium contents ranging from 11 to 25%. They are usually free from nickel but may contain certain other alloying elements, e.g. aluminium, molybdenum, niobium or titanium. Ferritic stainless steels containing between 17% and 25% chromium are an important group of materials because of their potentially lower materials cost compared with austenitic (18% chromium, 8% nickel) grades. They also have other physical and chemical property advantages such as lower co-efficient of thermal expansion, electrical resistivity and superior stress corrosion resistance particularly in the presence of chloride ions.

However, widespread utilisation of these materials has been limited by several factors. Ferritic stainless steels exhibit poor weldability and room temperature toughness, together with embrittlement after heating in the temperature range around 475^{o}C. They also show intergranular corrosion after heating at approximately 900^{o}C.

The lack of weldability and room temperature toughness can to some extent be overcome by the use of low interstitial contents. Although commercially available air melted materials conventionally contain a minimum of 0.05%C and 0.03%N, newer processes involving argonoxygen and electron beam refining can reduce the combined carbon and nitrogen interstitial content to 0.04% and 0.01% respectively.

Typical interstitial contents are : (1) (2) (3)

	Carbon %	Nitrogen %	Carbon & Nitrogen %
Basic Electric Arc.	0.05	0.03	0.08
Argon-Oxygen	0.01/0.02	0.02	0.04
Electron Beam	0.002	0.008	0.01

The combination of such very low carbon and nitrogen contents with 2% Mo in an 18% Cr steel gives corrosion resistance exceeding, in many cases, that of austenitic steels, with superior formability and weldability to the conventional ferritic grades.

With the exception of the phenomenon of 'roping' which is now known to be a textural effect produced during hot working [167][168], little systematic attention has been paid to ferritic stainless steel. As these steels are cheap alternatives to the nickel bearing austenitic stainless steel, there is a considerable need for a systematic investigation of the effect of composition on the cold working, annealing and cold forming characteristics of these materials.

The aims of the present work are to investigate :

i. The effects of composition in the cold working and recovery/recrystallisation characteristics of ferritic stainless steels;

ii. The development of textures in both the cold worked and re-crystallised conditions;

iii. The identification of the role of both second phase particles e.g. carbides and/or nitrides and solutes during recovery and recrystallisation, and in the development of recrystallisation textures;

iv. To relate the mechanical properties obtained from true stress-

true strain characteristics, e.g. uniform elongation, ε_u, rate of work hardening $\frac{d\sigma}{de}$ and $\bar{r}$ values, to the recrystallised structures and textures, and thereby to examine the effects of microstructure, textures, and composition on forming characteristics, under conditions of deep drawing and stretch forming. Tensile test parameters will also be related to forming characteristics, determined by deep drawing and Erichsen tests, wherever possible in an attempt to define structure-formability relationships with a view to the more efficient processing and usage of these steels.

Also it is hoped to identify the metallurgical features that limit ductility during forming, and the mechanism of failure.

CHAPTER TWO

2. FERRITIC STAINLESS STEELS

2.1 CONSTITUTION

The iron-chromium equilibrium diagram (fig 1) indicates the change in microstructure with an increase in the chromium content. Above 12%Cr the diagram shows that the steels are completely ferritic. However, in commercial materials the iron-chromium-carbon ternary system is more appropriate. A vertical section of this system is shown at 0.05%C (fig 2). The addition of carbon extends the gamma loop and also increases the composition range of the duplex austenite-ferrite phase field. As the chromium content is increased, the austenite transformation temperature increases, and above about 22%Cr, 0.05%C the steels are completely ferritic. Further increases in chromium merely increase the temperature of the $M_{23}C_6$ solvus line, i.e. the temperature at which $M_{23}C_6$ type carbide is completely dissolved in the ferrite. This was further illustrated by the work of Castro and Tricot[4] who determined the equilibrium between austenite and ferrite in ferritic stainless steels at hot rolling temperatures using the following alloys :

i.	0.045%C	17.3%Cr
ii.	0.080%C	15.7%Cr

The results of their work are shown in Figure 3 which illustrates variations in the percentage austenite with temperature and composition. It was found that the percentage austenite increased with increasing carbon content and decreased with increasing chromium content.

The austenite formed at these temperatures subsequently transformed to martensite during cooling to room temperature. As nitrogen is also an austenite stabiliser and is always present in ferritic stainless steels in varying amounts, a commercial 0.05%C 0.03%N steel will require in excess of the 22%Cr indicated in Figure 2 in order to be completely ferritic.

Ferritic stainless steel can therefore be divided into two categories :

i. 17%Cr steels which possess a duplex austenite/ferrite microstructure at a temperature of 1000°C, in which the amount of austenite is dictated by the interstitial level. This austenite transforms to martensite on cooling to room temperature;

ii. 25%Cr steels which have a fully ferritic microstructure from room temperature up to the melting point.

If however the martensite produced in steels of category i. is tempered in the temperature range 750°C - 800°C it can be converted to ferrite and carbide and therefore in all composition ranges between 17% and 25%Cr, the predominant phase is bcc ferrite.

Additions of molybdenum have been shown to raise the transformation temperature at which austenite begins to form,[7] and also reduce the percentage austenite for constant chromium and carbon contents. This is shown by the fact that additions of molybdenum to a 0.05%C 17%Cr steel reduced the overall hardness in the hot rolled condition while increasing the hardness of the ferrite by solid solution hardening.

According to the work of Bungardt et al[5] the ferrite forming ability of molybdenum is 1.5 times that of chromium. This would mean that an addition

of 1% by weight of molybdenum to a 17%Cr 0.05%C steel would produce a microstructure equivalent to that of 18.5%Cr 0.05%C steel.

Additions of niobium and titanium reduce the amount of austenite at given chromium, carbon and nitrogen contents to an even greater extent than does molybdenum. The effect of these additions is to reduce the carbon and nitrogen in solid solution by the formation of insoluble titanium/niobium carbonitrides. This has been further substantiated by the work of Pollard[6] using 25%Cr and 25%Cr 0.16%Ti steels. In the base composition, the nitrogen content varied from 0.023% at 927°C to 0.006% at 593°C. While the titanium bearing steel reduced the solubility of nitrogen to 0.0035% in the temperature ranges 1204-316°C. It is more difficult to quantify the ferrite forming tendency of niobium and titanium as these not only have a direct effect by minimising the austenite forming action of carbon and nitrogen, with which they are combined, but also are ferrite forming elements themselves. In certain materials, the titanium and/or niobium additions may not be sufficient to eliminate completely the austenite.

2.2 PRECIPITATES

Precipitates observed in high chromium steels are being reviewed because it has been reported by many workers that they influence recovery, recrystallisation, grain growth and textures.

2.2.1 Carbides and Nitrides

The solubility of interstitial carbon and nitrogen at room temperature is an order of magnitude less in bcc ferrite than in fcc austenite. Because of the low room temperature solubility, most of the carbon and nitrogen is present in the form of precipitates, particularly in the case of the higher

interstitial levels.

Precipitates are mainly of the type $M_{23}C_6$, M_7C_3 and M_2X where M denotes the metal atom. Both carbide and nitride particles dissolve on heating above 850°C, with the nitride dissolving faster than the carbide, and are completely in solution between 1000°C and 1100°C. On cooling from solution treatment temperatures carbides precipitate first and occur preferentially on the grain boundaries which are the most favourable sites kinetically.[8] This is not surprising as Pollard[6] showed that the solubility of carbon decreased more rapidly with temperature than that for nitrogen.

2.2.2 Carbides in the Fe-C-Cr System

The equilibrium diagram (fig 4)[5] shows that the carbides present at 700°C are M_3C, M_7C_3 and $M_{23}C_6$ in order of increasing chromium content. Increasing the carbon content stabilises the lower chromium content carbide at a constant chromium level, i.e. M_7C_3 or M_3C. This may be expected because a high carbon content will increase the carbide volume fraction, thereby diluting the metal: C ratio in an alloy of constant chromium content.

During the formation of $M_{23}C_6$ at 700°C, the carbide must form through the intermediate carbides M_3C and M_7C_3. To determine the intermediate carbides which may occur for a given composition, a line must be drawn from the co-ordinates of the carbon and chromium contents to the origin of the diagram. For a 0.05%C 17%Cr steel, M_7C_3 must form prior to $M_{23}C_6$. The equilibrium diagram indicates that only $M_{23}C_6$ should be present, after annealing at 750°C, but Bywater[9] and Leiber et al[10] observed M_7C_3 in 0.05%C 17%Cr and 0.02%C 10%Cr steels, after tempering in the range 600-800°C and 600-750°C respectively. According to Figure 2, M_7C_3 is a non-equilibrium carbide at 700°C and Bywater[9] explained its presence in terms of a partitioning of

chromium to the ferrite allowing austenite (martensite) to enter the three phase field at 6.5%Cr (fig 2). A more likely explanation is that it is a kinetic effect because M_7C_3 was still transforming to $M_{23}C_6$ and Shaw and Quarrell[11] showed that transformation was still proceeding after 1000 hours at 700°C.

Various carbides and nitrides have been reported in ferritic steels. However the most important types in ferritic stainless steel are $M_{23}C_6$, M_7C_3 and M_2X:

i. M_7C_3

This is a chromium rich carbide with trigonal structure based on that of Cr_7C_3. It has a very high solubility for iron which in fact may become the major alloying element with a metal:C ratio of 0.6. Henzko[12] in fact defined a composition $Fe_2Cr_5C_3$ in a 17%Cr steel. Molybdenum has a relatively low solubility in M_7C_3 the maximum metal:C ratio being 0.55[13].

ii. $M_{23}C_6$

This is again a chromium rich carbide having a complex face centred cubic structure. Iron can replace chromium up to a metal:atom ratio of 0.4. Henzko[12] defined the composition of $M_{23}C_6$ as $Fe_8Cr_{15}C_6$. Molybdenum also has considerable solubility in $M_{23}C_6$ and the composition of the carbide can be anywhere between $Cr_{23}C_6$ and $Fe_{21}Mo_2C_6$ depending on the alloy composition. $M_{23}C_6$ is usually a grain boundary phase and precipitates as less stable carbides dissolve.

iii. M_2X

M_2X denotes a general group of hexagonal carbides and nitrides,

'X' denoting either carbon or nitrogen. In many cases, both types of interstitial atoms are present. In ferritic stainless steels, the composition is usually quoted as Cr_2N. However, the work of Lagneborg[14] and Pollard[6] showed extensive solubility of carbon and nitrogen in Cr_2N. Due to extensive mutual solubility between isomorphous compounds, the phase Cr_2N is probably best represented by $(Cr\ Fe\ Mo)_2CN$.

Irvine et al.[15] suggested that in the presence of nitrogen, the carbide sequences in high (12%) chromium steels is not :

$$M_3C \text{ -- } M_7C_3 \text{ -- } M_{23}C_6$$

but is modified to :

$$M_3C \text{ -- } M_7C_3 \text{ -- } \frac{M_7C_3}{M_2X} \text{ -- } M_{23}C_6$$

2.2.3 Carbides in the Fe-Mo-C System

The principal carbides of the iron-molybdenum-carbon system are M_3C, $M_{23}C_6$, $M_a\ C_b$, M_6C and Mo_2C. $M_{23}C_6$ and $M_a\ C_b$ are not considered to be equilibrium phases but due to the slow approach to equilibrium, may persist for periods well in excess of 2000 hours at 700°C. For most practical purposes, they may be considered as 'equilibrium' phases in many steels, particularly $M_{23}C_6$.

With the addition of chromium, the iron-chromium-molybdenum carbide constitution diagram appears as in Figure 5[13]. This indicates that with 0-2% Molybdenum and 0-12%Cr, the principal carbides are M_3C, M_7C_3, $M_{23}C_6$ and M_6C at 700°C. It would appear that at 700°C, $M_{23}C_6$ is the

stable carbide in a basic 18%Cr 2%Mo steel. A molybdenum content in excess of 3% would be required to produce M_6C in an 18%Cr steel. During the formation of $M_{23}C_6$ in an 18%Cr 2%Mo steel, the carbide transformation sequences would be M_3C -- M_7C_3 -- $M_{23}C_6$. It is not certain how molybdenum affects the kinetics of the transformation as there appears to be little published information on this. It is thought, however, that due to the low solubility of molybdenum in M_7C_3 the presence of molybdenum will have little effect on the dissolution of M_7C_3. However, molybdenum may retard nucleation and growth of $M_{23}C_6$ because of the slower diffusion of molybdenum. In the presence of nitrogen, M_2X forms in preference to M_7C_3. Molybdenum has considerable solubility in M_2X and will therefore partition to it. It is thought that in the presence of nitrogen, molybdenum will considerably retard the rate of $M_{23}C_6$ formation.

2.2.4 Titanium and Niobium Carbo-nitrides

As carbide and nitride phases are isomorphous, titanium and niobium will tend to form carbo-nitrides of the type Nb (CN), Ti (CN) with fcc structures. In niobium steels, the principal carbides are NbC, M_7C_3 and $M_{23}C_6$ [16], but above 7%Cr at 700°C, M_7C_3 is not stable and the principal carbides are $M_{23}C_6$ and Nb C. The presence of M_7C_3 would appear doubtful, as niobium has been found to accelerate the M_7C_6 -- $M_{23}C_6$ reaction by removing the available carbon and thereby reducing the amount of M_7C_3 formed. It would be expected that titanium would behave similarly. Pollard[6] observed the precipitation of chromium carbide ($M_{23}C_6$) at titanium carbonitride particles during cooling in a 26%Cr 0.16%Ti steel. In austenitic steels, it was shown[17] that the relative amounts of $M_{23}C_6$ to Nb(CN) or Ti(CN) depended on the titanium or niobium to carbon ratio. Titanium or niobium contents above stoichiometry tended to favour the formation of Nb or Ti (CN), while those less than stoichiometry showed an increased amount of $M_{23}C_6$.

2.3 INTERMETALLIC COMPOUNDS

2.3.1 Sigma Phase

Sigma phase is an intermetallic compound of iron and chromium approximating to FeCr. In a 17%Cr steel, sigma phase is stable only at temperatures below 600°C (fig 6) where precipitation occurs very slowly, i.e. with an incubation time approaching 10^4 hours. The incubation time can be halved by cold working[18]. A 25% chromium steel will form sigma phase at temperatures below 650°C because increasing the chromium content extends the temperature range of sigma phase stability. Additions of ferrite formers such as silicon or molybdenum[19][20], which dissolve in sigma phase, lead to an increase in its rate of formation and to an extension of its range of stability, as a result of silicon and molybdenum increasing the degree of supersaturation. Sigma phase can be dissolved rapidly by heating at temperatures in excess of 800°C.

2.3.2 Chi Phase

The phase has the approximate composition ($Fe_{36}Cr_{12}Mo_{10}$). It occurs in 17%Cr steels at molybdenum contents in excess of 3.5%. Chi phase is stable over a wider temperature range than is sigma phase. Annealing at temperatures around 1000°C was required to eliminate it in an 18%Cr steel containing over 3.5% molybdenum[21].

2.3.3 Laves Phase

If titanium or niobium are added in considerable excess of that needed to combine with the carbon and nitrogen, they can lead to the formation of embrittling intermetallic compounds Fe_2M_3 or Fe_2M[177] where M signifies titanium or niobium.

2.3.4 The α' Phase

Ferritic stainless steels are particularly susceptible to 'embrittlement' if heated for even a short time in the temperature range 400°-600°C. This phenomenon was not characteristic of a process involving precipitation of carbide etc. Initially it was thought to be due to sigma phase or an intermediate phase prior to sigma phase formation. This idea was rejected because the embrittling effects were removed by heating to a temperature within the sigma phase field. More recently, Williams and Paxton[22] considered that embrittlement was due to the precipitation of the chromium rich α' phase in the miscibility gap in the iron-chromium equilibrium diagram. Theoretical confirmation of this was given by Kubaschewski and Chart[26] and electron microscopy[24][26] showed coherent particles of α' which is a bcc solid solution. Williams and Paxton[22] explained the variations in hardness, resistivity and Curie temperature at temperatures above the miscibility gap in terms of increased clustering with decreasing temperature. Lagneborg[14] observed the occurrence of coherent α' particles containing approximately 80%Cr in conjunction with chromium nitride needles, which formed preferentially at dislocations, inclusions and grain boundaries. He concluded that the precipitation of α' was enhanced by the local high chromium content associated with the chromium nitride particles. Williams[56] phase diagram for the iron-chromium system at low temperatures is reproduced in Figure 6.

2.4 MECHANICAL PROPERTIES AND STRUCTURE PROPERTY RELATIONSHIPS OF FERRITIC STAINLESS STEELS

The yield stresses of ferritic stainless steels are higher than austenitic stainless steels, 310-460 MN/N^2, compared with 230 MN/M^2 of austenitic stainless steels[162]. Ferritic stainless steels, however, work harden less rapidly than do austenitic stainless steels because of the lower work

hardening rate of bcc ferrite compared with fcc austenite. Structure-property relationships have been attempted, but were found to be complex and as yet not fully understood or quantified. The major factors affecting mechanical properties are grain size, solid solution hardening, and percentage martensite.

2.4.1 Grain Size

Refining the ferrite grain size increased both the yield stress and tensile strengths according to a Petch type relationship. However, because the measured ferrite grain size may not be the controlling one, high chromium ferrite grains contain many subgrains[27], as a result of incomplete recrystallisation. Thus the yield strengths and tensile strengths also depend on the subgrain size. This is the reason why structure-property relationships are complex. However, cleavage crack propagation is not impeded. Therefore the impact properties depend on the coarse observed grain size.

Because these steels have a bcc ferrite structure, they exhibit a ductile-brittle transition. The transition temperature is considerably higher than for mild steel because of the embrittling effect of chromium dissolved in the ferrite. The ductile brittle transition temperature decreases as the grain size decreases, but because these steels do not undergo phase transformation, they tend to have coarse grain sizes.

2.4.2 Solid Solution Effects

The solid solution hardening effects on fully ferritic structures are similar to those of low carbon steels. Additions of chromium and molybdenum increased the strength of the ferrite[7] due to lattice dilation effects[146]. However, because many of these steels are duplex, the strength also depends

on the amount of austenite (martensite) in the structure. Austenite formers, e.g. Ni, C, N etc., increase the strength rapidly by increasing the amount of austenite which transforms to martensite. Ferrite formers, e.g. Cr and Mo, while increasing the strength of the ferrite decrease the overall strength of the steel, by decreasing the amount of austenite.

Only when the structure is completely ferritic, does solid solution hardening become apparent. The interstitial solutes (carbon and nitrogen) increase the strength linearly; nitrogen increases the strength more than carbon because of a higher solubility. Both interstitial and substitutional solutes have been shown to decrease ductility and increase the impact transition temperature[162]. Additions of titanium to a 26%Cr 0.015%(C+N) steel have been shown to decrease the yield stress.[1] Thus, the effect of removal of (C+N) from solution was not balanced by solid solution hardening by titanium.

2.4.3 Martensite

Increasing the amount of martensite caused a linear increase in the tensile strength, but initially increasing amounts of martensite decreased the yield stress[27]. This was due to internal stresses; however, at martensite contents above 15-20% the yield stress begins to increase. However increasing the amount of austenite refines the ferrite grain size as it pins the ferrite grains thus preventing grain-growth. This further complicates the strengthening effects and also offsets the detrimental effects of martensite on impact properties.

2.5 COLD WORKING, ANNEALING AND RECRYSTALLISATION

There has been very little published work on the cold working and annealing

of ferritic stainless steel. Wright[133] carried out work on the cold working and annealing of a 26%Cr 1%Mo steel. During cold work, the steel behaved in a similar manner to other bcc metals, i.e. had a high initial rate of work hardening, but did not maintain a high work hardening rate. Annealing treatments showed that the steel tended to exhibit considerable amounts of recovery prior to recrystallisation. Recrystallisation was retarded by the additions of chromium and molybdenum when compared with a low carbon steel. However, in this investigation, recovery and recrystallisation were only examined in a superficial manner by hardness testing. There has been no published work on the recrystallisation kinetics of ferritic stainless steels, as a function of time, temperature and percentage reduction in steels containing varying Cr, C, N, Nb, Ti and Mo contents.

Bywater[161] observed that considerable quantities of austenite, present at hot rolling temperatures, tended to accelerate ferrite recrystallisation during hot rolling, while structures containing little or no austenite did not recrystallise, but rather tended to produce a polygonised structure. The presence of austenite must have a catalytic effect on the recrystallisation of ferrite; presumably by a nucleation process at the austenite-ferrite interface.

2.6 TEXTURES

There has been very little published work on the development of textures in ferritic stainless steels. However, the work of Yantas[164] and Wright[133] showed that deformation and recrystallisation textures produced in these alloys were similar to those in most bcc metals and alloys. This is hardly surprising because the later chapter on textures shows that the texture developed is very much a function of the crystal structure, i.e. deformation textures depend upon the operative slip systems while the

development of recrystallisation textures is a function of the stored energy of the textural component in the deformation texture.

2.7 $\bar{r}$ VALUES AND FORMABILITY

The effect of composition on $\bar{r}$ value was investigated by Bruckner and Berger[165]. $\bar{r}$ value was predicted directly from composition. No mention was made of the effect of texture on $\bar{r}$ value which has been shown to be of prime importance[127][128][129]. It is thought that the composition affects the $\bar{r}$ value due to its effect on the development of recrystallisation textures.

Schneider et al[166] showed that the $\bar{r}$ value in ferritic stainless steels increased with increasing cold reduction up to maximum reduction of 85%. By proper control of the cold rolling and annealing cycle, it was possible to develop $\bar{r}$ values of 1.5-1.7 equivalent to aluminium-killed drawing quality mild steel, and no earing. This indicates that a strong {111} <uvw> type texture was present[133]. At low reductions Δr was negative and earing was at 45° to rolling direction indicating a {100} <011> texture[133].

During forming operations ferritic stainless steels suffer from a phenomenon called 'roping'. This is a textural effect developed during hot rolling[167][168]. It manifests itself as ugly rope-like marks which are present after small deformations.

In one of the theories[167] it has been suggested that when {100} <011> or {110} <001> textures occur as clusters of grains or bands in a matrix of {111} <011>, the anisotropic deformation of these textures results in variations in the width to thickness ratio of the clusters or bands.

A second theory has been postulated[168] in which 'roping' can occur within a $\{111\}\ \langle 110\rangle$ texture due to asymmetric shape change of the adjacent crystals.

2.8 WELDABILITY

Welding is generally considered to be a major problem because :

i. The absence of a phase change allows very coarse grains to develop in the weld and heat affected zone, which induces brittleness[27]. This is a particular problem in 17%Cr low (C+N) and 25%Cr chromium steels, as most of the pinning particles dissolve in the ferrite between 1000°C and 1100°C. Above this temperature few pinning particles are present and therefore unrestricted grain growth occurs.

ii. If the composition of the steel is such that it passes through the edge of the gamma loop on heating or cooling, ferrite grains grow rapidly above the gamma loop, because of the absence of austenite or pinning particles. On cooling, a coarse widmanstatten structure of austenite forms. The austenite then tranforms to martensite, which gives marked embrittlement.

Post weld annealing can alleviate the martensite problem by tempering, but it cannot refine the ferrite grain size. Post weld annealing may also precipitate carbides or nitrides which both harden and embrittle the steel. The ferrite grains can be prevented from growing by the addition of titanium or niobium which combine with carbon and nitrogen to produce stable carbonitrides. The particles pin the grain boundaries at temperatures above the solution temperature for primary carbides.

However, the post weld annealing of niobium or titanium steels may precipitate Nb(CN) or Ti(CN) which causes hardening and embrittlement.

In lower interstitial content steels despite the good effects of low (C+N) on toughness and ductility, coarse grain sizes are a major problem due to the absence of pinning particles[27].

2.9 CORROSION RESISTANCE

It is well established that corrosion resistance is a function of the chromium content. The corrosion resistance is conferred by the ability of chromium to produce a passive layer at chromium contents in excess of 12%.

However, although general corrosion resistance was a function of chromium content, recent work[28] showed that resistance to intergranular attack was a function of interstitial content. In contrast to austenitic stainless steels which are susceptible to intergranular attack after heating in the range 650°C - 700°C, ferritic stainless steels are susceptible only after heating to temperatures in excess of 900°C. At this temperature, the solubility of carbon and nitrogen in ferrite is sufficiently high to cause precipitation of chromium rich carbides at grain boundaries during subsequent cooling. Intergranular attack may be overcome by annealing at temperatures in the range 650°C - 800°C which permits diffusion of chromium to the denuded areas adjacent to the precipitates.

Susceptibility to intergranular corrosion can be reduced in two ways :

i. By reducing the interstitial content to a low level thus preventing precipitation of chromium carbide;

ii. By additions of titanium or niobium which combine with the carbon and nitrogen as insoluble carbonitrides, so preventing chromium carbide precipitation. However, titanium is not so effective in preventing intergranular failure in oxidising media, as TiN and TiC are vigorously attacked.

In contrast to austenitic stainless steels, ferritic grades are not susceptible to stress corrosion unless they contain copper and nickel which form austenite (martensite). However, in the sensitised condition they are particularly vulnerable to a stress assisted intergranular corrosion, which can result in severe cracking.

In common with austenitic stainless steels, additions of up to 2%Mo have a beneficial effect on pitting resistance, and improve general corrosion resistance.

CHAPTER THREE

3. COLD WORKING, RECOVERY, RECRYSTALLISATION AND GRAIN GROWTH

3.1 COLD WORKING

Cold working is being reviewed as the mechanisms of recovery and recrystallisation depend upon the nature of the cold worked state. Annealed materials contain a low density of dislocations of the order of 10^6 lines cm^{-2}. In bcc metals, there is a rapid increase in the dislocation density as plastic deformation increases and the work hardening rate is high. With increasing reduction, the work hardening rate decreases rapidly. At deformations of less than 1%, dislocations are characterised by fairly straight lines. As deformation proceeds they become increasingly jogged, showing cusps and dislocation loops in the matrix.

Carrington et al[29] found that cusps or dislocations formed by the following reactions for dislocation on intersecting slip planes :

$$\frac{a}{2}\,[11\bar{1}] + \frac{a}{2}\,[\bar{1}11] = a\,[010] \qquad \text{(1)}$$

This reaction results in a decrease in energy, and leads to the formation of triple point nodes which are a common feature of bcc metals. The above dislocation interaction results in the tendency for dislocations inside individual grains to form a cell or subgrain type of structure, and cell formation was observed by many workers[29][30][31] in both polycrystalline and single crystal bcc metals. Cell boundaries are essentially tangles of three dimensional networks of dislocations produced by a reaction of the type given in equation (1). Increasing the degree of deformation causes the cellular structure to become more pronounced and reduces the cell size. It was found[32] that subgrains in cold deformed polycrystalline iron rolled

70% were 0.5 - 1μm in diameter with average misorientations from 2 - 6°. These variations in cell size and misorientation were correlated with the different orientations of the individual grains in which the cells had formed. This will be reviewed later in greater detail in the chapter concerned with textures.

The preceding work assumed that within individual grains the cell misorientation was relatively uniform. However, many workers reported deformation or transition bands formed within individual matrix grains or even in single crystals[33][34]. Transition bands are boundaries between the different parts of the crystal that have undergone different amounts of rotation during deformation, so that there is a high degree of misorientation across the boundaries. These sites are favourable for the nucleation of recrystallised grains.

After cold working, about 10% of the total energy expended in deformation is stored in the metal. The metal is therefore thermodynamically unstable and hence annealing will tend to revert it to its original state by some thermally activated process. Energy is released in two stages. Venturello et al[35] and Antonione et al[36] showed that two distinct slopes occur in hardness versus time or temperature curves for the annealing of iron containing carbon and nitrogen respectively. These two stages were interpreted in terms of recovery and recrystallisation. Recovery which comprises various stages of energy release, is concerned with the removal of strain energy, the annihilation and re-arrangement of dislocations and the removal of point defects (vacancies and interstitials). Recrystallisation however is concerned with the formation of strain free grains and the migration of their boundaries.

3.2 RECOVERY

3.2.1 Basic Recovery

Recovery is accompanied by softening of the cold worked material. Recovery was investigated in zone refined iron by Michalax and Paxton[37]. They evaluated the rate of recovery as a function of deformation temperature, annealing temperature and time. It was found that for a constant deformation and annealing temperature, recovery was characterised by a logarithmic time dependence. The fraction of residual strain hardening was related to the annealing time by :

$$1 - R = b - a \ln.t \qquad \text{——————} \quad (2)$$

where R is the fraction recovered, t is the time and a and b are constants. The fraction of residual strain hardening was expressed as :

$$1 - R = \frac{\sigma - \sigma_o}{\sigma_M - \sigma_o} \qquad \text{——————} \quad (3)$$

σ is the flow stress of the recovered material, σ_o is the flow stress of the fully annealed material, and σ_M is the flow stress of the cold worked material.

Michalax and Paxton[37] and Keh[38] observed a very sharp decrease in the flow stress in the early stages followed by a more gradual change. After longer annealing time, little or no change in flow stress was observed. Keh demonstrated that the initial decrease in the flow stress was associated with the annihilation of dislocations within the cells formed during cold work. During later stages of recovery, the number of dislocations decreased further but less rapidly. However, it was not known why the

initial flow stress remained constant while the dislocation density decreased. A Petch type relationship of flow against subgrain size would be expected leading to a decrease in the flow stress. This type of relationship was observed by Ball[39], who found that the flow stress of iron decreased with increasing subgrain size. Keh[38] postulated that the lack of substructure hardening in his work may be a function of the purity of the metal. He did not observe dislocation pile-ups at subgrain boundaries, which was the basis of the Petch theory, and therefore he concluded that when iron was sufficiently pure, the substructure hardening was negligible.

Michalax and Paxton[37] evaluated activation energies for recovery for a given residual strain hardening. They showed that the activation energy for recovery of iron increased as recovery proceeded. Kuhlmann[40] and Dorn et al[41] suggested that as deformation is heterogeneous; the most highly deformed regions recovered first. As recovery progressed, it became more difficult to make a thermally activated jump energetically feasible because of less assistance from fluctuations in local free energy. However, it would seem more reasonable to assume that there are several reactions occurring concurrently during recovery and that it can be divided into two main stages :

i. The first is concerned with the annihilation of dislocations of unlike sign and the removal of point defects. Values for the activation energy for the early stages of the recovery of iron were comparable with those for the migration of vacancies.

ii. The second is the formation of a stable dislocation array, i.e. the formation of low angle grain boundaries by polygonisation and the migration of those boundaries. In zone refined iron, the activation energy for the later stage of recovery was in excellent

agreement with that for self-diffusion of α iron[43], approximately 280 KJ/Mole.

Both stages involve climb, cross-slip, and glide of dislocations and can only occur if there is sufficient thermal activation. Seeger[42] postulated that recovery occurs by thermally activated double cross slip, that annihilated unlike screw dislocations. Thus, the activation energy was dependent on the length of the dislocations and the separation distance between them. A similar model for the annihilation of dislocation dipoles was analysed by Li[44] which considered the attractive force between two dislocations of opposite sign and showed that this varied inversely with their separation and directly with their mobility. Therefore, in the early stages of recovery, annihilation takes place mainly of dislocations which are close together, thus requiring very little thermal activation and hence, a low activation energy. At later stages, distances through which dislocations must move before annihilation can occur are greater, movement of dislocations requiring the diffusion of vacancies, which necessitates greater thermal activation, and hence a higher activation energy.

Subsequent or concurrent to the process of annihilation of dislocations is a process by which dislocations of like sign align themselves into a lower energy configuration. This process is known as polygonisation and was discovered independently by Cahn[45][46] and Beck[47]. A continuously bent lattice must contain an excess of dislocations of one sign, as also must cell boundaries, for there to be a misorientation between adjacent cells. Two types of boundaries are possible, namely a tilt or a twist boundary, or mixtures of both. If all the excess dislocations are edge dislocations, i.e. tilt boundary, the energy may be decreased by the alignment of the dislocations in a wall. To achieve polygonisation, dislocations must climb and glide and hence thermal activation is required, particularly

in the case of climb, for the diffusion of vacancies to dislocations. Therefore, the activation energy for this process would be expected to be greater than for dislocation annihilation.

Further decreases in stored energy occur when the cells begin to grow, or subgrain boundaries begin to migrate in order to decrease their energy. Two processes were observed for the growth of subgrains :

a. Subgrain growth

b. Subgrain coalescence and re-orientation.

These processes will be discussed later in the section on recrystallisation.

3.2.2 The Effect of Solute Elements on Recovery

Leslie et al[48][49] in experiments using pure iron and dilute iron alloys, Antonione et al[36] and Venturello et al[35] using pure iron containing interstitial solutes, studied the effects of solute elements on recovery and recrystallisation. Graphs of percentage softening against percentage recrystallisation for both pure iron and its alloys showed that for a constant percentage recrystallisation, more recovery occurred in the pure iron. This was attributed to retardation of recovery by solute atoms. At a temperature of 400°C, the time required for equal amounts of recovery for carburised and nitrided iron was 10^2 and 10^3 times respectively that for pure iron. Similar results were obtained using iron-manganese alloys. Little or no recovery occurred after fifteen hours at 400°C, but at 600°C the alloy recovered faster than the pure metal. Leslie[48] explained this in terms of an increased dislocation density in the deformed iron-manganese alloy compared with pure iron.

Earlier it has been stated that the rate of recovery was affected by the mobility of dislocations. It is known that the free energy of the system is lowered when solute atoms segregate to vacancies, dislocations or grain boundaries. Solute atoms segregated to dislocations thus reducing their mobility. In terms of the Cottrell[50] theory of dislocation 'atmosphere' formation, the rate of movement of the dislocation was controlled by the diffusion of the solute atom. Therefore the movement of dislocation is slow.

An increase in the temperature reduces the number of solute atoms which interact with dislocations and also increases their diffusion rate. If it is considered that the interaction energy is proportional to the number of interacting atoms, then the effect of temperature on the concentration of solute in the dislocation atmosphere is given by :

$$C = Co\, e^{\frac{-V}{kT}} \qquad \text{——————(4)}$$

where V is the interaction energy, k is Boltzmann's constant, T is temperature in ^{o}K, and C and Co are the solute concentrations at the dislocation and in the matrix respectively.

For carbon and nitrogen at low temperatures, there is a strong interaction between dislocations and the solute atoms. Hence, dislocation mobility is impeded to such an extent that only local annihilation and rearrangement is possible. As the temperature increases, the dislocation escapes from its 'atmosphere', i.e. the atmosphere 'boils off'. The temperature at which this occurs depends on the solute. For carbon and nitrogen in iron, the temperature at which the interstitial atoms begin to 'boil off' is around $400^{o}C$. Additions of substitutional solute atoms increase the strength of the interaction of the interstitial atoms with dislocation

because of a higher interaction energy. This is particularly the case with strong carbide or nitride formers, such as chromium, molybdenum, vanadium. In ferritic stainless steels, Lagneborg[14] found that carbide and nitride precipitates were associated with dislocation and grain boundaries, which suggests a strong interaction. Glen[51] carried out work using additions of manganese, chromium and molybdenum to low carbon steels, to measure the effects of substitutional elements on strain ageing. In general two strain ageing peaks occurred and were interpreted in terms of solute interactions with dislocations. The first, at around 200°C, was associated with carbon and nitrogen atoms diffusing to the dislocations during straining. The second was a result of either precipitation of an alloy carbide or nitride at the formation of M-C/M-N 'atmospheres' at the dislocation. In either case, diffusion of solute atoms to the dislocation was required. Although strain ageing peaks for carbon and nitrogen occurred at around 200°C for strain aged specimens, carbon and nitrogen had a considerable effect on recovery at 400°C[35][36]. Similar effects on recovery were also observed in iron-manganese alloys[48], indicating that 'atmospheres' were effective in retarding recovery at temperatures well in excess of the strain ageing peaks.

3.3 RECRYSTALLISATION

Basic recrystallisation is being reviewed in order to apply recrystallisation theories to ferritic stainless steels.

Recrystallisation is a process involving the nucleation and growth of strain free grains from a cold worked or recovered matrix. The work of Leslie et al[48] using pure iron showed that recrystallisation was a growth controlled process and that nuclei were present at zero time. However, in commercial materials, it has been shown that nuclei are not available

for growth at zero time and that the nucleation stage is probably more important than the growth stage in determining the rate of recrystallisation (31) (64) (70) (74) (76). General nucleation and growth will be the main feature of this discussion. The effect of orientation will be discussed later in relation to recrystallisation textures.

3.3.1 Nucleation

i. Currently, there are four suggested nucleation mechanisms :

The Classical Model

This was based on the assumption that the nucleus which was capable of growth was formed as a result of thermal fluctuations in the same manner as the classical theory of phase transformations (52). The change in free energy, on forming the embryo, was therefore given by Volmer's equation for a spherical grain :

$$\Delta F_T = 4\pi r^2 \gamma - \frac{4}{3}\pi r^3 \Delta F_v \qquad \text{(5)}$$

where ΔF_v is the difference in strain energy between the cold worked and recrystallised states, γ is the interfacial energy between strained and recrystallised regions. Bailey (53) and Cahn (54) and others showed that homogeneous nucleation in terms of Volmer's equation is almost impossible in recrystallisation. This was because of the high surface free energies of high angle boundaries compared with the small driving force of the stored energy of cold work resulting in activation energies and critical nucleus sizes which were far too large.

Heterogeneous nucleation is a possibility with the new grain forming a lens shaped region on a pre-existing grain boundary. The use of the theory of heterogeneous nucleation shows that the critical energy to form a nucleus can be reduced by a factor of :

$$\frac{(2 + \cos\theta)\ (1 - \cos\theta)^2}{2} \qquad \text{(6)}$$

(where θ is the angle of contact at the grain boundary)

This makes very little difference to the conclusion that nucleation is very unlikely by the classical nucleation model, as even with heterogeneous nucleation, the surface energy is prohibitively high compared with the driving force of cold work.

Pre-existing Nucleation Models

Modern theories of nucleation are based on models that the nucleus is pre-existing within the cold worked structure. The nucleus is thought to be formed by a recovery process. Orowan[55] pointed out that a potential pre-existing nucleus below the stable size as determined by Volmer's equation cannot vanish because its periphery is pinned by the dislocations surrounding it. Even though embryos do not seem able to disappear, Volmer's equation must be satisfied for growth of the nucleus to occur and the critical nucleus size, as indicated by Volmer's equation, must be exceeded.

Horiuchi and Gokyi[56] attempted to quantify the critical nucleus size in terms of the migration of a high angle grain boundary. The driving force for boundary migration, P, is given by :

$$P = P_e + P_f + P_r + P_c \qquad \text{(7)}$$

where P_e is due to strain energy, P_f is due to the interaction of solute atoms or precipitates, P_r is due to boundary energy and P_c is due to chemical energy. For a pure material, only P_e and P_r need to be considered. If for a spherical grain P_r is given by the following equation :

$$P_r = \frac{2\sigma}{R} \qquad \text{——————} \quad (8)$$

where R is the grain radius and σ is the grain boundary energy which is written as :

$$\sigma = A\theta(B - \ell n\theta) \qquad \text{——————} \quad (9)$$

where A and B are constants. By assuming a value of θ for a high angle grain boundary, the critical nucleus size for the migration of a high angle grain boundary is attained when :

$$P_e = P_r$$

or

$$P_e = \frac{2\sigma}{R} \qquad \text{——————} \quad (10)$$

It can be seen that factors which determine the strain energy, e.g. degree of cold work and/or prior recovery, have an effect on the critical nucleus size. Small degrees of cold reduction or large amounts of prior recovery increase the critical nucleus size because of a decrease in the driving force.

At present three models for pre-existing nucleus models are used :

a. Subgrain coalescence;

b. Subgrain growth;

c. Strain induced boundary migration.

The subgrain coarsening models are associated with heterogeneous nucleation. The assumption was that in the material pre-formed regions of high dislocation density exist which were strongly misoriented with respect to their environment. At first low angle grain boundaries (subgrains) are formed, and from these mobile high angle boundaries finally evolve at some places. This was considered to be possible in two ways, by 'subgrain growth' and by 'subgrain coalescence'.

a. Subgrain Coalescence

The process of subgrain coalescence was observed by Hu[30] and Goodenow[31] and occurs by the common elimination of boundaries between adjacent subgrains. One pre-requisite of subgrain coalescence was that re-orientation must occur in order to preserve continuity in the new grain. This was not the case for subgrain growth.

The process of subgrain coalescence was analysed by Li[57] in terms of a model in which grains are thought to rotate bodily by diffusion processes until they achieve coincidence. Li[57] showed that the time (t) taken for two subgrains to coalesce can be calculated from the following :

$$t = \frac{d_s^2 \, KT}{3D \, E_o \, b^2 j} \qquad \text{(11)}$$

where d_s is the subgrain size, D is the diffusion coefficient, b is the Burgers Vector, and j is the jog density. The value of E_o was estimated from the following equation, assuming edge dislocations :

$$E_o = \frac{\mu b}{4\ (1 - V)} \qquad \text{(12)}$$

where V is Poisson's ratio, and μ is the sheer modulus. Smith and Dillamore[58] attempted to use equation (11) to compare experimental results of subgrain growth in high purity iron, with the theoretical expression for subgrain coalescence. Using Li's[57] value for j they found that the experimentally determined growth rates were 4 - 5 orders of magnitude faster than predicted, and concluded that sub-boundaries migrate rather than coalesce.

Although Hu[59] has argued that metallographic evidence shows that subgrain coalescence does occur, this evidence may be ambiguous because of the experimental techniques used :

i. Direct observation in a thin foil heated in the electron-microscope;

ii. Observation of material annealed in bulk then thinned.

The first technique is highly suspect as processes observed in a heated thin foil may not take place in bulk material, due to dislocations being able to climb to a free surface.

The second technique allows a partially coalesced region to be observed, and therefore there was no evidence to suggest that subgrains were not in that state before thinning. Thinning may also allow coalescence to

take place because of dislocations gliding to a free surface.

b. Subgrain Growth

This involves the growth of subgrains to a point where high angle boundaries are formed, followed by the migration of those boundaries. This process of nucleation has been verified by many workers. Cahn[45][46] postulated that some subgrains grow preferentially to others, but he thought that recovery and recrystallisation were two separate stages. It was proved conclusively by Bollman[60] and many other workers that recovery and recrystallisation are competitive processes, i.e. recovery was still taking place in the unrecrystallised matrix.

A potential recrystallisation nucleus is invariably a subgrain which at a critical stage in its development is distinguished from its neighbours by a size advantage. Because the process of subgrain growth is analogous to grain growth of recrystallised grains, Smith and Dillamore used the approach to grain growth adopted by Hillert[61] for grain growth in a single phase material and were able to interpret their results in terms of sub-boundary migration. The size advantage required by a potential nucleus can be discussed in terms of the equations of Hillert[61] and Gladman[62]. These will be discussed in more detail later in the section on grain growth.

The rate of growth of a subgrain will depend on the

relative size advantage of that subgrain. The larger the subgrain with respect to the surrounding subgrains, the faster it will grow. Therefore only the larger subgrains will become viable nuclei. Both these models assumed that the grain size was heterogeneous, i.e. that there was a distribution of grain size, and indeed Smith and Dillamore[58] observed a considerable distribution in the cold worked subgrain size. The critical condition for nucleation was the formation of a high angle grain boundary, and so conditions that promoted a large lattice curvature, i.e. a high degree of cold reduction, deformation bands, and pre-existing grain boundaries make nucleation by subgrain growth easier. Because high angle grain boundaries can migrate several orders of magnitude faster than for low angle boundaries,once a high angle boundary is formed, it will consume the adjacent substructure by boundary migration.

c. Strain Induced Boundary Migration (SIBM)

In this process, a subgrain (subgrains) adjacent to a pre-existing grain boundary in one grain grows by migration of the boundary into the neighbouring grain. The process of SIBM was first observed by Beck and Sperry[63] in cold worked aluminium, Bailey and Hirsch[54] in silver and Leslie et al [64] in iron-0.08% copper observed SIBM by electron microscopy after moderate reductions. Bailey and Hirsch[54] thought SIBM to be an important mechanism in fine grained materials at moderate deformations because of the relatively small misorientations between

cold worked cells, making nucleation by subgrain growth difficult.

A model for strain induced boundary migration was discussed by Bailey[65]. Figure 7 illustrates a schematic representation of two pre-existing grains, A and B, of which a segment of grain boundary, of length 2L, bulges into grain A. If grain A has a higher dislocation density than grain B, grain B will bulge into grain A providing certain energy relationships are satisfied.

The basic condition required for the bulge to grow is given by :

$$L > \frac{2\sigma}{\Delta E} \qquad \text{(13)}$$

where σ is the surface energy and ΔE is the difference in stored energy per unit volume, across the grain boundary.

However, why SIBM was not observed after high deformations was not clear. Large deformations would favour a difference in dislocation density between adjacent grains, i.e. large values of ΔE, which would be favourable for SIBM. It may be that at large deformations, other recrystallisation mechanisms are more favourable, e.g. subgrain growth.

ii. Nucleation Sites

Recrystallisation has been observed at three types of site :

a. At pre-existing grain boundaries;

b. At inclusions or second phase particles;

c. In the interior of grains.

a. Pre-existing Grain Boundaries

The effectiveness of pre-existing grain boundaries as sites at which nucleation of recrystallised grains can occur has been well established. The exact nature of pre-existing grain boundaries in relation to nucleation however was not clear, but it was observed that crystal orientations change rapidly adjacent to and across pre-existing grain boundaries.

At least two mechanisms may operate at grain boundaries leading to the formation of recrystallised grains. One was that the boundary bows into the grain with the highest stored energy. This is certainly a possibility as grains of different orientations have differing degrees of stored energy[32][58]. Another mechanism was that a nucleus may develop from a subgrain at or near to a pre-existing grain boundary by a subgrain growth mechanism. This is also highly probable because of the higher stored energy near to the grain boundary. In terms of equation (10) the higher stored energy adjacent to grain boundaries leads to a decrease in the critical nucleus size, and therefore grain boundaries are favourable sites for nucleation.

b. Inclusions and Second Phase Particles

There have been many conflicting results concerning the role of second phase particles on the recrystallisation of metals. Some investigators reported that dispersed second phase particles accelerated recrystallisation whereas others reported an opposite effect. The most important factors were :

i. Particle distribution (i.e. the mean free path between each particle);

ii. Particle size;

iii. Whether particles were present during cold work or were formed during annealing.

Acceleration of recrystallisation was generally associated with large particle spacings. Martin[66] showed that an interparticle spacing of 8μm for internally oxidised copper accelerated recrystallisation. English and Backofen[67] observed new grains forming at the matrix/inclusion interface. On the other hand, all reported observations of particle-retarded recrystallisation were made on alloys for which the interparticle spacing was the order of 1μm or less.

Doherty and Martin[68] and Mould and Cotterill[69] investigated the effects of interparticle spacing on recrystallisation. Separation between particles was found to be more important than particle size, which was always below 1μm. Coarse spacings accelerated

recrystallisation whilst fine spacings retarded recrystallisation. Doherty and Martin (68) observed a critical spacing above which nucleation became easier. This spacing was correlated with the impingement of subgrains with second phase particles. It was found[70] that as the amount of second phase particles increased, an increased nucleation rate occurred and only particle sizes greater than the critical nucleus size acted as nuclei. They also observed a retarded recrystallisation rate with fine second phase particles. It seems a widely held opinion that the increase in recrystallisation by the larger second phase particles was a result of an increase in the nucleation rate. Very little effect on the growth rate was observed.

Several mechanisms were postulated as to why second phase particles are favourable sites for nucleation. It was reported by many workers that inhomogeneous deformation occurred at or near to the particle/matrix interface. It is difficult to observe this in heavily deformed metals, but light deformation of an iron-bismuth alloy produced higher observed dislocation densities in the region of second phase particles[64]. Doherty and Martin[68] accounted for the increased incidence of recrystallised grains on the basis that cold work increases the lattice curvature adjacent to the dispersed phase. However, it was found[71] that the misorientation between subgrains increased around carbide particles, average misorientations of 14^{o} in the region of particles compared with 8^{o} in the matrix

material. From the theory of Cahn[45] that subgrains grow until high angle boundaries are formed, regions adjacent to particles will have a higher lattice curvature than the matrix, with a resulting increase in the stored energy and therefore nucleation will be easier.

It was suggested[70] that increases in the nucleation rate may be due in part to increases in the dislocation density at the ferrite/carbide interface. They postulated that interfaces are always sites for nucleation as the particle occupies part of the interface between grain and matrix. Thus, the surface energy barrier for nucleation is reduced. In addition, increases in dislocation density increase the driving force for recrystallisation. From the theory of Cahn,[45] for the second phase particle to act as a nucleus it must be greater than the critical nucleus size defined by Volmer. Therefore, with increasing deformation, the critical nucleus size may decrease slightly so that smaller particles may be effective nuclei. The approach of Gladman assumed that the particle occupied part of the grain boundary. If a particle occupies part of the grain boundary interface, the energy associated with a grain boundary will be reduced. This means that the critical nucleus size for the migration of a high angle boundary will be reduced thereby giving easier nucleation. The particle size in the work of Doherty and Martin[68] and Mould and Cotterill[69] were less than 1 μm and thought to be smaller than the critical

nucleus size. This may explain why nucleation was not observed at the particle/matrix interface.

c. Nucleation within the Grain

In single phase metals, nucleation was observed at two distinctly different intragranular sites :

i. In regions of relatively uniform misorientations;

ii. In regions of high misorientations, e.g. deformation or transition bands.

In type (i) sites, subgrains grow by a mechanism previously outlined in the section on sub-boundary migration. This type of mechanism was observed only at moderately high deformations, since at lower deformations there is insufficient misorientation between adjacent subgrains to allow a high angle boundary to be created[72].

Nucleation in type (ii) sites was observed to be operative in single crystals of silicon iron[33][34]. Nucleation takes place at the deformation band/matrix interface in the region of the greatest misorientation. Misorientations as high as 52^{o} were observed between deformation band and matrix[34]. As deformation bands are regions of high misorientations, high angle boundaries are easily created, and hence they are regions where early nucleation takes place. Nucleation at deformation bands will be reviewed in greater detail later in the section on textures.

3.3.2 Particle Retarded Recrystallisation

Two types of particle retarded recrystallisation have been observed :

i. Retarded recrystallisation by a very fine dispersion of particles which were present before cold working;

ii. Retarded recrystallisation as a result of the precipitation of particles on subgrain boundaries or dislocations during annealing.

In steels, titanium carbide[73], niobium carbide[70][74] and vanadium carbide[70] were observed to belong to the former category, while aluminium nitride[31][75] and copper[64][76] represent the latter.

In aluminium alloys, Doherty and Martin[68] found a critical interparticle spacing below which nucleation was difficult. This was correlated with the impingement of subgrain boundaries with surrounding particles before nucleation occurred. This indicated that the critical interparticle spacing was dependent on the degree of cold reduction which, in fact, proved to be the case. Gladman et al[70] found similar results for steels containing fine dispersions of niobium carbide and vanadium carbide, which inhibited sub-boundary movement and retarded recrystallisation. Leslie[64] and Goodenow[35] found that the precipitation of copper and aluminium nitride decreased recrystallisation rates. However, there was one obvious difference between recrystallisation in the presence of a fine dispersion of second phase particles and recrystallisation with concurrent precipitation. For the latter to be effective, precipitation must take place before recrystallisation starts, i.e. during the recovery process. Once precipitation has taken place, the mechanisms involved in particle retarded recrystallisation were essentially the same. Since precipitation and

recrystallisation processes exert a mutual influence on each other, a brief survey of precipitation will be given :

i. Precipitation from Solid Solution

The incubation time, tp, required for precipitation from solid solution obeys the following equation :

$$\ln tp = \frac{(Q_D + Q_p)}{RT} - \ln A \qquad \text{(14)}$$

where Q_D is the activation energy for diffusion , Q_p is the activation energy for nucleating the precipitating phase, R is the gas constant, T is in degrees Kelvin, and A is a constant. The value of $\frac{Q_D}{RT}$ increases with decreasing temperature as Q_D is approximately constant, while the value of $\frac{Q_p}{RT}$ decreases with decreasing temperature as Q_p is infinite at the equilibrium temperature, T_E. The incubation time, tp, will therefore decrease with decreasing temperature, in a manner shown schematically in Figure 8. At lower temperatures, the incubation period increases because of diffusion control. Because the critical nucleus size for precipitation decreases with decreasing temperature, the particle size will also decrease, with resulting increase in the number of particles at a constant volume fraction. Also because of the decreasing solubility of solute atoms with decreasing temperature, the volume fraction of second phase particles further increases.

ii. Effect of Cold Work on Precipitation

The effect of prior cold work with few exceptions, increases

the rate of precipitation from supersaturated solid solution. This is presumably because of dislocations and subgrain boundaries acting as low energy sites for nucleation. In supersaturated solid solutions, precipitate particles nucleate from 'solute atmospheres' which are associated with dislocations. Increasing the degree of reduction decreases the incubation period required for precipitation from supersaturated solid solution because of an increased dislocation density. However, not only does prior cold work decrease the incubation period for nucleation, it has also been reported to suppress the formation of metastable precipitates[77]. This is because little or no barrier to nucleation of precipitates exists at dislocation, therefore the formation of a metastable product is less favourable. Wilson[78] found that during the tempering of a deformed medium carbon steel, the first discrete particles to precipitate were Fe_3C and not ε carbide.

iii. Particle Coarsening

Since particle coarsening is a pre-requisite for nucleation of recrystallised grains, in the presence of a fine dispersion of second phase particles, it will be briefly discussed. Particle coarsening was the subject of theoretical work by Lifshiftz and Sloyov[79] and by Wagner[80]. The two papers were fundamentally equivalent and analysed two different coarsening situations distinguished by the rate controlling process.

Both models assumed particle growth under conditions of Ostwald ripening (i.e. the growth of large particles at the expense of small particles for a given volume fraction of particles).

Thus, the driving force for growth was the decrease in the surface free energy/unit volume as a result of particle growth. Lifshiftz and Sloyov[79] assumed interface control where the rate determining process was the transfer of atoms across the particle/matrix interface. The Wagner[80] model assumed diffusion control where the rate of coarsening was limited by the rate of diffusion on the constituent atoms through the matrix. The Wagner equation can be expressed as follows :

$$(\overline{r_t})^3 - (r_o)^3 = \frac{8\sigma_p D\, Co\, V_m\, t}{9RT} \qquad \text{(15)}$$

where $\overline{r}_t$ is the average particle radius at a time, t, r_o is the average particle radius at the onset of particle coarsening, D is the diffusivity of the particle species in the matrix, Co is the concentration of the particle species in the matrix, σ_p is the surface energy between particle and matrix, R is the gas constant, T is in Kelvin. As the expression assumed that particle coarsening was dependent on the rate of diffusion of the substitutional element to the particle, therefore in the case of a multi-component system, particle coarsening will be controlled by the rate of diffusion of the slowest diffusing species.

The implication from this equation (15) is that compositional changes that reduce Co, will reduce the rate of particle coarsening by reducing the concentration gradient adjacent to the particle. This was found to be the case[81]. Aluminium contents in steels in excess of those stoichiometrically required to form aluminium nitride were found to increase the rate of particle coarsening. However, titanium contents less than those required to form titanium nitride produced titanium nitride particles in austenite which were

extremely resistant to coarsening[82]. This was thought to be in part because of the extremely low concentration of titanium in solution. However, coupled to this was the extremely low solubility of TiN in austenite. This will also reduce the particle coarsening rate, as dissolution of fine particles is a pre-requisite for growth of the coarser particles.

iv. Effects of Precipitation on Recrystallisation

Köster[83] discussed the precipitation-recrystallisation reaction in terms of four temperature ranges (fig 9) :

Range 1 : above T1, annealing in the single phase region normal recrystallisation takes place.

Range 2 : T1 - T2, recrystallisation was completed before precipitation starts therefore there is no effect on recrystallisation. This was as a result of a long incubation period for precipitation because of a low degree of supersaturation.

Range 3 : T2 - T3, Discontinuous recrystallisation with simultaneous precipitation.

Range 4 : below T3, continuous recrystallisation and precipitation.

The term 'discontinuous' referred to a normal recrystallisation mechanism, i.e. a nucleation and growth process, while 'continuous recrystallisation' referred to the growth of subgrains to form a high angle boundary, without the migration of the boundary.

The processes of 'continuous recrystallisation' and 'discontinuous recrystallisation' during the incubation period must be the same since they involve subgrain growth. It was assumed[83] that the critical condition for the replacement of 'discontinuous' by 'continuous' recrystallisation can be satisfied when the retarding force exceeds the driving force for boundary migration. However, it was not clear how in the presence of pinning particles, subgrain growth can take place while boundary migration cannot, since the driving force for boundary migration was greater than that for subgrain growth.

Below T2 in Figure 9, precipitation and recrystallisation exert a mutual influence on each other. In a deformed and supersaturated alloy, the volume fraction of second phase particles present before the start of recrystallisation at temperature T2 in Figure 9 was zero, i.e. t_p intersects t_r. As the temperature decreases an increasing number of precipitates are present before recrystallisation starts because of a decreased incubation period for precipitation, and a decreasing solid solubility; simultaneously the particle size also decreases.

If it is assumed that subgrain growth obeys the same laws as grain growth[58], when particles are situated at subgrain boundaries a minimal particle size is required for the unpinning of the subgrain boundaries. The following relationship was obtained by Meyzaud and Parnière[84]:

$$d_{crit} = \overline{D} \sqrt{\frac{f\, t^2}{2(t-1)}} \qquad \text{(16)}$$

where d_{crit} is the uniform size of particles, $\overline{D}$ is the mean subgrain diameter, f is the precipitated volume fraction, and $t = \frac{D}{\overline{D}}$ the size factor in the subgrain size distribution. Thus for a given subgrain size distribution, this critical particle size was roughly proportional to the mean subgrain diameter.

Since fine particles, an increased volume fraction of second phase particles and slow particle coarsening rates are favoured by low temperatures, the start of recrystallisation will increase dramatically with decreasing temperature. Goodenow[31] found that the increased incubation period for the start of recrystallisation coincided with an increased grain size which increased with decreasing temperature. This was discussed in terms of a decreasing nucleation rate with decreasing temperature. Because of sequential unpinning of subgrain boundaries, the time available for growth of the first nucleated grains, i.e. small values of $\overline{D}$, was increased resulting in an increased grain size. At lower temperatures, the rate of particle coarsening decreases and the volume fraction of particles increases. Therefore the time available for growth of the first nucleated grains will increase still further, resulting in a further decrease in the nucleation rate and an even coarser grain size.

v. Effects of a Fine Dispersion of Second Phase Particles on Recrystallisation

The mechanisms involved are similar to those for grain growth in the presence of second phase particles, which will be discussed in the section on grain growth.

3.3.3 Boundary Migration

i. General Boundary Migration

Once a subgrain attains a high angle grain boundary, the grain can grow by boundary migration provided that there is sufficient driving force. High angle grain boundaries are those with misorientation of greater than 10 - 15° with respect to the adjacent cold worked or recovered matrix. The rate of boundary migration obeys the following equation[85][86]:

$$V = M_G P \qquad \text{——————} \quad (17)$$

where V is the rate of boundary migration, M_G is the intrinsic migration rate and P is the driving force. The value of P increases with increasing cold reduction and decreases as a result of prior recovery. Values for M_G depend on the solute content, temperature and the presence of second phase particles. For very pure metals, M_G obeys the following relationship :

$$M_G = \frac{D_G}{KT} \qquad \text{——————} \quad (18)$$

where

$$D_G = D_o \, e^{-\frac{Q_{GB}}{KT}} \qquad \text{——————} \quad (19)$$

where D_G is the grain boundary diffusion rate, K is Boltzmann's constant, T is in Kelvin, D_o is the diffusion coefficient, and Q_{GB} is the activation energy for grain boundary diffusion. In fact, for very pure metals, many workers found the activation energy, Q, for recrystallisation approximates that for grain

boundary diffusion, Q_{GB}.

Early work by Vandameer and Gordon[87] showed that the growth rate was linear with time, and that the value of P was apparently constant with time. However, more recent work[48][49][86] showed this to be incorrect, the growth rate decreasing with time. This was attributed to concurrent recovery occurring in the matrix regions in front of the migrating grain boundary, thus lowering the driving force, P, for boundary migration.

ii. Effects of Impurities on Grain Boundary Migration

Small additions of impurities have an extremely strong influence on the recrystallisation of metals. The effect was found to be the greatest with the first very small quantities of alloying element added. Additional quantities showed comparatively little effect. The reasons for this are still not clear, apart from the fact that solute atoms interact with dislocations and grain boundaries and reduce their mobility.

Theories for retarded growth were advanced by Lücke and Detert[85], Gordon and Vandameer[86], Cahn[88] and Lücke and Stüwe[89][90]. These theories assumed that in solid solutions, elastic interaction exists between solute atoms and grain boundaries.

Lücke and Detert[85] were the first to attempt to formulate a quantitative theory for boundary migration in solid solutions. It was assumed that segregation of impurities would occur to a grain boundary and when the boundary moved the 'atmosphere' was carried along with the boundary. The concentration at the grain

boundary was assumed to obey the Boltzmann distribution function, i.e. equation (4), which was valid only at low concentrations. The rate of boundary migration was reduced at any temperature by the necessity for impurity atoms to diffuse along with the moving boundary. The theory predicted the following modes of boundary migration :

a. If the external force exceeded the maximum interaction force, the boundary was accelerated and broke away from the solute atmosphere and migrated at a rate determined by equation (17).

b. At low temperatures, and/or relatively high solute contents, the rate of migration, M_G, was controlled by the rate at which solute atoms diffuse with the boundary. In this case, the rate of boundary migration can be expressed by the following equation :

$$V = \frac{a^2}{2\sqrt{3}} \cdot \frac{D_o}{KT} \cdot \frac{P}{Co} \cdot e^{\left(-\frac{Q_D+V}{KT}\right)} \qquad \text{(20)}$$

where a is the lattice parameter, D_o is the bulk diffusion coefficient of the solute, Co is the atomic fraction of the solute, Q_D is the activation energy for bulk diffusion of the solute, and V is the interaction energy between the solute and grain boundary. Since the rate of boundary migration was assumed to be controlled by the diffusion of impurity atoms, the activation energy for boundary migration should approximate to that for volume diffusion. In fact higher activation energies were obtained than those predicted from the theory. It

was predicted that impurities which diffuse rapidly in the bulk matrix should have less influence in retarding the motion of a grain boundary than impurity atoms which diffuse more slowly. This prediction was not supported by experimental evidence[48][49].

Gordon and Vandameer[86] advanced a modified form of the Lücke and Detert[85] model of impurity controlled boundary motion. It assumed that the observed activation energy should be significantly less than that for bulk lattice diffusion of the impurity, since it represents the diffusion of the solute in the region near to the grain boundary and not in the undistorted lattice. Gordon and Vandameer[86] were able to explain experimental studies on zone refined aluminium with additions of up to 0.025% Cu in terms of this theory. However, the same contradiction which applied to the Lucke and Detert model, concerning the observed greater retarding effect of fast diffusing solutes, applied to their treatment. The modification predicted lower activation energies for boundary migration which in fact was the opposite of the experimental evidence.

Cahn[88], Lücke and Stüwe[89] developed a more rigorous treatment of the effects of impurity drag on grain boundary motion. Since these theories were quite similar, only that of Cahn[88] will be considered. The boundary was considered to be a planar discontinuity, charactersied by a diffusion coefficient and an interaction potential with solute atoms which unlike the previous theories was either positive or negative. For a stationary boundary, the distribution of solute atoms was assumed to be symmetrical about the centre line of the boundary.

Cahn considered two cases :

a. A low velocity case, which results in the impurity drag being proportional to the boundary velocity;

b. A high velocity case, which considered that the impurity drag was inversely proportional to the boundary velocity.

When the boundary velocity was zero, the drag was zero because of the symmetrical distribution of atoms at the stationary boundary. As the boundary moves, the distribution of atoms becomes asymmetrical. The number of asymmetrically disposed atoms increases with increasing velocity and the number of asymmetrically disposed atoms determines the drag exerted by the boundary, because the solute atoms are trying to return to their symmetrical distributions. At high velocities, the magnitude of the solute segregation is so reduced that it becomes the dominant factor and the drag diminishes with increasing velocity. A greater drag was predicted therefore for slowly diffusing species than for rapidly diffusing species, at low migration rates, whereas at high migration rates, rapidly diffusing species produce a greater retarding effect. This may explain the observations of Aust and Rutter[91][92][93] who found that rapidly diffusing solute elements retarded boundary migration to a greater extent than solute elements that diffused more slowly. Gordon and Vandameer[86] were also able to interpret experimental data for the recrystallisation of aluminium containing 0.025%Cu in terms of the theory of Cahn[88].

However, treatments discussed can only be related to dilute solutions and cease to be appropriate at quite modest concentrations.

This is because Boltzmann's distribution is assumed which may allow the boundary to become saturated at matrix concentration as low as 10^{-5} at %. Lücke and Stüwe[90] extended their theory to include more concentrated solutions. However, no experimental work has been forthcoming to verify the work[90]. Clearly this is an important area where more theoretical and experimental work is necessary.

iii. Effect of Second Phase Particles

Second phase particles have been shown to exert a retarding force on a mobile high angle grain boundary. The magnitude of this force, P_r, was assumed by Zener[94] to be :

$$P_r = \frac{3 f \sigma_b}{2 r} \qquad \text{(21)}$$

where f is the volume fraction, σ_b is the surface energy of the grain boundary, and r is the radius of the particle. For high degrees of deformation, large particles and/or low volume fractions, the effect of particles can be neglected because the driving force will be large when compared with the retarding force. However, at low degrees of deformation or if the particle diameter is small, i.e. of the order of 0.1μm and the volume fraction, f, is large, particles have a considerable effect in retarding the migration of a high angle grain boundary.

3.4 GRAIN GROWTH

The term 'grain growth' refers to phenomena involving an increase in the size of strain-free polycrystalline grains, following primary recrystallisation.

Two types of grain growth have been identified :

3.4.1 Normal Grain Growth

This is characterised by the maintenance of an equiaxed grain structure in which the distribution of grain sizes and shapes retains a constant form, i.e. this corresponds to changes that are indistinguishable from photographic magnification.

3.4.2 Abnormal Grain Growth or Secondary Recrystallisation

Under conditions of abnormal grain growth, the grain size is not invariant, as the grain size increases because of the development of a coarse irregular grain structure. The driving force for grain growth whether normal or abnormal is derived from the decrease in the grain boundary energy that occurs during grain growth.

3.4.3 Grain Growth in Single Phase Metals

Burke[95] formalised the concept of boundary curvature as the driving force for grain growth in the relationship :

$$\frac{dD}{dt} = \frac{K}{D} \qquad \text{(22)}$$

where D is the grain diameter, t is the time, and K is a constant. Equation (22) assumed that the rate of growth of grains was proportional to the radius of curvature of the average grain at a given instant in time. This assumption is valid only if grain boundaries behave in a similar manner to a soap film. In the case of a soap film, boundaries move as a result of gaseous diffusion caused by a pressure difference from one side

of the soap film to the other. The pressure difference is proportional to the curvature of the boundary. However, little is known about the mechanisms by which atoms on one side of a grain boundary cross the grain boundary and join the grain on the other side.

Equation (22) is usually expressed in an integrated form as :

$$D^2 - D_o^2 = Kt \qquad \text{(23)}$$

where D_o is the initial grain size. For small initial grain sizes, $D \gg D_o$ and therefore the equation is frequently expressed as :

$$D = K' t^{\frac{1}{2}} \qquad \text{(24)}$$

where $K' = \sqrt{K}$. At a superficial level, equation (24) has been confirmed by experimental data, but in general the time exponent of t was less than the ideal value of 0.5.

A more detailed treatment of grain growth was proposed by Hillert[61] who considered individual grains in an environment of a grain size distribution. Hillert's[61] equation was based on the generally accepted assumption that the rate of migration of a boundary depends on the product of intrinsic migration rate and driving force. The driving force was assumed to be because of the size difference between a critical grain size, Rcr, and the grain under consideration. The equation can be expressed as follows[61]:

$$\frac{dR}{dt} = \alpha M \sigma \left(\frac{1}{Rcr} - \frac{1}{R} \right) \qquad \text{(25)}$$

where R is the radius of the grain under consideration, Rcr is the critical radius, α is a constant, M is the intrinsic migration rate, and σ is

the grain boundary energy. Only grains larger than Rcr will grow, and the value of Rcr is $\frac{8}{9}$ the value of the mean grain size. Growth rate increases with increasing difference between Rcr and R because of an increasing driving force, and at values of R = 2Rcr grains become unstable, resulting in abnormal grain growth. However, although this theory has never been rigorously checked experimentally, Smith and Dillamore[58] were able to verify results involving the migration of sub-boundaries in terms of the theory.

An alternative approach to grain growth was considered by Gladman[62]. When a grain grows into and absorbs a neighbouring grain, two principal opposing energy changes occur :

i. The energy of the system is increased by the expansion of the interface of the growing grain;

ii. The energy of the system is decreased by the elimination of the grain interfaces in the grains into which the growing grain grows.

Gladman[62] considered a cubo-octahedron having a radius R growing into a matrix of regular grains of a similar shape, but having a mean radius R_o which may or may not be equal to R. If the ratio of the growing grain to its neighbour is z, an expression for energy may be written as :

$$En = \frac{8\sigma}{R_o} \left(\frac{2}{z} - \frac{3}{2} \right) \qquad \text{(26)}$$

where R_o is the mean radius, σ is the surface energy, and En is the energy change accompanying growth. This was the more likely case, as only large grains can grow at the expense of small grains. In normal grain growth, all grains which fulfil the condition where $z > 1.33$ can grow. Many grains

can fulfil this condition and hence general grain growth will occur.

Equations (25) and (26) infer that there will be a general slowing of the process as large grains impinge which increases the values of Rcr and Ro.

3.4.4 Effect of Second Phase Particles on Grain Growth

The interaction that results from the association of a grain boundary with a second phase particle arises from the reduction in total boundary area. For spherical particles that are assumed to be immobile and unchanged by their association with a grain boundary, the maximum retarding force, $\pi r \sigma$, results in cessation of growth when :

$$R = \frac{4f}{3r} \qquad \text{(27)}$$

where r is the particle radius, and f is the volume fraction. Gladman and Pickering[96] found that substitution of typical values for particle size and volume fraction into Zener's equation[94] indicated much larger grain sizes than observed. This was thought to be because of an over-estimation in the driving force for grain growth, as assumed value of $\frac{2\sigma}{R}$ relates to a contracting spherical surface with no attached surfaces.

Hillert[61] developed a generalised treatment for the effect of second phase particles. In the presence of second phase particles, equation (25) becomes :

$$\frac{dR}{dt} = \sigma M \left(\frac{1}{Rcr} - \frac{1}{R} \pm z \right) \qquad \text{(28)}$$

where z when multiplied by σ is the net restraining force due to second phase particles. The z term will always act against the movement of

boundaries, being positive for small grains and negative for large grains. However Hillert[61] did not consider the effect of precipitate distribution in detail, i.e. the volume fraction, particle size, and number of particles were not treated individually. A much better treatment was considered by Gladman[62]. Gladman[62] considered a uniform distribution of particles of radius r, and volume fraction f. If the energy released per particle due to grain growth is E_1 and the energy required to unpin a grain is equal to E_p, then :

$$E_1 = \frac{2s\pi r^2\sigma}{3 R_o f} \quad \frac{2}{z} - \frac{3}{2} \qquad \text{(29)}$$

and

$$E_p = 4r\sigma s \qquad \text{(30)}$$

where s is the boundary displacement required for unpinning. If the total energy change associated with the unpinning of a single particle is E_T, then :

$$E_T = E_p + E_1 \qquad \text{(31)}$$

Grain growth can still continue while E_T is negative, i.e. $E_1 > E_p$. However, as R_o increases during grain growth, the number of grains that satisfy the requirements for growth will be reduced until eventually grain growth ceases, i.e. $E_1 = E_p$. On the basis of the work of Lifshiftz and Sloyov [79] and Wagner[80] that the average particle radius varied with the cube root of time, it was suggested[61] that the accompanying grain growth should exhibit a time exponent of $\frac{1}{3}$. Recent analysis indicated a $t^{\frac{1}{4}}$ relationship for grain boundary particle coarsening[97].

At the cessation of grain growth, $E_T = 0$ therefore $E_p = -E_1$. Using

equations (29) and (30), Gladman[62] derived the following equation for the critical particle radius r^* for the growth of a grain of heterogenity ratio Z in a matrix of grains of size Ro, with a volume fraction of second phase particles f, such that :

$$r^* = \frac{6\,R_o\,f}{\pi}\left(\frac{3}{2} - \frac{2}{Z}\right)^{-1} \qquad \text{(32)}$$

Because all grains are pinned initially, and as particle coarsening is a continuous process, the largest grain will become unpinned first, i.e. the grain with the highest value of Z.

The rate of growth of this grain will accelerate as Z increases, while R_o remains unchanged as small grains remain pinned. Unpinning of another grain boundary occurs when coalescence of particles has progressed to a more advanced stage, thus allowing the unpinning of a second and slightly smaller grain. Therefore unpinning favours the development of grains at the upper end of the grain size distribution, so that abnormal rather than normal grain growth was predicted. In fact this was found to be the case[96].
Grain growth in the grain-coarsening temperature range in grain refined steels, occurred by a process of secondary recrystallisation rather than normal grain growth.

CHAPTER FOUR

4. TEXTURES

Preferred orientation is of practical significance in many applications. The most notable are in the formability of sheet metals, and in magnetic properties. In the former case the texture controls the working limits of sheet drawability and the nature and extent of earing, while the quality of both hard and soft magnetic materials depends on texture perfection.

There are two common methods of representing textures in sheet metals :

i. Normal or stereographic pole figures;

ii. Inverse pole figures.

These will be discussed later in the chapter describing the experimental details.

4.1 DEFORMATION TEXTURES

Deformation textures will be reviewed only with reference to bcc cold rolling because all the work in this investigation was on bcc metals.

4.1.1 Rolling Textures in BCC Single Crystals

These have been studied in bcc single crystals to examine textural changes in specific single crystal orientations, as a result of cold working. This work was carried out with a view to applying the results to polycrystalline metals. The most widely investigated unstable orientations were those with the <110> in the transverse direction. If the transverse direction

was taken to be $[1\bar{1}0]$, orientations with sheet normals between $[111]$ and $[110]$ rotate to (111) $[\bar{1}\bar{1}2]$ orientations, e.g. the (110) $[00\bar{1}]$ splits into the twin related orientations (111) $[\bar{1}\bar{1}2]$ and $(\bar{1}\bar{1}1)$ $[112]$ [34].

Orientations with sheet normals between $[001]$ and $[111]$ divide between (001) $[110]$ and (111) $[\bar{1}\bar{1}2]$. In a (100) $[001]$ orientation, rotation tended to be about the plane normal. Hu [34] found that after 70% reduction a single crystal of (100) $[001]$ gave a texture spread about (100) $[011]$. Early work indicated that $\{111\}\langle 112\rangle$ orientations were stable. However, later work by Hu and Cline [98] showed that single crystals of this orientation rotated towards $\{332\}\langle 113\rangle$ after 70% reduction.

4.1.2 Rolling Textures in BCC Polycrystalline Metals

There appears to be controversy regarding the deformation textures found in bcc metals after cold rolling. Dillamore and Roberts [99] reported that the most common description of a bcc rolling texture was a $\{100\}\langle 011\rangle$, with some rotational spread about the rolling direction and a minor component of $\{111\}\langle 112\rangle$. A preferred orientation of $\{111\}\langle 112\rangle$ with a minor component of $\{111\}\langle 110\rangle$ was reported in a low carbon steel after 90% reduction [100]. Further reductions to 97.5% produced a $\{100\}\langle 011\rangle$ texture with some $\{111\}\langle 112\rangle$. However, the majority of workers described the main component for many bcc metals as $\{100\}\langle 011\rangle$ with a $\{112\}\langle 110\rangle$ component always present and the $\{111\}\langle uvw\rangle$ component reported only in certain cases. The most likely explanation for the discrepancies is the starting texture of the hot band material, as it can be seen from the single crystal work that the initial crystal orientation influences the texture developed.

Another discrepancy was found between results obtained from inverse and

stereographic pole figures. Many workers found that using the inverse pole figure method, the {111} component was almost always greater than the {100} component. The {100} was only significant above 75% reduction. However, using {200} pole figures, the {100}<011> component was the major component in most cases. Hancock and Roberts[101] explained the discrepancy in terms of the multiplicity of the various texture components. For a {200} pole figure, two components satisfy {111}<112> and two components satisfy the {111}<110> while the {100}<011> is a single component. Thus, for a hypothetical texture consisting of equal proportions of {111} and {100}, the intensities due to each {111} component on a {200} pole figure would be about a quarter of that of the {100} component.

4.1.3 Theories of Texture Development

Early theories of texture development assumed a simple biaxial stress system[102][103], i.e. combined tension and compression. However, these theories were unable to explain the deformation textures observed in bcc metals.

Later theories were based on the plasticity theories of Sachs[104] and Taylor[105]. During rolling certain simple zones of orientations rotate so as to remain within the zone[106]. Rotation rates[107] for cubic metals were calculated using the homogeneous plasticity theory as defined by Taylor[105]. Rolling was assumed to be a plane strain mode of deformation and that bcc metals deform by pencil glide on a {110}<111> slip system. Results for the calculation of rotation rates, i.e. $\frac{d\phi}{d\varepsilon}$, the rate of rotation per unit rolling strain, as a function of the principal zone axes, having their axes parallel to either plane normal, rolling directions or transverse direction are given in Figure 10. Stable

orientations were considered to be those for which $\frac{d\phi}{d\varepsilon}$ was negative and metastable orientations were considered those for which the slope was positive. Only the {112} <110> was considered to be stable since this orientation was self-restoring after any displacement. This opposed the single crystal work of Hu[34] who showed that the {001} <110> orientation was quite stable. The present analysis indicated that the {001} <110> rotated towards the {112} <110> about the rolling direction.

After 70% reduction, the theory suggested that the deformation texture should lie between {100} and {211} , but experimental data showed that the centre of the orientation distribution was displaced towards {111}<110> . Bunge[107] discussed this in terms of a deviation from ideal plane strain conditions during rolling. However, it was shown [107] that a strain state approaching axisymmetrical compression was required to stabilise the {111} <uvw> orientations, which was impossible for rolling. Only slight deviations were required to stabilise the {001} <110> orientation which may account for the stability found in single crystals. Dillamore and Katoh[107] accounted for this in terms of a deviation from plasticity theory, which assumed that each grain must undergo the same shape change. In polycrystalline aggregates, the relative orientation of a grain with respect to the stress axis differs from grain to grain; softer grains because of their more favourable orientations deform at a lower stress than the less favourably oriented harder grains. For the metal to deform as a whole, at a lower stress level than predicted from homogeneous plasticity theory, the harder grains may deform in a different strain state at a lower stress level than required for homogeneous strain. It was proposed that the {111} <112> and {111} <110> adjusted their strain state to correspond to {11 11 8} <4411> and {112} <110> respectively which stabilises the {111} sheet normals. At higher deformations the ability to accommodate shear strain may diminish leading to a reduction in the intensity of the

{111} component and an increase in the more stable components, i.e. {001} <110> and {112} <110> .

4.2 RECRYSTALLISATION TEXTURES

The development of recrystallisation textures depends on factors such as degree of cold work, the presence of second phase particles, annealing temperature and the influence of grain growth following recrystallisation.

It was found[109] that the major recrystallisation texture component after 50% reduction was {110} <001> . Hu[34] found that after moderate cold reductions, {110} <001> recrystallised components were present in a deformed matrix of {111} <112> . It was found[109] that after 63% reduction the {110} <001> was accompanied by {111} <110> , which after 73% reduction was the major component. At higher reductions, i.e. 80% - 90% reduction, the {111} <110> was replaced by {554} <225> , which is 5^{o} from {111} <112> . The strong {100} <011> component in the deformation texture almost always decreased in intensity after recrystallisation.

The presence of fine second phase particles, either precipitated before deformation or during recovery, influenced the recrystallisation texture. Fine precipitate particles increased the intensity of the {111} components i.e. either {111} <112> or {111} <110>, at the expense of {100} <011> . Hutchinson[110] showed that AlN precipitation prior to recrystallisation decreased the intensity of the {110} <001> .

Grain growth following recrystallisation tended to increase the intensity of the major texture components as does secondary recrystallisation[111][112]. The theoretical basis of these phenomena will be discussed later.

Two theories have been proposed to explain recrystallisation texture development :

i. Oriented nucleation;

ii. Oriented growth.

4.2.1 Oriented Nucleation

This assumed that a recrystallisation nucleus orientation must be present in the deformed matrix or be evolved during the recovery process that precedes recrystallisation in most cases. In single phase metals it was suggested[113] that components of recrystallisation textures can be accounted for in terms of three types of nucleation mechanism :

i. In situ nucleation, by subgrain growth in regions of relatively uniform lattice curvature in the interior of grains;

ii. Nucleation at pre-existing grain boundaries;

iii. Nucleation at deformation bands.

It was concluded[113] that where in situ or grain boundary nucleation predominated, recrystallisation textures were well represented by the deformation textures. In the case of deformation band nucleation, textures quite different from the deformation textures may develop.

i. In Situ Nucleation in Grain Interiors

Nucleation within grains is observed only after moderately high deformations since at low deformations, the lattice curvature, i.e. misorientation between adjacent subgrains, is insufficient to allow a high angle boundary to be created. The effect of

subgrain orientation on the size and misorientation of subgrains was investigated in the cold worked condition after 70% reduction[32]. It was found that as the orientation of subgrains changed from (001) $[\bar{1}10]$ through to (110)$[\bar{1}10]$, the subgrain size decreased and the misorientation between adjacent subgrains increased.

Because dislocations were distributed mainly in the subgrain boundaries after heavy deformations, the dislocation density, ρ, could be related approximately to the subgrain size and misorientation by the following relationship :

$$\rho = \frac{\theta}{b\, d_s} \qquad \text{(33)}$$

where θ is the misorientation between adjacent subgrains, d_s is the subgrain diameter, and b is the Burgers vector. If the stored energy is considered as ΔF, then the stored energy can be evaluated in terms of orientation :

$$\Delta F = \frac{K\, \sigma_s}{d_s} \qquad \text{(34)}$$

where d_s is the subgrain diameter, K is a constant, and σ_s is the grain boundary energy, and is a function of the dislocation density.

The reason behind the orientation sensitivity of the dislocation density is crystallographic in origin. It was pointed out that increases in the stored energy corresponded to increasing Taylor 'M values'[32] where M obeys the following relationship :

$$M = \frac{\gamma}{\varepsilon} \qquad \text{(35)}$$

where γ and ε are the shear strain and tensile strain respectively. Therefore at any value of tensile strain, increasing the M value leads to an increase in the dislocation density. Later work showed[114] that not only did the stored energy increase with increasing strain, but the orientation dependence of stored energy increased with increasing strain.

From the basic assumption that the formation of a viable nucleus depends on the driving force available for subgrain growth, nucleation rate should therefore be orientation sensitive and during annealing the {110}<110> orientation should be nucleated first and therefore have the longest time for growth. Smith and Dillamore[58] found subgrain growth to be orientation sensitive during annealing and growth in the {110}<110> and {111}<110> orientations was much faster than in the {113}<110> and {001}<110> orientations. It was also observed that {110}<110> and {111}<110> had a much greater grain size distribution in the cold worked condition[58]. From the work of Hillert[61] and Gladman[62] subgrain size distribution may be at least as important as differences in sub-boundary misorientation.

Orientation determination of recrystallised grains during the early stages of recrystallisation confirmed a predominance of {111} grains parallel to the sheet surface[115] while the last grains to recrystallise had {100} planes parallel to the sheet surface. However, the low intensity of the {110}<110> component in cold worked materials, as it is only produced by a weak rotation about <110>, meant that it was unlikely to become a strong component. In the discussion of annealing textures[32], the major annealing texture centred on {111}<112> was completely ignored.

However, since this component has a similar'M value'to the {111} <110> component, it should have a similar dependence of nucleation rate on orientation, and can be discussed in a similar manner.

ii. Nucleation at Grain Boundaries

Grain boundaries have long been recognized as prominent sites for the nucleation of recrystallised grains. At least two possible mechanisms exist. Grain boundaries may either bow into the grain with the highest stored energy[64][65][66], i.e. SIBM, or a nucleus may develop from a subgrain by subgrain growth at or near to pre-existing grain boundaries. Both mechanisms favour the formation of recrystallised grains with sheet plane orientations in the range {100} - {411}. From the theoretical work of Bailey[65], for nucleation to take place at a high angle boundary by SIBM, it is necessary to have a steep energy gradient. From oriented nucleation theory[32], this should be most easily accommodated when a {100} grain lies adjacent to a {111} grain, and favours the formation of a {100} texture. However, although the formation of {100} <110> recrystallised components were discussed in terms of SIBM[32][116] no microstructural evidence was produced to substantiate this in ferritic steels.

Nucleation at the grain boundary by subgrain growth can also lead to the preferential nucleation of {100} sheet plane and orientations. Hutchinson[72] discussed unpublished work by Morris on the cold work structure at grain boundaries. Morris[72] found two distinct types of behaviour at grain boundary regions. In some cases there was no apparent change at the grain boundary

while in others bands of fine cells were found in the grains near to the grain boundary. The latter type was found to occur between grains of widely differing 'M value', e.g. between {111} and {100}. The dense substructure was found in the grains of low 'M value', presumably because of local work hardening in the softer grain in order to maintain stress continuity across the grain boundary during deformation. This should give rise to recrystallised orientations in the range {100} - {411}, and indeed Dunn[117] found that one third of grain boundary nucleated grains were within 25° of {100}.

iii. Nucleation at Deformation Bands

A theory for nucleation at deformation bands was discussed in detail by Dillamore et al[114]. Figure 11a illustrates a diagram of a deformation band. The vertical sub-boundaries (energy σ_t) are parallel to the deformation band and would be expected to have a large misorientation. The horizontal boundaries such as h_a and b_c are of energy σ_r, and have smaller misorientations. Figure 11b illustrates the structure of Figure 11a after annealing where the triple point angles have relaxed to an equilibrium configuration, with an angle ϕ such that :

$$\text{Cos}\,\phi = \frac{\sigma_r}{2\sigma_t} \qquad \text{——————} \quad (36)$$

A critical condition that would allow continued growth of the large subgrain, a h g f d b , would be if b and c came into contact before an equilibrium angle, ϕ , was achieved. This could be achieved if :

$$D_r > \frac{4}{3}\left(d_r + d_t\left[\frac{4\sigma_t^2}{\sigma_r^2} - 1\right]^{\frac{1}{2}}\right) \qquad \text{(37)}$$

i.e. if the particular subgrain length D_r was sufficiently long compared with the average transition band d_r. Figure 12 illustrates Equation 37 in terms of D_r/θ_t, where θ_t was the misorientation across a transition boundary. It can be seen that narrow subgrains, i.e. small d_t and small misorientations provide the most favourable conditions for growth.

The curvature of a deformation band was shown to be a function of d_t and σ_t (fig. 12) both of which increased with increasing deformation. Experimental work showed[118] that d_t reached a limiting value at high strains. Above this limiting strain, increases in misorientation can be achieved only by increases in θ_t. From Figure 12, the size advantage required by a potential nucleus increased with increasing θ_t for a constant value of d_t. Therefore at high strains, deformation bands may cease to be favourable sites for nucleation. This fact has sound practical basis as it was found[119] that the effectiveness of deformation bands as nucleation sites varied with deformation in heavily compressed iron-carbon alloys.

It was considered[114] that with the exception of the $\{112\}\langle 110\rangle$ component all orientations in bcc metals were metastable and therefore potentially deformation banding. However, whether the bands acted as nucleation sites depended upon the structure gradient away from the band. Favourable structures were those which had an increasing dislocation density away from the band, i.e. the metastable orientation from which the band formed should have a lower 'M value' than the stable orientation.

Transition band nucleation was predicted to be particularly favourable for the {110}<001>, favourable for the {100}<011> and less favourable for the {11, 11, 8}<4411>. Hu[34] observed nucleation of {110}<001> components at deformation bands. Deformation band nucleation may account for the strong {110}<001> texture found in some steels after 50% reduction[109]. This mode of nucleation is thought to predominate, since after 50% reduction, there is insufficient general lattice curvature generated to allow nucleation by subgrain growth on a large scale.

One important prediction from the work of Dillamore et al[114] was that different deformation band orientations may be important nucleation sites after differing degrees of deformation. The {110}<001> texture would be important at moderate strains, since at high strains nucleation would be unfavourable because of sharp lattice curvature, resulting in large values of D_r for nucleation.

In polycrystalline metals, {110}<001> nucleation occurred most readily on recrystallisation in coarse grained materials after 50 - 60% cold reduction. A coarse grain size favours the formation of deformation bands, since it will be easier to develop the initial curvature required for rotation in larger volumes of metal. Another reason for a predominant {110}<001> texture, not considered, was that in an initially coarse grained metal, fewer sites will exist for the nucleation of {100}<011> grain boundary nucleated components.

The {100}<011> and {11, 11, 8}<4411> orientations may be viable sites for nucleation at higher strains. The latter component was commonly observed after recrystallisation and may

arise from nucleation at deformation bands. However, nucleation of this component can also be discussed in terms of an in situ mechanism. Nucleation of {100} <011> component can also be discussed in terms of a grain boundary mechanism, so that the importance of deformation band nucleation in relation to these components was not clear.

Other orientations may be favourable sites for nucleation, i.e. those for which 'M values' were high on one side and low on the other side of the metastable orientation, e.g. {4411} <11, 11, 8>.

This may account for the increased {411} component in compressed iron-carbon alloys after recrystallisation[119], since in axi-symmetrical compression, rotation away from a {411} orientation is essentially the same as rotation from a {4411} <11, 11, 8> under conditions of plane strain, i.e. a rotation about a [1$\bar{1}$0] parallel to the transverse direction.

4.2.2 Oriented Growth

The theory of oriented growth is based on the relative migration rates of recrystallised grains as a function of the misorientation between the new grains and the matrix. It assumes that nuclei are so plentiful in a heavily deformed matrix that all orientations are present. Therefore nuclei which were favourably oriented with respect to the deformed matrix will grow more quickly and hence make a larger overall proportion of the recrystallisation texture.

In terms of Equation 17, oriented growth assumed that orientation selection was simply dependent on V as a function of the relative orientation of the

growing grain and the matrix. Δ F was assumed to be constant and independent of orientation and that the rate of growth is proportional to M . It was shown however that Δ F was not constant[32] but was dependent on orientation.

Initial results were confined to fcc metals; Liebmann et al[120] found that in aluminium, the maximum migration rate corresponded to a rotation of approximately 40° around the <111> axis. Ibe and Lücke[121] showed that for bcc metals, the maximum value of M occurred when the growing grain and the crystal being consumed were related by a 27° rotation around a common <110>.

Hu[34] found that deformed single crystals of {110}<001> orientation formed a twin related {111}<112> orientation. After recrystallisation the main texture component was a {110}<001> corresponding to a 35° rotation about a common <110> . This corresponded approximately to the maximum boundary mobility with respect to both rolling textures and was discussed in terms of oriented growth.

Dillamore[122] extended the ideas on oriented growth to consider the conditions for the growth of nuclei over the full growth range, for bcc metals. It was considered that the main principle governing the formation of recrystallisation textures was that :

i. The most likely nucleation sites were considered to be at grain boundaries and that the growing grain must be capable of rapid growth into two orientations, i.e. either side of the grain boundary. This was certainly over-simplified, as intragranular sites are equally favourable, particularly after heavy cold reductions.

ii. The ability for extended growth through the spread of orientations will enhance the probability of a nucleus forming part of the recrystallisation texture.

iii. Further enhancement will be obtained if in addition to being able to grow into its parent orientation, a nucleus can grow into other components of the deformation texture.

The ability for growth of a nucleus was determined by two parameters :

a. The angle α, which was the angle indicating the accuracy of location of {110} poles of the nucleus and matrix. It was defined as not greater than 5°.

b. The angle β which was the angular rotation of the near common pole. This was considered to be between 20° and 60°.

For material having a {112} <110> - {001} <110> textural spread, recrystallisation commenced as competition between orientations {111}<110> and {554} <225> (i.e. within 5° of {111} <112>). Initially the {111} <110> texture was said to have an advantage because of its greater probability for nucleation and its capacity for growth into its parent orientations. The {554} <225> was able to grow into a greater part of the deformation texture, since it was more favourably oriented for growth into the {112} <110> and {100} <011> components of the deformation texture.

4.2.3 Relative Merits of Oriented Nucleation and Oriented Growth

Most of the textural components observed after recrystallisation can be

predicted from both theories of oriented nucleation and oriented growth. However, the strong (001) [110] recrystallisation texture sometimes observed cannot be predicted from oriented growth. Both oriented nucleation and oriented growth are able to predict recrystallisation components arising from (110) [001] orientations. However, oriented growth cannot explain why this component becomes less favourable after moderately high deformations, i.e. 70% reduction, while still maintaining a 35^{o} rotation about <110> . Oriented nucleation was able to explain this in terms of deformation bands becoming unfavourable sites for nucleation when compared with in situ sites at high reductions.

It is thought that orientation selection on the basis of nucleation is the more likely event, since it has been proved almost conclusively that the nucleation is orientation dependent. Because nucleation always precedes growth this is more likely to be the process which determines the recrystallisation texture produced. Oriented growth is thought to be important only when two components have the same nucleation frequency.

4.2.4 The Effects of Second Phase Particles

It has been shown previously that second phase particles influence recrystallisation. As a rule, coarse particles accelerated recrystallisation while fine dispersions of particles, or particles precipitated during recovery, i.e. before nucleation, decreased the nucleation rate.

i. Large Particles

Gawne and Higgins[71] studied the effects of coarse cementite particles on the formation of recrystallisation textures. They found that particles acted as to reduce the stored energy

differences which exist after cold work. Similar misorientations were found for {100}<011> oriented regions adjacent to particles as for {111}<110> regions adjacent to particles. Recrystallised grains were observed to nucleate in {100}<011> regions by particle stimulated nucleation and the resulting texture was a weak rolling texture.

ii. Finely Dispersed and Precipitated Particles

The influence of fine scale precipitation on texture formation has been studied extensively in iron-based alloys[31][73][74][75][76][84][116]. Depending on the system used, fine dispersions of second phase particles present before cold working, or precipitation in the deformed or recovered structure before recrystallisation may produce similar effects. Niobium carbide[74] and titanium carbide belong to the former category, while aluminium nitride[31][75][84] and copper represent the latter. The presence of second phase particles present before recrystallisation has been shown to decrease the nucleation rate relative to the growth rate, since it was usually accompanied by an increase in the as-recrystallised grain size[31].

The textural changes that occur during recrystallisation can be discussed in terms of the orientation dependence of nucleation. If the nucleation of all components were retarded in equal proportions relative to their orientation dependence, then the time available for growth of the first formed grains would be increased. The recrystallisation texture will be strongly selected to the most favoured nuclei, on the basis of orientation dependence of nucleation. In steels, precipitates such as AlN, NbC, TiC and Cu tended to strengthen the {111} component at the expense of the

{100} component.

As nucleation in the presence of second phase particles is analogous to secondary recrystallisation, unpinning following particle coarsening will always take place first in a subgrain with the {111} plane parallel to the sheet surface, rather than with {100} subgrains parallel to the sheet surface. This was because of a higher sub-boundary energy[32] and greater size distribution of {111} oriented subgrains, compared with {100} oriented subgrains[58]. An equation, Equation 16, relating subgrain size to particle size required for the unpinning of subgrain boundaries has been derived[84] for AlN precipitates in mild steel. . Figure 140 shows the minimal particle size for the unpinning of subgrain boundaries increases as the orientation of subgrains goes from {111} through to {100} for a constant volume fraction of particles.

Hutchinson[110] also found that AlN precipitation suppressed the {110}<001> component, indicating that nucleation at transition bands is especially susceptible to interference by fine particles.

4.2.5 Texture Development during Grain Growth and Secondary Recrystallisation

At the end of primary recrystallisation, associated with the main components of the recrystallisation texture may be a rather diffuse spread of orientations.

During grain growth, the main textural components strengthened at the expense of the diffuse spread and there was usually a redistribution of density between components. In steels {110}<001> and {111}<uvw> components were enhanced during grain growth when they were the respective major components[109].

An explanation of this behaviour can be found in the mechanisms of grain growth and in the structure produced during primary recrystallisation. During grain growth, large grains grow at the expense of small grains. It was found[109] that the grain size distribution of the main component tends to be biased towards the larger sizes than the average distribution. According to the theories of grain growth[61][62], these grains will grow at the expense of smaller grains during grain growth and their texture will be correspondingly strengthened. It is not difficult to see why this is the case. The main textural component will be grains that have nucleated first and hence have the longest time for growth into the cold worked or recovered matrix and they will be the largest grains.

In the presence of second phase particles, it was found [111][112] that the major recrystallisation texture component, i.e. {111}<uvw>, increased dramatically during secondary recrystallisation. Gladman[62] showed that increasing the volume fraction of second phase particles limits the range of growing grains to a smaller fraction of those of the largest sizes. The influence of second phase particles causes a change from normal grain growth to secondary recrystallisation. Therefore, when there is an orientation bias in the grain size distribution, the range of growing grains is restricted even more closely to the favoured component during secondary recrystallisation than during normal grain growth, hence the dramatic increase in the {111} component during secondary recrystallisation.

CHAPTER FIVE

5. FACTORS AFFECTING FORMABILITY

Sheet forming operations which are extensively used in manufacturing processes are generally considered as a combination of drawing and stretching operations. It has often been held that suitability for such processes, which demand high ductility, can be assessed only by type, or simulated type testing. Such tests are difficult to perform and are frequently too time-consuming for use with experimental alloys.

Recently, attempts have been made to correlate performance under specific forming operations with the behaviour of metals in a simple test such as a uniaxial tensile test. This approach has obvious advantages, the test being widely accepted and rapidly carried out.

Relationships were found between certain parameters obtained from a tensile test and performance in actual forming operations. For example, uniform true strain prior to necking in a tensile test (ε_u) was correlated with the ability of a metal to be bent. Butler[123] showed the value of ε_u in stretch forming and bulging operations. Other workers[124] related ε_u to press formability. On the other hand, bendability was related to the true strain at fracture.[123]

Atkinson and Maclean related deep drawability with $\bar{r}$ value.[125]

5.1 PLASTIC ANISOTROPY AND CRYSTALLOGRAPHIC TEXTURES

A measure of the normal plastic anisotropy for sheet metals was defined by Lankford et al[126] in terms of the 'r value' :

$$r = \frac{\ln \frac{W_o}{W_1}}{\ln \frac{t_o}{t_1}} \qquad \text{(38)}$$

where W_o and t_o is the initial width and thickness, and W_1 and t_1 is the final width and thickness respectively. The 'r value' was shown to be dependent on the particular angle between the rolling direction of the sheet and the axis of the tensile specimen.

The 'r value' is usually expressed in terms of an average strain ratio $\bar{r}$:

$$\bar{r} = \frac{r_o + 2r_{45} + r_{90}}{4} \qquad \text{(39)}$$

where r_o, r_{45} and r_{90} are r values at 0^o, 45^o and 90^o to the rolling direction. The variation of 'r value', with different directions in the sheet, is termed planar anisotropy. A measure of planar anisotropy is Δr , where Δr is expressed as :

$$\Delta r = \frac{r_o + r_{90} - 2r_{45}}{2} \qquad \text{(40)}$$

Thus, a completely isotropic metal has a strain ratio of unity in all directions, i.e. $\bar{r} = 1$, and $\Delta r = 0$. The two parameters, $\bar{r}$ and Δr have been used as measures of plastic anisotropy of a sheet metal.

The origins of plastic anisotropy lie in the crystallographic texture which depends on the cold working and annealing cycle. Many attempts have been made to correlate the $\bar{r}$ value with the crystallographic texture in bcc metals. Usually a close correlation was found between $\bar{r}$ value and the intensity of {111} planes. Whiteley and Wise[127] related the $\bar{r}$ value to the density of {111}, {100}, and {110} planes parallel to the plane

of the sheet. High densities of {111} and {110} and low densities of {100} appeared to correlate with high $\bar{r}$ values. Held[128] correlated $\bar{r}$ values with the ratio of {111}:{100} and found that the higher the ratio of I{111}: I{100} texture parameters, the higher the $\bar{r}$ value. Dillamore[129] calculated $\bar{r}$ values based on a method by Hosford and Backofen[130] for idealised textures containing varying proportions of (111) and (100) planar orientations together with different volume fractions of random orientations. The calculated variation of $\bar{r}$ value, with the ratio of (111):(100), is shown in Figure 13 and compared with the experimental data of Held[128]. The variation was much more rapid than observed experimentally. This was thought to be because of the fact that in real metals, textures were not perfectly sharp and cannot be adequately described by just two components.

However, pole density measurements give no description of the planar anisotropy. Vieth and Whiteley[131] analysed theoretically the shape changes that take place in single crystals, because of crystallographic orientation. The analysis considered both restricted slip and pencil glide along <111> directions. The results are summarised in Figure 14 which illustrates the effect of strain ratio r as a function of the test direction for four crystal orientations. Experiments with single crystals confirmed these calculations which have also been confirmed by Fukuda[132].

The results agree with those of polycrystalline bcc iron and confirmed the favourable effect on $\bar{r}$ of a strong {111} texture and a weak {100} texture. In certain directions, {110} and {112} textures also show high r values. Hence, certain textures may be even more favourable than the {111} texture. It can be seen from Figure 15, $\bar{r}$ values exceeding 2.5 may be possible, if the right orientation can be developed. However, the perennial problem in relating polycrystalline deformation to single crystal properties is that additional slip systems operate as a result of mutual constraints

between grains, resulting in different r values from those predicted, by a single crystal approach.

An apparent anomaly also exists concerning the effect of the {110} component on $\bar{r}$ value. Wright[133] considered that the {110} component was undesirable in the development of high $\bar{r}$ values, while Vieth and Whiteley[131], Whiteley and Wise[127], considered that it had the opposite effect.

In the work of Hutchinson et al[109] there was evidence to suggest that average $\bar{r}$ values in excess of 1 may be obtained in steels containing considerable amounts of the {110}<001> component. Therefore it would appear that the {110}<001> component may not be undesirable for the development of high $\bar{r}$ values, as was suggested by Wright[133]. However, from the aspect of planar anisotropy it can be considered undesirable. High $\bar{r}$ values at 0° and 90° to the rolling direction, combined with low r values at 45° to the rolling direction lead to very high Δr values. In fact, in the r_{90} direction, an r value as high as 3 was obtained in the presence of some {110}<001>component[136].

The {111} components do not give rise to high Δr values. This was confirmed by Hutchinson et al[109] who found that once the {111}<110> became the major recrystallisation component, the value of Δr decreased. This was in agreement with the work of Vieth and Whiteley[131] who found high r values in all three directions for {111} components. In fact, in steels with strong {111}<112> components, the maximum r values occurred at 0°, 60° and 120° to the rolling direction rather than $0/90^{\circ}$. The variation in r value, Δr was only slight.

The {100} component was found not only to be undesirable in the development

of high $\bar{r}$ values, it also produces a high degree of planar anisotropy Δr. Unlike the {110} <001> component, the maximum r value occurred at r_{45}, and the minimum values at r_o and r_{90}. This was in agreement with the single crystal work of Vieth and Whiteley[131] who found at 0^o and 90^o to the rolling direction, r valuesof 0 was obtained, while at 45^o to the rolling direction, the r value was 1.

5.2 DEEP DRAWABILITY, $\bar{r}$ VALUE AND TEXTURE

In deep drawing, a flat disc can be formed into a cup shape by forcing it through a die by means of a punch of a cross section similar, but slightly smaller than that of the die. Deep drawability has been assessed by drawing blanks of successively increasing initial diameter, and the limiting blank diameter (LBD) has been defined as the blank diameter which has equal probability of fracture or success in the drawing operation. To standardise the drawability between different geometries, the LBD may be divided by the punch diameter, giving the limiting draw ratio (LDR). Although metals require sufficient ductility to be bent around the punch nose, the main factor in limiting deep drawability is the ratio of the stress to deform the metal under the stress system in the flange region, to the stress at the failure site. The stress states occurring in deep drawing are well documented. Over the punch profile, the stress state was somewhere between plane strain tension and balanced biaxial tension, while in the flange, the stress state varied from a circumferential compressive stress at the periphery of the flange, to approximately radial tension at the die-profile radius. There was a net circumferential compressive stress in the flange.

In plane stress, the yield locus for an isotropic metal was defined by Von Mises as :

$$\sigma_x^2 + \sigma_y^2 - \sigma_x \sigma_y = Y^2 \qquad \text{(41)}$$

where σ_x and σ_y are the principal stresses in the x and y directions, and Y is the uniaxial yield stress. The states of stress found in deep drawing are indicated in Figure 16, on a plane stress yield locus for an isotropic material, which illustrates that at yield, the radial stresses in the flange are lower than at the punch nose.

Hill[134] proposed that the yield function for an anisotropic plastic metal, under plane stress, should be a modification of the isotropic yield criterion of Von Mises. By assuming that r is uniform in the plane of the sheet, i.e. planar isotropy exists, Equation 41 becomes :

$$\sigma_x^2 - \frac{2\bar{r}}{1+\bar{r}} \sigma_x \sigma_y + \sigma_y^2 = X^2 \qquad \text{(42)}$$

where $\bar{r}$ is the average r value. The dependence of $\bar{r}$ for different plane stress combinations is illustrated in Figure 17, and it can be seen that textures favouring high $\bar{r}$ values, increase deep drawability since they lead to an increased flow stress in the failure zone (biaxial tension), relative to the drawing zone (tension - compression). However, the Hill[134] continuum model was shown to be a rather crude representation of crystallographic anisotropy. This is because its origins are not crystallographic in nature (i.e. derived from Von Mises). In fact, it was shown[135] that Hill's theory does not agree with the critical resolved shear stress law which casts doubt on the application of such a theory to considerations of anisotropy of a crystallographic origin.

However, despite the limitations of Hill's theory[134], good correlation was obtained between the average $\bar{r}$ value and the critical blank diameter (CBD), or limiting draw ratio (LDR), measured in a standardised cup-draw test for a range of ductile materials[136][137]. In fact, Wilson and Butler[136] found that despite differences in work hardening rates between

aluminium and copper, the $\frac{LDR}{\bar{r}}$ coefficients were not significantly different. This suggests that the ratio of stresses over the punch nose : the flange was of prime importance and over-shadowed any effect as a result of variations in the work hardening rate.

Another important but less reliable factor was shown to be the correlation between the variation in r value, with direction in the sheet, (i.e. Δr), and the severity of earing in deep drawn cups[136]. High values of Δr were correlated with the incidence of severe earing. Ears are created by the interaction of the circumferential hoop stress, that occurs in the flange of a component being deep drawn, and the planar anisotropy in the sheet, which causes certain directions to favour ears and others troughs. Thus, in maintaining a constant volume, ears are thin and troughs are thick. The troughs were related to the direction of low r value, while ears were related to the direction of highest r value. Thus textural components that favour maximum r values at 0° and 90° to the rolling direction produce $0/90^{\circ}$ earing, i.e. {110} <001>, while those that favour maximum r value at 45° to the rolling direction produce 45° earing, i.e. {001} <110>. The {111} <112> texture favours a maximum r value at 0° and 60° to the rolling direction which produces 6 ears.

In practical drawing applications, high Δr values leading to severe earing are avoided since ears must be removed after drawing. Therefore high $\bar{r}$ values are beneficial only when they are accompanied by low Δr values.

5.3 RELATIVE MERITS OF $\bar{R}$ VALUES AND CUPPING TESTS IN ASSESSING DEEP DRAWABILITY

The main advantage of the uniaxial tensile test over the cupping tests, even though the latter are obviously more representative of the applied stress systems, is that tensile tests are not affected by the incident process

variables, e.g. variation in lubrication. However, standardised cupping tests using plastic lubrication, e.g. polythene, have now been developed[138].

Cupping tests therefore have been able to provide a swifter, more convenient (and presumably more directly relevant) basis for the assessment of a material's response to drawability.

5.4 EFFECTS OF MICROSTRUCTURE AND COMPOSITION ON FORMABILITY

Since there has been an accumulation of evidence to suggest that the formability of metals is related to parameters derived from tensile tests, a knowledge of the metallurgical factors influencing these parameters would be desirable. Therefore, quantitative relationships between microstructure and true stress-true strain characteristics would be of value in determining the suitability of a material for cold forming operations.

For many metals, the shape of the plastic portion of the tension true stress-true strain curve may be described by a simple Ludwig type of equation :

$$\sigma = K\varepsilon^{n} \qquad \text{——————} \quad (43)$$

where σ is the true stress, ε is the true strain, n is the strain hardening index, and K is the strength coefficient. It can be shown that at the onset of necking, in a tensile test,

$$\varepsilon_u = n \qquad \text{——————} \quad (44)$$

ε_u is the uniform elongation.

In pressing operations, high values of n were shown to be useful in

avoiding strain concentrations, since a high degree of work hardening spreads the strain from the most heavily deformed regions to regions of lower strain and lower work hardening.

The most desirable stretch forming properties may be obtained by increasing the n value. However, high n values can be achieved only in metals of low stacking fault energy and/or in systems that undergo stress-induced transformations[139].

In mild steels, n values lie in the range 0.2 - 0.3. However, even though large increases in n values cannot be achieved in bcc metals, worthwhile improvements in formability can be achieved by maintaining as high n value as possible.

Morrison[140] reported that the n value of low carbon steels can be related to the grain size through the following equation :

$$n = \frac{5}{10 - d^{-\frac{1}{2}}} \qquad \text{(45)}$$

where d is the average grain diameter. However Woodhead[141] pointed that Morrison's data fits better to the expression :

$$n = \frac{6.7}{17 - d^{-\frac{1}{2}}} \qquad \text{(46)}$$

From Equation 45, a grain size of 100μm would give an n-value of 0.33 and for a grain size of 10μm, the n-value would be 0.24. In press forming operations the maximum grain size will be limited to 40μm indicating a maximum n value of 0.30, the maximum grain size being limited due to the orange peel effect, i.e. the development of a grainy surface during straining a coarse grain metal.

In many circumstances, however, n values do not give a very accurate description of work hardening because the true stress-true strain curve cannot be described with sufficient accuracy by Equation 43. It was reported[142] that for ferritic steels, it was possible to fit true stress-true strain data into a relationship of the form :

$$\sigma = a + b \ln \varepsilon + c(\varepsilon) \qquad \text{(47)}$$

where a, b, and c are constants; using this relationship, the work hardening rate was given by :

$$\frac{d\sigma}{d\varepsilon} = \frac{b}{\varepsilon} + c \qquad \text{(48)}$$

However, it was found to be more convenient and accurate to determine the work hardening rates as a function of true strain by the numerical manipulation of tensile data. Using tensile data, the value of ε_u may be determined since the flow stress and work hardening rate were shown to be equal at a true strain ε_u. Thus, factors which control ε_u may be resolved into those controlling the flow stress and those resulting from the work hardening rate, $\frac{d\sigma}{d\varepsilon}$. Factors which raise the flow stress relative to the work hardening rate will give low values of ε_u, whilst high work hardening rates promote high uniform ductilities.

Microstructural and compositional variables were reported as the major factors which influence flow stress and work hardening rate and hence maximum uniform elongation. The two main microstructural variables were grain size and volume fraction of second phase particles. Unlike n values it was reported[142][145] that grain size had no effect on the uniform elongation. This lack of any effect of grain size on uniform elongation was thought to be because of similar increases in both flow stress and work

hardening rates. In fact although decreasing the grain size increased the flow stress quite significantly, this was compensated by an increased yield extension and higher work hardening rates in fine grained steels. The increased work hardening rate was thought to be a result of shorter slip distance, requiring more dislocations to operate at a given strain, and thus producing a higher dislocation density[144]. On the other hand, refining the ferrite grain size increased the total strain to fracture ε_t. This was thought to be because the effect on the fracture stress was greater than its effect on flow stress.

However, there still appears to be controversy relating to the effect of grain size on ductility, in particular the uniform elongation, ε_u. Horta et al[145] reported that a coarse grain size promoted more uniform straining and therefore increased the ductility which certainly agreed with the findings of Morrison[140].

In terms of the work of Morrison[140], coarse grain sizes should promote high n values and hence a high work hardening rate.

Gladman, Holmes and Pickering[142], and Pickering[143] reported that at least in ferritic steels the work hardening rate was increased as the grain size decreased.

In practical forming applications for mild steels, coarse grain sizes have usually been preferred, with the proviso that they were not too coarse because of the influence of grain size on the magnitude of the yield extension. The finer the grain size, the larger the temper-rolling reduction required to suppress the formation of stretcher-strains which may lead to a greater potential loss in ductility due to strain ageing in rimming steels.

Increasing the volume fraction of second phase particles was found to decrease both uniform elongation and total ductility[142][143]. Although increasing the volume fraction of second phase particles over a small range of carbon and nitrogen contents was shown to have no effect on the flow stress, second phase particles increased the work hardening rate.

More important however, particles decreased the yield extension and therefore increased the flow stress at any given strain. Since the increased work hardening cannot compensate for the decreased yield extension, a lower uniform elongation results. The effect on total elongation, ε_t, resulted from particles acting as initiation sites for ductile failure.

Increasing alloying elements was shown to decrease the uniform elongation.[142][143] The relative effects of substitutional solutes on flow stress increased directly as the frictional stress, which was found to depend on the relative lattice dilation[146]. Increasing the solute content retards dislocation movement and therefore increases the number of dislocations for a given strain, hence an increase in the work hardening rate. However, alloying elements increased the flow stress relative to the work hardening rate, and hence decreased the uniform elongation, ε_u[142].

5.5 STRETCH FORMING TESTS

Simulated tests for stretch forming operations have been usually carried out either by punch stretching or by hydraulic bulge testing. In the former, a metal blank is clamped with a sufficient holding force to prevent drawing in of the specimen. Stretching is carried out using a hemispherical punch fixed to a hydraulic ram. In the hydraulic bulge test, a metal blank is clamped at its periphery in a die. Stretching is carried out using a hydrostatic pressure applied to one side of the blank, deforming

it into a symmetrical dome. The latter is thought to be the better test, since friction effects due to the action of the punch are eliminated.

In simulated stretch forming operations, the imposed strains vary from one of balanced biaxial strain at the polar region, to plane strain at the periphery. Two modes of unstable flow have been discussed[147].

The first mode was broadly and symmetrically distributed about the loading direction and was termed diffuse; it was encountered at ε_{d^*}, where ε_{d^*} is the true strain at which diffuse necking starts. The other mode beginning at ε_{1^*}, where ε_{1^*} is the true strain at which localised necking starts and involves a thin band of flowing metal at an angle α.

For diffuse necking :

$$Z_d = \frac{4(1 - x + x^2)^{\frac{3}{2}}}{(1 + x)(4 - 7x + 4x^2)} \qquad \text{(49)}$$

For localised necking :

$$Z_1 = \frac{2(1 - x + x^2)^{\frac{1}{2}}}{1 + x} \qquad \text{(50)}$$

where Z_d and Z_1 are the sub-tangents to the stress-strain curve at the beginning of diffuse and localised necking, and x is the stress ratio. A necessary condition for localised necking was that no strain be imposed on the non-deforming metal adjacent to the neck. Thus a local neck may be accommodated so long as $d\varepsilon_2 \gg 0$. From the Levy-Mises equation for an isotropic metal :

$$\frac{d\varepsilon_2}{d\varepsilon_1} = \frac{2x - 1}{2 - x} \qquad \text{(51)}$$

Therefore, $d\varepsilon_2 = 0$ was identified with $x = \frac{1}{2}$, and $Z_d = Z_1$. The angle α was determined by value of $d\varepsilon_2 : d\varepsilon_1$:

$$\tan \alpha = \left[\frac{x - 2}{2x - 1}\right]^{\frac{1}{2}} \qquad \text{(52)}$$

Therefore under uniaxial tension for an isotropic metal, $\alpha = 54^{\circ}44'$, while under plane strain condition (i.e. $x = \frac{1}{2}$) $\alpha = 90^{\circ}$.

Conditions for the onset of both diffuse and localised necking have been summarised in Figure 18. When $d\varepsilon_2 > 0$ $(x > \frac{1}{2})$ which should always be the case during stretch forming, a direction of zero extension does not exist, and therefore localised necking cannot be expected. In practical biaxial stretch forming operations, useful deformation may not necessarily be terminated by the onset of microscopic instability.

Horta et al[148] reported that in many cases limiting strains in biaxial stretching were inferior to those predicted from measurements in uniaxial tension. For example, a fine dispersion of carbide particles showed only slight reductions in ε_u, compared with much greater reduction in ductility in stretch forming. Also coarse grained decarburised sheets with average uniform elongations of 27% were associated with early strain localisation and 'premature' failure in biaxial stretching.

Wilson[176] also reported that stretch-forming limits based directly on the uniform elongation, ε_u, can be misleading. Materials with high yield stress/ UTS ratio and low ε_u due to a very fine grain size, pre-strained after complete recrystallisation, or with a fine dispersion of particles performed better than predicted from their ε_u values. However, steels with microstructural features that promoted local strain localisation, e.g. coarse grained structure and unfavourable carbide distributions, performed

less well in biaxial stretching than was predicted from measurements of ε_u. Clearly, microstructural inhomogenities are of greater importance in biaxial stretching than in uniaxial tension, which may to some extent invalidate the correlations between uniaxial tensile data and stretch-formability.

Plastic anisotropy influences the onset of instability in two different ways. Firstly, r determines the limiting stress ratio above which localised necking is not permitted[147]. If the sheet is characterised by high normal anisotropy $\bar{r} > 1$, the plane strain condition is not satisfied until the stress ratio is greater than 0.5[147]. The requirements of plane strain for various values of r have been plotted in Figure 19. As r was increased, there was a reduction in the range of stress ratio, over which working was permissible without localised necking occurring[147]. The second was on the influence of r value on the strain distribution across the bulge. High r values were correlated with a more uniform distribution of strain across the bulge. Horta et al[148] correlated this with the effect of increasing r on the increased yield stress in balanced biaxial tension, as compared with that for plane strain. Therefore increasing r promoted a more uniform strain distribution across the bulge, since the decreased yield stress towards the periphery (i.e. plane strain) would promote deformation in this region. However, an increasing $\bar{r}$ value was accompanied by a small reduction in the strain at the beginning of fracture during biaxial stretching. As a result, the bulge heights were relatively insensitive to variations in $\bar{r}$ in the range 1 - 2.[148]

5.6 FORMING LIMIT DIAGRAMS

Keeler[149] and Goodwin[150] introduced the concept of forming limit diagrams. The two principal surface strains were measured at the onset of fracture. These strains corresponded to the major and minor axis of

an ellipse. By varying the aspect ratios for elliptical dies in hydraulic bulging, it was possible to vary the major and minor strains at fracture and construct a forming limit diagram. However, although they are very useful in determining regions of critical strain in the practical pressing situation, many workers[147][169] found them almost insensitive to composition and microstructure, i.e. the fracture strain levels were almost identical for different metals that are quite different as regard microstructure and crystal structure. (Fig 20) The inability of forming limit diagrams to distinguish different stretching performance was highlighted by Haberfield and Boyles[169]. Comparing a 70/30 brass with a stabilised steel, the FLD gave no indication of the 12% increase in the pole height for the brass at fracture. The latter was due to the better strain distribution properties of brass because of a higher work hardening rate.

CHAPTER SIX

6. FRACTURE

Fracture is being reviewed to study the possible mechanisms of failure in ferritic stainless steels during tensile and forming tests.

Three types of fracture mechanisms are being reviewed :

i. Ductile;

ii. Instability as a result of localised necking;

iii. Brittle - cleavage.

The basic difference between the first two modes was proposed by Dillamore[129]. Ductile fracture may take place under a rising load without obvious strain localisation, while strain localisation was always required for instability. However, the distinction between the two failure modes is only one of degree when considering material quality. Since the basic mechanisms involved are the same for both modes, only ductile failure will be reviewed.

6.1 DUCTILE FRACTURE

The general mechanism of ductile failure has been agreed to be one of void nucleation, void growth and void coalescence.

6.1.1 Void Nucleation

Voids may nucleate by cracking at second phase particles, or by de-cohesion of the metal-particle interface :

i. Particle Cracking

Studies of carbide cracking in steels have usually centred on the initiation of cleavage failure[174]. The results however were of relevance to ductile failure and cracks which do not propagate beyond the carbide, or those which were arrested at the first grain boundary, may act as void nuclei. Cracking was reported to be dependent on three factors : particle size, particle orientation, and applied stress. Carbide particle size dependence on cracking was reported by several workers with conflicting results. In some cases, preferential cracking occurred at larger particles[151] (approximately 2μm linear intercept), while others reported an opposite effect[152]. It was observed[151][152] that the majority of cracked particles lay along the tensile axis, which can be explained in terms of a fibre loading model[152].

The proportion of cracked particles increased linearly with increasing strain[151][152][153] above a minimum threshold strain. However, it was shown[154] that carbide cracking was stress dependent and that the strain for initiation of voids because of particle cracking decreased with increasing volume fraction of carbides. This was presumably because of an increased flow stress as a result of an increased volume fraction of carbide.

ii. Interface De-cohesion

Void nucleation by interface de-cohesion was studied extensively in copper containing silica particles[155]. Thin foil electron microscopy taken from uniaxial tensile specimens showed voids

formed at the ends of spherical inclusions in line with the tensile axis.

It was shown[156] that for cavitation, in terms of a dislocation pile-up model, the interfacial tensile stress σ is given by :

$$\sigma = \frac{ax}{4kb} \qquad \text{(53)}$$

where 'x' is the diameter of the spherical particle, a is the shear strain, k is the dislocation pile-up length, and b is the burgers vector. The equation predicted a linear relationship which was found to be the case.

Thomason[157] analysed the effect of interfacial cohesive strength on ductility and showed the beneficial effect of maintaining an interface at particle poles normal to the tensile axis. A greater elongation was obtained by preventing lateral growth, thus complete particle/matrix separation must be controlled by the interfacial energy and the applied stress system.

6.1.2 Void Growth and Coalescence

A number of models have been advanced to describe hole growth and coalescence [158] [159]. McClintock assumed that voids were present at zero strain (which is rarely the case, e.g. carbides), and that their growth to a point where voids touched each other constituted the mechanism of ductile failure. However, in ductile fracture final failure usually occurs before the voids touch, by a shear mechanism.

The total strain at failure, εt , was given by :

$$\varepsilon_t = \frac{(1 - n) \ln \frac{l_b}{b_o}}{\text{Sin h } (1 - n)(\sigma_a + \sigma_b) / \frac{2\bar{\sigma}}{3}} \qquad \text{(54)}$$

where n is the work hardening exponent, l_b is the centre to centre spacing in the b direction where coalescence occurs, b_o is the initial particle size, σ_a and σ_b are the principle stresses (in directions a, b) and $\bar{\sigma}$ is the yield stress. It is immediately apparent that void growth leading to fracture occurs more rapidly following instability than during uniform straining, because the stress system in the neck changes from uni-axial to plane strain. This would indicate that in forming operations the level of the fracture strain decreases with increasing degrees of biaxiality. However, this was not the case and the fracture strain increased with increasing degrees of biaxiality.

Thomason[159] treated the problem as one of necking between adjacent voids consisting of square prismatic cavities in a plane strain field in a rigid plastic non-strain hardening solid. This predicted that necking occurred when the length of the element approximated to its width, and the experimental results of Edelson and Baldwin[175] compared well with the models predictions.

Gladman et al[154] developed the concepts proposed by Gurland and Plateau[160]. It was assumed that the strain concentrations adjacent to second phase particles were controlled by the frontal radius of curvature of the particles. The criterion for the onset of the propagation of a ductile crack was taken as the function of the ratio of the void width to near neighbour spacing. The relationship between the total strain at fracture, εt, and the amount and morphology of second phase particles is given by :

$$\frac{2}{3}\left(\frac{a}{s}\right) = f_o \left[1 + kr^2 \; e^{2(\varepsilon t - \varepsilon_o)} - \frac{k}{r^2}\right]^{\frac{1}{2}} \qquad \text{(55)}$$

for de-cohesion, and :

$$\left(\frac{a}{S}\right)^2 = f_o \frac{3k^{\frac{1}{2}}}{2r} \left[e^{2(\varepsilon_t - \varepsilon_o)} - 1\right]^{\frac{1}{2}} \qquad \text{(56)}$$

for particle cracking, where a is half the void width, S is the critical near neighbour void spacing, f_o is the initial volume fraction, ε_t is the total strain at fracture, and ε_o is the strain required to nucleate voids, k is the strain concentration, and r is the length-width ratio of the particles.

Therefore, it may be seen from these relationships that the value of ε_t decreased exponentially as the volume fraction of particles increased. Also, the equations illustrated the effect of increasing the length-width ratio of second phase particles to give a higher tensile ductility when the long axis of the particles was parallel to tensile axis, compared with plate-like inclusions parallel to the minor axis.

However, the perennial problem is that a uniform particle spacing was assumed which is rarely the case in practice. Experimental work[143] showed that premature coalescence occurred at lower strains than predicted from theory because of a local concentration of non-metallic inclusions.

Deformation concentration along localised shear bands has been reported in a number of metals. Such localisation has led to premature failure and lowering of ductility. The bands however were distinct from the shear between adjacent voids which has been assumed to be responsible for coalescence and final failure. Localised shear bands may engulf many particles and the instability from which they were derived was by no means clear.

6.2 BRITTLE FRACTURE

This mode of failure is characterised by river patterns observed on the fracture surfaces. The operative mechanism in brittle fracture is one of cleavage. Brittle fracture may be discussed in terms of three important stages : the nucleation of the crack, the initial growth of the crack, and the traversing of the first strong barrier which the crack meets, e.g. a grain boundary.

6.2.1 Crack Nucleation

The basic mechanisms of crack nucleation in the presence of second phase particles were essentially the same as those discussed in the section on ductile fracture and will not be discussed further.

6.2.2 Initial Growth and Fracture

Although the nucleation mechanisms are essentially similar during both modes of failure, the mechanisms of failure are entirely different. In ductile failure, crack growth is slow and stable and growth is by plastic deformation which relaxes stress concentrations at the crack tip. In brittle failure, crack propagation is unstable and, unlike ductile failure, most of the strain concentration at the crack tip is released by cracking.

Since these stages occur in series, the measured fracture stress, σ_f, will be that nominal stress at which the most difficult of the three steps is overcome. If the yield stress is less than the fracture toughness criterion, K_{I_c}, then the metal is partially or completely ductile, since any stress concentrations can be removed by plastic deformation. If the yield stress is greater than K_{I_c}, the metal will fail in a brittle manner.

CHAPTER SEVEN

7. EXPERIMENTAL METHODS

7.1 MANUFACTURE OF ALLOYS

The alloys were made in a high frequency induction furnace. The lower nitrogen content steels were vacuum melted, whilst the higher nitrogen steels were air melted. The furnace linings were of magnesite in both cases. The analyses are listed in Table I.

7.1.1 Methods of Manufacture

i. Vacuum Induction

The following materials were used :

a. Japanese iron

b. Chromium metal

c. Carbon (as graphite)

d. Low carbon ferro-silicon

e. Manganese metal

Plus additions of either :

a. Molybdenum, or

b. Titanium, or

c. Ferro-niobium.

Alloy additions were calculated on the basis of 100% yield, using a charge weight of 11 kg. Melting down was carried out under

argon at a reduced pressure. All additions were made during this period, with the exception of manganese and titanium which were made just prior to tapping to reduce vapourisation losses to a minimum. The charge was cast at a temperature of 1570°C.

ii. Air Melts

The following materials were used :

a. Swedish iron

b. Chromium metal

c. Carbon (as graphite)

d. Low carbon ferro-silicon

e. Manganese metal

Plus additions of either :

a. Molybdenum, or

b. Ferro-niobium.

With the exception of the ferro-silicon, all additions were calculated on the basis of 100% yield, using a charge weight of 18 kg. The ferro-silicon requirements were calculated on the basis of the silicon content, plus an addition of silicon equal to 0.5% of the iron charged. This allowance was made to de-oxidise the iron. The charge was cast at a temperature of 1570°C. The ingots were covered with exothermic powder to reduce 'pipe' losses to a minimum.

iii. Processing of Ingots, Hot Rolling and Annealing Treatments

The surfaces of each ingot were planed to reduce the incidence of

surface defects in the cold rolled strip. Also any ingot 'pipe' was removed. The ingots were forged at a starting temperature of 1175°C to slabs approximately 160 mm wide x 13 mm thick. All the slabs were hot rolled at 1175°C to 3.55 mm, 1.78 mm and 1.36 mm thick to give cold rolling reductions of 75%, 50% and 35% respectively at a constant strip thickness of 0.89 mm. Hot rolling was carried out using a 2 high, 1×10^6 newton-rolling mill with 250 mm diameter rolls. A constant strip thickness is of particular importance in formability testing as results for these tests vary with strip thickness.(170) The hot rolled strip was annealed at 1000°C for half an hour to produce a common microstructure and texture for the same composition, having different hot rolling reductions. The steels were annealed at 750°C to temper any martensite produced in the 17% steel by the previous treatment. Before cold rolling was carried out, the steels were de-scaled.

7.2 COLD ROLLING

Cold rolling was carried out using a 2 high, 1×10^6 newton mill with 250 mm diameter rolls, without lubrication, in increments of approximately 0.1 mm.

7.3 ANNEALING OF THE SPECIMENS FOR THE KINETIC AND MECHANISTIC WORK

The cold rolled strips were cut into 25 mm squares for annealing. Annealing treatments from ten seconds to 250 hours duration were carried out in a sodium carbonate/ sodium chloride salt bath for all reductions in the temperature range 620°C - 810°C. The temperature variability in the salt bath was ± 3°C.

7.4 SPECIMEN PREPARATION

Specimens were sectioned longitudinally. Similar sections were taken from the strip in the hot rolled condition after annealing at 1000°C and after softening at 750°C. The mounted specimens were prepared for metallographic examination in the usual way. Polished specimens were etched in a saturated solution of picric acid in alcohol with additions of 10% concentrated hydrochloric acid and 2% concentrated nitric acid. Etching was improved by allowing a sample of ferritic stainless steel to dissolve in the re-agent for half an hour before use.

7.5 HARDNESS TESTING

Hardness measurements were carried out using a vickers pyramid hardness indenter, at a load of 5 kg. Hardness measurements were carried out on the longitudinally sectioned and mounted specimens. The surface of each specimen was prepared to a 600 mesh finish. Hardness results were calculated by taking the average of at least six impressions. Microhardness tests were carried out using a pyramid indenter at a load of 0.05 kg.

7.6 QUANTITATIVE METALLOGRAPHY

7.6.1 Measurement of Volume Fraction

A systematic point count was used to determine volume fraction.

i. Statistical Analysis for Determining No. of Points to be Counted

Point counting assumes that the proportion of random points when placed on a microstructure, which fall in a given constituent, is

equal to the volume fraction of that constituent. However, it is difficult to achieve a random array of points. Therefore, a systematic array is used and the distribution of the constituent is assumed to be random. This is true only if the spacing of the points is large when compared with that of the constituent.

The volume fraction, Vf, of the constituent α is given by :

$$Vf = \frac{P_\alpha}{P} \qquad \text{(57)}$$

where P is the number of points falling in the constituent, and P is the total number of points. From a statistical analysis, it is possible to determine the number of points required for a given error. If the number of points required is P_α then the number of points in the constituent is given by :

$$P_\alpha = \frac{1}{\left(\frac{\sigma_{vf}}{Vf}\right)^2} \qquad \text{(58)}$$

where σ_{vf} is the standard deviation, Vf is the volume fraction of the constituents, and $\left(\frac{\sigma_{vf}}{Vf}\right)^2$ is the proportional variance.

Hence the total number of points to be counted, P, is given by :

$$P = \frac{P_\alpha}{Vf} \qquad \text{(59)}$$

ii. Inherent Errors other than Statistical

The two major sources of errors are :

a. Failure to observe a true section

The relationship between point fractions and volume

fractions are valid only when measurements are made on a two-dimensional section through the structure. Therefore, because of differential polishing, e.g. second phase particles, etching, or when a slice of a specimen is viewed in transmission as in transmission electron microscopy, the measured volume will be greater than the true fraction.

b. Lack of Resolution

The limited resolution of the microscope causes a diffuseness of the boundaries which introduces an uncertainty in estimating whether the point lies within the constituent. The relative error as a function of constituent size is given by :

$$\frac{\delta Vv}{Vv} = \frac{\lambda}{2NA} \times \frac{4.7}{D} \qquad \text{(60)}$$

where NA is the numerical aperture, λ is the wavelength of the incident beam, and D is the diameter of the constituent.

iii. Measurement of the Percentage Recrystallised

The number of points, P, required for a constant accuracy increases with the volume fraction of recrystallised areas. Therefore, to keep the total number of points to a minimum, the absolute degree of accuracy was varied between $\pm 1\%$ and $\pm 3\%$ depending on the volume fraction, at a confidence limit of 95%. At volume fractions above 50%, P_α, was considered to be the unrecrystallised regions. The value of Vf was determined from an approximate value obtained

from the first few values of the count. After approximately half the total number of points had been counted, a more accurate estimate of Vf was made which enabled a re-assessment of the values of P_α and the total number of points, P, to be calculated. The analysis was terminated when the total number of points, P, had been achieved. Point counting was carried out using a Swift point counter.

iv. Measurement of the Percentage Austenite

The procedure used was similar to that for the recrystallisation studies. Because austenite transformed to martensite during cooling, the percentage austenite was measured in terms of percentage martensite. It was assumed that the cooling rate was sufficient to suppress the austenite-ferrite transformation, i.e. the austenite transformed completely to martensite.

v. Measurement of the Volume Fraction of Second Phase Particles

Because it has been shown by Equation 60 that large errors are introduced when measuring the volume fraction of fine particles by point counting, extraction replica techniques and transmission electron microscopy was used to reduce resolution errors to a minimum. A grid was superimposed on the screen of a transmission electron microscope and the examination was carried out at a magnification of 4,000 times. A minimum of 2,000 points were counted on each specimen.

7.6.2 Grain Size Measurement

The mean linear intercept was used. This is often termed the Heyn or Jeffries

method and measures the chord length defined by the intersection of a random straight line by the grain boundaries on the plane of the polish. The mean linear intercept, mli, is defined as $\bar{d}$ where :

$$\bar{d} = \frac{l}{n} \qquad \text{(61)}$$

where l is the length of the random line on the planar surface, and n is the number of grain boundary intersections of this line. The mean linear intercept is obviously less than the true grain size because it includes sectioning effects. The true mean diameter, $\bar{D}$, is defined as :

Assuming a cubo-octahedron

$$\bar{D} \simeq 1.75\ \bar{d} \qquad \text{(62)}$$

i. The Accuracy of the Mean Linear Intercept

Statistically, the standard deviation of the mean is defined as :

$$\sigma_{\bar{d}} = \frac{\sigma_d}{\sqrt{N}} \qquad \text{(63)}$$

where N is the number of observations made, and σ_d is the standard deviation of the individual operations. If the relative error, α, is given by :

$$\alpha = \frac{\sigma_{\bar{d}}}{\bar{d}} \qquad \text{(64)}$$

as Woodhead[177] found empirically that the error of individual intercepts was :

$$\frac{\sigma_d}{\bar{d}} = 0.7 \qquad \text{(65)}$$

This relative error is :

$$\alpha = \frac{0.7}{\sqrt{N}} \qquad \text{(66)}$$

ii. Measurement of Grain Size

Because ferritic stainless steels exhibited a non-equiaxed, non-uniform grain size, measurements were determined using the two- and three-dimensional Heyn intercept methods, i.e. measurement in the longitudinal, transverse and thickness directions respectively. The two-dimensional methods were used to determine the grain size for the kinetic and textural studies. For the structure-property relationships, a more accurate three-dimensional method was used. The relative errors, at a 95% confidence limit, were ±10% and ±5% respectively. This required 196 and 784 intercepts respectively in each direction. The mean true diameter was calculated using Equation 62, while the average grain sizes were calculated using the following relationships :

for a two-dimensional case :

$$\text{Average grain diameter} = \frac{\bar{D}_L + \bar{D}_t}{2} \qquad \text{(67)}$$

for a three-dimensional case :

$$\text{Average grain diameter} = \frac{\bar{D}_L + \bar{D}_t + \bar{D}_w}{3} \qquad \text{(68)}$$

where $\bar{D}_L$, $\bar{D}_t$ and $\bar{D}_w$ are the average true grain diameters in the longitudinal, thickness and width directions respectively.

7.7 ELECTRON MICROSCOPY

Electron microscopy was carried out on the material in the hot rolled, hot rolled and annealed, hot rolled annealed and softened, cold rolled, and cold rolled and annealed conditions using thin foil and replica techniques. This allowed investigations to be made which were not possible by normal optical techniques. Thin foil techniques made it possible to examine the processes occurring during recovery and recrystallisation. Local orientations of recrystallised grains during the early stages of recrystallisation were determined by electron diffraction to investigate possible mechanisms of recrystallisation texture formation . Precipitates were also identified by electron diffraction. Replica techniques were mainly used to measure the volume fraction and particle sizes of precipitates in the tensile specimens. However, limited investigations were carried out on specimens in the hot rolled and annealed, and hot rolled and softened conditions to identify the distribution of precipitates.

7.7.1 Thin Foils

These were made by initially thinning the bulk material to approximately 0.75 mm in a solution of boiling aqua regia. Three millimetre discs were taken from the bulk specimens and reduced to 0.25 mm by grinding both faces on a 400 mesh grinding paper. Perforation was performed in a 'Polaron' polishing unit using solutions of perchloric acid and methanol. Many foils were also manufactured in a Struers unit in a solution of 94 parts acetic acid to 6 parts perchloric acid at a potential of 80 volts. The thin foils were examined using transmission electron microscopy at accelerating voltage of 100 and 1000 KV. The advantages of using the 1000 KV instrument over 100 KV were that :

i. The increased penetration allowed thicker specimens to be examined which are more representative of bulk materials;

ii. The improved penetration also allowed studies to be made of larger precipitated particles by electron diffraction.

7.7.2 Replica Techniques

The specimens in the polished and etched condition were coated with carbon in the usual manner. A grid pattern of approximately 3 mm square was scribed on to the replicated surface. Replicas were loosened from the metal surface by electrolytically etching in a solution of 6% nital at a potential of 20 volts and removed by immersing in alcohol and distilled water. They were collected on a 3 mm copper grid, dried and examined by transmission electron microscopy at accelerating voltages of 50 and 80 KV respectively.

7.7.3 Scanning Electron Microscopy

The fracture surfaces were examined using a scanning electron microscope at an accelerating voltage of 30 KV.

7.8 X-RAY DIFFRACTION

X-ray diffraction studies were carried out on cold worked, and cold worked and annealed specimens, to determine the effect of the degree of cold reduction and recrystallisation on texture formation. Two methods were used to follow the formation of textures, namely the inverse pole figure and full or stereographic pole figure.

7.8.1 Inverse Pole Figure

Inverse pole figures offer a convenient method of depicting the proportions of grains with various orientations referred to a unique axis. The unique axis is usually taken as the sheet normal.

i. Theory

In sheet specimens diffraction using a diffractometer takes place only from planes parallel to the sheet surface, when the sheet surface and the counter are inclined at θ and 2θ respectively to the X-ray beam. Thus, if the intensities are recorded at Bragg angles corresponding to particular diffracting planes, (hkl), a quantitative measurement of the percentage of planes of a particular orientation, with respect to the sheet normal, can be evaluated.

Inverse pole figures are represented in terms of 'P values' which are a measure of the statistical chance of any plane, (hkl), lying in the plane of the sheet. For a particular plane, (hkl), with values I(hkl) and R(hkl) :

$$P_{hkl} = \frac{\frac{I(hkl)}{R(hkl)}}{\frac{1}{n}\sum_{o}^{n}\frac{I(hkl)}{R(hkl)}} \qquad \text{(69)}$$

where I(hkl) is the intensity of the (hkl) reflection from the textured specimen, R(hkl) is the intensity corresponding to a random sample, and n is the number of reflections considered. Thus a 'P value' of 1 signifies a random orientation, while for 'P values' greater than 1, the plane is considered to have preferred orientation.

The value of R(hkl) may be determined by two different methods: from a randomly oriented powder of the same material, or by calculation. The intensity of X-rays diffracted from a particular plane in a single phase specimen in a diffractometer may be expressed as :

$$I = \frac{KR}{2\mu} \qquad \text{——————} \quad (70)$$

where I is the measured diffracted intensity, R is the theoretical diffracted intensity, K is a constant and μ is the absorption coefficient.

This is valid for a powder or a polycrystalline aggregate specimen with a completely random arrangement of crystals which is effectively of an infinite thickness, i.e. no transmission of X-rays. With these conditions, K and μ are constant and independent of the nature of the specimen. Hence :

$$R_{hkl} = \frac{1}{v^2}\left[(F)^2 P\left(\frac{1+\cos^2\theta}{\sin^2\theta\cos\theta}\right)\right]\left(e^{-2m}\right) \qquad \text{——————} \quad (71)$$

where F is the structure factor, which is the vectorial sum of the atomic scattering factors of the atoms comprising the unit cell, P is the multiplicity factor which allows for the contribution of equivalent planes to the reflection, m is the temperature factor, $\frac{1+\cos^2\theta}{\sin^2\theta\cos\theta}$ is the Lorentz-polarisation factor, and v is the volume of the unit cell

ii. Annealing of the Specimens

The cold rolled strips were cut into 25 mm squares for subsequent

annealing. Annealing treatments to produce a fully recrystallised structure were carried out in a muffle furnace in the temperature range 700°C - 1000°C.

iii. Specimen Preparation

Specimens for X-ray diffraction were ground on one face to 600 grade finish. The other face was coated with 'Lacomit' to allow a measured amount of metal to be removed from the specimen surface during thinning. The specimens were thinned to ¾ thickness in a solution of boiling aqua-regia. This was carried out to remove the surface texture which has been shown[107] to be unrepresentative of the bulk material.

iv. X-ray Diffraction

For the determination of pole figures, a large number of reflecting planes are desirable, but the accuracy of the intensity values at low and high angles, i.e. less than 10° and greater than 70°, is reduced. The X-ray radiation chosen was molybdenum, K_α, which is of short wavelength and therefore for bcc ferrite a large number of reflections are produced within the range 2θ equals 20° - 70°. For bcc ferrite, 11 lines can be scanned for 2θ values between 20° - 73°. Two of the X-ray lines are higher order diffractions, therefore the 'P value' represents the chances out of 9 of a particular plane lying in or close to the surface of the sheet compared with the chances of any of the 8 others being similarly situated. The (411) plane may be separated from the (330) because the latter plane is a higher order reflection of the (110) and therefore its intensity can be calculated from the intensity of the (110) plane.

Texture data was obtained by an X-ray diffraction technique using a Siemens diffractometer. Studies were carried out in both the cold worked and recrystallised conditions. In each case the specimen was rotated at 60 revolutions/minute to produce an average value of P_{hkl}. The counter scanning rate was $\frac{1}{2}^{o}$/minute in all cases. The intensity of the diffracted X-rays was measured using a scintillation counter linked directly to a strip chart recorder. Intensity measurements I(hkl) were obtained by measuring the area beneath 9 different diffraction peaks using a planimeter. R_{hkl} values were determined both by calculation using Equation 71 and by measuring the area under 9 diffraction peaks for a ferritic stainless steel powder. Figure 21 illustrates a typical trace for a textured material and for a random powder. Calculations were based on a single phase binary iron-chromium alloy. Little difference was found between the calculated and measured values. P values were calculated using Equation 69. For the correlation between texture and both limiting draw ratio and $\bar{r}$ value, a more accurate method of determining the area under each peak was carried out. This consisted of scanning each peak at $\frac{1}{4}^{o}$/minute and recording the total counts on a scaler. The background level was measured both sides of the peak and the average value subtracted from the total counts to give the total counts under the peak.

7.8.2 Normal Pole Figures

A normal pole figure is a three-dimensional distribution of orientations represented on a two-dimensional figure such that one set of planes are projected, e.g. {200} , but from many crystals. A preferred orientation produces regions of high pole density on the projection with a scatter about principal orientations. It is usual in the construction of pole figures to use the rolling plane as the basic circle and to plot the rolling direction

at the top and bottom of the figure. Thus, by measuring the angles between regions of high pole density and the rolling direction and sheet normals, it is possible to determine the crystallographic directions which are parallel to the rolling plane and the crystallographic orientation of the rolling plane respectively.

i. Experimental Method

The annealed specimens were taken from the tensile heads of the specimens used for the r value determination as this would allow a direct correlation between r value and texture. The cold worked specimens were those used for the inverse pole figure determinations. Selected specimens only were used to highlight the texture differences found by the inverse pole figure studies.

ii. Texture Determination

Texture determination was carried out using a Siemens Kristalloflex texture goniometer. Since the pole figure must be as complete as possible, the pole figure was scanned along a spiral path in accordance with the reflection method. For this method of analysis both the inclination angle, α, and the azimuth angle, ϕ, are varied continuously, such that a 5° change in the inclination angle corresponded to a 360° rotation of the azimuth angle. A full 360° rotation of the azimuth angle takes 6 minutes, hence a full scan of the pole figure, i.e. inclination angle 0° - 90°, takes 108 minutes.

The {200} planes were used as the reflecting planes as most workers found that {200} pole figures give the best representation of textures in bcc metals. Molybdenum K_{α} radiation was used as it

produces an intense diffracted beam. The values of θ and 2θ for $\{200\}$ planes for molybdenum K_α were determined from the X-ray traces. The intensity of the diffracted beam was measured using a scintillation counter linked to a strip chart recorder.

The graduated circle was rotated to the position $\alpha = 90^\circ$ and the azimuth angle was set at $\phi = 0^\circ$. The specimen was mounted at the centre of the goniometer head such that the rolling direction was parallel to the plane of the vertical ring. The glancing angle θ was set to correspond to the angle θ for a $\{200\}$ reflection. The angles α and ϕ were adjusted to coincide with a region of high pole density on the pole figure and the counter was adjusted to attain the maximum intensity in the 2θ position. The vertical circle and azimuth angle were returned to $\alpha = 90^\circ$ and $\phi = 0^\circ$, and the analysis started at a maximum pulse rate, consistent with the maximum intensity, at a chart speed of 1 cm/ minute.

iii. Determination of the Random Intensity Level

This was achieved by noting both the total number of counts and the time taken for a full scan, i.e. 6480 seconds. However, the random level is not constant for the first 20° of the scan and the count rate increases by a factor of 2 during this period. Therefore the count rate must be halved, which was achieved by altering the time factor. Because a full scan took 6480 seconds, the time to scan 20° equals 1440 seconds. The time factor was reduced by :

$$\frac{1440}{2} \text{ seconds}$$

i.e. the time reduced from 6480 seconds to 5760 seconds. The random level was determined from the following equation :

$$\text{Random level} = \frac{\text{Total counts}}{5760 \times I} \qquad (72)$$

where I is the maximum impulse rate in counts/second. The random level was drawn on the chart and labelled 1.0. The zero level was determined by determining the intensity after the counter was moved from the 2θ value corresponding to the {200} reflection. A grid was drawn corresponding to values of 0.5, 1.0, 1.5, 2.0 etc. times random. The intensity at any point on the spiral scan chart was transferred to the pole figure by means of a recording spiral. The points of equal intensity on the pole figure were joined to form contours from which individual pole peaks were identified and labelled.

7.9 MECHANICAL TESTING

Two forms of mechanical tests have been used, namely true stress-true strain, and r value determination.

7.9.1 Annealing

The tensile specimens were annealed in a vacuum tube furnace in the temperature range 800°C - 1000°C. The temperature variability in the furnace was ±10°C. A vacuum was used to reduce oxidation, de-carburisation and nitrogen pick-up.

7.9.2 True Stress - True Strain

Tensile specimens were produced to the dimensions given in Figure 22a(A).

Specimens were blanked from the cold rolled sheet at 0°, 45° and 90° to the rolling direction. However, this produced a cold worked edge approximately 0.075 mm deep which after annealing resulted in grain sizes different from those in the bulk material. (Fig 22b) This was removed by machining 0.25 mm/side from the gauge length.

Tensile specimens were strained to failure using an Instron testing machine at a cross head speed 0.2 cm/min. The load was measured using a 500 kg load cell linked to a potentiometric recorder. The load cell was re-calibrated between each test using a 20 kg load. The extension was measured using a 0 - 50% strain gauge extensometer with a 10 mm gauge length linked to a potentiometric recorder. Calibration was carried out between each test such that 25% extension, i.e. 2.5 mm extension, corresponded to 25 cm of chart movement. Thus load and extension could be measured simultaneously. Width and thickness measurements were taken as the average of six readings along the gauge length. The true stress, $\bar{\sigma}$, was :

$$\bar{\sigma} = \frac{P}{A_I} \qquad \text{(73)}$$

where P is the force in newtons, and A_I is the instantaneous cross sectional area. The instantaneous area A_I was calculated by assuming that during deformation up to the onset of necking, the specimen maintained a constant volume such that :

$$A_o \, l_o = A_I \, l_I \qquad \text{(74)}$$

such that :

$$A_I = \frac{A_o \, l_o}{l_I} \qquad \text{(75)}$$

where A_o and l_o were the initial area and length respectively and l_I was the length determined from extensometer readings. The true strain, ε, was given by :

$$\varepsilon = \ln \frac{A_o}{A_I} \qquad \text{(76)}$$

The true stress-true strain calculations were made using a digital computer. The rate of work hardening, $\frac{d\sigma}{d\varepsilon}$, was computed from the slope of the true stress - true strain curve at fixed increments of true strain.

7.9.3 r Values

Tensile specimens were produced to the dimensions given in Figure 22a(β). Specimens were taken at 0^o, 45^o and 90^o to the rolling direction and machined in the same manner as those for the mechanical tests. r values were calculated after 10% elongation; measurement was made using a 0 - 10% strain gauge extensometer. Straining was carried out using an Instron testing machine at a cross head speed of 0.5 cm/min. Although r values are determined from Equation 38, this leads to large inaccuracies because of measuring small changes in thickness. More accurate thickness strains were calculated from changes in width and length assuming a constant volume.

Assuming a constant volume, Equation 38 becomes :

$$r = \frac{\ln \frac{W_o}{W_1}}{\ln \frac{l_1 W_1}{l_o W_o}} \qquad \text{(77)}$$

where l_o and W_o are the initial length and width, and l_1 and W_1 are the final length and width.

Measurements of length and width were made using a microscope with a micrometer stage. Larger specimens were used for the r values, because these exhibit greater changes in width at equal strains and therefore smaller errors in measurement. Δ r was expressed using Equation 40.

7.10 FORMABILITY TESTS

These included Erichsen and Swift cupping tests.

7.10.1 Annealing

The specimens were annealed in a muffle furnace in the temperature range 800°C - 1000°C. Argon was passed over the specimens to reduce oxidation, de-carburisation and nitrogen pick-up. Any slight oxidation was removed with a fine grinding paper.

7.10.2 Erichsen Tests

These tests were determined using a Hille 4 x 10^5 newton press with ball and die diameters of 20 mm and 33 mm respectively. A clamping force of 1 x 10^5 newtons was used to prevent metal being drawn in to the die, to simulate stretching conditions. Combined lubrication of polythene and oil was used between the punch and the specimen to reduce friction. The ram speed was 25 mm/minute[172], load and punch travel were accurately calibrated to allow the depth at fracture to be measured directly from the punch travel at maximum load.

7.10.3 Swift Cupping Tests

Tests were carried out using a Hill 4 x 10^5 newton press which automatically

recorded punch load and travel. The ram and die diameter were 50 mm and 53.7 mm respectively. The initial thickness of the discs was measured using a micrometer. Testing was carried out at a ram speed of 200 mm/minute, with polythene lubrication on the die face only.

The discs were degreased in trichloroethylene just prior to drawing. A blank holder force of 1×10^4 newtons was used to prevent wrinkling. Specimens were machined into discs before annealing, between 103 and 121 mm in diameter in increments of 2 mm. The flash was removed with a file. Once an approximate critical blank diameter had been determined, further discs were machined to ±2 mm from this diameter, in 1 mm increments, to allow measurement of a more accurate critical diameter. The results were calculated in terms of the limiting draw ratio, LDR, where :

$$LDR = \frac{\text{critical blank diameter}}{\text{ram diameter}} \qquad \text{——— (78)}$$

The percentage earing was calculated from :

$$\text{Percentage earing} = \frac{\text{Height of the ear - height of the trough}}{\text{Average height of the cup}}$$

——— (79)

CHAPTER EIGHT

8. EXPERIMENTAL RESULTS

8.1 HOT ROLLED MICROSTRUCTURES

The steels were examined metallographically at three distinct stages of processing:

i. After hot rolling;

ii. After hot rolling and annealing for half an hour at 1000°C;

iii. After treatment ii. followed by a further anneal for half an hour at 750°C.

Longitudinal sections of the microstructures were examined at each stage to study the effect of thermal treatment on the grain size and phase distribution. At this stage the grain boundaries produced during hot rolling will be referred to as matrix grain boundaries. Typical hardness values at each stage of processing are given in Table II.

All the steels examined showed a marked resistance to recrystallisation after hot rolling and tended to form low energy subgrain boundaries within the matrix ferrite grains (fig 23a). After annealing for half an hour at 1000°C the steels recrystallised.

8.1.1 17% Cr Steels

Alloy (1) 17% Cr Low (C+N)

In this steel there was some evidence for recrystallisation at the matrix grain boundaries after hot rolling (fig 23a). Micro hardness tests showed

that recrystallised regions were softer than the surrounding matrix Table III. After being annealed at 1000°C the microstructure showed pools of martensite at the grain boundaries (fig 23b). Within the martensite there was still evidence of undissolved chromium carbide which was identified by electron diffraction as $M_{23}C_6$. From the distribution of the martensite pools, it was clear that they were areas of austenite formed at the matrix grain boundaries which subsequently transformed to martensite during cooling. The austenite had pinned the growing ferrite boundaries to produce a 'pancake' grain structure; annealing at 750°C tempered the martensite and precipitated $M_{23}C_6$ at the grain boundaries. It also produced precipitation within the ferrite grains adjacent to the martensite (fig 23c). The precipitates were identified as needles of Cr_2N with some $M_{23}C_6$. In the rest of the material, few precipitates were present. Thin foil electron microscopy showed that after annealing at 750°C the original martensite regions recrystallised to a fine grain size (fig 23d).

Alloy 1c did not show martensite in the microstructure after annealing at 1000°C, but comprised coarse polygonal ferrite grains due to the absence of austenite and other pinning particles. It should be noted that the carbon content of Alloy 1c was lower than that of either steels 1a or 1b (Table I). Annealing at 750°C precipitated $M_{23}C_6$ at the grain boundaries.

Alloy (2)- 17% Cr High (C + N)

In the hot rolled condition the structure comprised alternate bands of ferrite and martensite (fig 24a), the martensite clearly being identified by micro-hardness tests (Table III). Thin foil electron microscopy showed the martensite to be lath martensite (fig 24b). The ferrite grains were heavily elongated in the direction of rolling and showed low energy subgrain boundaries. These grains showed a marked increase in micro-hardness when

compared with annealed ferrite (Table III). Thin foil electron microscopy showed a recovered structure in the ferrite (fig 24b). The martensite regions were in the form of grains elongated in the direction of rolling and there were indications that the austenite tranformed to martensite without recrystallising. Carbides occurred at the ferrite/martensite interface, in the martensite and at the ferrite grain boundaries.

Annealing at 1000°C recrystallised the ferrite into 'pancake' grains (fig 24c) due to the pinning action of alternate bands of austenite. The austenite which appeared to have formed from previously martensite regions was distributed in bands and had subsequently re-transformed to martensite during cooling. This martensite contained $M_{23}C_6$ which had remained undissolved at 1000°C. However, most of the carbide at the ferrite grain boundaries and at the ferrite/austenite interface had been taken into solution at 1000°C. Thin foil electron microscopy showed that the austenite tranformed to a lath martensite (fig 24d).

After annealing at 750°C the martensite had tempered to ferrite and carbide, and carbide had precipitated at the martensite/ferrite interface and at the ferrite grain boundaries. Extensive fine precipitation had occurred in the ferrite, at the ferrite/martensite interface, identified as Cr_2N and $M_{23}C_6$.

There was more fine precipitation within the ferrite matrix than in the low carbon and nitrogen steel. This may be a result of chromium rejection by the austenite producing a concentration of chromium at the ferrite/austenite interface. The higher chromium content at the interface may produce increased supersaturation. In the former martensite regions two distinct sizes of $M_{23}C_6$ carbides were present, i.e. temper carbides and the much coarser previously undissolved carbides. Thin foil

electronmicroscopy showed that these areas were reluctant to recrystallise and tended to show a polygonised structure (fig 24e).

Alloy (3) 17% Cr High (C + N) 1% Mo

The microstructure of this steel in the hot rolled condition was similar to that of Alloy (2). However, the amount of martensite was less. At the ferrite/martensite interface, in the ferrite grains and in the ferrite grain boundaries there was evidence of $M_{23}C_6$ precipitation. Annealing at 1000°C produced a structure similar to that in Alloy (2). The pinning action of the austenite was not so effective as in Alloy (2), since the volume fraction was less at 1000°C due to the presence of molybdenum. The pinning action of the carbides was not so effective as that of austenite as numerous bands of coarse carbides (fig 25a) obviously originating from hot rolled ferrite grain boundaries were present within the ferrite grains. This was presumably due to rapid coarsening of carbide particles situated at grain boundaries which allowed unpinning of the boundary.

Annealing at 750°C tempered the martensite and further precipitation had taken place at the grain boundaries . Thin foil electronmicroscopy showed this steel to be resistant to recrystallisation in the original martensite areas. However, unlike the base steel no preferential precipitation took place at the ferrite/martensite interface.

Alloy (4) 17% Cr Low (C + N) 1% Mo

In Alloy (4)a pools of martensite were present at both matrix grain boundaries and within the grains. Alloy 4b showed a greater preponderance of substructure but there was little or no martensite in the microstructure.

The reason for this may be due to the slightly lower molybdenum content of Alloy 4a as compared with 4b (Table I).

After annealing at 1000°C new areas of austenite had nucleated at matrix grain boundaries and in the original martensite regions. Large undissolved carbides were present in the martensite and at the ferrite/martensite interface. Most of the boundary pinning resulted from the carbide precipitated at the matrix grain boundaries since the volume fraction of austenite was insufficient for pinning as shown by the fact that pinning was not so effective as in Alloy(1). The pinning action of the carbide particles was not as effective as the austenite in Alloys 1a and 1b because numerous bands of coarse carbides, similar in origin to those described for Alloy 3, were present within ferrite grains, i.e. the grain boundaries had broken free. (Fig 25a)

Alloy (5) 17% Cr low (C + N) + Ti

In this steel no subgrain formation was observed in the elongated ferrite grains but thin foil electronmicroscopy showed recovered structures (fig 25b). Titanium carbonitride particles were randomly distributed throughout the structure. At the grain boundaries, precipitates were identified as $M_{23}C_6$, indicating that an insufficient titanium addition had been made to suppress this reaction.

After annealing at 1000°C recrystallised grain boundaries were paralled to the rolling direction. Titanium carbonitride particles had little pinning action as few of these particles were associated with grain boundaries. The chromium carbide precipitated at the matrix grain boundary is believed to be responsible for the majority of the pinning action since it remained undissolved after annealing at 1000°C.

Martensite was not present in the microstructure indicating that the addition of titanium was sufficient to prevent austenite formation at 1000°C.

After annealing at 750°C there was further evidence of precipitation which was also indicated by the hardness results (Table II).

Alloy (6) 17% Cr High (C + N) + Nb

The grains contained copious amounts of Nb (CN) particles distributed randomly throughout the structure.

After annealing at 1000°C the niobium had not been capable of inhibiting recrystallisation. However unlike other steels the grains were relatively fine and equiaxed with some evidence of pinning by the coarse niobium carbonitride particles. The addition of niobium was sufficient to prevent austenite formation at 1000°C.

Alloy (7) 17% Cr Low (C + N) + Nb

As for the titanium steel, no subgrain formation was observed in the elongated ferrite grains, but the hardness after hot rolling indicated a recovered rather than a recrystallised structure. The structure was also characterised by randomly distributed niobium carbonitride particles.

Annealing at 1000°C recrystallised the steel into fine equiaxed grains in which some grain boundary pinning was evident. Again niobium additions were sufficient to prevent austenite formation at 1000°C.

8.1.2 25% Cr Steels

Alloy (8) 25% Cr Low (C + N)

The steels showed resistance to recrystallisation after hot rolling. At matrix grain boundaries precipitation of $M_{23}C_6$ had taken place. There was evidence of carbide precipitation within the deformed ferrite grains. As would be expected the 25% Cr steels did not contain martensite since the composition was outside the $\alpha + \gamma$ phase field.

After annealing at 1000°C the steel recrystallised and contained bands of carbides which showed the original hot rolled grains (fig 25c). These carbides had partially pinned the grain boundaries in some regions to produce a highly elongated grain structure. This pinning action was not completely effective as numerous carbide bands of obvious grain boundary origin were present within the ferrite grains.

There also was evidence of randomly distributed carbides.

Annealing at 750°C produced further precipitation at grain boundaries which was also indicated by the hardness (Table II).

Alloy (9) 25% Low (C + N) 1% Mo

The structure in the hot rolled condition was similar to that of the base steel.

After annealing at 1000°C the steel recrystallised to produce a microstructure similar to that of the base steel, and the pinning action was more effective.

However bands of carbide were still present within the ferrite. In comparison with the base composition there appeared to be a larger quantity of carbides for a given carbon content.

8.2 COLD WORKING CHARACTERISTICS

The cold working characteristics after annealing at 1000°C and softening at 750°C have been investigated by measuring the average increase in hardness ΔH, at 10, 20, 35, 50 and 75% reduction respectively. The results are shown in figure 26. The cold working characteristics are typical of bcc ferritic materials, i.e. the steels work harden quite rapidly initially, but do not maintain a high work hardening rate at higher strains.

The 17% Cr lower interstitial content steel exhibited a somewhat higher initial work hardening rate than the higher interstitial steel (fig 26A). Although this was not reflected by the tensile results this may be because the higher interstitial content did not allow full recrystallisation after annealing at 1000°C and softening at 750°C, thus producing a lower initial work hardening rate. The 25% Cr steel (fig 26A) showed a higher initial rate of work hardening than the 17% Cr steels.

In the molybdenum steels the initial work hardening rate of the 25% Cr steel was again higher than that of the 17% Cr steel (fig 26B). At 17% Cr in the molybdenum steels the lower interstitial content had again produced a high initial work hardening rate.

Titanium and niobium (fig 26C) both increased the initial work hardening rate compared with the base material at both interstitial levels. This

may be due to the effect of second phase particles. However, the lower interstitial niobium steel exhibited a higher overall work hardening rate than the higher interstitial counterpart. At the higher interstitial content additions of niobium increased the overall work hardening rate.

8.3 THE EFFECT OF ANNEALING

The property and microstructural changes that occur during annealing in ferritic stainless steels, after cold rolling, have been followed using hardness testing and metallographic point counting. The kinetics of recovery and recrystallisation were determined at 35%, 50% and 75% cold reduction after annealing in the temperature ranges 620°C - 810°C. Hardness values were expressed in terms of the change in hardness ΔH rather than in absolute terms, to take account of compositional effects which caused differences in the initial hardness. Fig. 27A shows a typical curve for the change in hardness ΔH with annealing time. In ferritic stainless steel there was a retarded softening at the completion of the recovery stage which has been termed the plateau region. Thus compositional effects on recovery may be separated from those on recrystallisation. Recovery has been described in terms of two parameters : the rate of recovery, ie. the slope of the curves, and the amount of recovery, ie. the change in hardness during the recovery stage prior to recrystallisation.

Point counting has been used to determine the recrystallisation kinetics at a constant temperature as a function of composition and degree of cold work. Fig. 27b shows schematically a typical curve of percentage recrystallisation against annealing time. Recrystallisation has been described in terms of two parameters: namely the incubation period for recrystallisation and the recrystallisation rate, ie. the maximum slope of the curve in Fig. 27B.

Hardness results have been used to illustrate specific recrystallisation effects. The end of the plateau stage coincided with the recrystallisation incubation period for most of the steels studies, indicating that recrystallisation was inhibited during the plateau stage.

Some of the recrystallisation kinetics have been interpreted in terms of the Arrhenius rate equation:

$$\log \frac{1}{t} = \log A - \frac{Q}{2303\ RT} \qquad \text{(80)}$$

where $\frac{1}{t}$ is the rate of recrystallisation in which t is the time in seconds for a given percentage recovery in hardness, where this is given by:

$$\text{Percentage recovery in hardness} \simeq \frac{\text{Actual } \Delta H}{\text{Total } \Delta H \text{ in the fully recrystallisation condition}} \qquad \text{(81)}$$

8.4 RECOVERY

The recovery stage will be described in terms of three effects namely cold work, composition and annealing.

8.4.1 The Effect of Cold Work

Fig. 28 illustrates the effect of cold work on the relative recovery rates for some ferritic stainless steels after annealing at 655°C, there being apparently little overall effect of cold working. However, decreasing amounts of cold work extended the plateau region between recovery and recrystallisation due to the accelerating effect of increasing cold work on recrystallisation. This indicated a marked polygonisation effect at low reductions.

8.4.2 The Effect of Temperature and Composition

Alloy (1) 17% Cr Low (C + N)

Annealing this steel at temperatures below 690°C led to a marked plateau region between recovery and recrystallisation. This plateau occurred at approximately a constant hardness and its extent increased with decreasing temperature (fig 29).

8.4.3 The Effect of Interstitial Content at 17% Cr

The recovery rate increased with increasing interstitial content after 35% and 50% cold reduction and annealing at 690°C (fig 30). Although the higher interstitial content steel apparently recovered more rapidly at the lower reductions, the plateau region between recovery and recrystallisation was considerably extended. In fact after 35% cold reduction, annealing the higher interstitial content steel below 750°C resulted in a distinct plateau between recovery and recrystallisation (fig 31). This plateau however did not occur at a constant hardness value. To a lesser extent the plateau was present after 50% cold reduction. However after 75% cold reduction no such plateau was observed (fig 32). This may be due to the higher degree of stored energy resulting in recrystallisation encroaching on the recovery region.

8.4.4 The Effect of Chromium Content at the Lower Interstitial Level

Increasing the chromium content from 17% to 25% increased the rate of recovery at 35% and 50% reduction after annealing at 690°C (fig 33). At lower temperatures the recovery rate of the 25% Cr steel decreased relative to that of 17% Cr steel (fig 34).

8.4.5 The Effect of Molybdenum at the Lower Interstitial Level

Alloy (4) 17% Cr Low (C + N) 1% Mo

The effects of additions of molybdenum to a 17% Cr low (C + N) steel were complex. At 35% reduction the molybdenum steel shows a faster recovery rate and an increased amount of recovery (fig 35). At the higher reductions the rate of recovery of the molybdenum steel was slower. Additions of molybdenum extended the plateau between recovery and recrystallisation. Unlike the base steel, annealing at temperatures below 750°C led to a distinct plateau between recovery and recrystallisation (fig 36). This plateau occurred at approximately constant hardness and its extent increased with decreasing annealing temperature.

Alloy (9) 25% Cr Low (C + N) 1% Mo

Additions of molybdenum to a 25% Cr steel had little effect at 35% reduction, but at 50% and 75% cold reduction decreased the recovery rate (fig 37). The plateau was again extended by additions of molybdenum.

Compared with Alloy 4, i.e. 17% Cr low (C + N) 1% Mo, at the lower reductions the 25% Cr steel recovered slightly more rapidly (fig 38). However, at 35% cold reduction the 17% Cr low (C+N) 1% Mo steel showed a slightly greater amount of recovery. At lower temperatures the plateau was extended in the 25% Cr molybdenum bearing steel. This may be due to an increased supersaturation of chromium carbides and nitrides in the 25% Cr steel which retards normal recovery processes.

8.4.6 The Effect of Molybdenum at the Higher Interstitial Level

At the higher interstitial content, Alloy 3, additions of molybdenum decreased both the rate and the amount of recovery that occurred prior to recrystallisation (fig 39). The plateau was also extended relative to the base steel. However unlike the base steel the plateau was present over a wide temperature range, at all cold reductions, and occurred at approximately a constant hardness value.

This steel also shows a distinct plateau effect after annealing at temperatures of 750°C and below (fig 40).

Compared with Alloy 4, i.e. the 17% Cr low (C + N)1% Mo steel, the rate of recovery was slower and the amount of recovery prior to recrystallisation was much less at the higher interstitial content (fig 41).

8.4.7 The Effect of Titanium at the Lower Interstitial Content Alloy(5)

Additions of titanium increased both the rate and the amount of recovery prior to recrystallisation (fig 42). Also when the steels were annealed at low temperatures they did not exhibit a distinct plateau between recovery and recrystallisation even after only 35% reduction (fig 34).

8.4.8 The Effect of Niobium at the Lower Interstitial Level

Niobium at the lower reductions increased both the rate and the amount of recovery prior to recrystallisation (fig 43). However, unlike titanium niobium extended the plateau even at temperatures up to 810°C (fig 44). Compared with the 17% Cr low (C + N) 1% Mo steel additions of niobium extended the plateau (fig 43).

8.4.9 The Effect of Niobium at the Higher Interstitial Level

At the higher interstitial level, additions of niobium decreased both the rate and the amount of recovery (Fig 45). At 75% cold reduction, niobium greatly extended the plateau while at 35% reduction there was very little effect.

Compared with the lower interstitial niobium steel, increasing the interstitial content decreased both the rate and the amount of recovery (Fig 46). Although increasing the intersitial content retarded recovery, the plateau was shorter at the higher interstitial content.

Compared with the 17% Cr high (C+N) 1% Mo steel, the plateau was generally shorter while the rate of recovery and amount of recovery were similar (Fig 46).

8.5 RECRYSTALLISATION

8.5.1 The Effect of Cold Working

Recrystallisation always took place more rapidly as the degree of cold work was increased (Fig 47).

8.5.2 The Effect of Composition after 75% reduction

i. The Effect of Interstitial Content

At the higher interstitial content, recrystallisation was retarded relative to the lower interstitial content (Fig 48). After annealing at 750^{o}C, the incubation period for recrystallisation increased only slightly while the rate of recrystallisation was

markedly decreased. At lower annealing temperatures, the retarding effect of the higher interstitial content was even greater.

ii. The Effect of Chromium at the Lower Interstitial Content

Additions of a further 8% Cr had very little effect on recrystallisation (Fig 49). At 750°C, the 25% Cr steel recrystallised more rapidly than the 17% steel. At the lower annealing temperatures, recrystallisation in the 25% Cr steel was retarded relative to that in the 17% Cr steel, resulting in a higher activation energy in the 25% Cr steel, as will be shown later.

iii. The Effect of Molybdenum at the Lower Interstitial Level

Alloy (4) 17% Cr Low (C+N) 1% Mo

After annealing at 750°C, additions of molybdenum increased the incubation period and decreased the recrystallisation rate (Fig 50). At lower temperatures, the retarding effect of molybdenum was even greater resulting in an increased activation energy. It can be seen from Figure 35 that the increased incubation period in the molybdenum steel resulted from an extended plateau between recovery and recrystallisation.

Alloy (9) 25% Cr Low (C+N) 1% Mo

At 25% Cr after annealing at 750°C, additions of molybdenum again increased the incubation period for recrystallisation and decreased the recrystallisation rate (Fig 51). At lower temperatures, the

retarding effect of molybdenum was similar to that observed in the 17% Cr steel. The extended incubation period again correlated with the extended plateau region in the molybdenum steel.

After annealing at 750°C, recrystallisation was slightly faster in the 25% Cr molybdenum steel than in the 17% Cr molybdenum steel (Fig 52). At lower temperatures, recrystallisation in the 25% Cr steel was retarded relative to that in the 17% Cr steel. This was in agreement with the extended plateau observed in the 25% Cr molybdenum steel (Fig 38).

iv. The Effect of Molybdenum at the Higher Interstitial Level Alloy (3)

At the higher interstitial content, additions of molybdenum increased the incubation period for recrystallisation (Fig 53). However, once recrystallisation had started, the rate of recrystallisation in the molybdenum steel was faster. The increased incubation period in the molybdenum steels correlated with extended plateau stage (Fig 39).

In comparison with the 17% Cr low (C+N) 1% Mo steel, the incubation period was increased (Fig 54), which was also in agreement with the extended plateau found in the higher interstitial content steel. However, although the incubation period was extended at 750°C, the higher interstitial content steel had a faster recrystallisation rate, despite the longer incubation period, 100% recrystallisation being achieved in the same time as in the lower interstitial steel (Fig 54). At lower temperatures this was not the case and recrystallisation was retarded in the higher interstitial content steel. However at higher temperatures than 750°C, the higher

interstitial content caused more rapid recrystallisation than in the lower interstitial content steel.

v. The Effect of Titanium at Lower Interstitial Level Alloy (5)

Additions of titanium had very little effect on recrystallisation (Fig 55). The incubation period was slightly retarded in the titanium steel, but the recrystallisation rate was faster, resulting in 100% recrystallisation being achieved slightly more rapidly in the titanium steel than in the base steel.

vi. The Effect of Niobium at the Lower Interstitial Level Alloy (7)

Unlike titanium, additions of niobium markedly increased the incubation period for recrystallisation and decreased the recrystallisation rate (Fig 56). This was particularly the case for the lower reductions which were very slow to recrystallise.

Niobium retarded recrystallisation to a much greater extent than molybdenum at the lower interstitial level (Fig 57). This was evident from comparing Figure 44 with Figure 36 which shows that in the niobium steels, the plateaux were extended relative to the molybdenum steels.

vii. The Effect of Niobium at the Higher Interstitial Level Alloy (6)

At the higher interstitial level, additions of niobium increased the incubation period for recrystallisation. However, once recrystallisation had started, the recrystallisation rate of the niobium steel was faster (Fig 58). The increased incubation

period was in agreement with the extended plateau observed in niobium steels.

In the niobium steels, recrystallisation always took place more rapidly at the higher interstitial level (Fig 59) probably as a result of an increased volume fraction of second phase particles.

8.5.3 The Effect of Composition and Cold Work on the Recrystallised Grain Size

The recrystallised grain size at a constant temperature of 750°C was measured using the Heyn intercept method when recrystallisation was just completed and before any discernible grain growth had taken place. It was observed that, as is usual, the recrystallised ferrite grain size became finer as the amount of prior cold deformation was increased (Figure 60).

In the 17% Cr steels (Fig 60a) increasing the interstitial carbon and nitrogen contents decreased the grain size for all cold reductions. The effect of cold reduction was much less marked at the higher interstitial content due to the nucleating action of carbide particles. The aspect ratio of the recrystallised grains increased with increasing interstitial content. Additions of molybdenum (Fig 60a) at both interstitial levels refined the grain size at all reductions.

Additions of titanium had no major effect on the grain size at 75% reduction (Fig 60b). The lower interstitial niobium steel behaved in a similar manner (Fig 60b). At the higher interstitial level, additions of niobium also had no effect on the average grain diameter at 75% reduction. At the lower reductions, however, the higher interstitial content niobium steel had a coarser grain size than the base 17% Cr higher interstitial content steel (Fig 60b). The aspect ratio of the recrystallised grains in the niobium

steels was much less at all reductions, i.e. the grains were less pancaked. In the niobium steels, the grain size was finer in the higher interstitial content steel which was also much less sensitive to variations in the amount of cold work.

The 25% Cr low (C+N) steel (Fig 60c) had a slightly finer grain size than the 17% Cr steel after 75% reduction and was much less sensitive to variations in the amount of cold work, while additions of molybdenum decreased the grain size, particularly at 35% and 50% reduction, due to a more uniform distribution of $M_{23}C_6$ particles.

8.5.4 The Effect of Annealing Temperature on the Grain Size

Figure 61 illustrates the effect of annealing temperature on the grain size after 75% reduction. Annealing the 17% Cr low (C+N), the 17% Cr low (C+N) + Ti and the 25% Cr steels below 690°C increased the grain size (Fig 61a) which coincided with the marked decrease in recrystallisation rate found in these steels. In the 25% Cr steel, slight increase in grain size was observed after annealing above 750°C.

Annealing the molybdenum and niobium steels below 750°C (Fig 61b) increased the recrystallised grain size. The ferrite grain size in these steels was found to increase progressively with decreasing temperature. This increase in the grain size was because of a decreased nucleation rate at lower annealing temperatures. The nucleation rate decreased progressively with decreasing annealing temperature resulting in the progressive increase in the grain size. The decreased nucleation rate was because of a precipitation-recrystallisation interaction which pinned the subgrain boundaries. Because of the sequential unpinning of subgrain boundaries, the time available for growth of the first nucleated grains was increased resulting

in an increased grain size. At lower annealing temperatures, the rate of particle coarsening decreased, therefore the time available for growth of the first nucleated grains increased still further resulting in further decreases in the nucleation rate and an even coarser grain size.

In the molybdenum steels, the 25% Cr steel showed a much greater increase in grain size than its 17% Cr counterpart (Fig 61b). This may be due to an increased supersaturation effect in the 25% Cr steel. Annealing at temperatures above 750°C resulted in slight increases in the grain size of the 25% Cr base steel. This is because of an increased growth rate at high temperatures.

8.5.5 The Effect of Temperature on Recrystallisation (Activation Energies)

Recrystallisation in ferritic stainless steels was especially retarded at the lower annealing temperatures so that there was an increased activation energy for recrystallisation. Since all steels exhibited this effect, only differences between individual steels will be described. Typical values for activation energies are given in Table V.

Increasing the chromium content from 17% Cr to 25% Cr increased the activation energy for recrystallisation (Fig 62). After 35% reduction, the 25% Cr steel showed an increased activation energy, after annealing at below 720°C. However, at 75% reduction both steels showed an increased activation energy after annealing below 690°C.

Increasing the interstitial content increased the activation energy for recrystallisation (Fig 63).

At the lower interstitial level, additions of molybdenum increased the

activation energy for recrystallisation at both chromium levels (Fig 64). This was presumably due to the marked plateau effect between recovery and recrystallisation found in the steels. In fact the incubation period for recrystallisation coincided with the end of the plateau at all temperatures. In the 25% Cr-Mo steels, annealing below 720°C led to an increased activation energy at all cold reductions. This was in agreement with the increased retarding effect of molybdenum on recrystallisation at low temperature in 25% Cr steels.

Additions of titanium had little effect on the activation energy in Table V.

At the higher interstitial level, additions of molybdenum increased the activation energy for recrystallisation. In the molybdenum steels, the activation energy also increased with increasing interstitial content.

Additions of niobium increased the activation energy at both interstitial levels.

8.6 TEXTURES

In the hot rolled and annealed condition, the textural components present were investigated by the inverse pole figure technique. As three different hot rolling reductions were used to give a constant sheet thickness, after three different cold rolling reductions, inverse pole figure data was determined at these three different hot rolled thicknesses. In the cold worked and recrystallised conditions, textural development was also followed using the inverse pole figure technique. The full textures of selected specimens were determined by normal pole figures.

8.6.1 Hot Rolled and Annealed Condition (Figs 66 - 69)

In the hot rolled and annealed condition, little difference was found in the textural components produced by different hot rolling reductions for any given steel. However slight differences existed between different alloy compositions. Figures 66 - 69 show typical inverse pole figures. No really strong texture was observed and on no occasion did the 'P value' of any component exceed 2. However, in five out of nine steels examined, the {110} was the strongest component. In alloy (5), the {100} was the strongest component. However, these differences were quite small.

8.6.2 The Effect of Cold Work and Composition on Texture Development

Figures 70 - 78 show the progressive changes in texture with increased cold reduction from 35% to 95% for the four main textural components, namely {110}, {111}, {100}, and {211}.

Alloy (1) 17% Cr Low (C+N) (Fig 70)

The {111} component increased progressively with increased cold reduction to a maximum of P = 3.6 after 75% reduction. Above 75% reduction, the {111} component decreased significantly with corresponding increase in the {100} component.

Alloy (2) 17% Cr High (C+N) (Fig 71)

At the higher interstitial content, and higher reductions the intensity of the {111} component was greater than at the lower interstitial level. The rapid increase in the {100} component above 75% reductions was not found at the higher interstitial level.

Alloy (5) 17% Cr Low (C+N) + Ti (Fig 72)

Unlike the base steel, the {111} component was a maximum at 95% reduction and its intensity was higher, i.e. P = 4.0 compared with 3.6. In this steel, the {100} component decreased initially up to 35% reduction and then increased proportionally with increasing cold reduction.

Alloy (7) 17% Cr Low (C+N) + Nb (Fig 73)

The {111} component attained a maximum after 95% reduction and its intensity was much greater than that for the base steel, i.e. P = 4.5 compared with 3.6. The higher intensity of the {111} component was presumably due to the remnant {111} component in the hot band (Fig 68). The {100} component in this steel was much lower than in the base steel.

Alloy (6) 17% Cr High (C+N) + Nb (Fig 74)

At the higher interstitial level, the {111} component attained a maximum 'P value' of 3.6 after 75% reduction. Above this reduction, it decreased to 2.4 at 95% reduction with corresponding increase in the {100} component.

Alloy (4) 17% Cr Low (C+N) 1% Mo (Fig 75)

In the molybdenum steel, the {111} component reached a maximum value of 3.6 at 90% reduction. Above 90% reduction, this component decreased slightly with a corresponding increase in the {100} component.

Alloy (3) 17% Cr High (C+N) 1% Mo (Fig 76)

At the higher interstitial content, the {111} component increased

progressively with increasing cold reduction to a maximum after 82% reduction. The {100} component increased progressively above 50% and reached a maximum at 95% reduction.

Alloy (8) 25% Cr Low (C+N) (Fig 77)

Unlike the 17% Cr low (C+N) steel, the {111} component increased progressively with increasing cold reduction to a maximum at 95% reduction. Above 35% reduction, the intensity of the {100} component increased and was a maximum value of P = 2 at 95% reduction. This was much lower than in the base 17% Cr steel.

Alloy (9) 25% Cr Low (C+N) 1% Mo (Fig 78)

Unlike the 17% Cr low (C+N) 1% Mo steel, the {111} component was a maximum after 95% reduction and its intensity was greater than that for the base steel, i.e. P = 4.0 compared with 3.6. Above 50% reduction, the {100} component increased to a maximum after 95% reduction. However, compared with the 17% Cr low (C+N) 1% Mo steel, the intensity was low, 2.4 compared with 2.9.

8.6.3 Summary of Effects

During cold rolling, the {110} component decreased progressively with increasing cold reduction, but the {211} component did not change significantly. The {111} component increased progressively with increasing cold reduction and even after only 35% this texture was quite well developed. In general the highest intensities of the {111} component were obtained in the steels with the highest intensities of the {110} and/or {111} in the hot bar, e.g. Alloy 7, 17% Cr low (C+N) + Nb. This may be explained in terms of

the {110} component splitting into two {111} components, and so higher {110} components in the hot band lead to higher {111} components after cold rolling. With increasing cold reduction, the rate of development of the {111} component decreased and in some steels, it actually decreased slightly at the higher reductions with a corresponding increase in the {100} component. The {100} component did not develop so rapidly as the {111} component and in steels with a remnant {100} component in the hot band, e.g. Alloys 1, 2 and 5, this component did not increase at all initially. Above 50% reduction, the {100} component increased progressively with increasing reduction to a maximum after 95% reduction.

8.6.4 Deformation Textures (Full Pole Figures)

At a constant cold reduction, the deformation textures in ferritic stainless steels were similar irrespective of composition, differing only slightly in degree. Therefore only typical examples of these textures have been illustrated. Examples of {200} pole figures for deformation textures are illustrated in Figures 79 - 81.

Figures 79a,b,c show the deformation textures developed in a 17% Cr high (C+N) steel after 35%, 50% and 75% cold reduction. After 35% reduction, the texture can be described as mainly {111} <112> and {100}<011> with rotational freedom about both the sheet normal and rolling direction. With increasing cold reduction, the {111} <112> component decreased and was replaced by some {111} <110> and {112} <110> components while the {100} <011> component increased. After 75% reduction, the major texture was a strong {100} <011> (4 times random) with a minor {112} <110> component.

Figures 80a,b,c show the deformation textures developed in a 17% Cr low (C+N)

steel after 35%, 75% and 95% reduction. After 35% and 75% reduction, the textures were similar to those at the higher interstitial level. After 95% reduction, this steel may be described as a very strong {100} <011> texture (4.5 times random) with a {112} <110> component.

Figure 81 shows the deformation texture developed in a 17% Cr low (C+N) + Nb steel after 95% reduction. This steel may be described as a strong {100} <011> (3 times random) with a {112} <110> component.

The stronger {100}<011> component in the base steel compared with the niobium steel agrees with the stronger {100} component found in the inverse pole figure work for this steel.

To summarise, at the lower reductions, the development of a {111} <112> component was favoured, but with increasing cold reduction, this tended to be replaced by {111} <110>, {112} <110> and {100} <011> components. In general, the effect of molybdenum, titanium, niobium and chromium content had little influence on the type of cold rolling texture developed.

8.6.5 Recrystallisation Textures

Figures 82 - 90 show the effect of cold reduction on the recrystallisation textures developed in ferritic stainless steels of different alloy compositions. In some steels, after 35% reduction, recrystallisation increased the {110} component and decreased both the {111} and {100} components. In those steels, this was particularly the case for the {111} component which decreased quite markedly at the expense of the {110} component. With increasing cold reduction, the {110} component decreased. The majority of steels also showed a decrease in the {111} and {100} components during recrystallisation after 35% reduction and in general the {111}

component decreased more than the {100} component. With increasing cold reduction, the {111} component increased and in some steels, it exceeded that of the cold worked condition after 75% reduction. Above 95% reduction, however, its intensity decreased in some cases. In general the {100} component decreased progressively with increasing cold reduction to a minimum after 95%. However, in all steels, {100} component decreased progressively relative to the cold worked condition with increasing cold reduction. Thus the {111} component increased at the expense of the {100} component with increasing cold reduction.

Alloy (1) 17% Cr Low (C+N) (Fig 82)

The effect of cold work on the recrystallisation textures formed in the base 17% Cr low (C+N), after annealing at 800°C, shows that after 35% reduction recrystallisation had increased the {110} component and decreased {111} and {100} components, particularly the {111} component. With increasing cold work, the {110} component decreased and the {111} component increased to a maximum at 95% reduction. However, even after 75% reduction, the {111} component was weak, i.e. P = 1.9, and it was only at reductions greater than 83% that it exceeded the intensity of the cold worked condition. The {100} component decreased progressively with increasing cold reduction to a minimum after 95% reduction.

Alloy (2) 17% Cr High (C+N) (Fig 83)

The effect of cold work on recrystallisation texture formation after annealing at 800°C is shown in Figure 83. The intensity of the {100} component increased considerably after annealing, P 2.7 compared with P 1.4, in the 35% cold worked condition. With increasing cold reduction, the {100} component decreased in the recrystallised condition and above 75% reduction it remained

constant. The higher the interstitial content, the greater was the {100} component.

Above 82% reduction, however, the {111} component exceeded that of the cold worked condition and at all reductions, the {111} component in the higher interstitial content steel exceeded that of the lower interstitial content steel, in the recrystallised condition. The {110} component was not changed significantly by recrystallisation.

Alloy (7) 17% Cr Low (C+N) + Nb (Fig 84)

The effect of cold work on the recrystallisation texture in the 17% Cr low (C+N) + Nb steel after annealing at 990°C is shown in Figure 84 . The higher temperature of 990°C was used because of the sluggish recrystallisation in niobium steels. After 35% reduction, the {111} component decreased slightly compared with the cold worked condition, but this decrease was less marked than in the base steel. The {111} component increased progressively to a maximum value after 90% reduction, but the {100} component remained approximately constant. Above 90% reduction, the {100} component, however, increased slightly at the expense of the {111} component. The {110} component remained almost unaltered during recrystallisation.

Alloy (6) 17% Cr High (C+N) + Nb (Fig 85)

The effect of cold work on the recrystallisation texture in the 17% Cr high (C+N) + Nb steel after annealing at 990°C showed that the {111} component increased to a maximum after 95% reduction. However, compared with the lower interstitial content niobium steel, the 'P value' of the {111} component was low. Unlike the base 17% Cr steel, it did not show the considerable increase in {100} component compared with the unannealed condition, at

low reductions. Above 50% reduction, the {100} component increased and reached a maximum at 95% reduction.

Alloy (5) 17% Cr Low (C+N) + Ti (Fig 86)

The effect after annealing at 800°C showed that titanium was similar to niobium at the lower interstitial level. The titanium steel did not show an increase in {100} component above 90% reduction. Clearly both additions of titanium and niobium at the lower interstitial level favour the development of a strong {111} component after recrystallisation.

Alloy (4) 17% Cr Low (C+N) 1% Mo (Fig 87)

After annealing at 850°C, the {111} component reached a maximum value at 95% reduction, but the {100} component decreased with increasing cold reduction to a minimum after 95% reduction. As with additions of titanium and niobium, molybdenum added to a 17% Cr low (C+N) steel favoured the development of a strong {111} component. However, at the lower reductions, it was not so effective as niobium or titanium.

Alloy (3) 17% Cr High (C+N) 1% Mo (Fig 88)

In contrast to the base steel, the molybdenum steel annealed at 850°C did not show the increase in the {100} component after 35% reduction. In fact the intensity of both {100} and {111} components decreased after 35% reduction. The {111} component reached a maximum value after 90% reduction and exceeded that of the unannealed condition after 75% reduction. The {100} component was approximately constant up to 90% reduction and increased slightly at the expense of the {111} component above 90% reduction. Compared with the lower interstitial content, this steel did not show such

a high {111} : {100} ratio. However, in general, it showed a higher {111} : {100} ratio than either the base steel or the niobium steel at the higher interstitial level.

Alloy (8) 25% Cr Low (C+N) (Fig 89)

After 35% reduction and annealing at 800°C, the steel behaved in a similar manner to the 17% Cr low (C+N) steel. The {110} component was not so intense in the 25% Cr steel as in the 17% Cr steel. Although the base 25% Cr low (C+N) steel behaved similarly to the 17% Cr low (C+N) at the lower reductions, with increasing cold reduction, the {111} component was increased in the 25% Cr steel. The {100} component decreased with increasing cold reduction.

Alloy (9) 25% Cr Low (C+N) 1% Mo (Fig 90)

At 35% reduction, these alloys behave similarly to the 25% Cr base steel. With increasing cold reduction, the {111} component was increased compared with the base steel. The {100} component decreased progressively with increasing cold reduction.

8.6.6 Recrystallisation Textures (Full Pole Figures)

A number of {200} pole figures were determined for different alloy compositions after recrystallisation. Since titanium and niobium showed similar textures after 35% and 50% reduction, only data for the niobium steel has been illustrated.

Figures 91a-d show the recrystallisation textures developed in a 17% Cr low (C+N) steel after 35%, 50%, 75% and 95% cold reduction and annealing at 800°C.

After 35% reduction, the major textural component was a {110} <001> (3.5 time random) with a minor {100} <011> (2 times random). These were still the major components after 50% reduction. The strong {110} <001> component found after 35% and 50% reduction was in agreement with the marked increase in the {110} component found in the inverse pole figure data. After 75% reduction, the strong {110} <001> component disappeared with a corresponding increase in the {111} <112> component. There was considerable rotational freedom about the sheet normal. The {100} <011> component was the major component at 2.5 times random, with extensive rotational freedom about the rolling direction. After 95% reduction, the {111} <112> component increased and was now equal in intensity to the {100} <011> component.

Figures 92a-c show the recrystallisation textures developed in a 17% Cr high (C+N) steel after 35%, 50%, and 75% cold reduction and annealing at 800°C. After 35% cold reduction, the major component was {100} <011> at 3.5 times random. After 50% reduction, the {100} <011> was still the major component at 2.5 times random, with a minor {111} <112> component. With increasing cold reduction, the {111} <112> component increased to 2 times random with extensive rotational freedom about the sheet normal. The intensity of the {100} <011> remained virtually constant at 3.0 times random with extensive rotational freedom about the rolling direction.

Figures 93a-c show the recrystallisation textures in a 17% Cr low (C+N) + Nb steel annealed at 990°C. After 35% reduction, no texture component was particularly strong and the texture may be described as a {111} <112> (2 times random) with {100} <011> and {110} <001> components, with rotational freedom about the sheet normal and rolling directions. At 50% cold reduction the intensity of the {111} <112> increased from 2.0 to 2.5 times random and after 75% reduction, the texture was characterised by an even stronger {111} <112> texture with rotational freedom about the sheet normal. A

weak {100} <011> texture with rotational freedom about the rolling direction was also present.

Figure 94 shows the recrystallisation textures in a 17% Cr low (C+N) + Ti steel after 75% reduction and annealing at 800°C. The texture developed was similar to that for the 17% Cr low (C+N) + Nb steel after 75% reduction. It is evident from Figures 93 and 94 that additions of titanium and niobium favour the development of a strong {111} <112> texture.

The remaining five alloys, after 75% reduction, had textures which could be described as a {111} <112> component with rotational freedom about the sheet normal and a {100} <011> component with rotational freedom about the rolling direction.

Figure 95 shows the recrystallisation textures in a 17% Cr high (C+N) + Nb steel after 75% reduction annealed at 990°C. Unlike the lower interstitial niobium steel, it was not characterised by as strong a {111} <112> texture. The texture may be described as a {111} <112> and {100} <011>.

The development of recrystallisation textures in 17% Cr molybdenum steels after 75% cold reduction is shown in Figures 96 and 97. At the lower interstitial level, the texture was a major {111} <112> component (2.5 times random) with a {100} <011> component (2.0 times random). Compared with the base steel, the {111} : {100} ratio was higher in the molybdenum steel, but was not so high as in the titanium or niobium steels at the lower interstitial level. At the higher interstitial level, unlike the base steel, the texture was not characterised by a strong {100} <011> component. The major component was {111} <112> (2 times random) with a {100} <011> component (1.5 times random). Clearly, additions of molybdenum favoured the development of {111} <112> during recrystallisation; however, they

were not so effective as titanium or niobium at the lower interstitial level.

A {200} pole figure for a 25% Cr low (C+N) steel after 75% cold reduction annealed at 800°C is shown in Figure 98. Unlike the base 17% Cr low (C+N) steel, the 25% Cr steel showed a major {111} <112> component (2 times random) with a {100} <011> component (1.5 times random).

Figure 99 shows the recrystallisation texture in a 25% Cr low (C+N) 1% Mo steel after 75% reduction annealed at 850°C. The addition of molybdenum had increased the intensity of the {111} <112> component (3.0 times random) compared with the base 25% Cr low (C+N) steel. A {100} <011> component was also present. Clearly molybdenum additions again favoured the development of a {111}<112>texture.

8.7 MICROSTRUCTURAL FEATURES

Microstructural features were examined both optically and by electron microscopy. The features observed were used to interpret some of the kinetic and textural work.

8.7.1 Cold Work Condition

Metallographic examination of the cold worked condition showed that some matrix grains contained distinct bands or striations whereas others did not. After 35% reduction (Fig 100a) some grains showed distinct parallel bands. Examination under polarised light (Fig 100b (1) and (2)) showed these to be deformation bands. After 75% reduction, individual matrix grains showed that grains containing deformation bands were harder than those without such bands (Fig 100c). Typical microhardness values are given in Table VI. Thin foil

electron microscopy showed that cell formation typical of bcc metals was observed in regions of relatively low misorientation (Fig 100d). In other regions, deformation banding was observed (Fig 100e) and in these regions, the misorientation across subgrain boundaries was high.

8.7.2 Recovery and Recrystallisation

During recovery, matrix grains containing deformation bands tended to recover more rapidly (Fig 101). These grains also tended to be the first to recrystallise even in alloys containing nucleating particles, e.g. the titanium and niobium steels. Recrystallisation was often completed in these regions before nucleation had started in other grains. Optical microscopy showed the predominant sites for nucleation of recrystallisation to be deformation bands, second phase particles and grain boundaries. Electron diffraction showed that the predominant orientations found at deformation bands were $\{110\}_\alpha$, $\{111\}_\alpha$, and $\{100\}_\alpha$ parallel to the foil plane, i.e. rolling plane. The former was predominant at lower reductions, while the latter orientations were predominant after 75% reduction. At second phase particles, the predominant orientation at the particle/ferrite interface after short annealing times was $\{111\}_\alpha$ parallel to the rolling plane, while at grain boundaries, it was $\{100\}_\alpha$ parallel to the rolling plane. Electron microscopy showed evidence for nucleation by a subgrain growth mechanism (Fig 102a), and the recrystallisation generally occurred by nucleation and boundary migration (Fig 102b). Recrystallisation by subgrain growth took place most rapidly in grains with $\{111\}_\alpha$ parallel to the rolling plane.

17% Cr Low (C+N)

After annealing for 30 seconds at 655°C, precipitation was observed at subgrain

boundaries (Fig 103a). These precipitates were identified as $M_{23}C_6$. At higher temperatures, e.g. 720°C, recrystallisation had started before precipitation occurred. In regions where particles were present prior to cold work, e.g. tempered martensite regions and the ferrite/martensite interface, a fine recrystallised grain size was observed (Fig 103b). This was because of grain boundary pinning by fine second phase particles which were identified as $M_{23}C_6$.

After 35% reduction (Fig 103c) nucleation for recrystallisation was associated with deformation bands and grain boundaries. At deformation bands, nucleation took place at the matrix/deformation band interface. Electron microscopy showed that $\{110\}_\alpha$ orientations parallel to the rolling plane were associated with deformation bands. A high proportion of grains nucleated at or near to the grain boundary had $\{100\}_\alpha$ orientations parallel to the rolling plane. Enhanced nucleation took place at the grain boundary (Fig 103d) and nucleation appeared to be associated with $M_{23}C_6$ precipitates at the grain boundary. In Figure 103d, recrystallisation occurred in a $\{100\}_\alpha$ matrix grain parallel to the rolling plane while the adjacent $\{111\}_\alpha$ matrix grain was just beginning to recrystallise at the grain boundary. The grain boundary precipitates pinned the grain boundary between matrix grains A and B, thus preventing migration of recrystallised grain A into matrix grain B. In the fully recrystallised condition, the grain size was very variable (Fig 103e).

After 75% reduction early nucleation was associated with matrix grains containing deformation bands (Fig 103f). Nucleation took place in colonies parallel to the bands. The grain size associated with these grains was very fine and recrystallisation was often completed in some matrix grains before others had started to recrystallise (Fig 103g). Figure 103h shows a $\{110\}_\alpha$ oriented grain in a region of $\{111\}_\alpha$ oriented subgrains

and recrystallised grains. The elongated nature of the grain indicated that it originated from a deformation band.

The $[002]$ direction in the recrystallised grain, grain A, is approximately parallel with the $[\bar{1}\bar{1}2]$ direction in the matrix. This indicates that the recrystallised grain had a $\{110\}\langle 001\rangle$ texture while the matrix had a $\{111\}\langle 112\rangle$ texture. It is thought that during rolling, the $\{111\}\langle 112\rangle$ deformation texture formed from a $\{110\}\langle 001\rangle$ texture in the hot band by rotation about a common $\langle 110\rangle$ tranverse direction, i.e. $[1\bar{1}0]$. This resulted in small amounts of remnant transition band of $\{110\}\langle 001\rangle$ orientation. During recrystallisation, the recrystallised grain, i.e. grain A, nucleated at the transition band, resulting in a $\{110\}\langle 001\rangle$ recrystallised grain.

17% Cr High (C+N)

This steel had a two phase structure of ferrite and austenite after annealing at 1000°C, and the austenite during cooling transformed to martensite. This was subsequently tempered after annealing at 750°C. Therefore, the microstructural effects in this steel may be divided into two types, i.e. those occurring in the tempered martensite, and those occurring in the ferrite. After 35% reduction, recrystallised grains were not observed in the prior martensite regions until after annealing for four hours at 690°C. In the ferrite many matrix grains had recrystallised after the same annealing time. Recrystallisation occurred predominantly by grain boundary nucleation. At higher temperatures, nucleation was easier. Figures 104a, b, and c show the microstructural changes after 35% reduction and annealing for 1, 4 and 32 mins at 750°C. After annealing for 1 min at 750°C, nucleation occurred at grain boundaries and at the ferrite/martensite interface (Fig 104a). After this treatment, recrystallisation nuclei were also present at deformation

bands, but the grain boundary sites predominated. No recrystallised grains were observed in the tempered martensite regions. The predominant mode of nucleation was still at grain boundaries, after annealing for 4 mins at 750°C, and the tempered martensite regions were beginning to temper further (Fig 104b). After 32 mins at 750°C (Fig 104c), the tempered martensite regions were diffuse, and grains were observed within these regions.

The amount of resolvable carbide within the ferrite grain had also increased. With increasing cold reduction, the rate of tempering of the tempered martensite increased.

Electron microscopy showed that the predominant sites for nucleation of recrystallised grains were at the ferrite/carbide interface in the tempered martensite and at grain boundaries in the ferrite. In the tempered martensite regions recrystallisation was enhanced compared with the lower interstitial level; compare Figure 105a and 105b. In fact even at temperatures as low as 620°C, recrystallisation started at the ferrite/carbide interface after only 30s. At all temperatures, nucleation took place at the ferrite/carbide interface of the coarser carbides (greater than 1μm). These were identified as $M_{23}C_6$. The predominant orientation found at the ferrite/carbide interface was $\{111\}_\alpha$ parallel to the rolling plane, but other orientations such as $\{100\}_\alpha$ and $\{311\}_\alpha$ parallel to the rolling plane were observed. In fact in several cases, more than one orientation was found to nucleate at the same particle (Fig 105c). Examination of the cold worked state showed that a range of orientations was present near to carbides. Although early recrystallisation was enhanced in these steels, after much longer annealing times no further grain growth had taken place. After annealing for 125 h at 620°C (Fig 105d) and after 32 mins at 690°C, (Fig 105e), fine recrystallised grains were in evidence in regions of high particle density. The grain boundaries were pinned by fine

particles of $M_{23}C_6$ approximately 0.25μm in diameter. In these prior martensite regions, further softening took place by a secondary recrystallisation mechanism, following the unpinning of grain boundaries. (Fig 105f) Thus, fine recrystallised grains could not be resolved optically in the tempered martensite regions even after long annealing times.

In the ferrite grains, recrystallised grains nucleated at or near to matrix grain boundaries had a high incidence of $\{100\}_\alpha$ orientations parallel to the rolling plane. (Fig 105g) Recrystallisation took place in a grain of $\{100\}_\alpha$ while the adjacent matrix grain $\{111\}_\alpha$ was just beginning to recrystallise. There was also evidence of precipitation on the substructure and even after four minutes at 720°C, very little recovery was in evidence. The ferrite grains did not recrystallise so readily. In fact in these regions recovery was still taking place after 125 hours at 620°C (Fig 105h). Clearly in the ferrite grains where no coarse particles were present, recrystallisation was retarded at the higher interstitial level.

17% Cr Low (C+N) + Ti

Electron microscopy of this steel after 35% reduction showed a well developed polygonised structure after annealing for 10 seconds at 720°C (Fig 106a). The subgrain size was always coarser than that of the base steel, compare Figure 106a with Figure 106b.

Nucleation occurred preferentially at the ferrite/Ti(CN) interface, (Figs 107a and b). Nucleation of recrystallised grains was also observed at deformation bands. Recrystallisation nucleation took place after annealing for only 30 seconds at 620°C. Nucleation occurred adjacent to the particle while the surrounding substructure was just beginning to recover. The orientation of the grain nucleating at the ferrite/Ti(CN) interface was $\{111\}_\alpha$ parallel

to the rolling plane. In fact a high proportion of grains nucleating adjacent to particles had this orientation.

Another preferred site for nucleation in this alloy was at matrix grain boundaries. However, unlike the previous alloys it occurred by grain boundary migration, not dissimilar from strain induced boundary migration (Fig 107c). Electron microscopy showed that, unlike the base steel, migration occurred across the matrix grain boundary into the neighbouring grain (Fig 107d). Electron diffraction patterns of matrix grains A and B and recrystallised grains 1 and 2 showed that matrix grain A was related to B by a 30° rotation about the $\{111\}_\alpha$ sheet normal. The orientation of the recrystallised grain was within the 30° orientation spread. Although nucleation was observed at grain boundaries, there was no evidence of strain induced boundary migration in the specimens examined by electron microscopy.

The Niobium Steels

In these steels, nucleation of recrystallised grains occurred at the ferrite/Nb(CN) interface (Figs 108a and b). Nucleation at the particles occurred more readily at the higher interstitial content, particularly at the lower reductions. This may be because of a lower degree of recovery prior to recrystallisation, at the higher interstitial level, i.e. a greater driving force. Electron microscopy showed that in both steels, the common orientation adjacent to Nb(CN) particles was a $\{111\}_\alpha$ parallel to the rolling plane (Fig 108c). At the higher interstitial content, recrystallisation nucleation also took place at chromite inclusions (Fig 108d). Nucleation was also observed at matrix grain boundaries. After annealing at 750°C, precipitates were observed at subgrain boundaries, and were identified as Nb(CN) (Fig 108e).

17% Cr Low (C+N) 1% Mo

Figures 109a and b show the stages of recovery, after 35% reduction and annealing at 690°C. In Figure 109a after annealing for 30 seconds, recovery had started and there was evidence of the formation of subgrain boundaries. After annealing for 2 minutes, low angle grain boundaries typical of a polygonised structure were in evidence (Fig 109b). Longer annealing times showed no significant increase in the subgrain size, even after annealing for 16 mins at 690°C. Figure 109c shows evidence of precipitation at subgrain boundaries, which had presumably pinned the boundaries. After 75% reduction, pinning was in evidence at subgrain boundaries (Fig 109d) and the precipitates were identified as $M_{23}C_6$. In some regions pinning was in evidence by fine $M_{23}C_6$ present before cold work (Fig 109e).

Recrystallisation at all reductions took place preferentially at bands of carbides of previous grain boundary origin (Fig 109f). Electron microscopy (Fig 109g) showed evidence of recrystallisation at the ferrite/$M_{23}C_6$ interface and electron diffraction showed that a high proportion of grains nucleated adjacent to $M_{23}C_6$ had {111} orientations in the plane of the foil.

17% Cr High (C+N) 1% Mo

Figures 110a-d show a sequence of micrographs, cold worked and annealed for ½, 2 and 8 mins at 690°C. Compared with the lower interstitial content molybdenum steel, very little recovery had taken place. In fact the structure was not changed appreciably by annealing and even after annealing for 8 minutes at 690°C, no significant change was observed.

Figures 111a and b show the microstructural changes after 35% reduction and

annealing for 8 mins and 32 mins at 750°C.The micrographs show that precipitate coalescence in the tempered martensite regions was required before nucleation. The rate of particle coalescence increasedwith increasing cold reduction and annealing temperature. However, unlike the base steel, nucleation was observed optically in the tempered martensite regions, and recrystallisation proceeded by a grain boundary migration process. The nucleation rate was very high in the tempered martensite regions which were always the first to recrystallise. Nucleation also occurred in the ferrite at grain boundaries and at particles of previous grain boundary origin.

Electron microscopy showed that nucleation took place at the ferrite/carbide interface (Fig 111c) and the predominant orientation adjacent to particles was $\{111\}_\alpha$ parallel to the rolling plane. However, in this steel recrystallisation nucleation in the regions of $M_{23}C_6$ was not so prolific, and after short annealing times tended to be associated only with $M_{23}C_6$. Pinning of fine recrystallised grains was in evidence by particles 0.05 - 0.2 μm in diameter (Fig 111d).

25% Cr Low (C+N)

Unlike the 17% Cr steel, nucleation took place at carbide particles at all reductions (Fig 112a). The particles were distributed in bands clearly of some prior grain boundary origin. Electron microscopy (Fig 112b) showed evidence of precipitation at subgrain boundaries.

25% Cr Low (C+N) 1% Mo

Figures 113a and b show the stages of recovery after 35% reduction and annealing at 690°C. After annealing for 30 seconds, recovery had started

and there was evidence of the formation of subgrain boundaries. Annealing for 2 minutes gave low angle grain boundaries typical of a polygonised structure. Further annealing showed no significant increase in the subgrain size, even after 16 mins at 690°C.

As with the base steel, recrystallisation nucleation took place at bands of carbide of obvious prior grain boundary origin (Fig 113c). Electron microscopy showed evidence of precipitation at subgrain boundaries after annealing for 1 min at 690°C (Fig 113d).

8.8 MECHANICAL AND FORMABILITY TESTS

8.8.1 Annealing treatments

All the specimens for mechanical and formability tests were annealed to give a fully recrystallised structure. Annealing treatments were chosen on the basis of the inverse pole figures, i.e. the treatment that gave the highest {111} : {100} ratio. The annealing treatments given to each alloy are included in Table VII.

8.8.2 Effect of Cold Work and Composition on the r Value

Figures 114a-j show the effect of cold reduction on r_o, r_{45}, r_{90} and $\bar{r}$ values for the nine alloys studied.

In general the average r value, $\bar{r}$, increased with increasing cold rolling reduction. With the exception of alloy (2) (17% Cr high (C+N) steel), the maximum r value always occurred at r_{90} and in general exceeded unity even after only 35% cold rolling reduction. Alloys (1), (8) and (9) (i.e. 17% Cr low (C+N), 25% Cr low (C+N) and 25% Cr low (C+N) 1% Mo steels) showed a

maximum r_{90} after 50% reduction. In contrast to the other alloys examined, the maximum r value in the 17% Cr high (C+N) steel after 35% reduction was at r_{45}. After 75% reduction, the $\bar{r}$ value was not affected by interstitial content. Additions of titanium and niobium at the lower interstitial level favoured the development of higher $\bar{r}$ values than those in the base 17% Cr steel. The higher interstitial content niobium steel did not produce such high $\bar{r}$ values as the lower interstitial content niobium steel, but the $\bar{r}$ values were higher than in the higher interstitial content base 17% Cr steel. Increasing the chromium content increased the $\bar{r}$ value after 75% reduction. Additions of molybdenum favoured the development of higher $\bar{r}$ values at both interstitial and chromium levels.

8.8.3 The Effect of Texture on $\bar{r}$ Value

A graph of $\bar{r}$ value versus $\log_{10} \frac{I_{(111)}}{I_{(100)}}$ is shown in Figure 115. A regression analysis showed that :

$$\bar{r} = 0.36 \log_{10} \frac{I_{(111)}}{I_{(100)}} + 0.77 \qquad \text{(82)}$$

at 95% confidence level.

The correlation coefficient was +0.86 indicating a high degree of correlation. Clearly increasing the intensity of the {111} component and/or decreasing the {100} component favoured the development of high $\bar{r}$ values.

In Table VIII, the values for r_o, r_{45}, r_{90} and $\bar{r}$ and the LDR together with the values of $P_{(hkl)}$ have been included for each alloy. In Table IX, the values for $\bar{r}$ and LDR have been calculated in terms of texture parameter regression equations, i.e. Equations 82 and 84, for the nine alloys studied at 35%, 50%, 75%, 82%, 90% and 95% reduction. This shows generally the

beneficial effect of high cold reductions in the development of recrystallisation textures for good deep drawability.

8.8.4 Mechanical Properties

The values of yield stress, uniform elongation, ε_u, and grain size are given in Table X. These parameters are represented in terms of the average of the three directions relative to the rolling direction.

i. The Effect of Composition

The effect of composition has been described only after 75% reduction.

The Effect of Interstitial Content at 17% Cr

Yield stress and yield extension increased with decreasing interstitial content (Fig 116). This was because of the finer recrystallised grain size in the lower interstitial content which increased the yield stress to a much greater extent than increases in interstitial content. The latter effect was presumably because of the limited interstitial solubility. However, no explanation can be offered for the finer recrystallised grain size at the lower interstitial level.

The uniform elongation decreased slightly with increasing interstitial content because increasing the interstitial content increases the flow stress relative to the work hardening rate.

The Effect of Chromium Content (Fig 116)

Increasing the chromium content from 17% to 25% increased the yield stress, in spite of the coarser grain size of the 25% Cr steel, because of solid solution hardening. In the higher chromium content steel, the yield extension decreased because of a coarser grain size.

The Effect of Molybdenum at the Lower Interstitial Level (Figs 117,118)

Additions of molybdenum increased the yield stress at both chromium levels because of solid solution hardening by molybdenum.

The Effect of Molybdenum at the Higher Interstitial Level (Fig 118)

Additions of molybdenum increased the yield stress and yield extension compared with the base steel because of solid solution hardening by molybdenum and a finer grain size. However, molybdenum decreased the initial work hardening rate compared with that of the base steel because of a smaller volume fraction of second phase particles.

In the molybdenum steels, increasing the interstitial content increased the yield stress, yield extension and work hardening rates. The yield extension and yield stress increased because of the finer grain size at the higher interstitial content. The increased initial work hardening rate was because of the increased volume fraction of second phase particles at the higher interstitial level. The uniform elongation decreased slightly with increasing interstitial content because increasing the interstitial content increased the

flow stress relative to the work hardening rate.

The Effect of Titanium (Fig 119)

Additions of titanium decreased the yield stress and yield extension compared with the base 17% Cr steel because of a coarser grain size in the titanium steel, and because titanium removed some of the carbon and nitrogen from solid solution, thereby reducing the solid solution hardening effects of the interstitial atoms. The addition of titanium however was insufficient to inhibit the discontinuous yield point by removing all the carbon and nitrogen from solid solution.

The Effect of Niobium at the Lower Interstitial Content

The niobium steel behaved in a similar manner to the titanium steel (Fig 119). However, additions of niobium did not reduce the yield stress to the same extent as titanium, eventhough the steel had a much coarser grain size. This indicates one of two possibilities :

a. The niobium was not as effective as titanium in removing carbon and nitrogen from solution;

b. Some solid solution hardening was present from excess niobium in solid solution.

Niobium additions decreased the yield extension, because of the coarser grain size compared with the base steel, but were insufficient to inhibit the discontinuous yield point.

The Effect of Niobium at the Higher Interstitial Content

Additions of niobium had little effect on the yield stress and yield extension (Fig 120), but caused a lower initial work hardening rate as a result of a smaller volume fraction of second phase particles. Niobium additions increased the uniform elongation because in the base steel, the flow stress increased relative to the work hardening rate when compared with the niobium steel.

In the niobium steels, increasing the interstitial content had little effect on the yield stress in spite of the finer grain size at the higher interstitial level. This was due to a difference in the Nb:(C+N) ratio in the two alloys, the Nb:(C+N) ratio of the lower interstitial level was 15:1 compared with 8.5:1 at the higher interstitial level (see Fig 139), thus the amount of niobium in solid solution was greater at the lower interstitial level. Therefore the solid solution hardening by niobium at the lower interstitial level was able to compensate for the grain size difference between the two steels. At the higher interstitial level, the yield extension was shorter because of the greater volume fraction of second phase particles.

ii. The Effect of Cold Reduction

In general, the yield stress and yield extension increased quite markedly with increasing cold reduction (Fig 121) because the grain size decreased.

8.8.5 Factors Affecting the Limiting Drawing Ratio

i. The Effect of Composition and Cold Work on the LDR (Figs 122a-c)

With the exception of the 17% Cr high (C+N) Nb steel, increasing cold reduction increased the limiting drawing ratio (LDR). In the base 17% Cr steels, after 35% reduction, the higher interstitial content steel had a lower LDR than the lower interstitial content steel. However, at the higher reductions there was no difference between the two steels. Increasing the chromium content from 17% to 25% increased the LDR above 50% reduction. Additions of titanium and niobium to a base 17% Cr low (C+N) steel increased the LDR. At the higher interstitial level, niobium additions increased the LDR up to 50% reduction, when compared with the base steel. However, at the higher interstitial level, niobium additions did not produce such favourable limiting drawing ratios. Molybdenum additions increased the LDR at both 17% and 25% Cr levels at both interstitial levels. In fact, in molybdenum steels, chromium content and interstitial content had no effect on the LDR.

ii. The Effect of Texture and $\bar{r}$ Value on the LDR

Graphs of limiting drawing ratio versus $\bar{r}$ values and log $\frac{I_{(111)}}{I_{(100)}}$ are shown in Figures 123 and 124. Regression analysis showed that :

$$\text{LDR} = 0.26\,\bar{r} + 0.98 \quad \text{at 95\% confidence level} \qquad \text{——— (83)}$$

$$\text{LDR} = 0.13 \log \frac{I_{(111)}}{I_{(100)}} + 2.17 \quad \text{at 95\% confidence level} \qquad \text{——— (84)}$$

The correlation coefficients were +0.89 and +0.75 respectively indicating a high degree of correlation. Clearly the LDR was very dependent on $\bar{r}$ value and texture. Composition appeared to have little effect, apart from its effect on texture.

8.8.6 The Effect of Cold Reduction and Composition on Δr and Percentage Earing (Fig 125)

In the majority of cases, both Δr values and percentage earing increased with increasing cold reduction. The 17% Cr high (C+N) steel after 35% reduction showed a negative value for Δr and earing at 45° rather than $0/90^{\circ}$ to the rolling direction. With increasing cold reduction, the earing mode became $0/90^{\circ}$ and Δr was positive. All the other alloys showed $0/90^{\circ}$ earing and positive values of Δr. The lower interstitial content base 17% Cr and 25% Cr steels, and the 25% Cr steel containing molybdenum showed a maximum value for Δr after 50% reduction. This was because of a high r_{90} value in these steels. However, only the 25% Cr steel containing molybdenum showed maximum earing after 50% cold reduction. In this steel, however, the Δr value was much greater than in either base 17% or 25% Cr steels. The 17% Cr high (C+N) 1% Mo steel had a small positive Δr value after 35% reduction which was also reflected in slight $0/90^{\circ}$ earing. The high Δr values found in the 17% Cr low (C+N) titanium and niobium steels were not altogether reflected in the percentage earing.

Figure 126 shows the percentage earing versus Δr (degree of planar anisotropy). A regression analysis showed that :

$$\text{Percentage earing} = 17.4\,\Delta r - 0.17 \qquad \text{——————} \quad (85)$$

at 95% confidence level.

The correlation coefficient was +0.83 indicating a high degree of correlation. Photographs showing the earing mode are included in Figure 127.

8.8.7 Erichsen Tests

The Erichsen values obtained are given in Table XI. Values of grain size, minimum values of uniform elongation and the degree of orange peel are also included. In general, the maximum Erichsen value occurred after 75% cold reduction. In contrast to expectations, higher Erichsen values were obtained at the higher interstitial level in both the base 17% Cr and 17% Cr 1% Mo steels. The 25% Cr steels showed lower Erichsen values than the 17% Cr steel. The above results were in general not reflected in the elongation. At the lower interstitial level, both titanium and niobium steels showed high Erichsen values. However, both these steels had relatively high uniform elongations. At the higher interstitial level, the Erichsen values were in general slightly lower in the niobium steel than in the base steel, although they had greater uniform elongations. In the niobium steels, the Erichsen value was greater at the lower interstitial level, even though the uniform elongations were comparable. The best correlation was obtained between Erichsen values and the minimum value of ε_u. However, a correlation coefficient of +0.52 represents a poor correlation.

The degree of 'orange peel', as would be expected, increased with increasing grain size. A photograph showing the degree of orange peel in the Erichsen tests is included in Figure 128.

8.9 FRACTURE

8.9.1 Tensile Specimens

All of the specimens examined failed by a ductile mode of failure. There

was always considerable necking of the specimens before final failure.

8.9.2 Swift Tests

With the exception of one steel, the 17% Cr high (C+N) + Nb steel, after 75% reduction, there was always considerable necking before fracture. Fracture always took place at the punch nose radius (Fig 129). Regions of brittle fracture were observed in the 17% Cr high (C+N) + Nb steel (Fig 130). The 'river markings' appeared to propagate from particles (Fig 130) indicating that particles acted as stress raisers, thus promoting brittle fracture locally. The other steels failed by a ductile mode.

8.9.3 Erichsen Tests

Fracture in general took place approximately parallel to the rolling direction.

17% Cr Low (C+N)

In this steel, the failure mode was ductile. After 75% reduction, regions of ductile dimples were separated by shear steps (Fig 131). At the lower reductions, much shear was in evidence between regions of ductile dimples because of the coarser grain size.

17% Cr High (C+N)

Again the failure mode was ductile; however, the ductile dimples were finer and more numerous than in the lower interstitial content steel because of the increased volume fraction of second phase particles (Fig 132) at the higher interstitial level, which acted as nucleation sites for voids. The large

amounts of shear failure observed at the lower reductions in lower interstitial content steel, were not observed due to increased void nucleation.

25% Cr Low (C+N)

Ductile fracture was again the failure mode. After 75% reduction, regions of ductile dimples were separated by shear steps similar to the lower chromium content steel. Voids also tended to be arranged in bands (Fig 133a and b) probably originating from the bands of $M_{23}C_6$ observed in this steel.

17% Cr Low (C+N) + Ti

This steel failed exclusively by ductile failure.

17% Cr Low (C+N) + Nb

In this steel, the majority of the failure mode was ductile. However, small regions of brittle failure were observed on the fracture surface (Fig 134). This may be due to local stress concentrations at niobium carbide particles, which promoted brittle fracture locally. This did not occur in the titanium steel because of the lower yield stress.

17% Cr High (C+N) + Nb

As with the lower interstitial content niobium steel, small regions of brittle failure were observed. This may again be because of local stress concentrations at second phase particles, or chromite inclusions. Figure 135 shows a typical brittle region; note the chromite inclusions on the fracture surface. After 75% reduction large cracks were observed, at the centre of the fracture running parallel to the rolling plane Fig(136a).These cracks were

associated with chromite inclusions (Fig 136b). A section through the fracture showed cracks originating from chromite inclusions (Fig 136c).

17% Cr Low (C+N) 1% Mo

The failure mode was ductile. However, large cracks were present, at the centre of the fracture parallel to the rolling plane (Fig 137a). There was evidence to suggest that they were associated with bands of carbide originating from prior grain boundaries (Fig 137b). Many such bands were observed on the fracture surfaces.

17% Cr High (C+N) 1% Mo

The fracture surfaces were similar to the base steel.

25% Cr Low (C+N) 1% Mo

Regions of brittle failure were observed in all the specimens. After 75% reduction shear steps were observed similar to those in the base composition. The fractured specimens contained large cracks at the centre of the fracture, parallel to the rolling plane (Fig 138a). There was again evidence to suggest that cracks originated from bands of $M_{23}C_6$. Voids originating from $M_{23}C_6$ were observed on the shear face (Fig 138b). Many bands of voids were observed on the fracture surfaces.

CHAPTER NINE

9. DISCUSSION

9.1 RECOVERY

Before the effects of composition on recovery are discussed for ferritic stainless steels, general effects of composition on the recovery of α iron will be considered. Although recovery is a complex process involving several concurrent reactions, it can be divided into two stages :

i. The first stage was concerned with the annihilation of dislocations and the removal of point defects;

ii. The second stage was the formation of low angle grain boundaries and the migration of these boundaries.

Both stages involve climb, glide and cross slip of dislocations and can therefore occur only with sufficient thermal activation.

It has been shown[36][37] that additions of interstitial atoms retarded the recovery process in α iron, which effect was attributed to solute 'atmospheres'. Additions of manganese[48][49] and molybdenum retarded recovery to an even greater extent. It is generally known that additions of substitutional elements, e.g. Mn, Cr and Mo, to a low carbon steel produced two strain ageing effects. Glen[51] discussed these in terms of the interaction of solute atoms with dislocations. The first effect occurred at about 200^{o}C and was as a result of diffusion of carbon and nitrogen to the dislocations during straining. The second at a higher temperature was because of the formation of substitution - interstitial

atmospheres which required diffusion of the substitutional solute atoms to the dislocations. In ferritic stainless steels[14], Cr_2N particles were observed at dislocations indicating chromium - interstitial interaction. It is thought therefore that during the pre-precipitation stage, the recovery rate will be controlled by the diffusion rate of the substitutional solute atoms. Precipitation was important only in the second stage of recovery as precipitates existed only at subgrain boundaries. The effect of precipitation on both recovery and recrystallisation will be discussed later.

9.1.1 The Effect of Interstitial Content

After 35% and 50% cold reduction the plateau between recovery and recrystallisation was extended at the higher interstitial level in the base 17% Cr steel. In fact after 35% cold reduction, annealing the higher interstitial content base 17% Cr steel at temperatures below 750°C (Fig 31) resulted in a distinct plateau between recovery and recrystallisation stages. This plateau however did not occur at a constant hardness.

Electron microscopy showed two distinct microstructures after short annealing times :

i. In prior austenite regions fine recrystallised grains were nucleated by coarse $M_{23}C_6$ particles. The grain boundaries were subsequently pinned by a fine dispersion of $M_{23}C_6$, 0.25 μm in diameter which was formed during tempering prior to cold working.

ii. In regions free from coarse $M_{23}C_6$ particles, i.e ferrite grains, a normal recovery process was observed.

In the plateau region further cell growth and hence softening was prevented by the pinning action of the fine dispersion of $M_{23}C_6$ at the grain boundaries In terms of the Gladman[62] equation, reproduced again for the ease of the discussion, the critical particles size, r^+, for the unpinning of grain boundaries obeys the following relationship, shown earlier :

$$r^+ = \frac{6\ R_o\ f}{\pi} \left[\frac{3}{2} - \frac{2}{Z}\right]^{-1}$$

where R_o is the matrix grain radius, f is the volume fraction of particles in the microstructure, and Z is the heterogenity factor. Because there is a critical particle size for a given volume fraction of particles and grain structure, further grain growth and hence softening can occur only when sufficient particle coalescence has taken place to allow the grain boundaries to become unpinned. According to the Wagner[80] diffusion model, particle growth under conditions of Ostwald ripening may be described by : (shown earlier)

$$(\bar{r}_c)^3 - (r_o)^3 = \frac{8\ \sigma_p\ D\ C_o\ V_m}{9\ RT} \cdot t$$

where $\bar{r}_c$ is the average particle radius at time t, r_o is the average particle radius at the onset of particle coarsening, D is the diffusivity of the atomic species in the matrix, C_o is the concentration of the atomic species in the matrix, V_m is the particle molar volume, σ_p is the surface energy between particle and matrix, R is the gas constant, and T is in Kelvin. Thus, in a base 17% Cr steel, the rate of growth of $M_{23}C_6$ will be controlled by the diffusion of chromium, therefore at lower temperatures the plateau region will be extended because of slower particle growth. Two reasons may explain why the plateau did not occur at a constant hardness:

a. At lower temperatures, precipitation at subgrain boundaries may

become increasingly important because of an increased supersaturation of carbides and nitrides, and grain boundaries will be pinned by precipitating particles at a finer grain size. Electron microscopy showed that particle pinning by dispersed carbides was still an important mechanism at temperatures as low as 620°C.

b. At higher temperatures, because of the faster diffusion rate of chromium, some particle growth may take place prior to recrystallisation and result in a slight increase in the interparticle spacing and hence more growth of the recrystallised grains before pinning of their boundaries.

The recovery rate increased with increasing interstitial content after 35% and 50% reduction. This may be accounted for by recrystallisation rather than a recovery process because recrystallisation was observed at coarse $M_{23}C_6$ particles after very short annealing times. In the lower interstitial steel this was not the case at the lower reduction.

9.1.2 The Effect of Chromium

At 620°C both the initial rate of recovery and the amount of recovery were less in the 25% Cr base steel than the 17% Cr steel (Fig 31). This may be because of an increased supersaturation of carbides and nitrides which was indicated by the change in hardness with annealing time (Fig 34). It is considered that the beginning of the plateau in ferritic stainless steels is because of precipitation at subgrain boundaries. In the 25% Cr steel, the plateau occurred after shorter annealing times indicating an increased supersaturation of carbides and nitrides. The increased supersaturation led to chromium-interstitial 'atmospheres' being formed more rapidly and hence a slower initial rate of recovery at 620°C in the 25% Cr

steel. The increased supersaturation resulted in more rapid precipitation therefore subgrain boundaries were pinned after shorter annealing times, which reduced the amount of recovery.

However, after annealing at 690°C (Fig 33), the initial rate of recovery was faster in the 25% Cr than in the 17% Cr steel after 35% and 50% cold reduction. The effect of chromium may be discussed in terms of the greater increase in hardness, ΔH, after 35% and 50% cold reduction in the higher chromium steel. At the lower interstitial level, in the base 17% and 25% Cr steels, chromium-interstitial 'atmospheres' tend to segregate to dislocations during annealing. Therefore the rate of recovery was dependent on the diffusion of chromium and on the stored energy. In the 25% Cr steel greater increases in hardness were found after 35% and 50% cold reduction and therefore an increased rate of recovery was observed.

9.1.3 The Effect of Molybdenum in the 17% Cr Steels at the Lower Interstitial Level

Additions of molybdenum in general decreased the rate of recovery, and extended the plateau between recovery and recrystallisation. Additions of molybdenum caused molybdenum-interstitial 'atmospheres' to be formed at dislocations, rather than chromium-interstitial 'atmospheres' because molybdenum has a higher affinity for carbon and nitrogen than chromium. As the rate of recovery depends upon the diffusion rate of molybdenum, the rate of recovery was slower in the molybdenum steel.

The plateau region formed between recovery and recrystallisation resulted from the precipitation of $M_{23}C_6$ at subgrain boundaries and the cessation of subgrain growth. An equation relating subgrain size to particles size and volume fraction has been obtained[84]:

$$d_{crit} = \bar{D} \sqrt{\frac{f\ t^2}{2(t-1)}}$$

where d_{crit} is the critical particle size for the unpinning of subgrain boundaries, $\bar{D}$ is the mean subgrain diameter, f is the precipitated volume fraction, and t is the size factor in the subgrain size. Therefore, for the same particle size, subgrain size and volume fraction of particles, the critical particle diameter for unpinning of subgrain boundaries will be the same. The particles precipitated in both the base 17% Cr and the molybdenum steels were identified as $M_{23}C_6$. However, in the molybdenum steel, the lattice parameter of the $M_{23}C_6$ was slightly larger indicating molybdenum dissolved in the carbide. In terms of Equation 15, the rate of particle growth depends upon the diffusion of the substitutional solute atom in the high chromium ferrite.

In the base 17% Cr steel, this was determined by chromium, while in the molybdenum steel by molybdenum. Because the diffusion rate of molybdenum in the high chromium ferrite was slower than that of chromium, the critical particle size, d_{crit}, for the unpinning of subgrain boundaries was only achieved after longer annealing times. As the end of the plateau stage co-incided with the condition for the unpinning of some subgrain boundaries, the plateau stage in the molybdenum steels was extended, relative to the base 17% Cr steel.

9.1.4 The Effect of Molybdenum at 25% Cr

In general additions of molybdenum decreased the rate of recovery and increased the plateau between recovery and recrystallisation. The explanation for this is similar to that for the 17% Cr molybdenum steel and will not be discussed further. However, after annealing at 690°C the

plateau was extended in the 25% Cr molybdenum steel relative to the 17% Cr molybdenum steel. This was probably because of the increased supersaturation effect of chromium carbide and nitride at lower temperatures. In terms of Equation 16, the increased supersaturation results in an increased volume fraction of precipitates at subgrain boundaries. If the particle coarsening characteristics are similar to those in the 17% Cr molybdenum steel, the annealing time to achieve d_{crit} will be increased in the 25% Cr molybdenum steel, resulting in an increase in the extent of the plateau.

9.1.5 The Effect of Molybdenum in the 17% Cr Steels at the Higher Interstitial Level

Molybdenum decreased the rate and the amount of recovery that occurred prior to recrystallisation. The plateau was also extended in the molybdenum steel relative to the base steel.

In the molybdenum steel, unlike the base steel, electron microscopy showed that a true recovery process was taking place. Recrystallisation was restricted to the ferrite / $M_{23}C_6$ interfaces and regions away from coarse carbides consisted of a fine recovered structure. This was probably because of the formation of molybdenum-interstitial 'atmospheres' which slowed down dislocation re-arrangement and the formation of subgrain boundaries. The extended plateau formed between recovery and recrystallisation because of precipitation of $M_{23}C_6$ at subgrain boundaries. Lattice parameter measurements of the $M_{23}C_6$ indicated molybdenum solution, resulting in a slower particle growth rate and a longer plateau.

The rate and amount of recovery in the molybdenum steels was lower at the higher interstitial content as shown by electron microscopy. The change in hardness, ΔH, with annealing time indicated an increased degree of supersaturation of carbides and nitrides in the higher interstitial content

steel. In terms of a molybdenum-interstitial 'atmosphere' effect, at the higher interstitial level, the 'atmosphere' formed more rapidly because of the increased degree of supersaturation and therefore the initial rate of recovery was slower. The decreased amount of recovery prior to recrystallisation can also be discussed in terms of an increased degree of supersaturation. Subgrain boundaries will be pinned after shorter annealing times which reduced the amount of recovery.

At the higher interstitial level, the plateau between recovery and recrystallisation was extended. The plateau region which formed resulted from precipitation at subgrain boundaries which pinned the subgrain boundaries. There are two opposing factors which occur at the higher interstitial contents in the molybdenum steels :

i. The increased supersaturation resulted in an increased volume fraction of precipitate and therefore an increase in the critical particle size for the unpinning of subgrain boundaries.

ii. The finer subgrain size at the higher interstitial level decreased the value of the critical particle size, d_{crit}, for a constant precipitate volume fraction, f.

Assuming that the particle coarsening characteristics were not affected by the interstitial content the extended plateau at the higher interstitial content means that (i.) more than compensated for effects due to (ii.).

9.1.6 The Effect of Titanium

Additions of titanium increased the rate of recovery. After annealing at lower temperatures, a distinct plateau between recovery and recrystallisation

was not observed.

Additions of titanium were in excess of stoichiometry and therefore lowered the solubility of carbon and nitrogen compared with the base steel. Because of the lower solubility of interstitials the solute atmospheres at dislocation formed more slowly and therefore the rate of recovery was increased. Since the precipitates observed at subgrain boundaries after annealing at lower temperatures were identified as $M_{23}C_6$, in the titanium steel, the particle coarsening characteristics will be very similar to those in the base steel. The reduced solubility of interstitials resulted in a smaller volume fraction of precipitates at subgrain boundaries, therefore pinning was less effective and the distinct plateau was not observed.

9.1.7 The Effect of Niobium at the Lower Interstitial Level

Additions of niobium, like titanium, increased the rate of recovery. However, unlike titanium, niobium extended the plateau between recovery and recrystallisation.

Like titanium, additions of niobium were in excess of stoichiometry and therefore lowered the solubility of interstitials compared with the base steel. Therefore, the explanation for the increased rate of recovery was similar to that for the titanium steel. However, unlike titanium, the precipitates observed at subgrain boundaries, after annealing were identified as NbC and not $M_{23}C_6$. In terms of Equation 16, the particle coarsening characteristics will depend on the diffusion of niobium. As the diffusion rate of niobium in high chromium ferrite was much slower than that of chromium, the plateau was extended in the niobium steel.

The plateau was also extended in the niobium steel relative to the lower

interstitial content molybdenum steel. This was because of the slower rate of diffusion of niobium compared with that of molybdenum, resulting in longer annealing times for sub-boundary unpinning to take place.

9.1.8 The Effect of Niobium at the Higher Interstitial Level

In general, niobium additions increased the length of the plateau at the higher interstitial level. This was because the precipitates observed at subgrain boundaries after annealing were identified as NbC and not $M_{23}C_6$, with a result that subgrain boundaries were more effectively pinned in the niobium steel due to the slower diffusion of niobium compared with chromium.

Increasing the interstitial content decreased both the rate and the amount of recovery and decreased the extent of the plateau. The explanation for the former lies in the Nb :(C + N) ratios of the two steels (Fig 139). Both steels had niobium contents in excess of the stoichiometric ratio. However, at the higher interstitial level, the Nb : (C+N) ratio was lower than at the lower interstitial level, 8.5:1 compared with 15:1, therefore the solubility of the interstitials was greater at the higher interstitial level. In terms of a solute 'atmosphere' effect, the 'atmosphere' formed rapidly at the higher interstitial level because of increased supersaturation and therefore the initial rate of recovery was slower. The decreased amount of recovery prior to recrystallisation can also be discussed in terms of an increased degree of supersaturation. Subgrain boundaries will be pinned after shorter annealing times, which reduced the amount of recovery.

The plateau region resulted from precipitation and pinning of the subgrain boundaries. The shorter plateau at the higher interstitial level was because of the increased driving force for recrystallisation which resulted in subgrain boundaries being unpinned after shorter annealing times.

At lower annealing temperatures ferritic stainless steels are characterised by a distinct plateau in the ΔH with annealing time curve between recovery and recrystallisation stages. In the molybdenum steels and niobium steels, distinct plateaux were observed after annealing at 750°C and below, while in the low (C+N) base steels, plateaux formed only at lower temperatures. The extent of the plateaux increased with decreasing temperature and the end of the plateau coincided with the incubation period for recrystallisation. Electron microscopy showed evidence of precipitation at subgrain boundaries after annealing at lower temperatures. At higher temperatures, i.e. above 750°C, no precipitation was observed. Köster[83] formulated a basic interpretation of the mechanisms involved in the mutual influence of precipitation and recrystallisation in a supersaturated solid solution in terms of the temperature dependence for the start of the two processes. A schematic representation of the relationship between the incubation period for recrystallisation, t_r, and precipitation, t_p, as a function of annealing temperature is shown by Figure 9. At higher temperatures, i.e. above 750°C, precipitation does not occur and recrystallisation proceeds without the influence of precipitation in a solid solution. The process controlling the rate of recrystallisation will be a solute drag effect, where the rate of recrystallisation will be controlled by the diffusing atomic species.

At temperatures below T_1 but above T_2 in Figure 9, the minimum incubation period, t_r, was less than that for precipitation, t_p. However, the nucleation rate in ferritic stainless steels was orientation sensitive, as are most commercial metals, and therefore the incubation period, t_r, for nucleation of recrystallised grains of less favourable orientations was greater than for precipitation, t_p, and the subgrain boundaries of these orientations were pinned.

At temperatures below T_2 the incubation period for precipitation, t_p, was always less than for recrystallisation, t_r. If it is assumed that subgrain growth obeys the same laws as grain growth following recrystallisation,[58] no effect will be observed if the particles are precipitated in a random manner, because of their small volume fraction. Because particles were situated at subgrain boundaries, the pinning action was effective even at low volume fractions and a minimum particle size, d_{crit}, was required to allow growth of the largest subgrain (Equation 16). The start of the plateau was considered to represent the pinning of subgrain boundaries by precipitated particles. The end of the plateau stage coincided with the incubation period for recrystallisation, t_r, representing the time taken for the initial unpinning of subgrain boundaries. Once subgrain boundaries become unpinned they can migrate rapidly by virtue of the size advantage of the growing subgrains, to form recrystallised grains. As only a few subgrain boundaries were unpinned at any one time, the nucleation rate decreased, resulting in a coarse grain size.

The extent of the plateau increased with decreasing temperature.

Two factors were responsible for this :

i. As the annealing temperature was decreased the rate of particle coarsening decreased because of a slower diffusion rate. Therefore, the annealing time to exceed the critical particle size for the unpinning of subgrain boundaries, d_{crit}, increased.

ii. As the annealing temperature was decreased, the degree of supersaturation of carbides and nitrides increased leading to an increased volume fraction of precipitated particles. Therefore the critical particle size for the unpinning of subgrain

boundaries increased which resulted in longer incubation periods.

The recrystallisation rate increased and the extent of the plateau decreased with increasing cold reduction. The effect of cold work on the recrystallisation rate can be discussed in terms of the accepted theories of recrystallisation. At lower reductions, the stored energy was less resulting in a decrease in the relative rates of nucleation and boundary migration. Cold work affects the precipitation/recrystallisation reaction in two ways :

a. At lower reductions the stored energy of cold work was less and the mean subgrain diameter was larger. In terms of Equation 16, the average critical particle diameter is roughly proportional to the subgrain diameter, therefore the critical particle diameter for the unpinning of subgrain boundaries increased with decreasing cold reduction.

b. The activation energy for diffusion increased as the dislocation density decreased[173], therefore the annealing time required for the unpinning of subgrain boundaries was still further increased at lower reductions, which resulted in a longer plateau stage at lower reductions.

Activation energies for recrystallisation were observed to increase with decreasing cold reduction. The activation energy for recrystallisation is proportional to the activation energy for diffusion of the solute species, e.g. Cr in high chromium ferrite. Because the activation energy for diffusion increases with decreasing dislocation density[173] therefore the activation energy for recrystallisation was observed to increase with decreasing reduction.

9.2.1 17% Cr Low (C+N)

Annealing this steel at temperatures below 690°C resulted in an increased activation energy for recrystallisation and an increased grain size which also increased with decreasing temperature. At higher temperatures, recrystallisation proceeded without the influence of precipitation. In the temperature range 690° - 750°C, precipitation occurred during recrystallisation, both at subgrain boundaries and at recrystallisation fronts. However, at these temperatures, particle coarsening took place rapidly because of the higher temperatures and any precipitates at subgrain boundaries had little effect on recrystallisation. Annealing at temperatures below 690°C, the incubation period for precipitation, t_p, was always less than for recrystallisation, t_r, and precipitation was observed exclusively at subgrain boundaries. The precipitates pinned the subgrain boundaries and inhibited recrystallisation. Before recrystallisation occurred, particle coalescence was required to unpin the subgrain boundaries, which was controlled by the diffusion of chromium. The presence of precipitates at subgrain boundaries decreased the recrystallisation nucleation rate relative to a precipitate free structure, therefore the activation energy increased after annealing below 690°C. As the annealing temperature was decreased below 690°C the recrystallisation nucleation rate was increasingly retarded because of a slower diffusion rate of Cr and an increased supersaturation of carbides and nitrides. It can be seen from Figure 140 that with increasing volume fraction of precipitate, the critical particle diameter for the unpinning of subgrain boundaries, d_{crit}, became increasingly dependent on the mean subgrain diameter. Therefore with decreasing temperatures fewer subgrain boundaries became unpinned leading to a decreased nucleation rate and a coarser grain size.

9.2.2 The Effect of Interstitial Content

At the higher interstitial content, recrystallisation was retarded relative to the lower interstitial content steel. At lower annealing temperatures the retarding effect was even greater resulting in a higher activation energy in the higher interstitial content base 17% Cr steel.

At the higher interstitial content, two distinct microstructural regions were observed :

i. In the prior austenite regions electron microscopy showed that fine recrystallised grains were nucleated by coarse $M_{23}C_6$ particles. Nucleation took place at the ferrite/carbide interface and recrystallisation occurred very rapidly, even at low temperatures[70][71]. However, a fine dispersion of $M_{23}C_6$, 0.25μm in diameter, which was produced during tempering, pinned the fine recrystallised grain boundaries. In these regions further softening occurred by either a grain growth or secondary recrystallisation mechanism, after sufficient particle coalescence had taken place to allow some grain boundaries to become unpinned.

ii. In the ferrite grains, recrystallised nuclei predominated at former grain boundaries and electron microscopy showed evidence of nucleation at these sites. However, a fine dispersion of $M_{23}C_6$, 0.25μm in diameter, precipitated in the ferrite before cold working, pinned the grain boundaries of the fine potential recrystallisation nuclei. After sufficient particle coalescence had occurred for unpinning of the grain boundaries, recrystallisation proceeded by nucleation and boundary migration. Therefore unlike the lower interstitial content base 17% Cr steel recrystallisation

always occurred in the presence of a fine dispersion of carbide particles.

At lower temperatures, i.e. 690°C, particle coarsening occurred slowly because of the relatively slow rate of diffusion of chromium, and recrystallisation was markedly retarded at the higher interstitial content. However, at higher temperatures, i.e. 750°C, because of the increased rate of diffusion of chromium, particle coarsening took place more rapidly and the retarding effect on recrystallisation at the higher interstitial level relative to the lower interstitial level was reduced. This results in a higher activation energy for recrystallisation at the higher interstitial level in the base 17% Cr steels.

9.2.3 The Effect of Chromium Content

The activation energy for recrystallisation increased in the 25% Cr low (C+N) compared with the 17% Cr low (C+N) at all cold reductions. In fact after 35% reduction unlike the 17% Cr steel, the 25% Cr steel showed an increase in the activation energy for recrystallisation after annealing below 720°C.

After annealing at lower temperatures, i.e. below 720°C, there was an indication of an increased supersaturation of carbide and nitrides in the 25% Cr steel. The overall effect of supersaturation was to increase the temperature at which mutual precipitation occurred. At 35% reduction, unlike the 17% Cr steel, the incubation period for precipitation was less than for recrystallisation after annealing below 720°C. In this temperature range, precipitates pinned the subgrain boundaries leading to a reduction in the recrystallisation nucleation rate and an increased activation energy for recrystallisation. After 75% reduction, this was

not the case and the activation energy increased after annealing below 690°C. This was because of :

i. The temperature for which $t_p < t_o$ decreased with increasing cold reduction.

ii. The driving force for subgrain growth increased with increasing cold reduction, therefore in terms of Equation 16, subgrain boundaries will be less effectively pinned at higher reductions.

At lower annealing temperatures, i.e. 690°C, recrystallisation was slightly retarded in the 25% Cr steel relative to the 17% Cr steel, while at the higher annealing temperatures the converse applied, which resulted in the increased activation energy found in the 25% Cr steels.

The decreased recrystallisation rate at the lower temperatures was because of the increased supersaturation of carbides and nitrides mentioned earlier. At higher temperatures, i.e 750°C, precipitation did not influence recrystallisation in either the 25% Cr or 17% Cr steels. In the 25% Cr steel, unlike the 17% Cr steel, many grains were nucleated at intra-granular $M_{23}C_6$. The nucleating action of these particles increased the nucleation rate of the 25% Cr steel relative to the 17% Cr steel. This was further indicated by the finer grain size observed in the 25% Cr steel. Therefore the 25% Cr steel recrystallised faster at 750°C than the 17% Cr steel.

9.2.4 The Effect of Molybdenum in the 17% Cr Steels at the Lower Interstitial Level

After annealing at 750°C additions of molybdenum increased the incubation period and decreased the recrystallisation rate, but at lower temperatures, i.e. 690°C, the retarding effect of molybdenum was even greater, resulting

in a higher activation energy for recrystallisation in the molybdenum steel. The retarding effect of molybdenum at lower temperatures was accompanied by an increased grain size.

After annealing at 690°C precipitates were observed at subgrain boundaries by electron microscopy, resulting in subgrain boundary pinning. The reasons why precipitation was more effective in the molybdenum steel were:

i. Because of the slower recrystallisation, the incubation period was increased relative to that for precipitation.

ii. Although the precipitates were identified as $M_{23}C_6$, the lattice parameter of the carbide was increased indicating molybdenum solution in the carbide. In terms of the Wagner equation[80] the rate of particle coalescence depends upon the diffusion rate of molybdenum. Because molybdenum has a slower diffusion rate than that of chromium, the rate of particle coalescence decreased in the molybdenum steel, resulting in a decreased nucleation rate and a coarser grain size. Therefore the incubation period for recrystallisation increased relative to the base 17% Cr steel after annealing at 690°C.

At higher temperatures, i.e. 750°C, and above, precipitation had no influence on recrystallisation and recrystallisation took place in a solid solution. Because of the slower rate of diffusion of molybdenum the rate of subgrain growth was slower, resulting in a decreased recrystallisation rate in the molybdenum steel. However, because the activation energy for unpinning of subgrain boundaries is greater than that for subgrain growth in a solid solution[173], the retarding effect of molybdenum on recrystallisation at 750°C relative to 690°C was reduced.

Unlike the base 17% Cr steel, after 35% reduction the molybdenum steel showed an increased activation energy for recrystallisation after annealing below 720°C. Because of the slower recrystallisation rate in the molybdenum steels, after 35% reduction, the incubation period for precipitation was less than for recrystallisation after annealing below 720°C.

9.2.5 The Effect of Molybdenum in the 25% Cr Steel at the Lower Interstitial Level

This steel showed similar effects to the 17% Cr low (C+N) 1% Mo steel and therefore the basic mechanisms will not be discussed again. However, the higher chromium steel recrystallised more slowly at 690°C and more rapidly at 750°C than the 17% Cr molybdenum steel. Unlike the 17% Cr molybdenum steel, annealing below 720°C resulted in an increased activation energy. At 750°C no precipitation occurred before recrystallisation therefore the increased volume fraction of undissolved $M_{23}C_6$ resulted in an increased nucleation rate and hence faster recrystallisation. This was further indicated by the finer recrystallised grain size observed in the 25% Cr molybdenum steel. However, in the 25% Cr molybdenum steel there was an increased supersaturation effect of carbides and nitrides resulting in the incubation period for precipitation being less than for recrystallisation after annealing below 720°C. Therefore the precipitates pinned the subgrain boundaries and decreased the recrystallisation rate resulting in a higher activation energy.

9.2.6 The 17% Cr High (C+N) 1% Mo Steel

Two effects will be discussed :

i. The Effect of Molybdenum at the Higher Interstitial Level in the 17% Cr Steels

At the higher interstitial content additions of molybdenum increased the incubation period for recrystallisation. Once recrystallisation started the molybdenum steel recrystallised faster than the base steel. The increased incubation period in the molybdenum steel correlated with the extended plateau observed in the change in hardness against annealing time curves.

In the base steels, at temperatures of 690^{o}C and above, the majority of subgrain boundary pinning was due to precipitates present before cold work. However, in the molybdenum steels, while pinning by fine carbides present before cold work occurred, it was not so important as in the base steel because :

a. The volume fraction of martensite was less due to the presence of molybdenum;

b. No extensive precipitation took place in the ferrite prior to cold work.

At temperatures of 750^{o}C and below, the extended plateau in the molybdenum steel was due to a precipitation/recrystallisation interaction. In both steels precipitates were identified as $M_{23}C_6$. Therefore because they contained molybdenum and due to the slower diffusion of molybdenum compared with chromium, the $M_{23}C_6$ particles coarsened more slowly in the molybdenum steel than in the base steel (Equation 15) resulting in an increased incubation period.

Electron microscopy and hardness tests showed great differences in stored energy between the two steels, i.e. the molybdenum steel underwent very little recovery compared with the base steel.

The high degree of stored energy in the molybdenum steel resulted in a very high nucleation rate for recrystallisation, therefore once recrystallisation started, it took place rapidly. The higher nucleation rate of the molybdenum steel compared with the base steel was further substantiated by the recrystallised grain size, which despite a higher volume fraction of nucleating particles in the base steel, was finer in the molybdenum steel. In the base steel, although particles coarsened more rapidly, due to the lower stored energy, sequential unpinning of subgrain boundaries took place more slowly.

ii. The Effect of Interstitial Content in the 17% Cr Mo Steels

In comparison with the 17% Cr low (C+N) 1% Mo steel, the incubation period for recrystallisation was increased, which was in agreement with the extended plateau at the higher interstitial content. However, although the incubation period for recrystallisation was extended at 750°C, the higher interstitial content steel had a faster recrystallisation rate. Despite the longer incubation period, recrystallisation was achieved in the same time as in the lower interstitial content steel. At lower temperatures, this was not the case, and recrystallisation was retarded in the higher interstitial content steel, while at higher temperatures than 750°C, the higher interstitial content showed more rapid recrystallisation. This resulted in a higher activation energy for recrystallisation at the higher interstitial level.

The change in hardness, Δ H, with annealing time indicated an increased

degree of supersaturation of carbides and nitrides in the higher interstitial content steel. In the higher interstitial content steel, after annealing at 750°C, the incubation period for precipitation was less than for recrystallisation.

The increased degree of supersaturation of carbides and nitrides resulted in a greater volume fraction of precipitates at subgrain boundaries, hence a longer incubation period for the unpinning of subgrain boundaries. At 750°C the increased supersaturation of carbides and nitrides had only a slight effect on the incubation period for recrystallisation because of the relatively rapid coalescence of precipitates at this temperature. The higher stored energy and increased volume fraction of nucleating particles resulted in a higher nucleation rate at the higher interstitial content, and therefore recrystallisation was achieved in the same time in both steels. However, with decreasing temperature slow particle coalescence resulted in a much longer incubation period at the higher interstitial level and recrystallisation was retarded. At higher temperatures, i.e. above 750°C, precipitation had no effect on recrystallisation. Therefore because of the higher recrystallisation nucleation rate, the higher interstitial content steel recrystallised more rapidly.

9.2.7 The Effect of Titanium

Titanium had little effect on recrystallisation. This was because in the titanium steel, the precipitates at subgrain boundaries were identified as $M_{23}C_6$; therefore there was little effect on nucleation. The slight increase in the recrystallisation rate may be due to a higher nucleation rate as a result of nucleation at undissolved Ti(CN) particles. However, this was not reflected by the grain size.

9.2.8 The Effect of Niobium

Additions of niobium increased the activation energy for recrystallisation at both interstitial levels. This was because of the higher activation energy for diffusion of niobium compared with chromium in high chromium ferrite.

i. The Effect of Niobium at the Lower Interstitial Level

Unlike titanium, additions of niobium increased the incubation period for recrystallisation and decreased the recrystallisation rate. Solute drag effects may account for the decreased recrystallisation rate. At higher temperature, i.e. above 750°C, solute drag effects were important due to the absence of precipitation at subgrain boundaries. However, at 750°C, unlike the base steel, precipitation of NbC was observed at subgrain boundaries.

Precipitates are more effective in retarding recrystallisation than are solutes, therefore the major retarding effect was due to precipitates at temperatures of 750°C and below. At 750°C, in the base steel, recrystallisation took place in the absence of precipitation. In the niobium steel the rate of particle growth depended upon the diffusion of niobium. Because of the slow rate of diffusion of niobium, even at 750°C, recrystallisation was retarded. At the lower reductions, recrystallisation was retarded even further compared with the base 17% Cr steel. This was because of the much higher degree of recovery prior to recrystallisation in the niobium steel, which resulted in a lower stored energy and a larger subgrain size. In terms of Equation 16, the critical particle size for the unpinning of subgrain boundaries increased, therefore recrystallisation was even further retarded in the niobium steel. Niobium retarded recrystallisation to a much greater extent than molybdenum due to the slower rate of diffusion of niobium.

ii. The Effect of Niobium at the Higher Interstitial Level

Additions of niobium increased the incubation period for recrystallisation as shown by the extended plateau observed in the steels.

At the higher interstitial level, the niobium steel behaved in a similar manner to the molybdenum steel. The incubation period was related to the rate of coarsening of niobium carbide particles which pinned the subgrain boundaries. Because the diffusion rate of niobium was much slower than that of chromium, the incubation period for recrystallisation was increased. However, unlike the base steel, a high degree of stored energy was retained in the less recovered structure. Because of this many subgrain boundaries were unpinned at the same time leading to a high nucleation rate. Therefore once recrystallisation had started, the high nucleation rate led to a rapid recrystallisation relative to the base 17% Cr steel.

In the niobium steels, recrystallisation always took place more rapidly at the higher interstitial level. On first reflection, it may appear that this was just a particle stimulated nucleation effect[70][71]. However, the lower interstitial content niobium steel underwent a much higher degree of recovery prior to recrystallisation. In terms of a precipitation/recrystallisation interaction, a lower stored energy and larger subgrain size leads to :

a. A larger critical particle diameter, d_{crit}, before subgrain boundaries were unpinned;

b. The lower stored energy decreased the rate of diffusion and therefore the rate of particle growth.

Therefore the incubation period for recrystallisation was extended and the nucleation rate decreased at the lower interstitial level in the niobium steel. The decreased recrystallisation nucleation rate was also reflected in the recrystallised grain sizes of the two steels, i.e. the higher interstitial content steel had a much finer recrystallised grain size at 35% and 50% reduction.

9.3 THE DEVELOPMENT OF DEFORMATION TEXTURES

During cold rolling, the {110} component decreased and the {111} component increased progressively with increasing cold reduction and even after only 35% cold reduction, this texture was quite well developed. The {100} component did not develop so rapidly, full pole figures showing that the {111} component was in fact the {111}<112> texture. However, unlike the inverse pole figure work, the {100} component, i.e. {100}<011> texture was equally as strong. The discrepancy arising between the results obtained from inverse and full pole figures may be discussed in terms of the multiplicity of the textural components[101]. For a {200} pole figure, two components satisfy the {111} <112> texture whereas the {100} <011> is a single component. Thus, for a texture containing equal proportions {111} <112> and {100} <011> texture, the intensity of the {111} <112> component would be half that of the {100} <011> component.

It is well established that the {110} <001> component splits into two {111} <112> components after only low reductions[34]. Therefore, the sharp increase in the {111} component and the resulting {111} <112> texture was produced by the splitting of the {110} <001> component present in the hot band. The {111} <112> was still the major component after 50% reduction.

However, with increasing reduction, the rate of development of the {111} component decreased, and in some steels it decreased slightly with a corresponding increase in the {100} component. Full pole figures showed that after 75% reduction, the {111}<112> component decreased and was replaced by some {111}<110> and {112}<110> components. Above 50% reduction, the {100} component increased progressively with increasing reduction and full pole figures showed this to be the {100}<011> texture.

Above 50% reduction, the {111}<112> decreased in intensity because it is not a stable component. It has been reported[114] that during rolling the {111}<112> component rotated about the sheet normal towards the {111}<110> resulting in an increase in this component with increasing cold reduction. However, with increasing cold reduction, this component also rotated about the rolling direction to form the stable {112}<110> texture. The {100}<011> component increased with increasing reduction because the {100}<011> component can be considered to be stable during rolling[107].

After 95% reduction, the major texture was the {100}<011> with a {112}<110> component and minor {111}<110> and {111}<112> components. The {111}<110> component was stronger than the {111}<112>. However, the lower interstitial niobium steel, with the stronger {110} component in the hot band, had a stronger {112}<110> and {111}<110> and a weaker {100}<011> than the base 17% Cr steel after 95% reduction.

In the steels with a low {110} component in the hot band, the supply of orientations to produce the {111}<112> soon becomes exhausted resulting in the decrease in the {111} component at higher reductions. However, in steels with a relatively strong {110} in the hot band, e.g. Alloy 7, the supply of orientations to produce {111}<uvw> components was not so

easily exhausted, therefore there was a gradual increase in the {111} component with increasing reductions. At high reductions the {111}<uvw> components rotated towards {112}<110> resulting in a stronger {112}<110> component.

9.4 THE DEVELOPMENT OF RECRYSTALLISATION TEXTURES

9.4.1 Alloy (1) 17% Cr Low (C+N)

After 35% cold reduction, recrystallisation increased the {110} component and decreased the {111} and {100} components. Full pole figures showed that the major texture was a {110}<001> with a minor {100}<011> component. These were the textures after 50% cold reduction, but a minor {111}<112> component was also present. The basic mechanisms of nucleation will be examined to see why the {110}<001> became the major texture after recrystallisation, even though it was not represented in the deformation texture.

The basic mechanisms of recrystallisation nucleation are :

i. Grain boundary;

ii. Deformation band;

iii. In-situ, i.e. nucleation within the grain;

iv. Particle stimulated nucleation.

At low reductions, the in-situ mechanism was not favourable because there was insufficient lattice curvature to allow nucleation by a subgrain growth mechanism. Particle stimulated nucleation was not an important mechanism in this steel because nucleating particles were present only in the prior austenite regions, which represented only 4% of the total structure. At low cold reductions, both grain boundary nucleation and deformation band

nucleation were particularly favourable. Grain boundary nucleation sites are particularly favourable for the development of {100}<011> textures[32][72]. However, in this steel, the effectiveness of grain boundary nucleation was reduced, because of the coarse grain size in the 'hot band' resulting in a slightly decreased {100}<011> component when compared with the cold worked state.

Nucleation at deformation bands has been shown to be highly favourable at low and moderate reductions[34][114]. Metallographic examination and thin foil electron microscopy showed that nucleation for recrystallisation was associated with deformation bands, and electron diffraction showed that the predominant orientation was the {110} parallel to the plane of the sheet. The {110}<001> texture developed by nucleation at deformation bands. Although the {110}<001> component represented only a small volume fraction of the deformation texture, because of the high stored energy of this component it nucleated first, and therefore had considerable time for growth before impingement occurred, thus allowing it to become the major component of the recrystallisation texture. Because of the low nucleation potential of in-situ nucleated orientations, e.g. {111}<112>, they were consumed by the {110}<001> resulting in a reduced intensity of the component compared with the cold worked state.

With increasing cold reduction, the {110} component decreased and the {111} component increased to a maximum after 95% cold reduction. However, even after 75% reduction, the {111} component was weak, P_{hkl} = 2.1, and it was only at reductions greater than 82% that it exceeded that of the cold worked condition. The {100} component decreased progressively with increasing cold reduction to a minimum after 95% reduction. Full pole figures showed that the major textures were {111}<112> and {100}<011>.

It has been shown[32] that the distribution of stored energy depended on the crystallographic orientation of the cold worked metal. For in-situ nucleation within the major texture components the stored energy and therefore nucleation rate increased in the order {100}<011> - {211}<110> - {111}<uvw>. Therefore in terms of in-situ nucleation mechanisms the {111} components nucleated first and had the longest time for growth before impingement occurred. Because with increasing cold reduction the stored energy of the {111}<uvw> components increased relative to the other components[114], the nucleation potential of the {111}<uvw> component increased resulting in the increased {111} component with increasing cold reduction. Because of the low stored energy of the {100} component, it was consumed by the {111} components. The intensity of the {110} component decreased above 50% reduction as nucleation for recrystallisation from deformation bands of this orientation become less favourable[114].

9.4.2 Alloy (2) 17% Cr High (C+N)

Unlike the lower interstitial content steel, the intensity of the {100} component increased considerably after 35% reduction. The reason for this sharp increase lies in the microstructure of the higher interstitial steel, in which the ferrite grains were 'pancaked', produced by the pinning action of austenite during the pre-cold working treatment.

At the higher interstitial level, the 'pancaked' nature of the grains was much more pronounced than at the lower interstitial level. The work of Morris[72] and Dillamore et al[32] indicated that grain boundary sites are particularly favourable for the nucleation of {100} components. Thin foil electron microscopy showed that a high proportion of grains nucleated at the grain boundary had {100} in the plane of the sheet. For a constant grain volume, the grain boundary area increases as the grains

become increasingly 'pancaked'. Therefore because of the increased amount of grain boundary area, at the higher interstitial level, nucleation of the {100} component was particularly favourable, leading to an increase in the {100} component after 35% reduction. Electron microscopy indicated that grain boundary nucleation occurred by a subgrain growth mechanism. The grain boundary bowing mechanism considered by Dillamore et al[32] was unlikely because $M_{23}C_6$ particles situated at the matrix grain boundary pinned the boundary and prevented strain induced boundary migration.

The {111} component was always greater at the higher interstitial content in the base 17% Cr steels. The reason for the stronger {111} component at the higher interstitial content was due to particle stimulated nucleation. Thin foil electron microscopy showed that {111} orientations, in the plane of the sheet, were capable of being nucleated at the ferrite/$M_{23}C_6$ interface after only 35% cold reduction. A possible mechanism for this will be discussed later. Unlike the lower interstitial steel, nucleation at in-situ sites was possible after 35% reduction because of the increased lattice curvature adjacent to particles and the lower energy barrier for recrystallisation. This resulted in stronger {111} components at the higher interstitial level.

9.4.3 The Effect of Titanium and Niobium at the Lower Interstitial Level

As the effects due to additions of titanium and niobium were similar, the mechanisms of recrystallisation texture formation will be discussed for these steels together. Unlike the base steels, the {111} component decreased only slightly compared with the cold worked condition after 35% cold reduction. The major texture was {111}<112>. The {100} component decreased relative to the cold worked state. A minor {110}<001>

component was observed in the full pole figures.

After short annealing times, electron microscopy showed a tendency for {111} orientations to nucleate at the ferrite/(Nb or Ti) CN interface, after only 35% reduction. This was because of an increased lattice curvature adjacent to second phase Ti(CN) or Nb(CN) particles resulting in an increased stored energy. This phenomenon was observed in all steels with nucleating particles present at intragranular sites, whether Ti(CN), Nb(CN) or $M_{23}C_6$. Because regions adjacent to particles had a higher stored energy, this produced effects similar to an increase in cold reduction. Therefore within the major textures the order of stored energy remained the same, i.e. increased from {100}<011> → {111}<uvw>. The stored energy of the {111}<uvw> therefore increases relative to the {100}<011> in regions adjacent to particles, compared with the matrix. Unlike the base steel, the {111}<112> component can nucleate more easily within its parent orientation. As a result of competition between {111}<112> and deformation band nucleated grains, e.g. {110}<001>, the latter were reduced in intensity compared with the base steel. This results in the {111} component being almost as strong as in the cold worked condition. The {100} component decreased in intensity compared with the {111} component because of its low stored energy.

With increasing cold reduction the {111} component in the titanium and niobium steels continued to increase relative to the base 17% Cr low (C+N) steel. This was because particle stimulated nucleation increased the nucleation potential of {111} components relative to the other components.

9.4.4 17% Cr High (C+N) + Nb

Unlike the base 17% Cr steel the higher interstitial level niobium steel

did not show the considerable increase in the {100} component during recrystallisation after low reductions. The {111} component was also stronger after 35% in the high (C+N) niobium steel. The reason for this was associated with the hot band microstructure of each. The niobium steel contained a uniform distribution of coarse Nb(CN) particles, while the base high (C+N) steel consisted of alternate bands of ferrite and tempered martensite (austenite). In the latter steel nucleating particles were restricted to the tempered martensite regions.

As second phase particles were favourable sites for nucleation of the {111} component, the nucleating action of the uniform distribution of Nb(CN) reduced the effectiveness of grain boundary nucleated {100} component. Therefore the {100} component was less intense in the high (C+N) niobium steel than in the base 17% Cr high (C+N) steel.

In the niobium steels, the {100} component was always greater at the higher interstitial level. This was because of a finer initial grain size which resulted in more favourable conditions for nucleation of the {100} component.

9.4.5 Alloy (4) 17% Cr Low (C+N) 1% Mo

Like additions of titanium and niobium, molybdenum added to a 17% Cr low (C+N) steel favoured the development of a strong {111} component. However, at the lower reductions it was not so effective as either titanium or niobium at the lower interstitial levels. Electron microscopy showed a tendency for {111} orientations to nucleate at the ferrite/$M_{23}C_6$ interface. However, unlike the titanium or niobium steels, the particles were distributed in bands and not uniformly distributed throughout the microstructure and thus they were not so effective in reducing the deformation band nucleation,

resulting in a weaker {111} texture than in the niobium or titanium steel at the lower interstitial level. However, particle stimulated nucleation of the {111} component increased the intensity of this component in the molybdenum steel compared with the base 17% Cr low (C+N) steel.

9.4.6 Alloy (3) 17% Cr High (C+N) 1% Mo

In contrast to the base steel, the higher interstitial content molybdenum steel did not show the increase in the {100} component after 35% cold reduction. Two factors are responsible for this :

i. The grains of the high (C+N) molybdenum was not so 'pancaked' as the base steel, thus reducing the chance of nucleating the {100} component.

ii. Coarse $M_{23}C_6$ particles were present within the ferrite grains, which were favourable for nucleating the {111} component so further reducing the effectiveness of the grain boundary nucleated {100} component.

In the molybdenum steels, the {100} component was always greater at the higher interstitial level, resulting in a lower {111} : {100} ratio. This may again be explained in terms of the hot band microstructure. The higher interstitial content molybdenum steel had a more pronounced 'pancake' grain structure in the hot band because of the pinning action of the increased volume fraction of austenite. The increased grain boundary area favours the development of a stronger {100} component.

9.4.7 The Effect of Chromium Content

After 35% reduction the 25% Cr steel behaved in a similar manner to the 17% Cr steel. The {110} component was not so intense in the 25% Cr steel

as in the 17% Cr steel which was consistent with the stronger {111} at 25% Cr. Although the base 25% Cr steel behaved similarly to the 17% Cr steel at the higher reductions, the {111} component was increased at 25% Cr.

Particle stimulated nucleation after 35% reduction resulted in nucleation of the {111} component and decreased the intensity of the deformation band nucleated {110} component compared with the 17% Cr steel. With increasing reduction, particle stimulated nucleation resulted in further nucleation of the {111} component. Therefore the {111} component increased in the 25% Cr steel relative to the 17% Cr steel.

9.4.8 The Effect of Molybdenum at 25% Cr

After 35% reduction, these alloys behaved similarly to the 25% Cr base steel, but had stronger {111} and weaker {110} components. With increasing reduction, the {111} component increased relative to the base steel. This can again be discussed in terms of particle stimulated nucleation of the {111} component, which reduced the effectiveness of the deformation band nucleated {110} component. The particles were more randomly distributed in the molybdenum steel than in the base steel and occurred in a larger volume fraction. This resulted in more effective formation of the {111} component and a stronger {111}<112> texture than in the base steel.

9.4.9 Summary of Recrystallisation Texture Formation

Recrystallisation texture formation has been shown to depend on two major factors :

1. The degree of cold reduction;

2. The microstructure of the hot band, e.g. second phase particles, grain size and grain shape.

The above factors influenced the recrystallisation sites which in turn determined the recrystallisation texture.

The recrystallisation sites were :

i. Grain boundaries - favouring a {100} texture;

ii. Deformation bands at low reductions - favouring a {110} texture;

iii. In-situ - favouring a {111} texture;

iv. Particle stimulated nucleation at in-situ sites - favouring a {111} texture.

At the lower reductions, i.e.up to 50% cold reduction, grain boundaries and deformation bands were the most important nucleation sites for recrystallisation. In-situ sites leading to the formation of {111} textures were not favourable at low reductions because insufficient lattice curvature was generated at low strains to allow nucleation by subgrain growth.

In steels where particle stimulated nucleation was prevalent, e.g. Ti and Nb, the development of a {111} type texture was observed even after only 35% and 50% cold reduction. Thin foil electron microscopy showed that recrystallised grains nucleated at the particle/matrix interface. Electron diffraction showed that the most common orientation of these grains was a {111} in the plane of the sheet. This was because of an increased lattice curvature adjacent to second phase particles, resulting in an increased stored energy. Because regions adjacent to particles had a higher stored energy, this produced effects similar to increases in cold reduction. Therefore within the major textures, the order of stored

energy remained the same, i.e. increased from {100}<011> → {111}<uvw>. The stored energy of the {111}<uvw> texture therefore increases relative to the {100}<011> texture in regions adjacent to particles, compared with the matrix. Unlike the base steel, the {111} components nucleated readily within the {111} component of the deformation texture.

Grain boundary nucleation favoured the formation of {100} type textures. A high dislocation density was generated adjacent to the grain boundary in grains of {100} in the plane of the sheet when the neighbouring grain has a higher 'M value', e.g. {111} [72]. Thus, the high stored energy at grain boundaries in {100} grains results in a favourable site for nucleation of the {100} component.

Deformation band nucleation at low reductions led to the development of a {110} type texture, particularly in coarse grained steels, e.g. 17% Cr low (C+N) steel. Both optical and electron microscopy showed that deformation band nucleation of recrystallised grains was an important mode of nucleation at low reductions. Electron diffraction showed that grains nucleated at deformation bands tended to have {110} in the plane of the sheet. It has been shown [34] [109] [114] that at low and moderate reductions, deformation band nucleation of recrystallised grains led to the formation of a {110} type texture. This was because deformation bands are regions of high local stored energy and hence of high nucleation potential.

With increasing cold reduction, the {111} component increased progressively while the {100} component in general decreased with increasing cold reduction. This was because nucleation for recrystallisation at in-situ sites and by particle stimulated nucleation became increasingly favourable with increasing cold reduction. Electron microscopy showed that both these sites were favourable for nucleation of {111} recrystallised grains

after 75% reduction.

The reason why {111} nucleated preferentially to other orientations was that the stored energy in the cold worked metal depends on the crystallographic orientation. Within the major components, the stored energy and hence nucleation frequency increases from {100}<011> → {111}<uvw> textures[32] and the difference in stored energy increases with increasing cold reduction[114]. Therefore the {111} component consumes the {100} component and the {100} component decreases in intensity. At very high reductions in some steels, the {100} component increases slightly at the expense of the {111} component. Heavy deformations provided a large area of grain boundary because the grain boundary area increased with increasing cold reduction. On the basis that grain boundary nucleation of recrystallised grains gives rise to {100} components, the slight increase in the {100} component at high reduction was because of grain boundary nucleation.

9.5 MECHANICAL PROPERTIES

Regression analyses showed the following results, at 95% confidence level, for fully recrystallised structures with no subgrains :

1. Yield Strength, σ_y

$$\sigma_y = 36.3 + 8.5 \times \%Cr + 57.9 \times \%Mo - 107 \times \%Ti + 15.9\ d^{-\frac{1}{2}}\ Mn/m^2$$

Correlation Coefficient + 0.96 ———— (86)

Recent unpublished work by Bywater[178] showed the following regression equation for 17% Cr ferritic stainless steels :

$$\sigma_y = 40 + 8.2 \times \%Cr + 13.5\ d^{-\frac{1}{2}} \quad \text{———— (87)}$$

Recent equations[179][180] for yield strength of a polygonal ferrite structure in plain silicon killed carbon-manganese steels containing up to 0.25% C are :

$$\sigma_y = 88 + 15.1\ d^{-\frac{1}{2}} \qquad \text{(88)}$$

for specimens which were cooled rapidly, and :

$$\sigma_y = 62 + 15.1\ d^{-\frac{1}{2}} \qquad \text{(89)}$$

for slow cooled specimens. Clearly the frictional stress, σ_o, was much lower in ferritic stainless steels than in C-Mn steels, containing up to 0.25% C. This was presumably because of chromium reducing the solubility of interstitials in solid solution, particularly nitrogen, thus reducing the frictional stress. The ky term obtained in the present work was similar to that found in the C-Mn[179][180] steel, i.e. 15.9 cf 15.1, indicating that grain size effects in ferrite are independent of the chromium content.

Carbon and nitrogen had little effect on the yield stress indicating that the amount of carbon and nitrogen in interstitial solid solution did not vary appreciably with interstitial content. Titanium additions significantly decreased the yield stress by reducing the solubility of interstitials compared with the base 17% Cr steel. However, niobium did not show any significant effects, therefore the decrease in the yield stress in the 17% Cr low(C+N) +Nb steel when compared with the 17% Cr low (C+N) steel was because of a coarser recrystallised grain size. The reason why the niobium steel did not show the same effect as the titanium steel was due to the annealing temperature, 990°C in the niobium steel, compared with 800°C in the titanium steel. The higher annealing temperature increased the solid solubility of the interstitials (Figure 139) in the niobium steel compared

with the titanium steel and therefore no significant effect of niobium was observed.

Both chromium and molybdenum increased the yield stress, but the effect of molybdenum was much the greater. The solid solution hardening effect of chromium obtained in this investigation was almost identical to the one obtained by Bywater[178] (8.5 cf 8.2). The greater solid solution hardening effect of molybdenum than chromium on the yield stress was because of their relative effects on lattice dilation[146]. Because the atomic diameters of chromium and iron are similar there was very little lattice dilation and therefore only slight increases in the yield stress. However, because molybdenum has a much larger atomic diameter than that of iron the increased lattice dilation results in a marked increase in the yield stress. Although the solid solution hardening coefficients for chromium in Equations 86 and 87 and molybdenum in Equation 86 have been reported similar to those in low carbon steel[27], the effects may be more complex than first realized. The solid solution hardening coefficients for chromium and molybdenum in Equations 86 and 87 are significantly greater than those in low carbon steels[180] indicating an increased efficiency of strengthening due to the interaction with interstitial elements to form complex clusters.

2. Work Hardening rate at 0.1 True Strain

Work hardening at 0.1 true strain =

$$862 + 112.8 \times \%Mo + 29.5\ d^{-\frac{1}{2}} \text{ in } Mn/m^2 \text{ at a 95\% confidence level} \quad (90)$$

Correlation coefficient = + 0.45

The only significant compositional effect was that of molybdenum which increased the work hardening rate. The effects of solute on work hardening depends on the relative lattice dilation[146]. Because molybdenum increases

the relative lattice dilation, it retards dislocation movement and therefore increases the number of dislocations at a constant strain, which increases the number of dislocation interactions and therefore increases the work hardening rate.

Decreasing the ferrite grain size increased the work hardening rate. This can be attributed to the shorter slip distances in the ferrite in a fine grained steel which requires more dislocations to operate for any given strain, and therefore leads to an increased work hardening rate. The coefficient of $d^{-\frac{1}{2}}$ is similar to that obtained for the work hardening of low carbon low alloy steels[180].

9.6 THE EFFECT OF MICROSTRUCTURE, TEXTURE AND R VALUE ON FORMABILITY

9.6.1 Deep Drawability and $\bar{r}$ Value

A regression analysis (Equation 82) showed that the $\bar{r}$ value increased as the ratio of {111} : {100} increased which was in agreement with the work of Held[128]. Deep drawability as measured by the limiting drawing ratio (LDR) was dependent on the average $\bar{r}$ value and texture. Increasing the $\bar{r}$ value and the ratio of {111}:{100} components increased the limiting drawing ratio. (Equations 83 and 84) Variations in chromium and interstitial contents and additions of molybdenum, titanium and niobium had little effect apart from their effect on texture and $\bar{r}$ value. It can be seen from Figure 17 that during deep drawing the radial stress in the flange is lower than at the punch nose and that textures favouring high $\bar{r}$ values increase the deep drawability because they increase the flow stress at the punch nose, relative to the flange. Since deep drawability was not affected by composition, the ratio of stress at the punch nose to those at the flange were of prime importance during deep drawing and overshadowed any

effect due to changes in composition.

The limiting draw ratio increased with increasing reduction because the {111} : {100} texture ratio increased with increasing reduction. In the majority of cases, both Δr and percentage earing increased with increasing cold reduction. The reason for this was related to the textures observed in these steels. The {100} component, i.e. {100}<011> texture favours maximum r value at 45° to the rolling direction, producing 45° ears and a negative Δr value. The {111} component, i.e. {111}<112>, should produce six ears, but because of the considerable rotational spread about the ideal orientation tends to produce in practice only four ears. At low reduction, the {111} : {100} texture ratio is low and in the majority of alloys, the textures are not well defined, therefore the 0/90° earing tendency of the {111} component was counteracted by the 45° earing tendency of the {100} component resulting in small 0/90° ears. With increasing cold reduction, the {111} : {100} ratio increases resulting in increased Δr and percentage earing.

i. Alloy (1) 17% Cr Low (C+N)

r_{90} increased to a maximum after 50% cold reduction, and then decreased up to 75% reduction. This steel had a strong {110} <001> texture after 50% reduction and in the work of Hutchinson et al[109] there was evidence to suggest that high r_{90} values were obtained in steels with strong {110}<001> textures. Above 50% reduction the {110} component decreased and the r_{90} value decreased. In this steel, both the average $\bar{r}$ value and LDR were low because of an unfavourable {111} : {100} ratio.

ii. The Effect of Interstitial Content

In the 17% Cr high (C + N) steel,

in contrast to all the other alloys examined, the maximum r value was at r_{45} after 35% cold reduction, which resulted in a negative Δr and 45° earing. The $\bar{r}$ value and LDR were also much lower after 35% reduction at the higher interstitial level. The reason for this was the strong {100}<011> component at the higher interstitial level, which produced the maximum r value at 45° to the rolling direction and therefore 45° earing and a negative Δr value. Low $\bar{r}$ values and LDR's are also consistent with the presence of a strong {100}<011> component. With increasing cold reduction Δr became positive and the earing was at 0/90° to the rolling direction. After 75% cold reduction, the $\bar{r}$ value and LDR were not affected by interstitial content. This was because with increasing cold reduction the {100} component decreased and the {111} component increased with a result that Δr became positive and the earing was at 0/90° to the rolling direction. The $\bar{r}$ value and LDR increased because of an increase in the {111} : {100} ratio with increasing cold reduction.

iii. The Effect of Titanium and Niobium

Additions of titanium and niobium favoured the development of higher $\bar{r}$ values and LDR's than the base low interstitial steel because of a higher {111} : {100} texture ratio.

iv. 17% Cr High (C+N) Nb

In contrast to the higher interstitial level base steel, in the niobium steel, the higher r values were at r_{90} and r_0 and not r_{45},

with a result that Δr was positive and earing was at $0/90^{\circ}$ to the rolling direction. This was because of a weaker {100} component, i.e. higher {111} : {100} ratio, in the niobium steel. At the higher interstitial level, niobium additions did not produce such favourable $\bar{r}$ and LDR values because of lower {111} : {100} ratios at the higher interstitial level. In fact after 75% cold reduction, the LDR of the 17% Cr high (C+N) + Nb was much lower than could be explained on the basis of the $\bar{r}$ value and {111} : {100} ratio. Examination of the fracture surface (Figure 130) showed initiation of brittle failure at chromite and carbide particles which led to premature failure.

v. The Effect of Chromium Content

Increasing the chromium content increased both $\bar{r}$ value and LDR after 75% reduction because of higher {111} : {100} ratios. The high r_{90} value in this steel after 50% reduction may be due to the {110} component present in this steel.

vi. The Effect of Molybdenum

Additions of molybdenum increased both $\bar{r}$ value and LDR after 75% reduction because of higher {111} : {100} ratios.

9.6.2 The Effect of Cold Work and Composition on the Erichsen Value

The Erichsen value in general increased with increasing cold reduction, i.e. the maximum value was observed after 75% reduction. This was because of a finer recrystallised grain size with increasing cold reduction. The results for the uniform elongation however did not show any effect of ε_u

with decreasing grain size. Gladman et al[142] also showed that grain size had little effect on ε_u. Horte et al[148] and Wilson[176] reported that coarse grain sheet steels with high uniform elongations performed less well in biaxial stretching than was predicted from measurements of uniform elongations, ε_u. A finer grain size has been shown to increase the work hardening rate relative to a coarse grain size at a constant strain[142]. However, because the yield stress was also increased by a finer grain size, little effect of grain size on ε_u was observed. In stretch forming operations much higher strains are required for instability than in uniaxial tension. Therefore the increasing work hardening rate at finer grain sizes can more than compensate for the increased yield stress, and the higher work hardening rate produces a more uniform strain distribution across the punch. Also necking in stretch forming up to final failure is diffuse and not localised[147]. Finer grain sizes increase the total ductility, ε_t,[142] because of the increased work hardening which reduces the rate of propagation of the ductile crack. Because the necking is always diffuse in stretch forming, it does not restrict the stretching limit and total ductility may become important.

In contrast to the tensile results, higher Erichsen values were obtained at the higher interstitial level in both the base 17% Cr and 17% Cr 1% Mo steels when compared with their low interstitial counterparts. Only after 75% reduction were the Erichsen values comparable. This may be due to a grain size effect. The 17% Cr low (C+N) 1% Mo showed particularly low Erichsen values after 35% and 50% cold reduction which was not reflected by the tensile results. In the Erichsen tests cracks were initiated at bands of carbides (Figure 137) leading to a reduction in the ductility. However, in the uniaxial tensile work, no such cracks were observed at bands of carbides. Clearly microstructural inhomogenities were of greater importance in biaxial stretching than in uniaxial tension.

Additions of titanium and niobium at the lower interstitial level, tended to increase the Erichsen value when compared with the base steel, even though small regions of brittle fracture were observed in the niobium steel. This was because of a more uniform distribution of carbide/nitride particles, a reduction in grain boundary carbide and the absence of tempered martensite in the structure. Since the criteria for the onset of propagation of a ductile crack is a function of void width to near neighbour spacing[154], for a constant particle fraction, a more uniform distribution of particles results in a greater ductility before the onset of the ductile crack.

At the higher interstitial level, in the niobium steels, the Erichsen values were slightly lower even though they had similar uniform elongations. This was due to the formation of cracks (Figure 136) at exogeneous chromite particles which resulted in premature failure. These were not in evidence in the uniaxial tensile specimens.

The base 25% Cr steel had much lower Erichsen values than its 17% Cr counterpart, although very little difference was found between the two steels in terms of tensile elongation. Again bands of carbides were probably responsible for the reduction in the Erichsen values of the 25% Cr steel.

Unlike the deep drawability, a good correlation was not obtained between Erichsen values and uniaxial tensile data. The best correlation was between the minimum value of the tensile uniform elongation and the Erichsen value with a correlation coefficient of + 0.5. Although finer grain sizes in almost every case conferred adequate Erichsen values, a coarse grain size did not always produce poor results, e.g. titanium and niobium steels. This results in a poor correlation between grain size and Erichsen value, i.e. correlation coefficient 0.2. Clearly many variables are involved when determining good stretch formability which, unlike deep drawability, was

more dependent on the microstructure.

9.6.3 Factors Affecting Formability of Ferritic Stainless Steels

It was evident that high cold reductions before recrystallisation were beneficial in producing adequate formability in ferritic stainless steels, since they improved both deep drawability and stretch formability. Some of the improved stretch formability with fine grain sizes may be lost in these steels since they exhibit yield points. The finer the grain size, the larger the temper-rolling reduction required to suppress the formation of stretcher-strains, hence a greater potential loss in ductility. At 17% Cr, in the condition examined, no improvement in formability was obtained by decreasing the interstitial content, in fact at low cold reductions stretch formability was better at the higher interstitial content. Additions of titanium and niobium, at the lower interstitial level to a 17% Cr base steel, were beneficial in improving formability. They tended to aid the formation of a high $\frac{I(111)}{I(100)}$ ratio and produce a microstructure which gave good stretch formability for a ferritic stainless steel. It was shown by regression analysis that as the ratio of $\frac{I(111)}{I(100)}$ increased, the $\bar{r}$ value and the deep drawability increased. High $\bar{r}$ values increased the flow stress at the failure site (punch nose) relative to the drawing zone (the flange). Additions of niobium at the higher interstitial level were not particularly beneficial. At 17% Cr, molybdenum additions improved the deep drawability because molybdenum increased the $\frac{I(111)}{I(100)}$ texture ratio, but produced an inferior stretch formability at the lower interstitial level, because of the coarser grain size at the lower interstitial level. Increasing the chromium content from 17% - 25% improved the deep drawability because it increased the $\frac{I(111)}{I(100)}$ texture ratio, but stretch formability was inferior to the 17% Cr steel. Additions of molybdenum at 25% Cr improved the deep drawability but had little effect on the stretch formability.

CHAPTER TEN

10. SUMMARY, CONCLUSIONS, RELEVANCE TO INDUSTRY AND RECOMMENDATIONS

10.1 SUMMARY AND CONCLUSIONS

The following conclusions have been drawn :

Recovery and Recrystallisation

1. Increasing the interstitial content in the base 17% Cr steels appeared to increase the rate of recovery. However, electron microscopy showed that the softening effect was associated with recrystallisation in the prior martensite regions, and was not a true recovery process.

2. Increasing the chromium content had no overall effect on recovery rate.

3. In general, additions of molybdenum retarded recovery at both chromium and interstitial levels. This was because molybdenum-interstitial 'atmospheres' form at dislocations, rather than chromium-interstitial 'atmospheres', because molybdenum has a higher affinity for carbon and nitrogen than chromium. As the rate of recovery depends on the diffusion of the solute 'atmosphere' with the dislocation, the rate of recovery was slower in the molybdenum steel.

4. At the higher interstitial level, in the molybdenum steels, the rate and amount of recovery decreased due to an increased supersaturation effect of carbides and nitrides. In terms of a molybdenum-interstitial interaction, because of the increased supersaturation, the 'atmosphere' formed more rapidly and therefore the rate of recovery decreased at the higher interstitial level.

5. Additions of titanium increased the rate of recovery because titanium lowered the solubility of carbon and nitrogen, thus reducing the effectiveness of chromium-interstitial atmospheres at dislocations and increasing the rate of recovery.

6. Additions of niobium increased the rate of recovery at the lower interstitial level and decreased the rate of recovery at the higher interstitial level. This was because of different niobium-interstitial ratios in the two steels.

7. In the majority of these steels, a distinct plateau was observed at lower temperatures between recovery and recrystallisation. The extent of the plateau depended upon temperature, cold reduction and composition, and was associated with the pinning of subgrain boundaries by precipitating particles during recovery. The end of the plateau coincided with the incubation period for recrystallisation, which was interpreted in terms of the unpinning of subgrain boundaries leading to the formation of recrystallised grains. Therefore factors which decreased the rate of particle growth, i.e. additions of molybdenum and niobium, decreasing cold work or temperature, increased the extent of the plateau.

8. In contrast to expectations, increasing the chromium content from 17% - 25% had little effect on the rate of recrystallisation.

9. At 17% Cr increasing the interstitial content decreased the rate of recrystallisation due to the presence of a dispersion of undissolved $M_{23}C_6$ which pinned subgrain boundaries and retarded nucleation of recrystallisation. A higher activation energy for recrystallisation was observed at the higher interstitial level, because recrystallisation always took place in the presence of a dispersion of second phase particles.

10. Additions of molybdenum at both chromium levels in the lower interstitial content steels retarded recrystallisation. This was because of the slower diffusion rate of molybdenum which decreased the rate of subgrain growth. Additions of molybdenum increased the activation energy for recrystallisation.

11. At the higher interstitial level, in a 17% Cr steel, additions of molybdenum increased the incubation period for nucleation because of the slower diffusion rate of molybdenum. However, because of a higher stored energy in the molybdenum steel once recrystallisation started, the molybdenum steel recrystallised faster. In the molybdenum steels, a higher interstitial content favoured a faster recrystallisation rate at higher temperatures and a slower recrystallisation rate at lower temperatures, and thus increased the activation energy for recrystallisation.

12. Additions of titanium had little effect on recrystallisation kinetics.

13. Niobium markedly retarded recrystallisation at the lower interstitial level in the 17% Cr steels because of the slower diffusion rate of niobium.

14. At the higher interstitial level, additions of niobium increased the incubation period for nucleation of recrystallised grains, but once recrystallisation started, the niobium steel recrystallised faster than the base steel due to a higher stored energy. In the niobium steels, the higher interstitial content steel recrystallised faster than the lower interstitial steel because of a lower degree of recovery before recrystallisation.

Deformation Textures

15. At low reductions, the {111} component developed rapidly to give a strong {111}<112> texture after 35% reduction. This texture developed from the 'splitting' of the {110}<001> texture in the hot band. With increasing cold reduction, the {111}<112> was replaced first by the {111}<110> texture, and then by the more stable {112}<110> and {100}<011> textures.

Recrystallisation Textures

16. Increasing the degree of cold reduction increased the {111} component and decreased the {100} component. This was because within the major texture components, the stored energy of the {111}<uvw> component increased relative to other components, therefore its intensity increased after recrystallisation. Because of the low stored energy of the {100} component, it was consumed by the {111} component.

The {100} component, in some steels, increased at the expense of the {111} component above 90% cold reduction. This was because of the increase in the grain boundary area at high reductions which favoured nucleation of the {100} component.

17. In the 17% Cr low (C+N) steel, a strong {110}<001> texture was found after 35% and 50% reduction, which was because of deformation band nucleation. At the higher interstitial level in the base 17% Cr steels, a strong {100}<011> was favoured after 35% reduction because of grain boundary nucleation.

18. Additions of titanium and niobium at the lower interstitial level

tended to favour development of a {111}<112> texture at all reductions because nucleation of {111} oriented grainswas favoured at particle/ferrite interfaces.

19. Additions of molybdenum also favoured the development of a {111} <112> texture.

$\bar{r}$ Values and Formability

20. Good correlations were obtained between $\bar{r}$ values, LDR andthe ratio of the I(111) : I(100) texture and between LDR and $\bar{r}$ value. Both deep drawability and $\bar{r}$ value increased as the ratio of the I(111) / I(100) texture increased, indicating the beneficial effect of a strong {111} component.on deep drawability. The limiting drawing ratio was increased by increasing the degree of cold reduction by additions of titanium and niobium at the lower interstitial level and by additions of molybdenum because of their beneficial effects on the I(111) : I(100) texture ratio.

21. A good correlation was obtained between Δ r and the degree of earing, and ears were formed in the directions of maximum r value. The 17% Cr high (C+N) steel after 35% reduction showed 45° earing while the maximum r value was at 45° to the rolling direction. This was due to a strong {100}<011> texture in this steel. The other alloys showed varying degrees of 0/90° earing and maximum r values at 0 and 90° to the rolling direction.

22. The Erichsen value tended to increase with increasing cold reduction.

23. Additions of titanium and niobium at the lower interstitial level

in general improved the Erichsen value, because of their more uniform particle distribution.

24. Decreasing the interstitial content did not improve the Erichsen values in the base 17% Cr and 17% Cr molybdenum steels.

25. In the lower interstitial steels containing molybdenum and in the 25% Cr steels, low Erichsen values were obtained because of crack initiation at bands of carbides and non-metallic inclusions.

Mechanical Properties

26. Additions of molybdenum and chromium increased the yield stress because of their effects on lattice dilation. Titanium however decreased the yield stress because it removed interstitials from solid solution.

27. The work hardening rate was increased by refining the grain size and by additions of molybdenum.

10.2 RELEVANCE TO INDUSTRIAL APPLICATIONS

It is a widely held opinion that good corrosion resistance, weldability and adequate stretch formability can be obtained only by the use of low interstitial contents. However, processes to produce low interstitial contents in ferritic stainless steels are expensive, e.g. AOD or electron beam melting and refining. In the present investigation it has been shown that the formability was not improved by the use of low interstitial contents, i.e. both deep drawability and stretch formability were as good in the air melted 17% Cr steel as in vacuum melted low interstitial grade. Therefore, where adequate formability only is required, i.e. weldability and good corrosion

resistance are not of prime importance, there is no advantage in using expensive low interstitial content steel as the commercial air melted material performs adequately.

In applications where improved corrosion resistance and weldability is required, additions of molybdenum (up to 2%) or niobium (1%) to an air melted base 17% Cr steel may be an alternative and less expensive method of producing improved corrosion resistance and weldability when compared with the low interstitial content base steel. Certainly the results of the present investigation indicate that only slight losses in stretch formability are obtained by the additions of 1% molybdenum or 1% niobium to a base 17% Cr high (C+N) steel (i.e. Erichsen values of 12.4 mm for the base steel compared with 12.0 mm for Mo steel and 11.7 mm for the Nb steel) after 75% cold reduction.

The results for the niobium steel were fairly good considering the fact that numerous bands of chromite inclusions were present in this steel.

Additions of molybdenum improve the weldability to some extent, but not so well as niobium, as the perennial problem in welding ferritic stainless steels, martensite (austenite), is still present. After the addition of 1% molybdenum the martensite content was reduced from 30% to 20% in a high interstitial 17% Cr steel. The niobium steels examined did not contain martensite and had stable Nb(CN) particles that reduce grain growth in the heat affected zone during welding and hence should improve weldability.

10.3 RECOMMENDATIONS FOR FURTHER WORK

The major applications of these steels is in the production of consumable goods which require adequate formability, e.g. sinks, motor car trim etc.

Because these steels have a bcc ferritic structure, their stretch formability is relatively poor compared with austenitic stainless steels. However, it has been shown from the present work that deep drawability was considerably affected by the $\bar{r}$ value and texture. Therefore, the recommendations for further work are based on treatments which increased the (111):(100) texture ratio and increased the $\bar{r}$ value and LDR.

1. It is recommended that the specimens be annealed in the range 600°C - 700°C to utilise the possible beneficial effect of precipitation prior to recrystallisation on the formation of recrystallisation textures. During this reaction, in terms of the orientation dependence of nucleation, if nucleation of all components is retarded in equal proportions, then the time available for growth of the first formed grains is increased. Therefore, the recrystallisation texture will show increased selectivity towards the most favourably oriented nuclei, i.e. the {111} texture should increase relative to a precipitate free structure.

2. It is recommended to solution treat the low interstitial content 17% Cr and 25% Cr steels to increase the volume fraction of second phase particles precipitated prior to recrystallisation. The increased volume fraction of precipitates should lead to further strengthening of the {111} texture components at the expense of the {100} components (Fig 139)[84]. Examine the effects of the extra precipitation on the recovery and recrystallisation kinetics.

3. It is recommended to examine the effect of grain size in the hot band condition on the intensity of the {100} component in the recrystallised condition after different degrees of cold work. The present investigation indicated that fine hot band grain sizes tended to increase the intensity of the {100} component and decrease the intensity of the {111} component.

Therefore, by selecting heat treatments to give a range of hot band grain sizes, an inter-relationship between initial grain size and the {100} component may be established. Coarse grain sizes should increase the intensity of the {111} component compared with the {100} component after recrystallisation and should therefore be beneficial in producing steel with good deep drawability.

4. It is recommended to investigate the effect of a double cold rolling reduction with an interstage anneal, to investigate the effect of the initial texture on the final texture after different degrees of cold reduction in both the cold work and recrystallised condition. The present investigation indicated that the starting texture influenced the development of the deformation texture. Steels with {111} and {110} components in the hot band produced a stronger {111} component in the deformation texture, and therefore must increase the {111} component after recrystallisation. Therefore cold rolling and annealing cycles to produce different prior textures is of interest in producing steels with good deep drawability.

5. It is recommended to investigate the effect of grain growth following recrystallisation on texture development. Grain growth in mild steels and other steels tend to favour development of a strong {111} texture due to selective grain growth of this component.

6. It is recommended to examine the effects of treatments 1 - 5 on $\bar{r}$ values, tensile properties and formability.

REFERENCES

1. R N Wright; Welding Journal Research Supplement, Oct 1971

2. T C Dumond et al; IAMI, Jan 1974, P 25

3. K E Pinnow et al; Metals Eng Quarterly, Aug 1975, P 32

4. R Castro and R Tricot; Metal Treatment and Drop Forging, Oct 1964, p.401

5. K Bungardt, E Kunze and E Horn; Archiv Eisenh, 1958, 29(3), 193

6. B Pollard; Metals Technology, Jan 1974, P 31

7. J W Fielder et al; Private Communication

8. E Baerlecken et al; Stahl u Eisen, 81 1961, 768

9. K A Bywater; Private Communication

10. F Lieber et al; Thyssen Forshung, 1971, 3, 145

11. S W K Shaw and A G Quarrel; JISI, 1957, 185, 10

12. T Heczko, Berg-u-Luttern; ML 92 (1947), 125

13. R Smith; PhD Thesis, Sheffield University, 1959

14. R Lagneborg; Trans ASM, 1967, 60, 67

15. K J Irvine et al; JISI, 1960, 195, 386

16. K C Mills et al; JISI, 1961, 7, 9

17. J M Adamson; DPhil Thesis, Cambridge University, 1972

18. G Herbsleb; VGB - Speisewasserlagung, 1967, 64

19. K Bungardt et al; Archiv Eisenh 34 (1963) 465

20. H J Schuller; Archiv Eisenh 26 (1956) 513

21. Unpublished work by Climax Molybdenum; Reported by W Schmidt and O Jarleborg; Climax Molybdenum Publication, Ferritic Stainless Steels with 17% Cr

22. R O Williams and H W Paxton; JISI, March 1957, P 497

23. O Kubaschewski and T G Chart; J Inst Metals, 1964-65, 93, 329

24. M J Blackburn and J Nutting; JISI, July 1964, P 610

25. R O Williams; TAIME, August 1958, P 497

26. R M Fisher et al; TAIME, 1953, P 690

27. F B Pickering; Welded and Heat Resisting Steels, Conference Heat-Treatment Aspects of Metal Joining Processes, London, 1971, P 85

28. R A Hooper; Private Communication

29. W Carrington et al; Proc Royal Soc, 1960, Vol A 259, P 203

30. Hsun Hu; TAIME, 1964, Vol 230, P 572

31. R H Goodenow; Trans ASM, Vol 59, 1966, 804

32. I L Dillamore et al; Met Sci Journal, 1967, 1, 49

33. J L Walter and E F Koch; ACTA Met, 1963, 11, 923

34. Hsun Hu; Recovery and Recrystallisation of Metals, 1963 (Gordon and Breach) P 311

35. G Venturello et al; TAIME, Dec 1963, Vol 227, 143

36. C Antonione et al; TAIME, June 1964, Vol 230, 700

37. J T Michalax and H W Paxton; TAIME, 1961, Vol 221, 850

38. A S Keh; Direct Observations of Imperfection in Crystals, Interscience New York, 1962, P 213

39. C J Ball; JISI, 191, 232, 1959

40. D Kuhlmann; Z Physik, 124, 468, 1948

41. J E Dorn; TAIME, 1949, Vol 185, P 948

42. A Seeger; Phil Mag, 1958, Vol 2, 323

43. R J Borg and C E Birchenall; TAIME, 1960, Vol 218, P 980

44. J C Li; Recrystallisation, Grain Growth, and Textures, ASM Seminar, 1965, P 45

45. R W Cahn; Proc of the Physical Soc (London), A60 1950, 323

46. R W Cahn; J Inst Metals, 76 1949, 121

47. P A Beck; J Appl Phys, 20, 1948, 633

48. W C Leslie et al; TAIME, 221, 1961, P 691

49. W C Leslie et al; TAIME, 221, 1961, P 982

50. A H Cottrell; Progress in Metal Physics, 1953, Vol 4, P 205

51. J Glen; JISI, May 1957, Vol 186, P 21

52. J Burke and W Turnbull;Progress in Metal Physics, 1952, 3, 220

53. R W Cahn; Recrystallisation, Grain Growth and Textures, 1966, P 99

54. J E Bailey and P B Hirsch; Phil Mag, 1960, 5, 485

55. E Orowan; In Dislocations in Metals, AIME, New York, 1954, 181

56. S Horiuchi and I Gokyi; Textures in Research and Practice, Springer-Verlag, P 312

57. J C Li; Journal of Applied Physics, Vol 33, No 10, Oct 1962

58. C J E Smith and I L Dillamore; Met Science Journal, 1970, Vol 4, 161

59. Hsun Hu; Z Metallkunde, 1969, 60, 69

60. W Bollman; J Inst Metals, 1958-59, Vol 87, 439

61. M Hillert; ACTA Met, 1965, 13, 227

62. T Gladman; Proc Royal Soc, 1966, P 298, Vol 294

63. P Beck and P Sperry, J Appl Physics, 1950, 21, 150

64. W C Leslie et al; "Iron and Its Dilute Solid Solutions", P 119, 1961, New York (Amer Inst Mech Eng)

65. J E Bailey; Phil Mag, 8, Vol 5, P 833

66. J W Martin; Metallurgia, 1957, 55, 161

67. W T English and W A Backofen; TAIME, 230, 1964, 396

68. R D Doherty and J W Martin; J Inst Metals, 1962-63, Vol 91, P 332

69. P R Mould and P Cotterill; J Mat Sci, 2, 1967, P 241

70. T Gladman et al; JISI, May 1971, P 380

71. D Gawne and G T Higgins; Textures in Research and Practice (Springer-Verlag) P 319

72. W B Hutchinson; Metal Science, 1974, Vol 8, P 185

73. R H Goodenow and J F Held; Met Trans, 1970, 1, 2507

74. P R Mould and J M Gray; Met Trans, 1972, 3, 3121

75. W C Leslie et al; Trans Am Soc Metals, 1954, 46, 1470

76. B J Duggan; PhD Thesis, Univ Birmingham, 1972

77. W Gruhl and G Wasserman; Metall, 1954, 8, 20

78. D V Wilson; ACTA Met, 1957, 5, 293

79. I M Liftshiftz and J V Sloyov; J Phys Chem of Solids, 1961, 19, 35

80. C Wagner; Z Electrochem, 1961, 65, 581

81. D T Gawne and R C Hudd; Texture and Properties of Materials, The Metals Society, Cambridge, 1975

82. T George and J J Irani; BISRA Rep No Mg/C/32/68

83. U Koster; Metal Science, 1974, Vol 8, P 151

84. Y Meyzaud and P Parniere; Textures and Properties of Materials, 4th Int Conf on Texture, Cambridge, July 1975, The Metals Soc

85. K Lücke and K Detert; ACTA Met, 1957, Vol 5, 628

86. P Gordon and R Vandameer; TAIME, 224, 1962, 917

87. R Vandameer and P Gordon; TAIME, 215, 1959, 577

88. J W Cahn; ACTA Met, 10, 1962, 789

89. K Lücke and H P Stüwe; Recovery and Recrystallisation of Metals, 1963

90. K Lücke and H P Stüwe; ACTA Met, 1971, 19, 1087

91. J W Rutter and K Aust; TAIME, 1960, Vol 218, 682

92. K Aust and J W Rutter; TAIME, 1959, Vol 215, 820

93. K Aust and J W Rutter; TAIME, 1959, Vol 215, 119

94. C Zener; Reported by C S Smith; TAIME, 1949, 175, 15

95. J E Burke; TAIME, 1949, 180, 73

96. T Gladman and F B Pickering; JISI, 1967, 205, 653

97. H O Kircher; Met Trans, 1971, 2, 2861

98. H Hu and R S Cline; TAIME, 224, 784, 1962

99. I L Dillamore and W T Roberts; Met Reviews, 1965, 10, 271

100. R H Heyer et al; Flat Rolled Products, AIME, Met Soc, Conf 16, 1962, 29

101. J Hancock and W T Roberts; JISI, May 1967, 205 (5), P547

102. E A Calnan and C J B Clews; Phil Mag, 1951, 42, 616

103. I L Dillamore and W T Roberts; ACTA Met, 1964, 12, 281

104. G Sachs; Z Ver Eng, 1928, 72, 734

105. G I Taylor; J Inst Metals, 62, 1938, 307

106. I L Dillamore et al; Met Sci Journal, 1968, 2, 161

107. I L Dillamore and H Katoh; Met Sci Journal, 1974, 8, 21

108. H J Bunge; Kristall u Technik, 1970, 5, 145

109. W B Hutchinson et al; JISI, 1969, 1479

110. W B Hutchinson; PhD Thesis, Birmingham University, 1969

111. D Gawne and G T Higgins; JISI, July 1971, 562

112. C Dasarathy and R C Hudd; ACTA Met, Vol 15, Oct 1967, 1665

113. I L Dillamore and H Katoh; Met Sci Journal, 1974, 8, 73

114. I L Dillamore et al; Proc Royal Soc, 1972 (A), 329, 405

115. I L Dillamore and W B Hutchinson; Proc of the Int Conf on Sci and Tech of Iron and Steel, ISIJ, P 877

116. B J Duggan and W T Roberts; Metals Sci, 1975, Vol 9

117. A Dunn; PhD Thesis, University of Liverpool, 1968

118. H Hu; "Textures in Research and Practice", P 312, 1969, Berlin (Springer-Verlag)

119. I L Dillamore and H Katoh; Texture 1974, Vol 1, P 151

120. B G Liebmann et al; Z Metallkunde, 1956, 47, 57

121. G Ibe and K Lücke; "Preferential Growth During Recrystallisation in Single Crystals", Deutsche Gesellschaft Fur Metallkunde, London, 1964

122. I L Dillamore; TAIME, 1965, 233, 702

123. R D Butler; Sheet Metal Industries, 1964, 705

124. H Black and L W L'Herbier; Metal Prog, June 1962

125. M Atkinson and I Maclean;IDDRG, Coll, London, 1964

126. W T Lankford et al; Trans ASM, 1950, 42, 1197

127. R L Whitely and D E Wise; Flat Rolled Products III, P 47, Interscience Pub , New York, 1962

128. J F Held; "Mech Working and Steel Processing IV", AIME Conf, Vol (1966), P 3

129. I L Dillamore; BDDRG, SYMP, Birmingham, April 1972

130. W F Hosford and W A Backofen; "Fundamentals of Deformation Processing", P 259 (1964), Syracuse, NY, (Univ Press)

131. R Vieth and R L Whitely; IDDRG Col, London, 1964

132. N Fukuda; TISIJ, 8, 1968, 68

133. J C Wright; Sheet Metal Inds, May 1974, 263

134. R Hill; Proc Royal Soc, A, 193, 281

135. I L Dillamore; T Am Soc Metal, Vol 58, 1965, 150

136. D V Wilson and R D Butler; JIM, 1961-62, Vol 90, P 473

137. D V Wilson; JIM, 1966, Vol 94, P 84

138. M Atkinson and I Maclean; Sheet Metal Inds, 1965, 42, 190

139. I L Dillamore, W T Roberts and D V Wilson; ISI Spec Report, 117, P 37

140. W B Morrison; T Am Soc Metals, 1966, 59, 824

141. J H Woodhead; ISI Conf, 1971, P 230

142. T Gladman et al; JISI, 1970, P 172

143. F B Pickering; Towards Improved Ductility and Toughness, Japan, 1971, P 9

144. D J Dingley and D Maclean; ACTA Met, Vol 15, May 1967, P 885

145. R M S B Horta et al; JISI, 1971 March, P 169

146. T Gladman and F B Pickering; ISI Spec Report 81, 1963, 10

147. S P Keeler and W A Backofen; T Am Soc Metals, Vol 56, 1963, P 25

148. R M S B Horta et al; J Mech Sci, 1969, P 231

149. S P Keeler; Soc of Auto Eng, No 650535, 1965

150. G M Goodwin; Soc of Auto Eng. No 680093, 1968

151. J Gurland; ACTA Met, 1972, 20, 735

152. T B Lindley et al; ACTA Met, 1970, 18, 1127

153. B J Brindley; ACTA Met, 1970, 18, 325

154. T Gladman et al; ISI Spec Report, P 68

155. I G Palmer and G C Smith; Met Soc AIME Conf, 47, 1966

156. M F Ashby; Phil Mag, 1966, 14, 1157

157. P F Thomason; Met Sci Journal, 1971, 5, 64

158. F A McClintock; Trans ASME 1968, 90, 363

159. P F Thomason; JIM, 1968, 96, 360

160. J Gurland and J Plateau; Trans ASM, 1963, Vol 50, P 442

161. K A Bywater; Private Communication

162. R A Hooper et al; Sheet Metal Inds, Jan 1976, P 26

164. M Yantas, Reported by I L Dillamore, W T Roberts and D V Wilson; "Stainless Steels", 37-50 1969, London, the Iron and Steel Institute

165. K G Brickner and J A Berger; Sheet Metal Inds, Jan 1976, P 26

166. S G Schneider et al; Metals Eng Quarterly, Feb 1974, P 40

167. M C Chao; TASM, 1967, 60, 37

168. H Takechi et al; TRJIM, 1967, 8, 4, 233

169. A B Haberfield and M W Boyles; Sheet Metal Inds, July 1973, P 400

170. D Imbusch et al; Stahl U Eisen, 94 (1974), Nr 8, 11 April, P 343

172. J Woodthorpe and R Pearce; Sheet Metal Inds, 1969, 46, 1061

173. P Cotterill and P R Mould; Recrystallisation and Grain Growth in Metal, Surrey Univ Press

174. C H McMahon and M Cohen; Int Conf on Fract, Sendai Japan, 1965

175. B Edelson and W Baldwin; (Trans ASM) 1962, 55, 230

176. D V Wilson; ISI, Spec Report, P 28

177. M Semchyshen et al; Towards Improved Ductility and Toughness, Climax Molybdenum (1971), 239/253

178. K A Bywater; Private Communication

179. D Dulieu; Low Carbon Structural Steels for the Eighties, the Institution of Metallurgists, Spring Residential Course, 1977, Series 3, No 6, P 1 - 8

180. F B Pickering; The Optimisation of Microstructures and their Relationship to Mechanical Properties, Chicago, Oct 1977

TABLE I

ANALYSES OF STEELS USED

ALLOY No	ANALYSIS C	Si	Mn	Cr	N	OTHERS
1a	0.024	0.43	0.81	16.9	0.008	
1b	0.025	0.45	0.76	16.76	0.008	
1c	0.019	0.41	0.80	16.66	0.008	
2	0.063	0.41	0.93	17.32	0.037	
3	0.061	0.35	0.89	17.1	0.032	0.91 % Mo
4a	0.023	0.43	0.83	16.7	0.010	0.86% Mo
4b	0.023	0.43	0.83	16.78	0.0135	0.98% Mo
5a	0.022	0.40	0.82	16.82	0.018	0.14% Ti
5b	0.026	0.43	0.82	16.72	0.0084	0.16% Ti
6	0.063	0.42	0.71	17.1	0.047	0.91% Nb
7a	0.024	0.41	0.85	16.89	0.014	0.45% Nb
7b	0.019	0.45	0.86	16.94	0.015	0.043%Nb
8a	0.031	0.42	0.91	24.75	0.0135	
8b	0.023	0.46	0.85	24.45	0.0130	
8c						
9a	0.022	0.40	0.84	24.6	0.0135	0.96% Mo
9b	0.029	0.40	0.85	24.2	0.018	0.96% Mo

TABLE II

HARDNESS OF STEELS PRIOR TO COLD ROLLING

Alloy No	Hot Rolled	Hot Rolled and Annealed at 1000°C	Hot Rolled and Annealed at 1000°C and Softened at 750°C
1a	170	160	140
1b	173	161	140
1c	167	150	137
2	265	230	180
3	255	190	169
4a	175	164	152
4b	183	172	153
5a	175	142	135
5b	170	145	134
6	186	150	144
7a	188	148	139
7b	196	146	140
8a	196	183	162
8b	186	175	165
9a	208	197	176
9b	208	194	174

TABLE III

MICROHARDNESS VALUES 50 GMS

Alloy No	Area Measured	Micro HD Value 50 gms
1 As rolled Condition	Recrystallised areas	140
	Recovered areas	181
2	As Hot Rolled Ferrite	197
	Martensite	342
	Annealed 1000°C Ferrite	156
	Martensite	400
3	As Hot Rolled Ferrite	209
	Martensite	456
	Annealed 1000°C Ferrite	172
	Martensite	365

TABLE IV

MEASURED VOLUME FRACTION OF AUSTENITE (MARTENSITE) AFTER ANNEALING AT 1000°C

Alloy No	Percentage Austenite (Martensite) After Annealing at 1000°C
1 17% Cr Low (C+N)	4%
2 17% Cr High (C+N)	32%
3 17% Cr High (C+N) 1% Mo	20%
4 17% Cr Low (C+N) 1% Mo	1%

TABLE V

ACTIVATION ENERGIES

	ALLOY	DEGREE OF COLD WORK	ACTIVATION ENERGY Q K. JOULES/MOLE
1	17% Cr Low (C+N)	35%	321
		50%	297
		75%	268
2	17% Cr High (C+N)	75%	390
3	17% Cr High (C+N) 1% Mo	75%	462
4	17% Cr Low (C+N) 1% Mo	35%	389
		75%	355
5	17% Cr Low (C+N) + Ti	75%	238
6	17% Cr High (C+N) + Nb	75%	452
7	17% Cr Low (C+N) + Nb	75%	418
8	25% Cr Low (C+N)	35%	351
		75%	298
9	25% Cr Low (C+N) 1% Mo	35%	389
		75%	334

TABLE VI

TYPICAL MICROHARDNESS VALUES FOR MATRIX GRAINS WITH AND WITHOUT BANDS IN A 17% Cr Low (C+N) STEEL

	Microhardness 50 Grammes Load
Matrix Grains with Bands	360
Matrix Grains without Bands	240

TABLE VII

ANNEALING TREATMENTS

ALLOY NO	COMPOSITION	DEGREE OF COLD WORK	TREATMENT
1	17% Cr Low (C+N)	35% 50% 75%	20 Minutes at 800°C
2	17% Cr High (C+N)	35% 50% 75%	25 Minutes at 800°C
3	17% Cr High (C+N) 1%Mo	35% 50% 75%	40 Minutes at 850°C
4	17% Cr Low (C+N) 1%Mo	35% 50% 75%	40 Minutes at 850°C
5	17% Cr Low (C+N) +Ti	35% 50% 75%	20 Minutes at 800°C

ALLOY NO	COMPOSITION	DEGREE OF COLD WORK	TREATMENT
6	17% Cr Low(C+N)+Nb	35% 50% 75%	15 Minutes at 990°C
7	17% Cr High(C+N)+Nb	35% 50% 75%	10 Minutes at 990°C
8	25% Cr Low (C+N)	35% 50% 75%	20 Minutes at 800°C
9	25% Cr Low(C+N) 1%Mo	35% 50% 75%	15 Minutes at 850°C

TABLE VIII

ALLOY NO	COLD REDUCTION	r_0	r_{45}	r_{90}	$\bar{r}$	Δr	LDR	P_{hkl} of Planes Parallel to the Rolling Plane								
								110	200	211	310	222	321	411	420	332
1	75%	0.89	0.46	1.0	0.72	+0.48	2.2	0.5	0.9	1.01	0.62	2.47	0.5	1.19	0.7	1.04
	50%	0.73	0.53	1.62	0.85	+0.65	2.18	2.15	1.31	0.78	0.69	1.66	0.64	0.98	0.53	0.25
	35%	0.8	0.56	1.4	0.83	+0.54	2.18	1.44	1.31	0.86	1.22	0.83	0.85	0.88	0.69	0.91
2	75%	0.72	0.65	1.04	0.77	+0.23	2.22	0.69	1.09	0.99	0.36	3.11	0.27	1.29	0.48	0.7
	50%	0.79	0.6	0.86	0.71	+0.22	2.22	0.27	2.03	1.23	0.64	1.4	0.52	1.31	0.54	1.01
	35%	0.29	0.84	0.66	0.66	-0.37	2.12	0.33	2.72	1.25	0.34	1.21	0.47	0.73	0.14	1.77
3	75%	1.1	0.78	1.65	1.08	+0.6	2.28	0.6	0.70	0.09	0.57	3.64	0.48	0.69	0.54	1.0
	50%	0.88	0.72	1.17	0.87	+0.31	2.22	0.41	0.6	1.02	0.51	2.74	0.67	1.09	0.52	1.34
	35%	0.65	0.85	1.24	0.89	+0.095	2.20	0.50	0.73	1.09	0.77	1.84	1.08	1.03	0.48	1.48
4	75%	1.26	0.83	1.43	1.09	+0.52	2.28	0.41	0.39	0.09	0.43	3.79	0.46	0.66	0.86	1.31
	50%	0.87	0.71	1.18	0.86	+0.32	2.22	0.72	0.94	0.76	0.81	1.84	0.59	1.56	0.67	1.1
	35%	0.81	0.69	1.18	0.84	+0.31	2.18	0.86	1.3	1.23	1.44	1.02	0.8	1.32	0.25	0.83
5	75%	1.44	0.75	1.86	1.18	+0.9	2.38	0.22	0.49	0.94	0.7	3.5	0.6	0.81	0.36	1.39
	50%	1.37	0.81	1.66	1.16	+0.71	2.28	0.26	0.58	1.02	0.8	2.33	0.75	1.1	0.52	1.65
	35%	1.02	0.83	1.54	1.06	+0.45	2.24	0.36	0.7	1.0	0.61	2.17	1.01	0.77	0.6	1.75

ALLOY NO	COLD REDUCTION	r_o	r_{45}	r_{90}	$\bar{r}$	Δr	LDR	Phkl of Planes Parallel to the Rolling Plane								
								110	200	211	310	222	321	411	420	332
6	75%	1.04	0.55	1.15	0.82	+0.55	2.1	0.7	0.82	0.82	0.76	2.45	0.52	1.36	0.8	0.73
	50%	0.86	0.73	1.45	0.94	+0.43	2.24	0.97	0.72	0.92	0.93	2.41	1.03	0	1.05	1.07
	35%	0.87	0.9	1.35	1.01	+0.21	2.20	0.96	0.88	0.98	0.83	2.24	0.84	0	1.08	1.16
7	75%	1.4	0.75	1.89	1.2	+0.89	2.36	0.15	0.41	0.52	0.28	5.42	0.44	0	0.31	1.47
	50%	1.27	0.89	1.65	1.17	+0.57	2.28	0.44	0.67	0.71	0.6	3.3	0.87	0	0.82	1.57
	35%	1.095	0.71	1.47	1.0	+0.57	2.24	0.31	0.48	0.78	0.51	4.24	0.58	0	0.76	1.31
8	75%	1.11	0.82	1.40	1.03	+0.45	2.24	0.48	0.84	0.64	0.46	3.44	0.7	0.78	0.52	1.11
	50%	0.81	0.61	1.45	0.91	+0.52	2.14	1.1	0.76	0.94	0.67	1.36	0.87	1.30	1.0	0.94
	35%	0.78	0.64	1.28	0.84	+0.39	2.2	0.79	0.66	0.93	0.86	1.81	0.95	0.93	0.88	1.17
9	75%	1.26	0.95	1.61	1.19	+0.49	2.28	0.73	0.69	0.55	0.28	5.5	0.3	0.21	0.11	1.36
	50%	0.94	0.57	1.9	1.0	+0.85	2.22	0.73	0.69	0.96	0.67	2.2	0.69	1.19	0.72	1.13
	35%	0.74	0.64	1.14	0.79	+0.3	2.18	0.55	0.72	0.85	0.86	1.69	0.71	0.52	0.91	1.14

TABLE IX

ALLOY NO	DEGREE OF COLD REDUCTION	$\frac{I_{(111)}}{I_{(100)}}$	$\bar{r} = 0.36 \log \frac{I(111)}{I(100)} + 0.77$	$LDR = 0.13 \log \frac{I(111)}{I(100)} + 2.17$
1	35	0.61	0.69	2.14
17% Cr Low (C+N)	50	1.2	0.79	2.18
	75	2.7	0.92	2.22
	82	4.3	0.99	2.25
	90	6.8	1.08	2.27
	95	7.92	1.09	2.28
2	35	0.43	0.63	2.12
17% Cr High (C+N)	50	0.69	0.71	2.14
	75	2.7	0.92	2.22
	82	4.21	0.99	2.25
	90	4.94	1.01	2.27
	95	5.76	1.04	2.28
3	35	2.47	0.91	2.22
17% Cr High (C+N) 1% Mo	50	4.47	1.00	2.25

ALLOY NO	DEGREE OF COLD REDUCTION	$\frac{I_{(111)}}{I_{(100)}}$	$\bar{r} = 0.36 \log \frac{I(111)}{I(100)} + 0.77$	$LDR = 0.13 \log \frac{I(111)}{I(100)} + 2.17$
3	75	4.43	1.00	2.25
	82	8.07	1.09	2.28
	90	8.21	1.09	2.28
	95	4.09	0.99	2.25
4	35	0.79	0.73	2.15
17% Cr Low (C+N) 1% Mo	50	2.0	0.87	2.20
	75	5.21	1.02	2.26
	82	10.56	1.14	2.30
	90	12.11	1.15	2.31
	95	15.63	1.19	2.32
5	35	3.12	0.94	2.23
17% Cr Low (C+N) + Ti	50	4.06	0.98	2.24
	75	7.22	1.07	2.28
	82	8.9	1.11	2.29
	90	10.56	1.13	2.30
	95	13.00	1.17	2.31

ALLOY NO	DEGREE OF COLD REDUCTION	$\frac{I_{(111)}}{I_{(100)}}$	$\bar{r} = 0.36 \log \frac{I(111)}{I(100)} + 0.77$	$LDR = 0.13 \log \frac{I(111)}{I(100)} + 2.17$
6	35	2.5	0.91	2.22
17% Cr High (C+N) + Nb	50	3.37	0.95	2.23
	75	2.96	0.93	2.23
	82	3.55	0.96	2.24
	90	3.44	0.96	2.23
	95	3.37	0.95	2.23
7	35	8.73	1.1	2.29
17% Cr Low (C+N) + Nb	50	5.0	1.02	2.26
	75	13.04	1.17	2.31
	82	13.5	1.17	2.31
	90	13.44	1.17	2.31
	95	8.35	1.1	2.28
8	35	2.04	0.88	2.21
25% Cr Low (C+N)	50	1.79	0.86	2.20

ALLOY NO	DEGREE OF COLD REDUCTION	$\frac{I_{(111)}}{I_{(100)}}$	$\bar{r} = 0.36 \log \frac{I(111)}{I(100)} + 0.77$	$LDR = 0.13 \log \frac{I(111)}{I(100)} + 2.17$
8	75	4.1	0.99	2.24
	82	6.72	1.06	2.27
	90	10.0	1.13	2.30
	95	19.2	1.23	2.33
9	35	2.37	0.90	2.21
25% Cr Low (C+N) 1% Mo	50	3.17	0.95	2.23
	75	18.5	1.22	2.33
	82	12.6	1.16	2.31
	90	14.1	1.18	2.31
	95	15.13	1.19	2.32

TABLE X

COMPOSITION	COLD REDUCTION	TEST DIRECTION RELATIVE TO THE ROLLING DIRECTION	YIELD STRESS Mn/m^2	UNIFORM ELONGATION TRUE STRAIN	AVERAGE UNIFORM ELONGATION TRUE STRAIN	AVERAGE GRAIN DIA μM	PERCENTAGE SECOND PHASE PARTICLES
Alloy 1		0^o	312	0.191			
17%CrLow(C+N)	75%	45^o	331	0.182	0.18	18.3	0.85%
		90^o	329	0.167			
		0^o	243	0.199			
	50%	45^o	251	0.182	0.185	68.2	
		90^o	259	0.173			
							0.7%
		0^o	225	0.174			
	35%	45^o	254	0.157	0.168	107	
		90^o	228	0.174			
Alloy 2		0^o	261	0.173			
17%CrHigh(C+N)	75%	45^o	277	0.166	0.168	23.6	
		90^o	271	0.166			
							2%
		0^o	282	0.182			
	50%	45^o	297	0.166	0.164	23.3	
		90^o	296	0.144			

COMPOSITION	COLD REDUCTION	TEST DIRECTION RELATIVE TO THE ROLLING DIRECTION	YIELD STRESS Mn/m^2	UNIFORM ELONGATION TRUE STRAIN	AVERAGE UNIFORM ELONGATION TRUE STRAIN	AVERAGE GRAIN DIA. μM	PERCENTAGE SECOND PHASE PARTICLES
Alloy 2	35%	0°	300	0.144	0.144	25.4	2%
		45°	282	0.149			
		90°	288	0.144			
Alloy 3 17% CrHigh(C+N) 1%Mo	75%	0°	363	0.174	0.171	16.2	
		45°	378	0.166			
		90°	374	0.174			
	50%	0°	342	0.182	0.171	20.2	1.7%
		45°	345	0.157			
		90°	359	0.174			
	35%	0°	318	0.182	0.168	25.4	
		45°	336	0.165			
		90°	332	0.157			
Alloy 4 17%CrLow(C+N) 1%Mo	75%	0°	321	0.174	0.185	32.6	1%
		45°	341	0.174			
		90°	328	0.207			

COMPOSITION	COLD REDUCTION	TEST DIRECTION RELATIVE TO THE ROLLING DIRECTION	YIELD STRESS Mn/m^2	UNIFORM ELONGATION TRUE STRAIN	AVERAGE UNIFORM ELONGATION TRUE STRAIN	AVERAGE GRAIN DIA. μM	PERCENTAGE SECOND PHASE PARTICLES
Alloy 4	50%	0^o	282	0.191	0.168	82.5	1%
		45^o	309	0.174			
		90^o	291	0.14			
	35%	0^o	274	0.199	0.18	102	1%
		45^o	289	0.174			
		90^o	286	0.166			
Alloy 5 17%Cr Low (C+N) + Ti	75%	0^o	262	0.191	0.185	32.4	1.2%
		45^o	264	0.182			
		90^o	259	0.182			
	50%	0^o	214	0.211	0.186	71	1.22%
		45^o	231	0.165			
		90^o	216	0.182			
	35%	0^o	214	0.182	0.181	86.1	
		45^o	234	0.170			
		90^o	226	0.191			

COMPOSITION	COLD REDUCTION	TEST DIRECTION RELATIVE TO THE ROLLING DIRECTION	YIELD STRESS Mn/m^2	UNIFORM ELONGATION TRUE STRAIN	AVERAGE UNIFORM ELONGATION TRUE STRAIN	AVERAGE GRAIN DIA. μM	PERCENTAGE SECOND PHASE PARTICLES
Alloy 6							
17%CrHigh(C+N)+Nb	75%	0°	263	0.182			
		45°	280	0.191	0.188	46.2	
		90°	265	0.191			
	50%	0°	249	0.191			
		45°	258	0.174	0.185	58.2	1.8%
		90°	250	0.191			
	35%	0°	255	0.199			
		45°	259	0.173	0.185	57.6	
		90°	250	0.182			
Alloy 7							
17%CrLow(C+N)+Nb	75%	0°	258	0.199			
		45°	301	0.165	0.182	70.3	1.2%
		90°	280	0.182			
	50%	0°	225	0.199			
		45°	240	0.174	0.188	96	1.3%
		90°	232	0.191			

COMPOSITION	COLD REDUCTION	TEST DIRECTION RELATIVE TO THE ROLLING DIRECTION	YIELD STRESS Mn/m^2	UNIFORM ELONGATION TRUE STRAIN	AVERAGE UNIFORM ELONGATION TRUE STRAIN	AVERAGE GRAIN DIA. μM	PERCENTAGE SECOND PHASE PARTICLES
Alloy 7	35%	0^o	219	0.218	0.197	121.5	1.3%
		45^o	225	0.182			
		90^o	220	0.191			
Alloy 8 25%CrLow(C+N)	75%	0^o	329	0,174	0.174	32.3	1.1%
		45^o	345	0.174			
		90^o	339	0.174			
	50%	0^o	319	0.182	0.171	40.5	1.3%
		45^o	337	0.166			
		90^o	331	0.166			
	35%	0^o	299	0.182	0.171	74.5	1.2%
		45^o	307	0.166			
		90^o	317	0.166			
Alloy 9 25%Cr Low (C+N) 1%Mo	75%	0^o	383	0.182	0.171	39.5	1.3%
		45^o	401	0.166			
		90^o	380	0.174			

COMPOSITION	COLD REDUCTION	TEST DIRECTION RELATIVE TO THE ROLLING DIRECTION	YIELD STRESS Mn/m^2	UNIFORM ELONGATION TRUE STRAIN	AVERAGE UNIFORM ELONGATION TRUE STRAIN	AVERAGE GRAIN DIA. μM	PERCENTAGE SECOND PHASE PARTICLES
Alloy 9	50%	0^{o}	365	0.174	0.171	53.3	1.4%
		45^{o}	386	0.157			
		90^{o}	360	0.182			
	35%	0^{o}	356	0.174	0.166	78.6	
		45^{o}	367	0.157			
		90^{o}	361	0.166			

TABLE XI

COMPOSITION	COLD REDUCTION	ERICHSEN VALUE MMS	GRAIN SIZE μM	DEGREE OF ORANGE PEEL	MIN. UNIFORM ELONGATION TRUE STRAIN
Alloy 1 17% Cr Low (C+N)	75% 50% 35%	12.3 10.9 10.5	18.3 68.2 107	No orange peel Heavy orange peel	0.167 0.173 0.157
Alloy 2 17% Cr High (C+N)	75% 50% 35%	12.4 12.3 11.25	23.6 23.3 25.1	Very slight orange peel	0.166 0.144 0.144
Alloy 3 17% Cr High (C+N) 1%Mo	75% 50% 35%	12.0 11.2 11.8	16.2 20.2 25.4	Very slight orange peel	0.166 0.157 0.157
Alloy 4 17% Cr Low (C+N) 1%Mo	75% 50% 35%	11.6 9.5 10.1	32.6 82.5 102.4	Slight orange peel Heavy orange peel	0.174 0.14 0.166
Alloy 5 17% Cr Low (C+N) + Ti	75%	12.2	32.4	Slight orange peel	0.182

COMPOSITION	COLD REDUCTION	ERICHSEN VALUE MMS	GRAIN SIZE μ M	DEGREE OF ORANGE PEEL	MIN.UNIFORM ELONGATION TRUE STRAIN
Alloy 5	50%	12.1	71	Orange peel	0.165
17% Cr Low (C+N)+Ti	35%	12.1	86.1	Heavy orange peel	0.170
Alloy 6	75%	11.7	46.2		0.182
17% Cr High (C+N)+Nb	50%	11.4	58.2	Orange peel	0.174
	35%	10.4	57.6		0.173
Alloy 7	75%	12.2	70.3		0.165
17% Cr Low (C+N)+Nb	50%	11.5	96.0	Heavy orange peel	0.174
	35%	12.2	121.5		0.182
Alloy 8	75%	10.2	32.2	Slight orange peel	0.174
25% Cr Low (C+N)	50%	9.7	40.5	Orange peel	0.166
	35%	10.2	74.5	Heavy orange peel	0.166
Alloy 9	75%	10.5	39.5	Orange peel	0.166
25% Cr Low (C+N) 1% Mo	50%	10.3	53.3	Heavy orange peel	0.157
	35%	10.4	78.6		0.157

Fig (1)

The iron-chromium equilibrium diagram

Fig (2)

A vertical section of the iron-chromium-carbon ternary diagram at 0.05%C

Fig (3)

Variation of austenite-ferrite equilibrium with temperature and composition as determined by Castro and Tricot (4)

Fig (4)

Carbide constitution diagram for iron-carbon-chromium alloys at 700°C

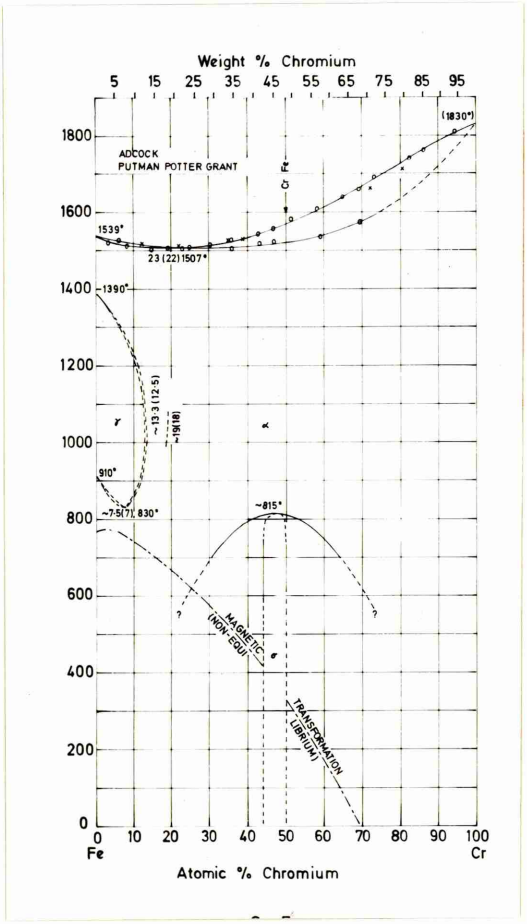

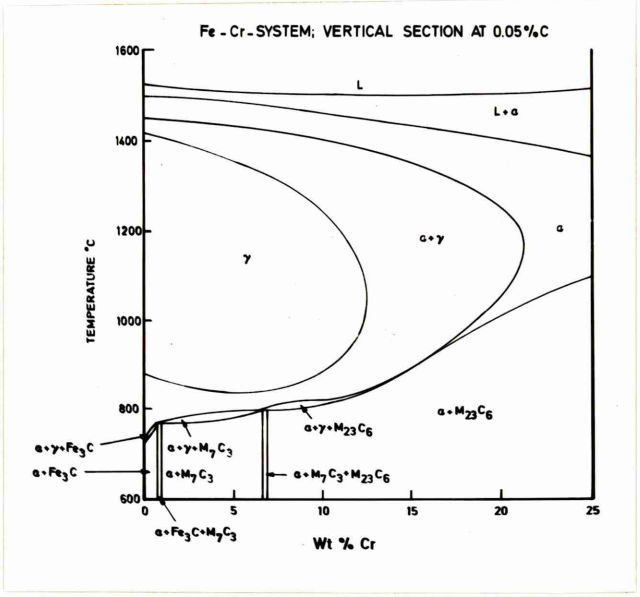

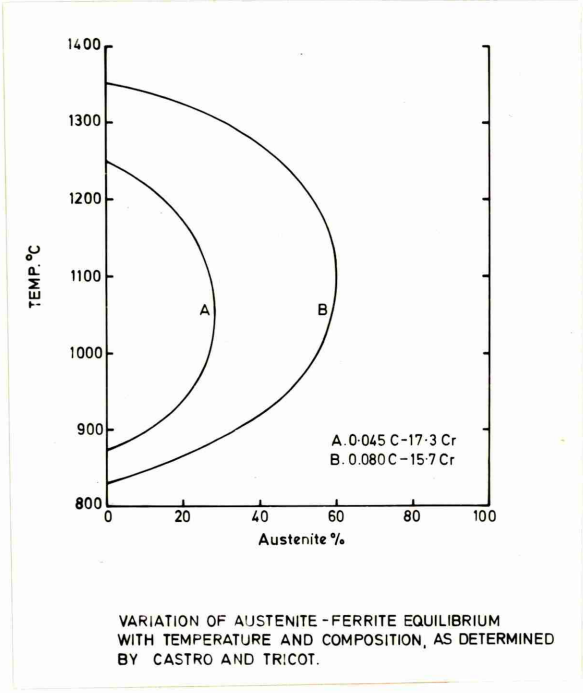

VARIATION OF AUSTENITE - FERRITE EQUILIBRIUM WITH TEMPERATURE AND COMPOSITION, AS DETERMINED BY CASTRO AND TRICOT.

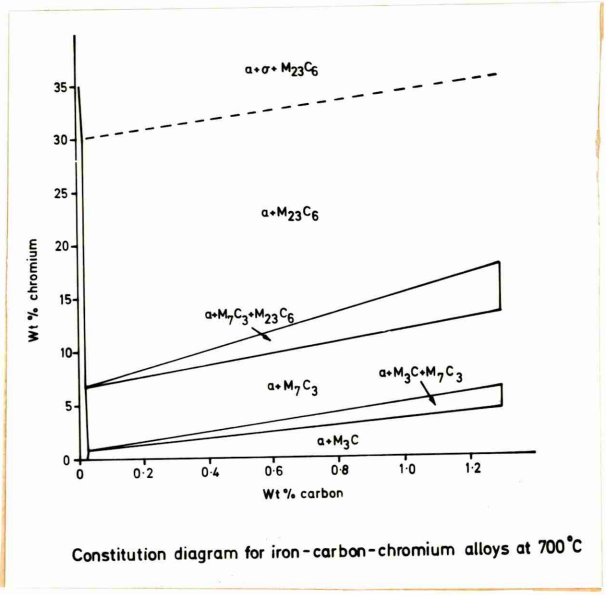

Constitution diagram for iron - carbon - chromium alloys at 700°C

Fig (5)

Carbide constitution diagram at 700°C in 0.2%C steels

Fig (6)

Low temperature phase diagram of the iron-chromium system Williams (25)

Fig (7)

Schematic representation of grain-boundary bulging Bailey (65)

Fig (8)

Schematic 'C' curve for the effect of temperature on the incubation period for precipitation t_p

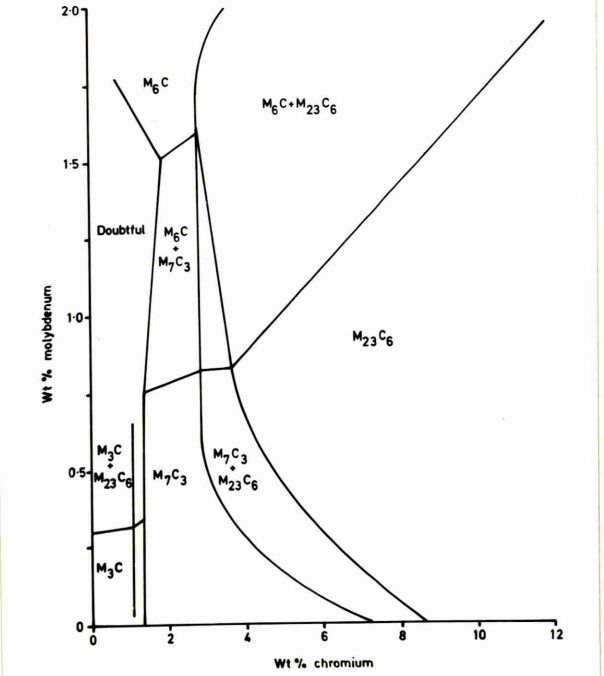

Carbide constitution at 700°C in 0·2% C steels

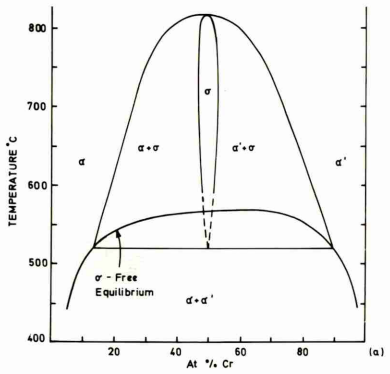

LOW-TEMPERATURE PHASE DIAGRAM OF THE Fe-Cr SYSTEM, AFTER WILLIAMS

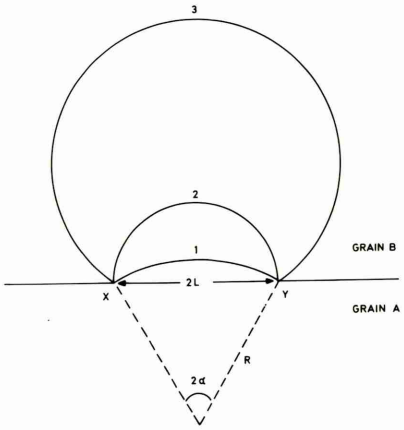

SCHEMATIC REPRESENTATION OF GRAIN-BOUNDARY BULGING. BAILEY.

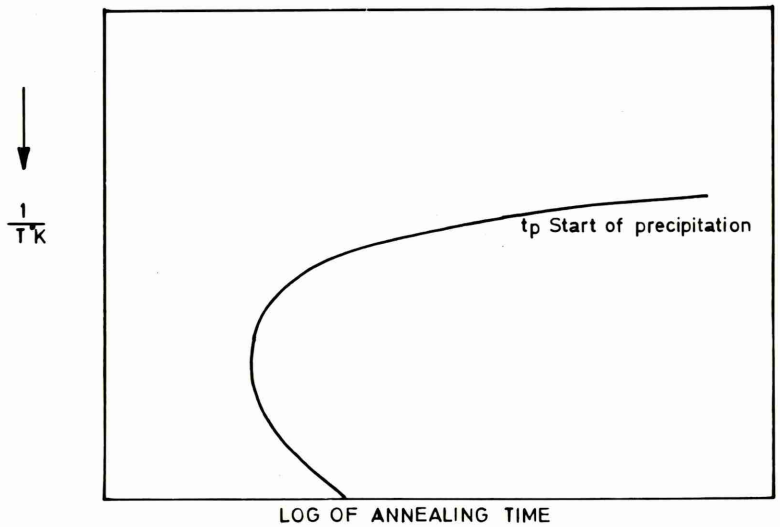

Fig (9)

Schematic representation of the relationship between the incubation period for precipitation t_p and recrystallisation t_r as a function of annealing temperature

Fig (11)

Schematic representation of a transition band

Fig (10)

Taylor factors (M) and rotation rates during rolling $\frac{d\phi}{d\epsilon}$

Fig (12)

A plot of D_r against θ_t

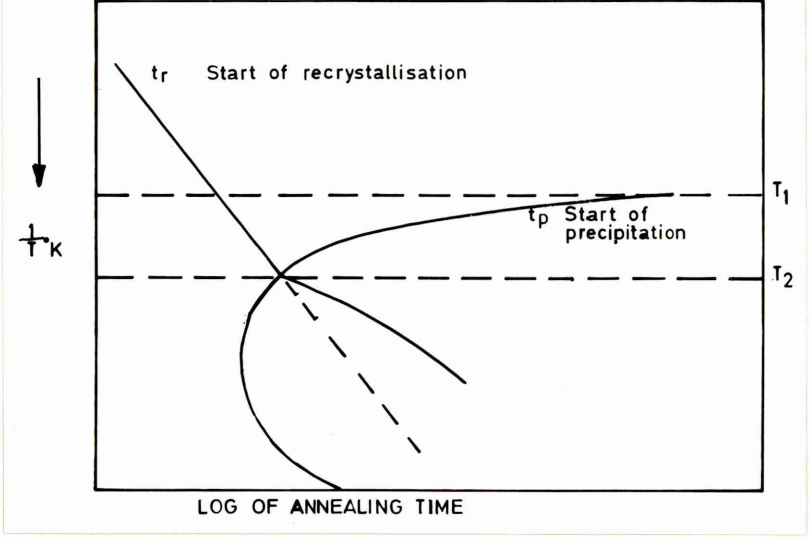

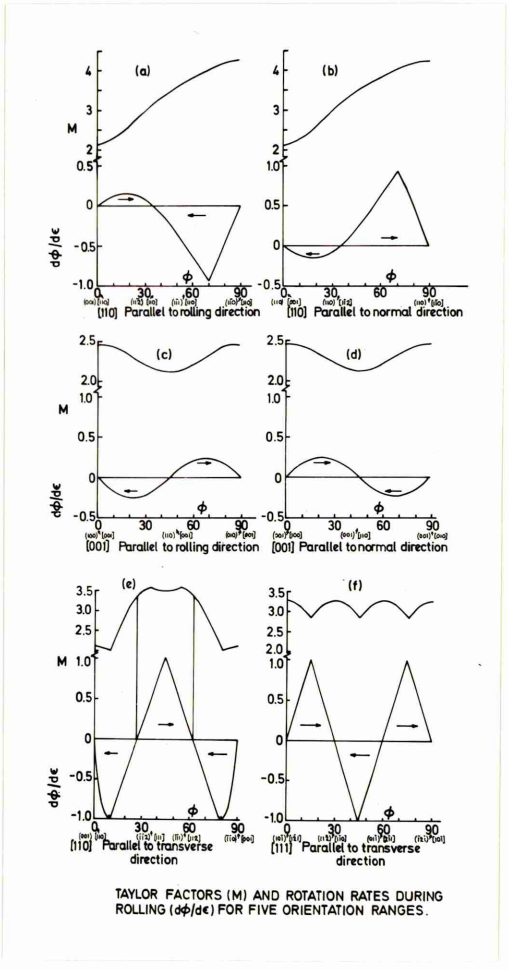

TAYLOR FACTORS (M) AND ROTATION RATES DURING ROLLING ($d\phi/d\epsilon$) FOR FIVE ORIENTATION RANGES.

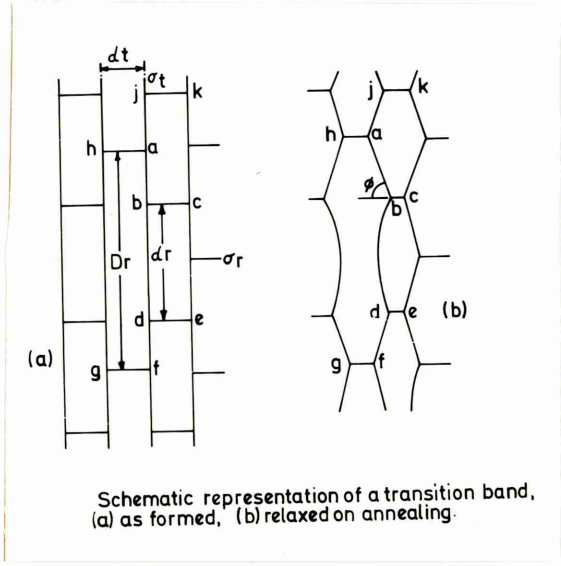

Schematic representation of a transition band, (a) as formed, (b) relaxed on annealing.

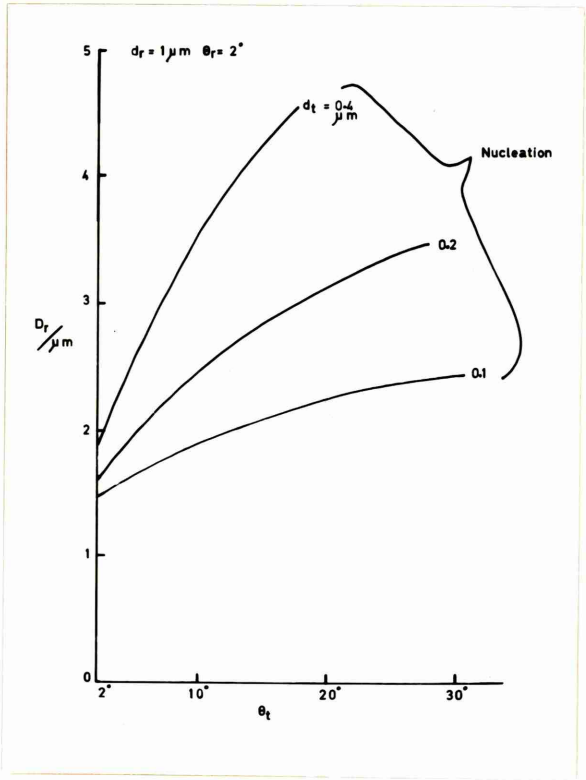

Fig (13)

$\bar{r}$ value - texture relationship calculated from homogeneous plasticity theory for various proportions of (111):(100) texture ratio. Full line shows the experimental $\bar{r} - \frac{I(111)}{I(100)}$ relationship of Held[128]

Fig (14)

Plots of r value versus texture based on the single crystal work of Vieth and Whitely[131] for different test directions relative to the rolling and transverse directions in the sheet

Fig (15)

A unit triangle showing the effect of texture on r value for single crystals

Fig (16)

Plane stress yield locus for an isotropic material

Fig (17)

Plane stress yield locus for an anisotropic material

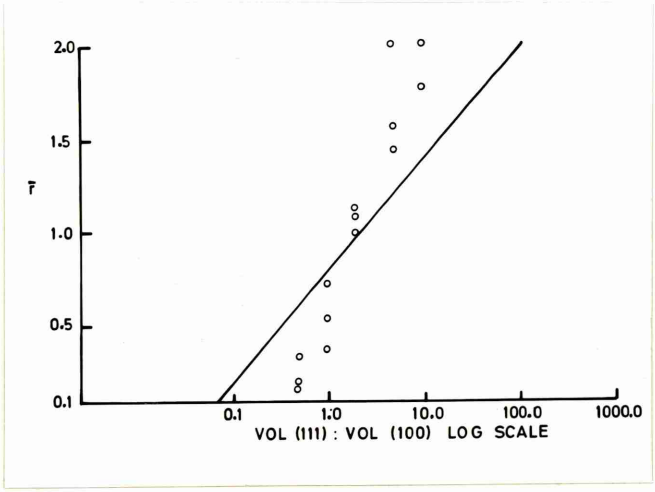
2.0
1.5
1.0
0.5
0.1
r̄
0.1
1.0
10.0
100.0
1000.0
VOL (111) : VOL (100) LOG SCALE

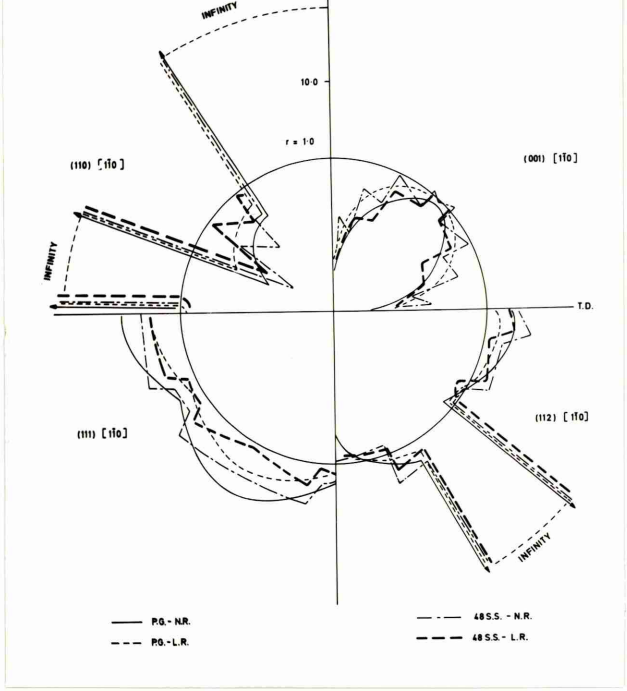
INFINITY
10·0
r = 1·0
(110) [1̄10]
(001) [1̄10]
INFINITY
T.D.
(111) [1̄10]
(112) [1̄10]
INFINITY
P.Q.- N.R.
P.Q.- L.R.
48 S.S. - N.R.
48 S.S. - L.R.

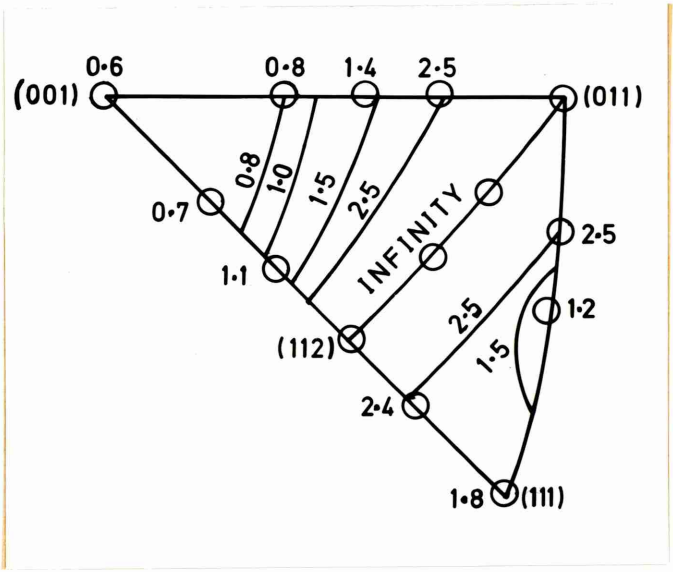
0·6
0·8
1·4
2·5
(001)
(011)
0·8
1·0
1·5
2·5
INFINITY
0·7
2·5
1·1
1·2
2·5
1·5
(112)
2·4
1·8
(111)

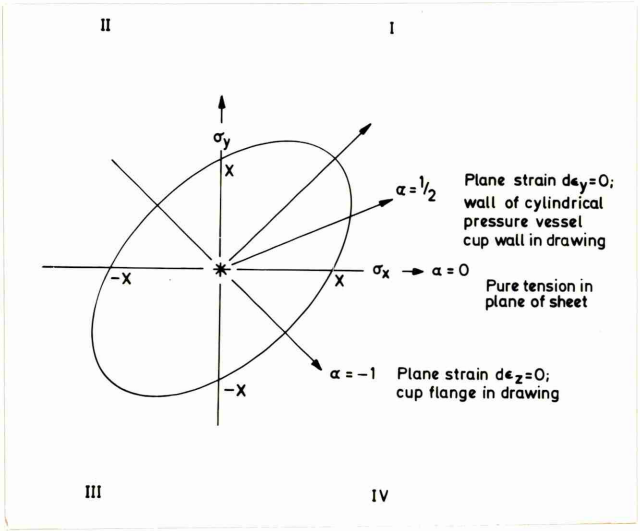
II
I
σy
X
α = 1/2
Plane strain dεy=0;
wall of cylindrical
pressure vessel
cup wall in drawing
−X
X
σx
α = 0
Pure tension in
plane of sheet
α = −1
Plane strain dεz=0;
cup flange in drawing
−X
III
IV

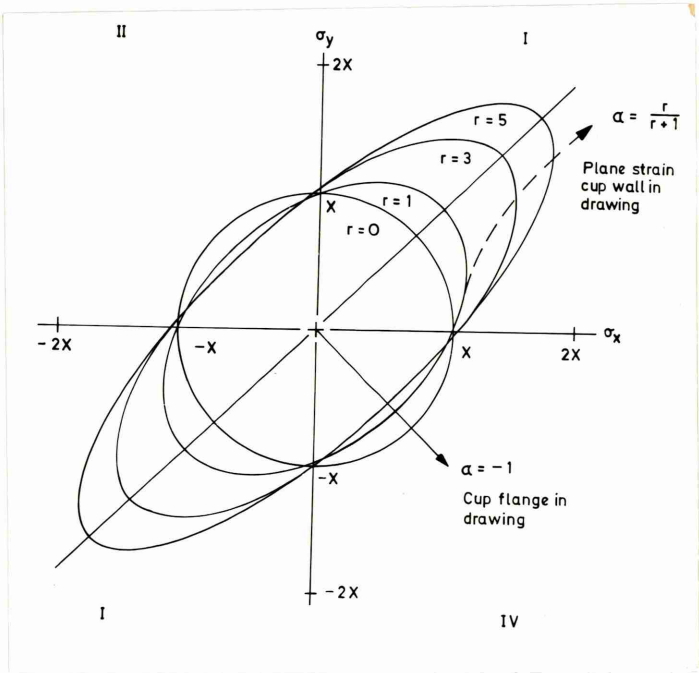
II
σy
I
2X
r = 5
α = r/(r+1)
r = 3
Plane strain
cup wall in
drawing
r = 1
X
r = 0
−2X
−X
X
2X
σx
α = −1
Cup flange in
drawing
−X
−2X
I
IV

Fig (18)

The effect of stress ratio X on the conditions for the onset of diffuse and localised necking

Fig (19)

The effect of $\bar{r}$ value on the conditions for the onset of localised necking

Fig (20)

A schematic forming limit diagram

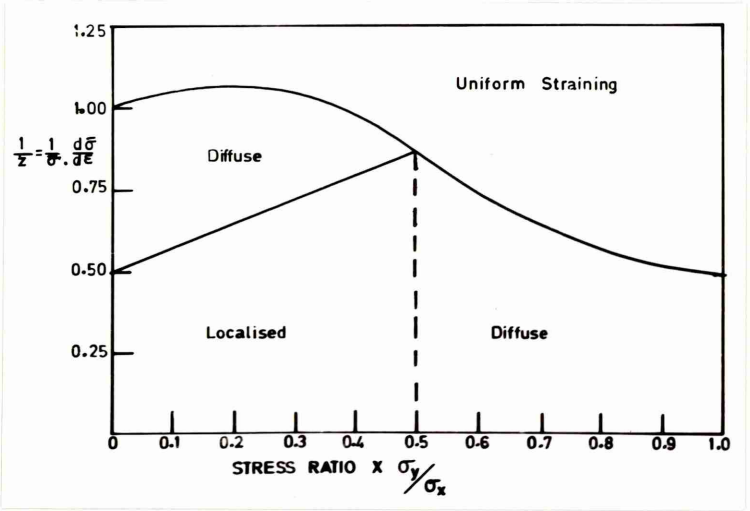
1.25
1.00
0.75
0.50
0.25
Uniform Straining
Diffuse
Localised
Diffuse
0
0.1
0.2
0.3
0.4
0.5
0.6
0.7
0.8
0.9
1.0
STRESS RATIO X σy/σx

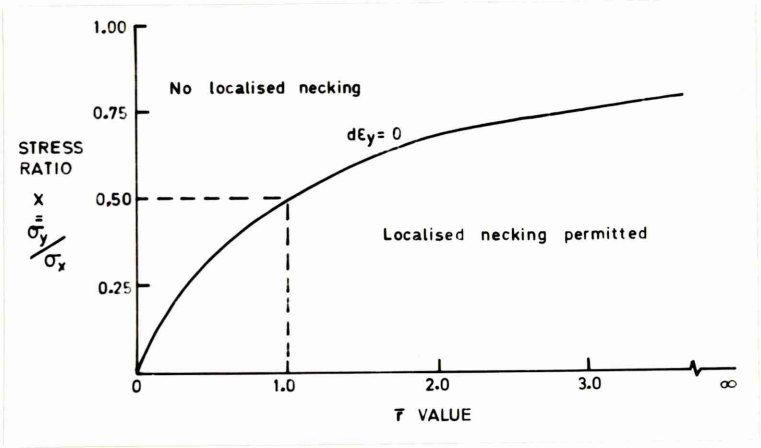
1.00
0.75
0,50
0.25
No localised necking
dεy= 0
Localised necking permitted
STRESS RATIO X = σy/σx
0
1.0
2.0
3.0
∞
r̄ VALUE

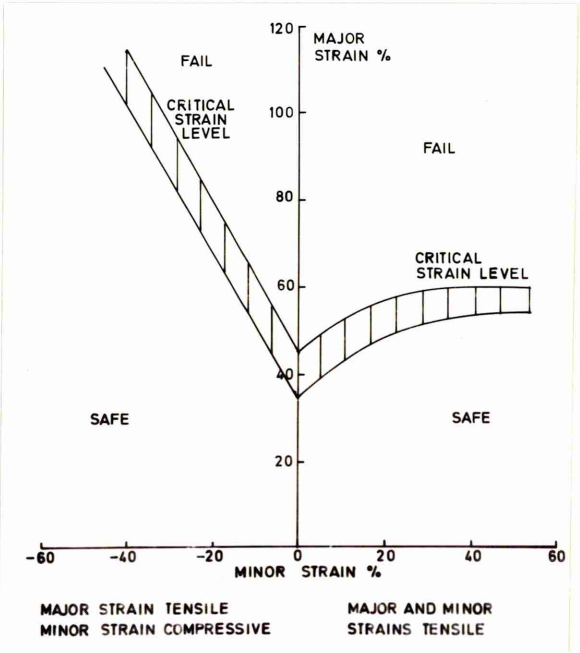
120
100
80
60
40
20
MAJOR STRAIN %
FAIL
CRITICAL STRAIN LEVEL
FAIL
CRITICAL STRAIN LEVEL
SAFE
SAFE
-60
-40
-20
0
20
40
60
MINOR STRAIN %
MAJOR STRAIN TENSILE
MINOR STRAIN COMPRESSIVE
MAJOR AND MINOR
STRAINS TENSILE

Fig (21)

X ray diffraction traces for
powder and textured specimens

(1) Powder specimen

(2) Textured specimen after
95% cold reduction

Fig (22a)

Dimensions of the tensile
specimens used in this investigation

Fig (22b)

Sheared edge on tensile and cupping
test specimens after annealing

Magnification X 400

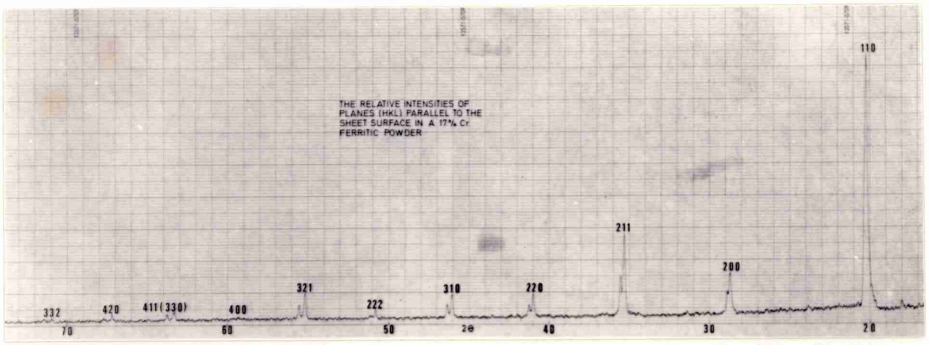
THE RELATIVE INTENSITIES OF PLANES (HKL) PARALLEL TO THE SHEET SURFACE IN A 17% Cr FERRITIC POWDER
110
211
200
321
310
220
332
420
411(330)
400
222
70
60
50
2θ
40
30
20

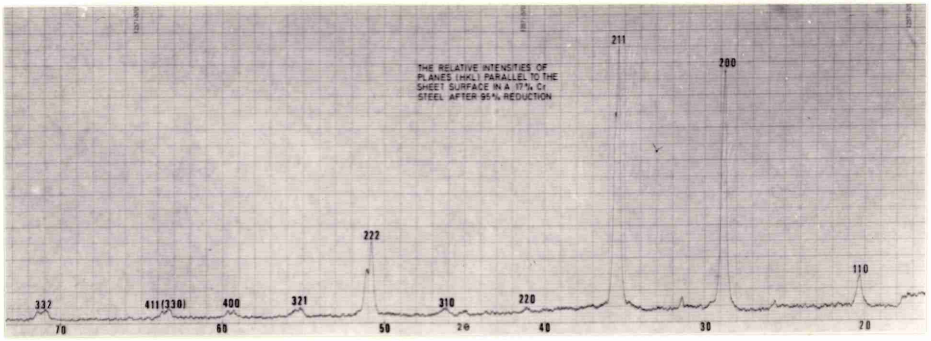
THE RELATIVE INTENSITIES OF PLANES (HKL) PARALLEL TO THE SHEET SURFACE IN A 17% Cr STEEL AFTER 95% REDUCTION
211
200
222
110
332
411(330)
400
321
310
220
70
60
50
2θ
40
30
20

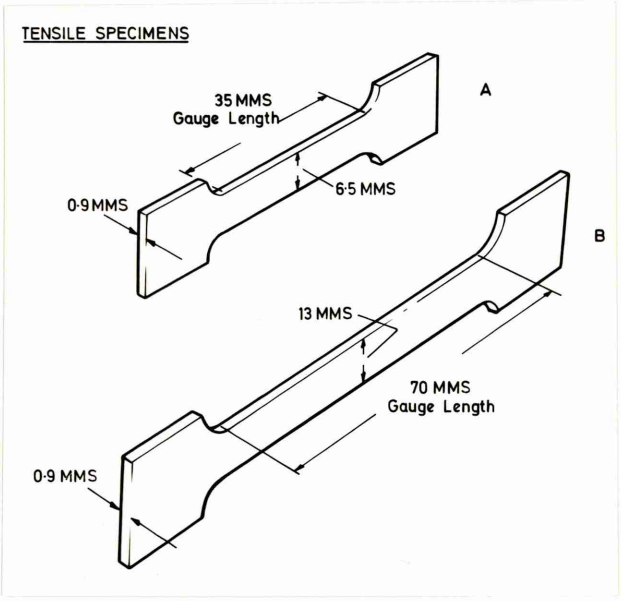
TENSILE SPECIMENS
35 MMS
Gauge Length
A
6·5 MMS
0·9 MMS
B
13 MMS
70 MMS
Gauge Length
0·9 MMS

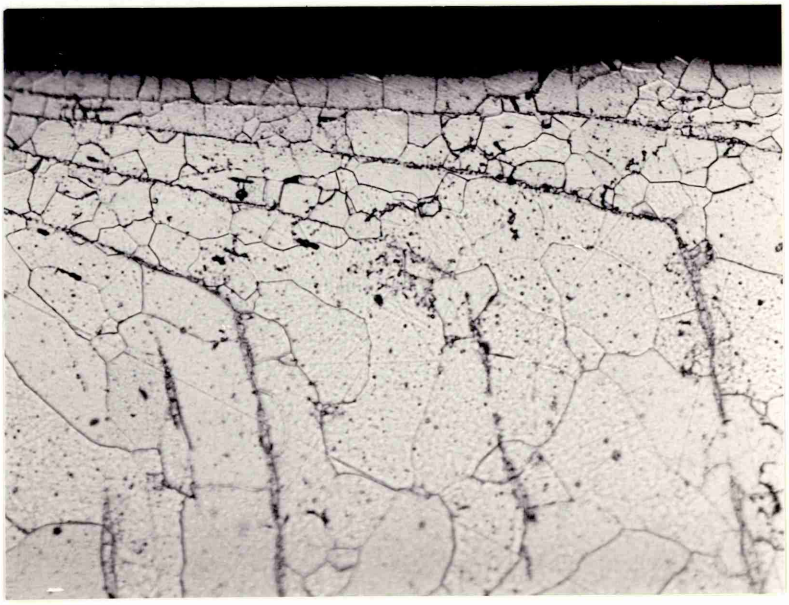

Fig (23a)

Optical Micrograph 17%Cr low(C+N) steel in the hot rolled condition

Magnification X 400

Fig (23b)

Optical Micrograph 17%Cr low(C+N) steel after hot rolling and annealing at 1000^{o}C for half an hour

Magnification X 160

Fig (23c)

Transmission electron micrograph, (replica), 17%Cr low(C+N) steel after hot rolling annealing at 1000^{o}C for half an hour and softening at 750^{o}C for half an hour

Magnification X 5000

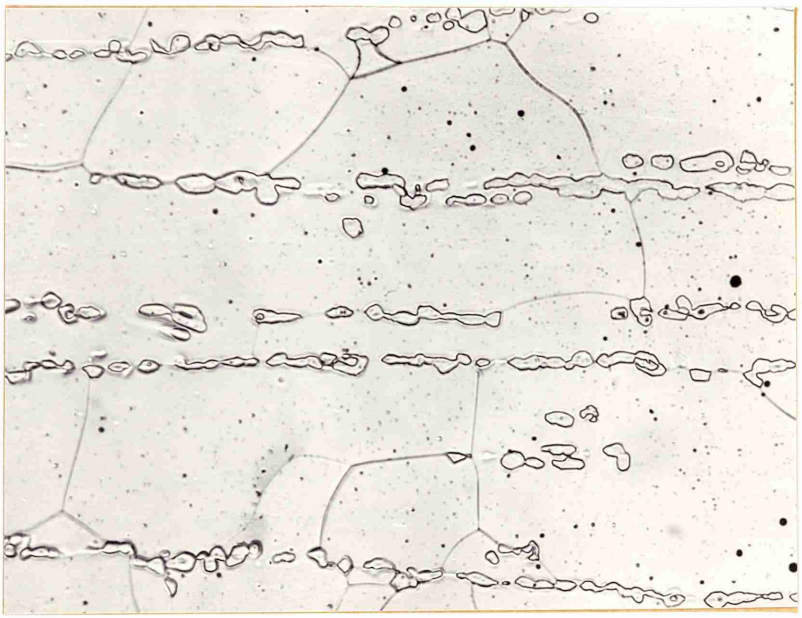

Fig (23d)

Transmission electronmicrograph, (Thin foil), 17%Cr low(C+N) steel in the same condition as Fig (23c)

Magnification X 12,000

Fig (24a)

Optical micrograph, 17%Cr high(C+N) steel, in the hot rolled condition

Magnification X 160

Fig (24b)

Transmission electronmicrograph, (Thin foil), 17%Cr high(C+N) in the hot rolled condition

Magnification X 12,000

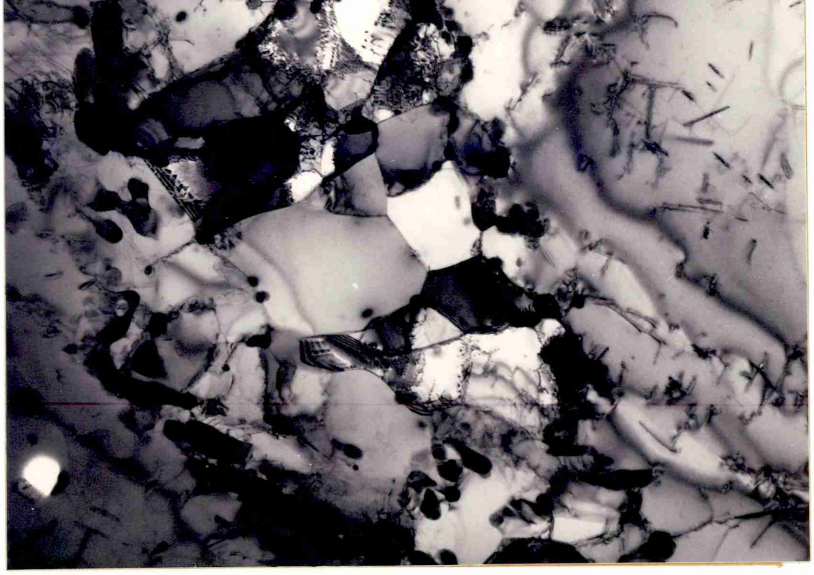

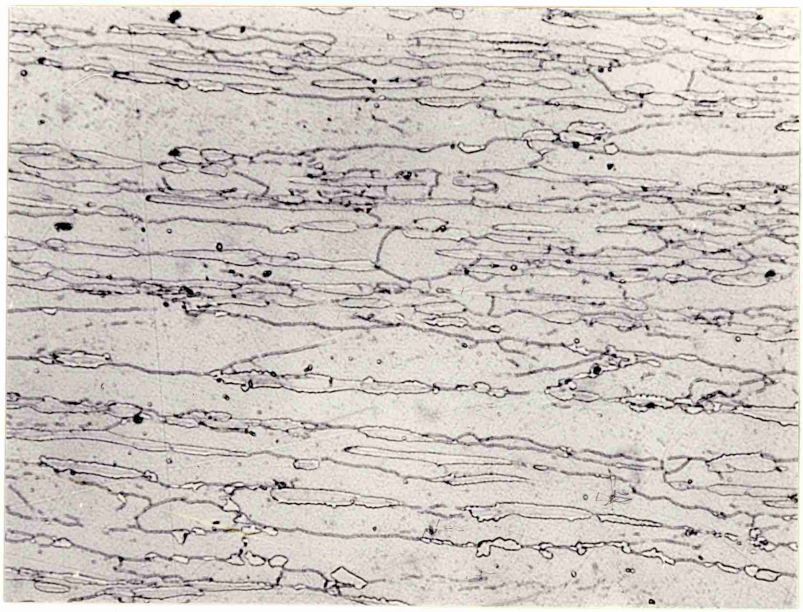

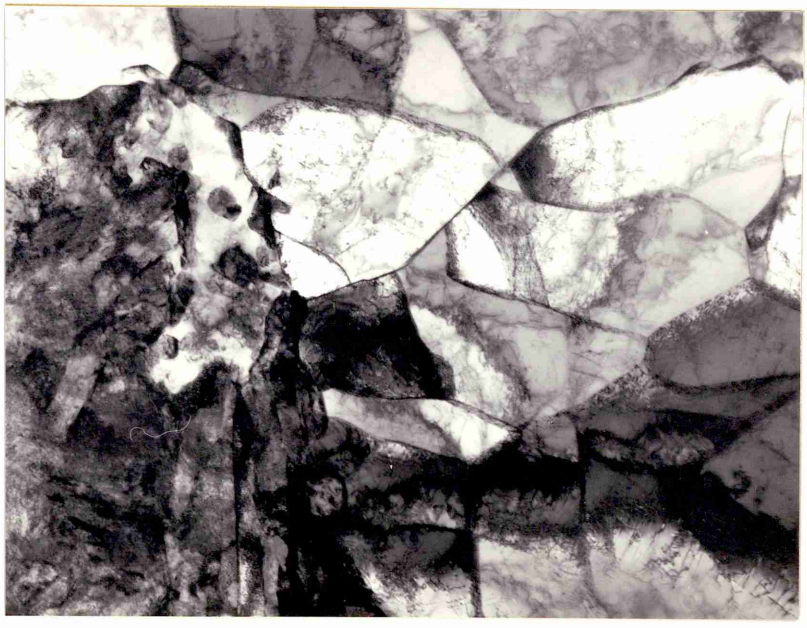

Fig (24c)

Optical micrograph, 17%Cr high(C+N) steel after hot rolling and annealing for half an hour at 1,000°C

Magnification X 160

Fig (24d)

Transmission electronmicrograph, (Thin foil), 17%Cr high(C+N) steel in the same condition as Fig (23c)

Magnification X 25,000

Fig (24e)

Transmission electronmicrograph, (Thin foil), 17%Cr high(C+N) steel after hot rolling annealing at 1,000°C for half an hour and softening at 750°C for half an hour

Magnification X 20,000

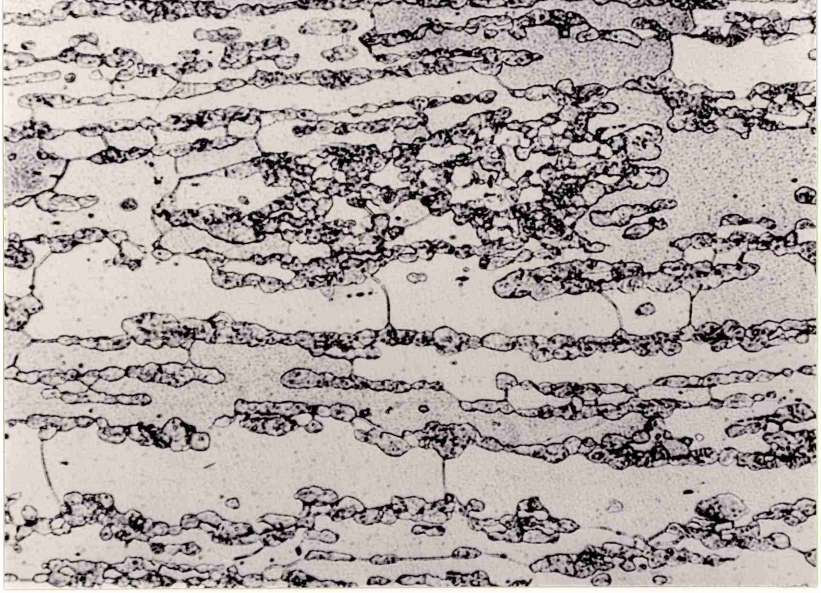

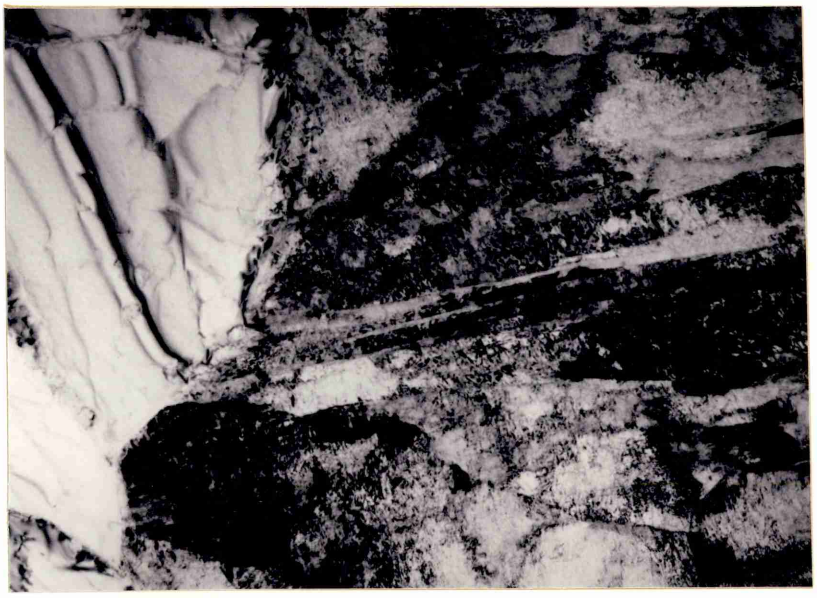

Fig (25a)

Optical micrograph, 17%Cr low(C+N) 1%Mo steel after hot rolling and annealing at 1000°C for half an hour

Magnification X 160

Fig (25b)

Transmission electronmicrograph, (thin foil), 17%Cr low(C+N)+ Ti steel after hot rolling

Magnification X 15,000

Fig (25c)

Optical micrograph 25%Cr low(C+N) steel after hot rolling and annealing at 1000°C for half an hour

Magnification X 160

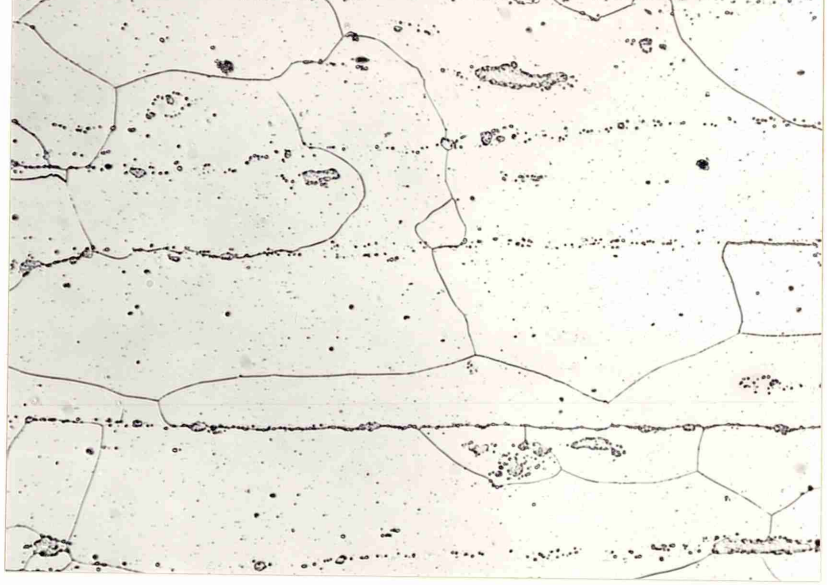

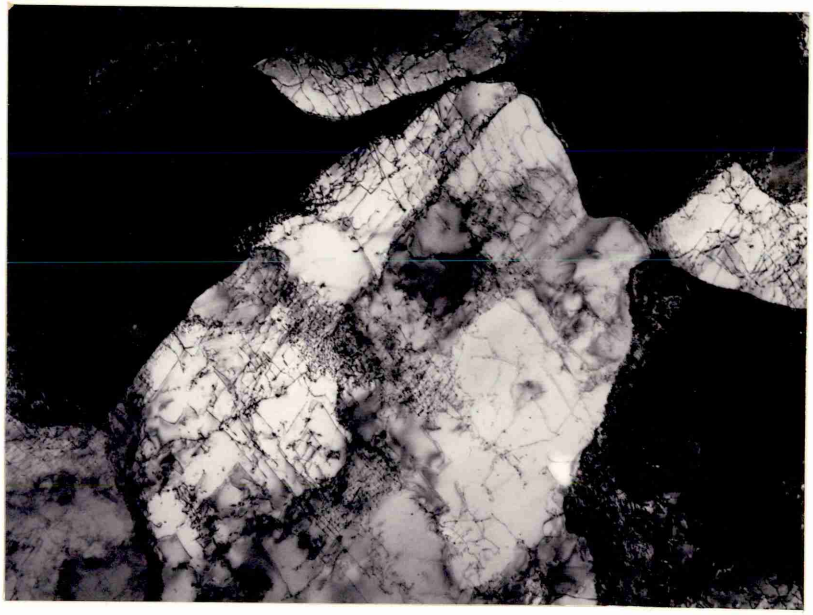

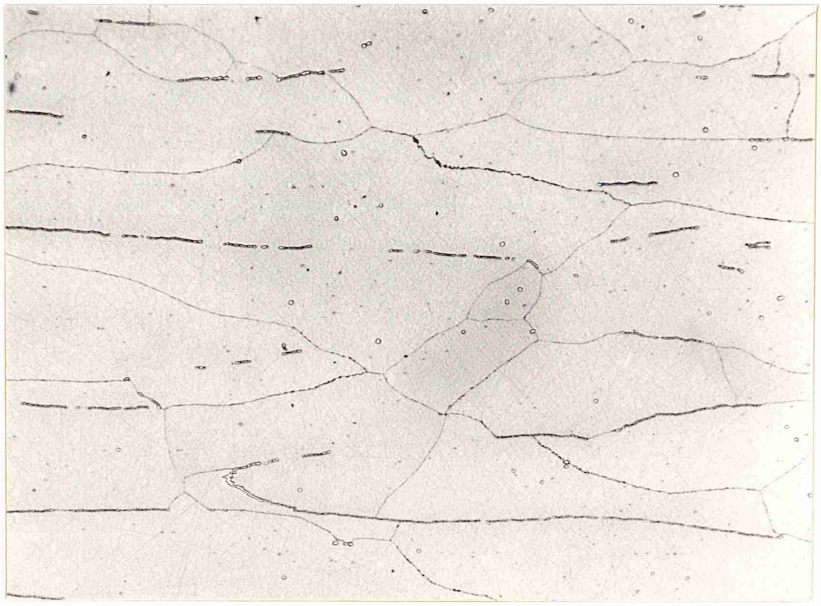

Fig (26)

Cold working characteristics

Fig (27)

Schematic curves for the change in hardness, ΔH versus annealing time and percentage recrystallised versus annealing time.

Fig (28)

The effect of cold work on the relative rates of recovery.

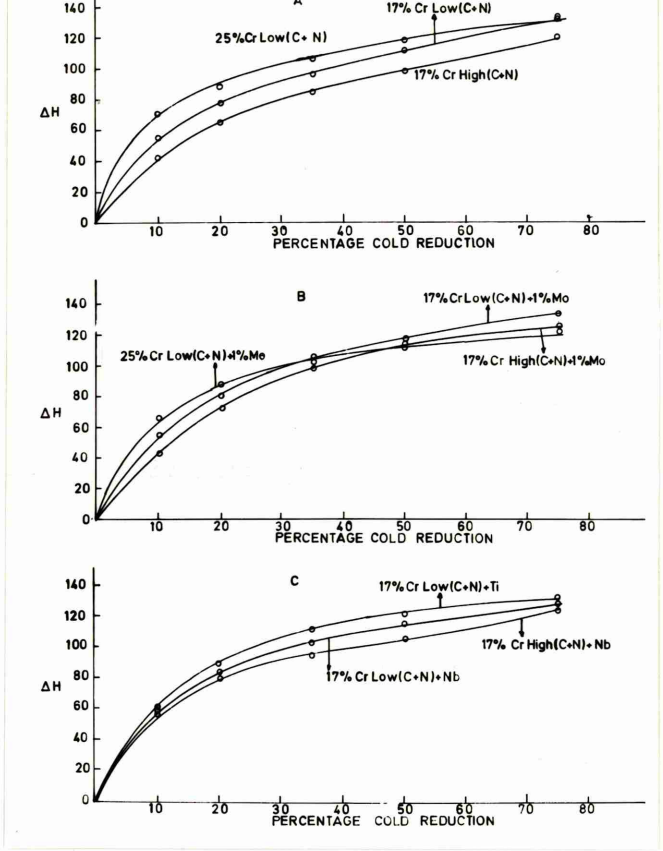
A
17% Cr Low(C+N)
25% Cr Low(C+N)
17% Cr High(C+N)
ΔH
PERCENTAGE COLD REDUCTION
B
17% Cr Low(C+N)+1% Mo
25% Cr Low(C+N)+1% Mo
17% Cr High(C+N)+1% Mo
ΔH
PERCENTAGE COLD REDUCTION
C
17% Cr Low(C+N)+Ti
17% Cr High(C+N)+Nb
17% Cr Low(C+N)+Nb
ΔH
PERCENTAGE COLD REDUCTION

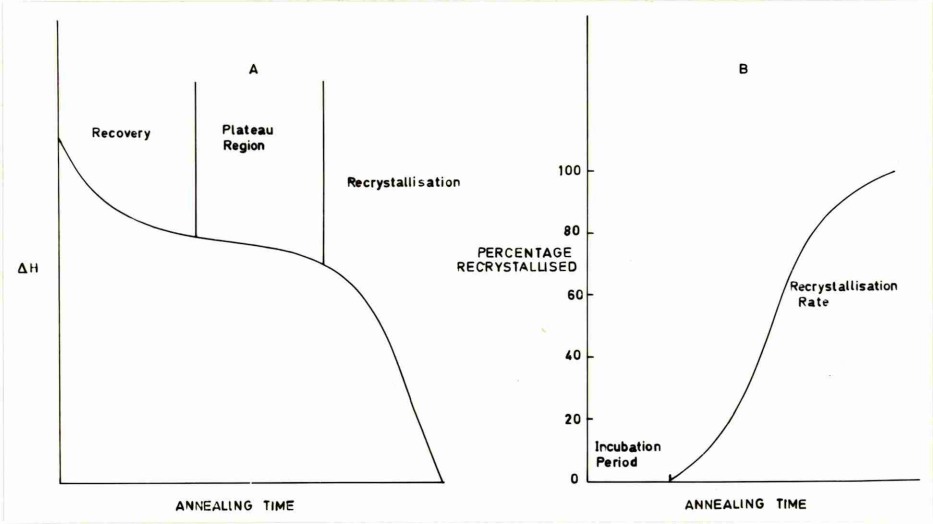
A
Recovery
Plateau Region
Recrystallisation
ΔH
ANNEALING TIME
B
PERCENTAGE RECRYSTALLISED
Recrystallisation Rate
Incubation Period
ANNEALING TIME

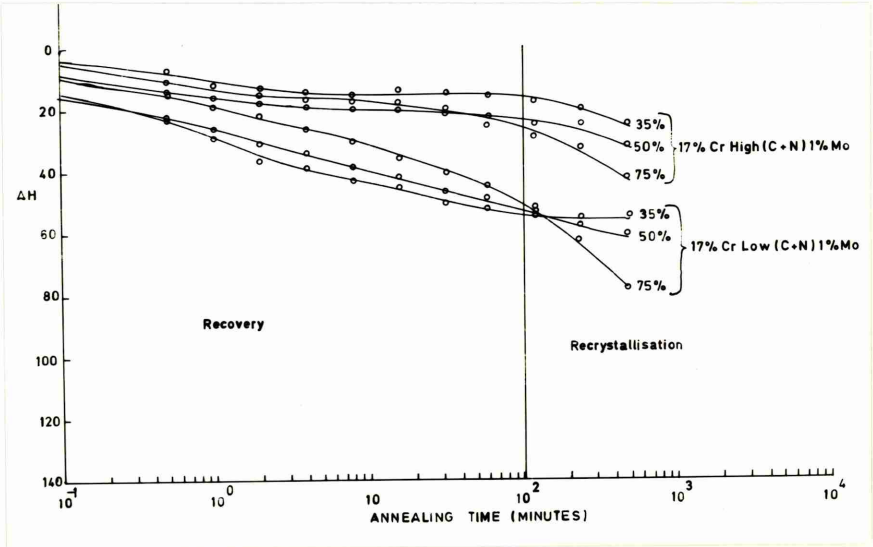
35%
50%
75%
17% Cr High (C+N) 1% Mo
35%
50%
75%
17% Cr Low (C+N) 1% Mo
ΔH
Recovery
Recrystallisation
ANNEALING TIME (MINUTES)

Fig (29)

The effect of annealing temperature on the softening of a 17%Cr low(C+N) steel after 35% cold reduction

Fig (30)

The effect of interstitial content on recovery rate in base 17%Cr steel after annealing at 690°C

Fig (31)

The effect of annealing temperature on the softening of a 17%Cr high(C+N) steel after 35% cold reduction

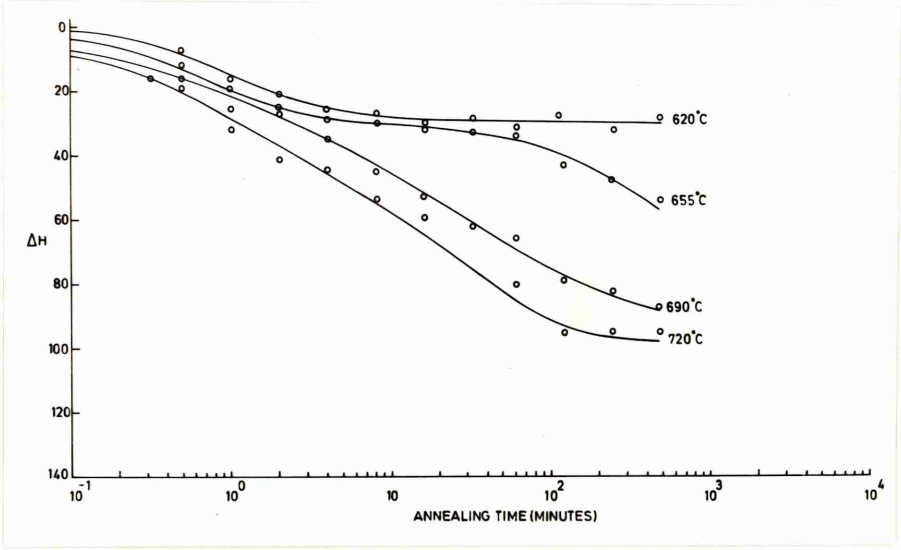
0
20
40
60
80
100
120
140
ΔH
620°C
655°C
690°C
720°C
10^{-1}
10^{0}
10
10^{2}
10^{3}
10^{4}
ANNEALING TIME (MINUTES)

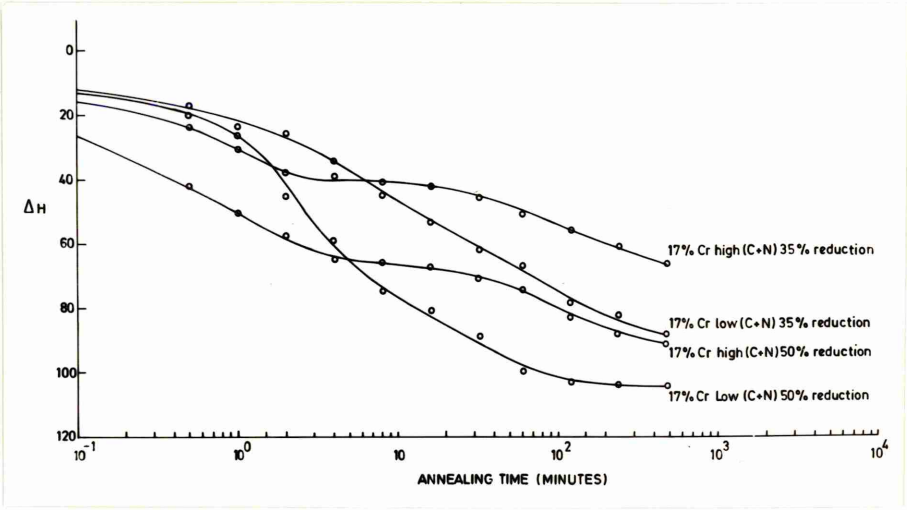
0
20
40
60
80
100
120
ΔH
17% Cr high (C+N) 35% reduction
17% Cr low (C+N) 35% reduction
17% Cr high (C+N) 50% reduction
17% Cr Low (C+N) 50% reduction
10^{-1}
10^{0}
10
10^{2}
10^{3}
10^{4}
ANNEALING TIME (MINUTES)

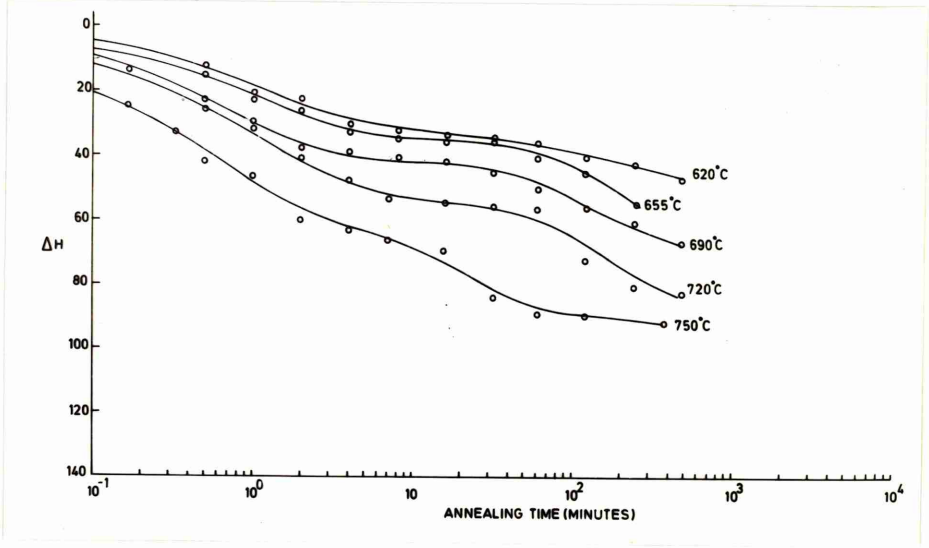
0
20
40
60
80
100
120
140
ΔH
620°C
655°C
690°C
720°C
750°C
10^{-1}
10^{0}
10
10^{2}
10^{3}
10^{4}
ANNEALING TIME (MINUTES)

Fig (32)

The effect of annealing temperature on the softening of a 17%Cr high(C+N) after 75% cold reduction

Fig (33)

The effect of chromium content on the rate of recovery after annealing at 690°C

Fig (34)

The effect of chromium and additions of titanium on the rate of recovery after annealing at 620°C

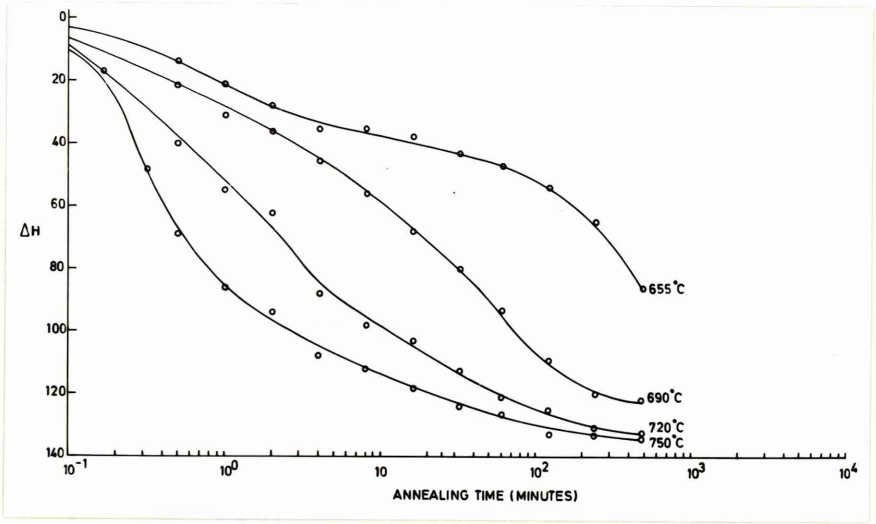
ΔH
0
20
40
60
80
100
120
140
10^{-1}
10^{0}
10
10^{2}
10^{3}
10^{4}
ANNEALING TIME (MINUTES)
655°C
690°C
720°C
750°C

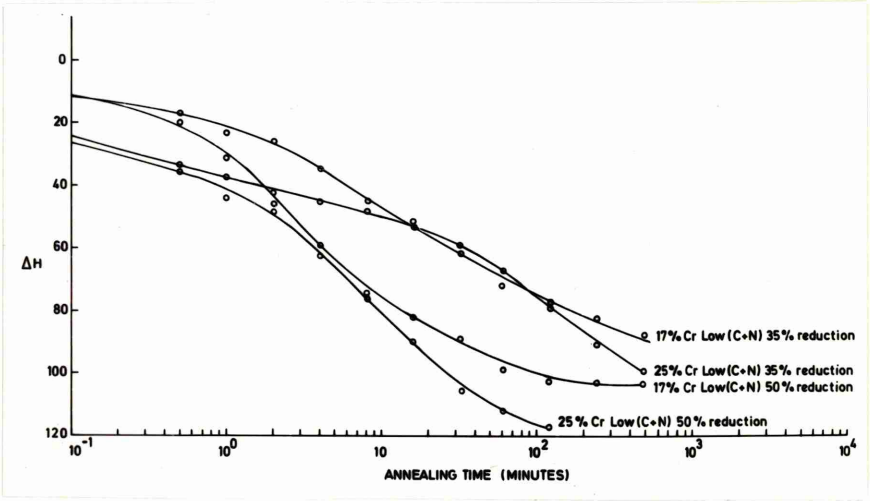
ΔH
0
20
40
60
80
100
120
10^{-1}
10^{0}
10
10^{2}
10^{3}
10^{4}
ANNEALING TIME (MINUTES)
17% Cr Low (C+N) 35% reduction
25% Cr Low (C+N) 35% reduction
17% Cr Low (C+N) 50% reduction
25% Cr Low (C+N) 50% reduction

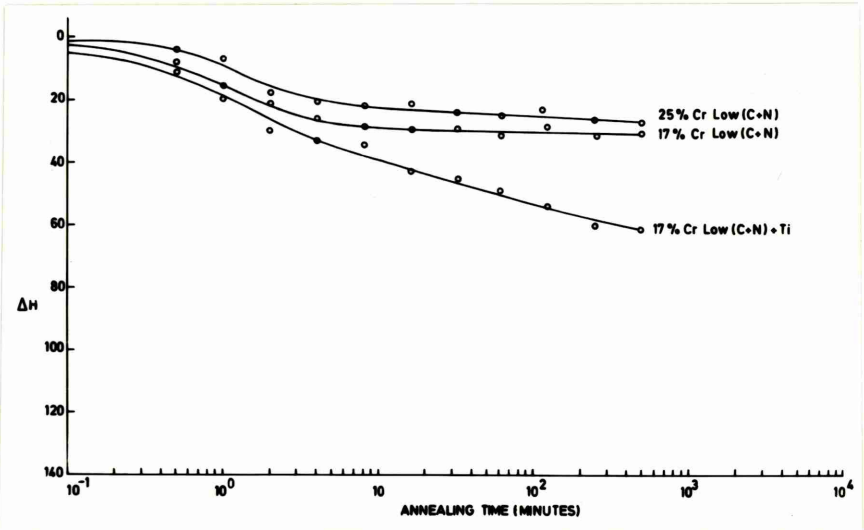
ΔH
0
20
40
60
80
100
120
140
10^{-1}
10^{0}
10
10^{2}
10^{3}
10^{4}
ANNEALING TIME (MINUTES)
25% Cr Low (C+N)
17% Cr Low (C+N)
17% Cr Low (C+N) + Ti

Fig (35)

The effect of molybdenum on the rate of recovery in a 17%Cr low interstitial content steel after annealing at 655^{o}C

Fig (36)

The effect of annealing temperature on the softening of a 17%Cr low(C+N) 1%Mo steel after 35% cold reduction

Fig (37)

The effect of molybdenum on the rate of recovery in a 25%Cr low interstitial content steel

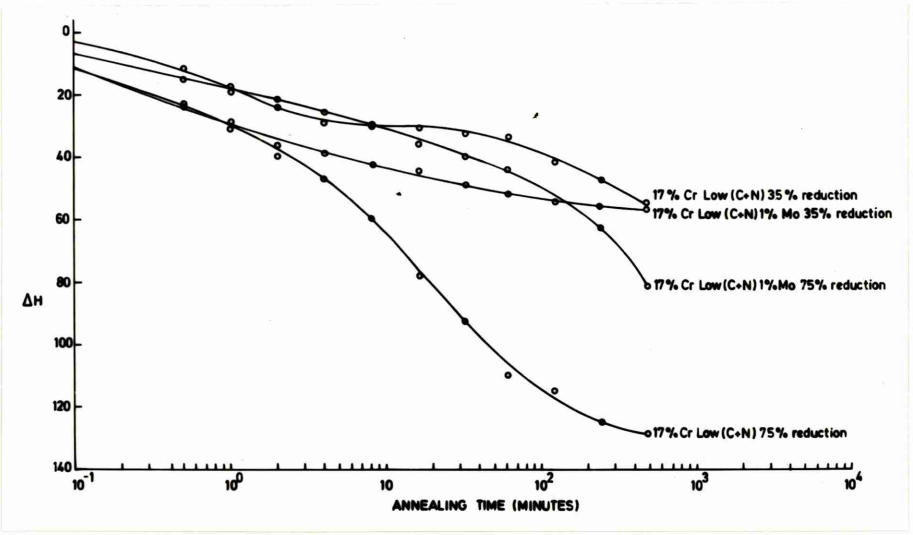
0
20
40
60
80
100
120
140
ΔH
10⁻¹
10⁰
10
10²
10³
10⁴
ANNEALING TIME (MINUTES)
17 % Cr Low (C+N) 35 % reduction
17% Cr Low (C+N) 1% Mo 35% reduction
17% Cr Low (C+N) 1% Mo 75% reduction
17% Cr Low (C+N) 75% reduction

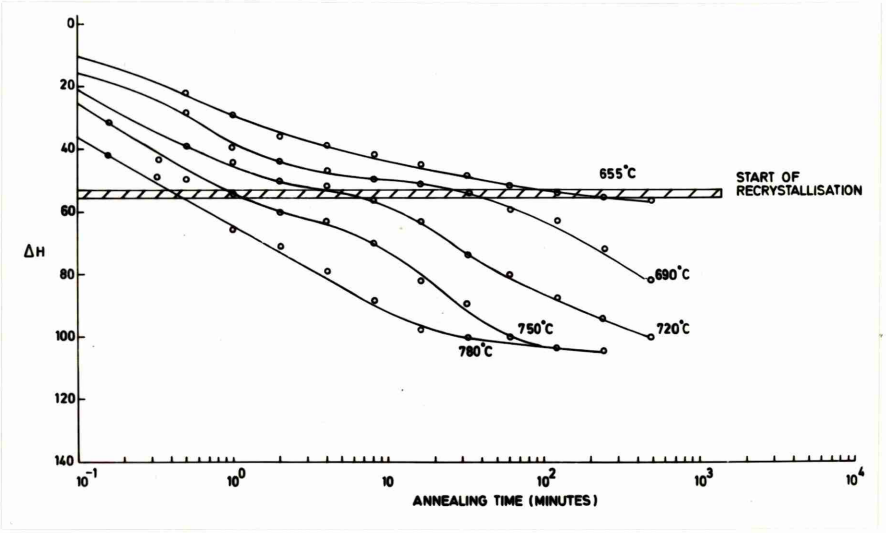
0
20
40
60
80
100
120
140
ΔH
10⁻¹
10⁰
10
10²
10³
10⁴
ANNEALING TIME (MINUTES)
655°C
START OF RECRYSTALLISATION
690°C
720°C
750°C
780°C

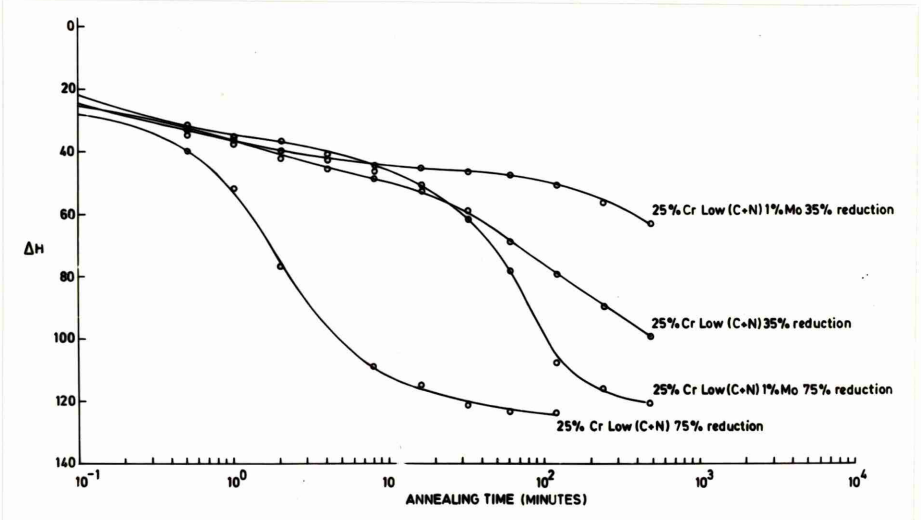
0
20
40
60
80
100
120
140
ΔH
10⁻¹
10⁰
10
10²
10³
10⁴
ANNEALING TIME (MINUTES)
25% Cr Low (C+N) 1% Mo 35% reduction
25% Cr Low (C+N) 35% reduction
25% Cr Low (C+N) 1% Mo 75% reduction
25% Cr Low (C+N) 75% reduction

Fig (38)

The effect of chromium content on the rate of recovery in the low interstitial content molybdenum steels

Fig (39)

The effect of molybdenum on the rate of recovery in a 17%Cr high(C+N) steel

Fig (40)

The effect of annealing temperature on the softening of a 17%Cr high(C+N) 1%Mo steel

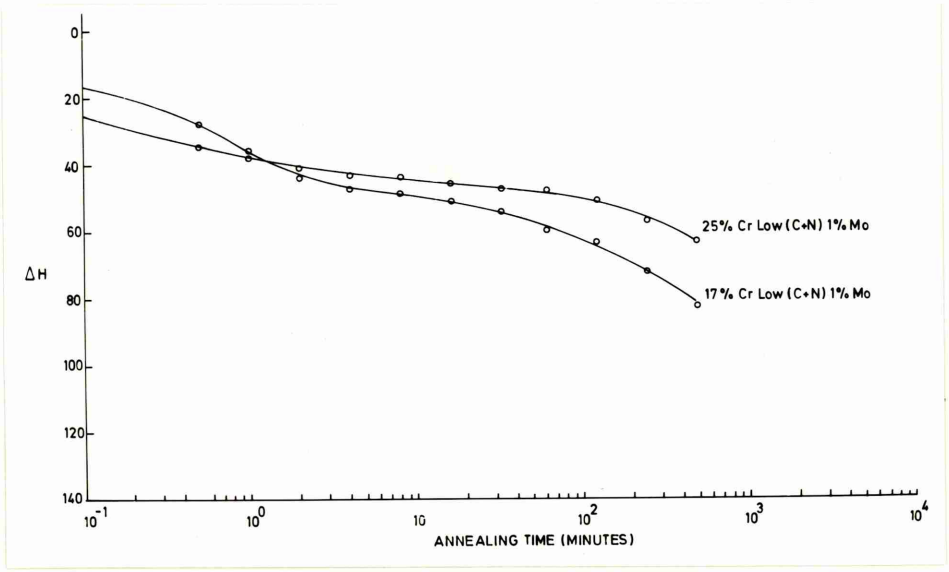
0
20
40
60
80
100
120
140
ΔH
25% Cr Low (C+N) 1% Mo
17% Cr Low (C+N) 1% Mo
10^{-1}
10^{0}
10
10^{2}
10^{3}
10^{4}
ANNEALING TIME (MINUTES)

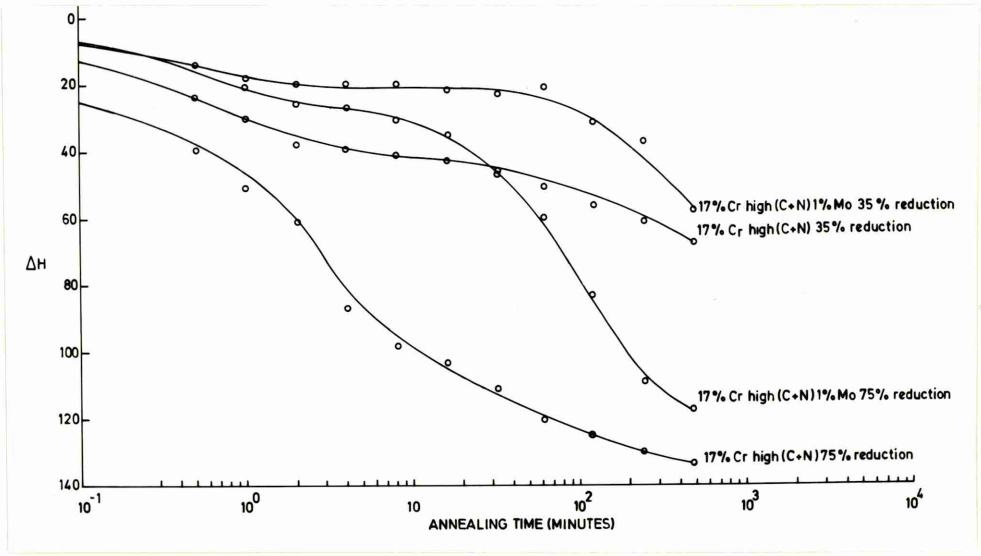
0
20
40
60
80
100
120
140
ΔH
17% Cr high (C+N) 1% Mo 35% reduction
17% Cr high (C+N) 35% reduction
17% Cr high (C+N) 1% Mo 75% reduction
17% Cr high (C+N) 75% reduction
10^{-1}
10^{0}
10
10^{2}
10^{3}
10^{4}
ANNEALING TIME (MINUTES)

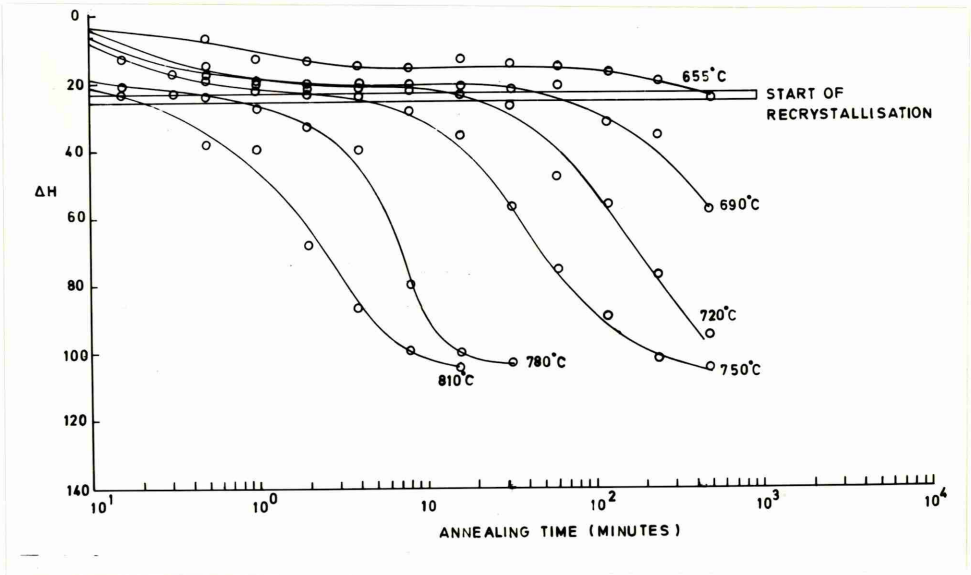
0
20
40
60
80
100
120
140
ΔH
655°C
START OF
RECRYSTALLISATION
690°C
720°C
750°C
780°C
810°C
10^{1}
10^{0}
10
10^{2}
10^{3}
10^{4}
ANNEALING TIME (MINUTES)

Fig (41)

The effect of interstitial content on the rate of recovery in the molybdenum steels at 17%Cr

Fig (42)

The effect of titanium additions on the rate of recovery in a 17%Cr low interstitial content steel

Fig (43)

The effect of niobium on the rate of recovery in a 17%Cr low interstitial content steel, and a comparison between the effects of niobium and molybdenum on the rate of recovery in 17%Cr low interstitial content steels

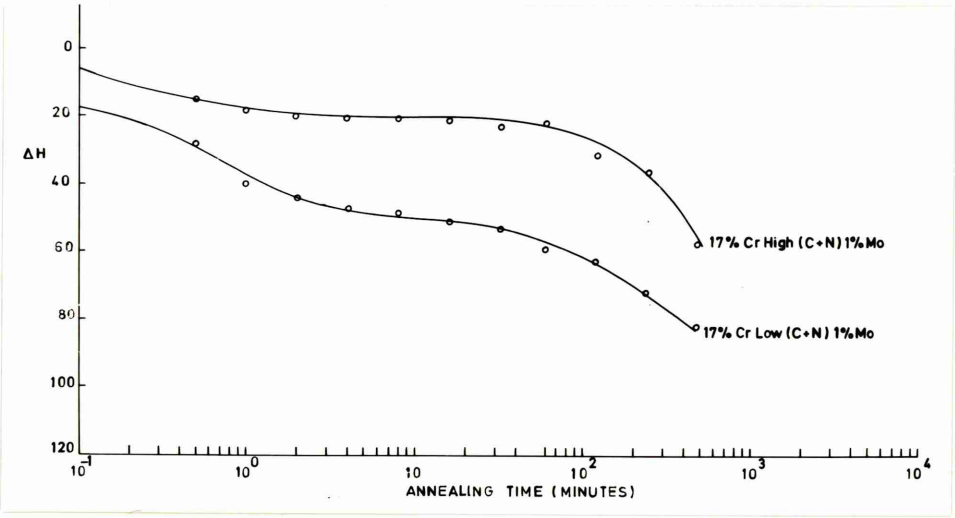
0
20
ΔH
40
60
80
100
120
10^{-1}
10^{0}
10
10^{2}
10^{3}
10^{4}
ANNEALING TIME (MINUTES)
17% Cr High (C+N) 1% Mo
17% Cr Low (C+N) 1% Mo

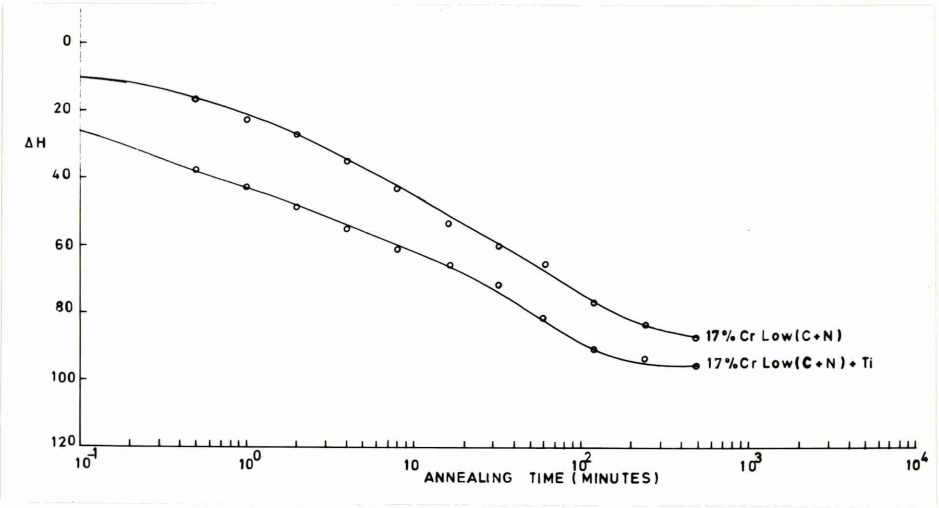
0
20
ΔH
40
60
80
100
120
10^{-1}
10^{0}
10
10^{2}
10^{3}
10^{4}
ANNEALING TIME (MINUTES)
17% Cr Low (C+N)
17% Cr Low (C+N) + Ti

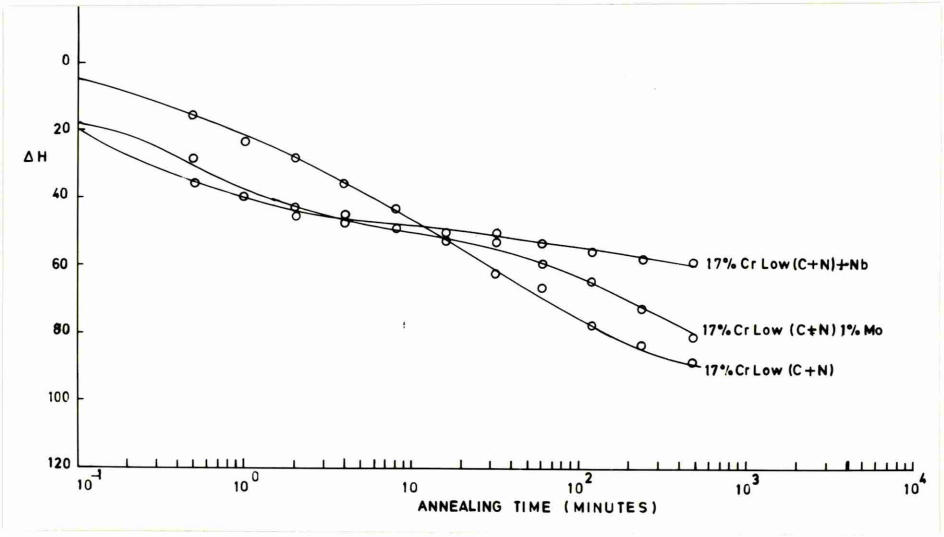
0
20
ΔH
40
60
80
100
120
10^{-1}
10^{0}
10
10^{2}
10^{3}
10^{4}
ANNEALING TIME (MINUTES)
17% Cr Low (C+N)+Nb
17% Cr Low (C+N) 1% Mo
17% Cr Low (C+N)

Fig (44)

The effect of annealing temperature on the softening of a 17%Cr low(C+N) + Nb steel after 35% cold reduction

Fig (45)

The effect of niobium on the rate of recovery of a 17%Cr high interstitial content steel

Fig (46)

The effect of interstitial content on the rate of recovery in the niobium steel, and a comparison between the effects of molybdenum and niobium on the rate of recovery in 17%Cr high interstitial content steel

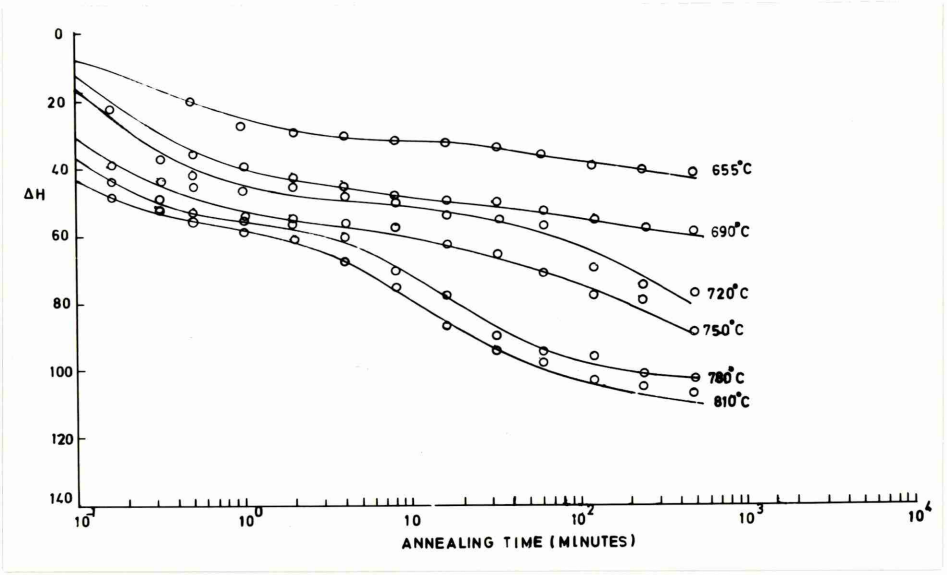
0
20
40
60
80
100
120
140
ΔH
655°C
690°C
720°C
750°C
780°C
810°C
10^{-1}
10^{0}
10
10^{2}
10^{3}
10^{4}
ANNEALING TIME (MINUTES)

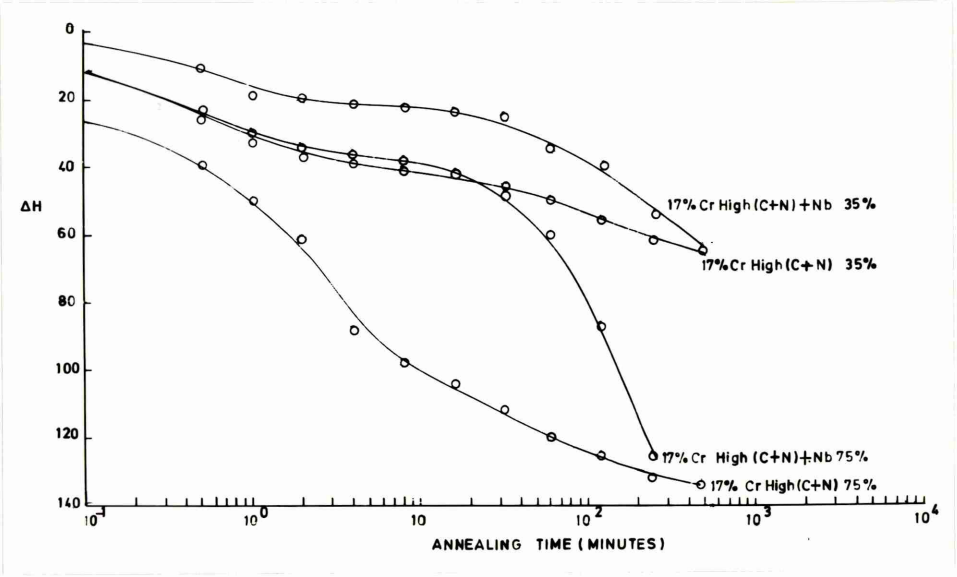
0
20
40
60
80
100
120
140
ΔH
17% Cr High (C+N) + Nb 35%
17% Cr High (C+N) 35%
17% Cr High (C+N) + Nb 75%
17% Cr High (C+N) 75%
10^{-1}
10^{0}
10
10^{2}
10^{3}
10^{4}
ANNEALING TIME (MINUTES)

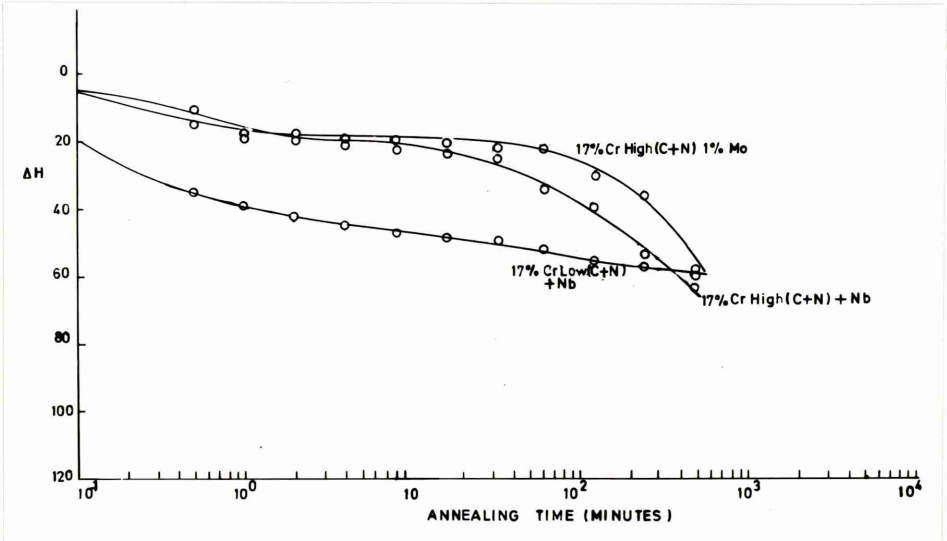
0
20
40
60
80
100
120
ΔH
17% Cr High (C+N) 1% Mo
17% Cr Low (C+N) + Nb
17% Cr High (C+N) + Nb
10^{-1}
10^{0}
10
10^{2}
10^{3}
10^{4}
ANNEALING TIME (MINUTES)

Fig (47)

The effect of cold work on recrystallisation

Fig (48)

The effect of interstitial content on recrystallisation in base 17%Cr steels

Fig (49)

The effect of chromium content on recrystallisation

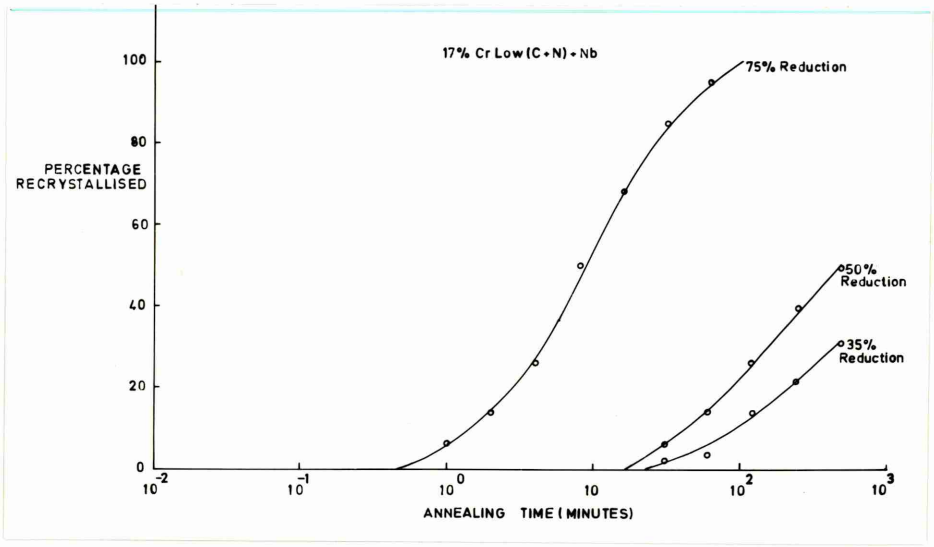
17% Cr Low (C+N) + Nb
75% Reduction
50% Reduction
35% Reduction
PERCENTAGE RECRYSTALLISED
ANNEALING TIME (MINUTES)

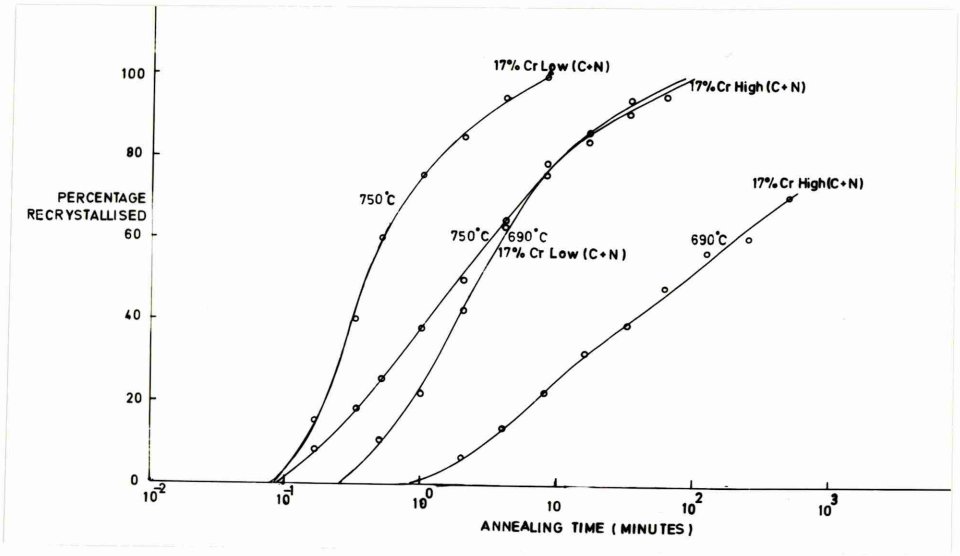
17% Cr Low (C+N)
17% Cr High (C+N)
750°C
750°C
690°C
17% Cr Low (C+N)
690°C
17% Cr High (C+N)
PERCENTAGE RECRYSTALLISED
ANNEALING TIME (MINUTES)

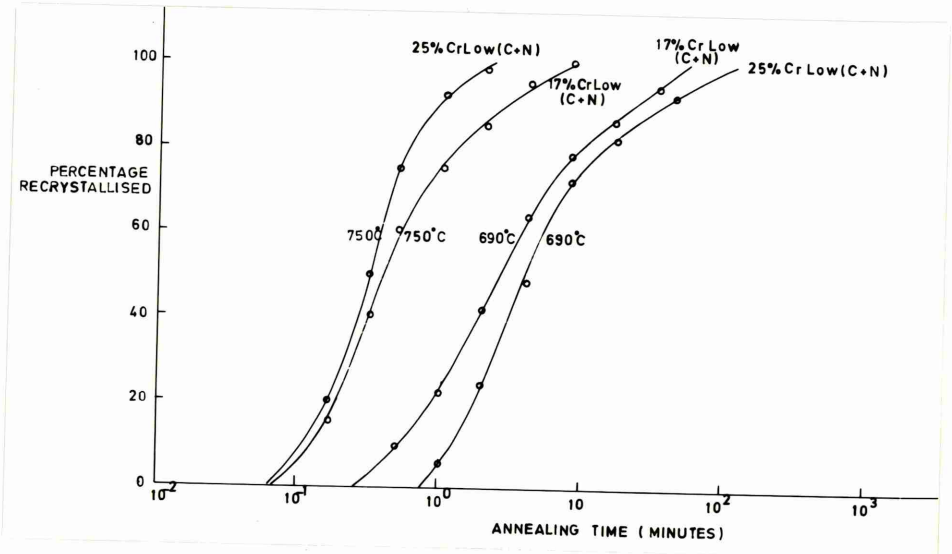
25% Cr Low (C+N)
17% Cr Low (C+N)
17% Cr Low (C+N)
25% Cr Low (C+N)
750°C
750°C
690°C
690°C
PERCENTAGE RECRYSTALLISED
ANNEALING TIME (MINUTES)

Fig (50)

The effect of molybdenum on recrystallisation in 17%Cr low interstitial content steels

Fig (51)

The effect of molybdenum on recrystallisation in 25%Cr steels

Fig (52)

The effect of chromium content on recrystallisation in the molybdenum steels

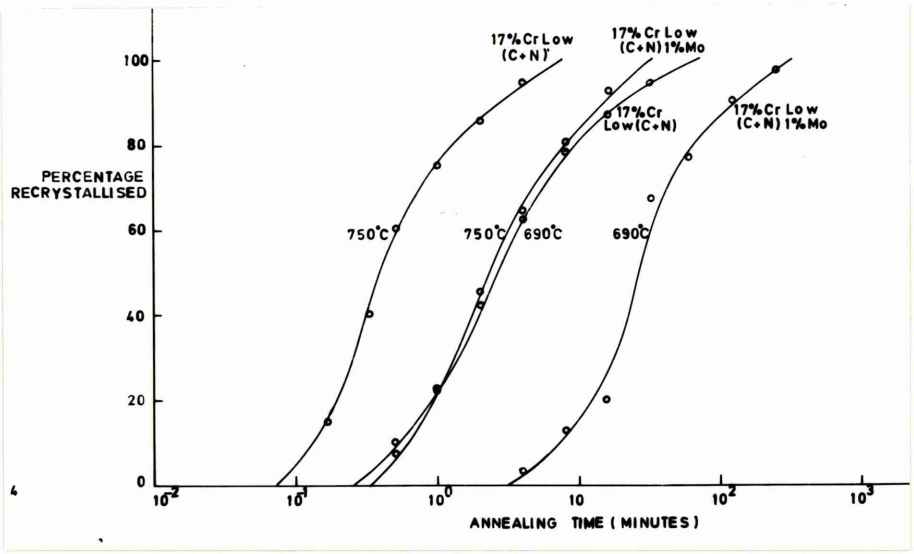
17% Cr Low (C+N)
17% Cr Low (C+N) 1% Mo
17% Cr Low (C+N)
17% Cr Low (C+N) 1% Mo
750°C
750°C
690°C
690°C
PERCENTAGE RECRYSTALLISED
ANNEALING TIME (MINUTES)

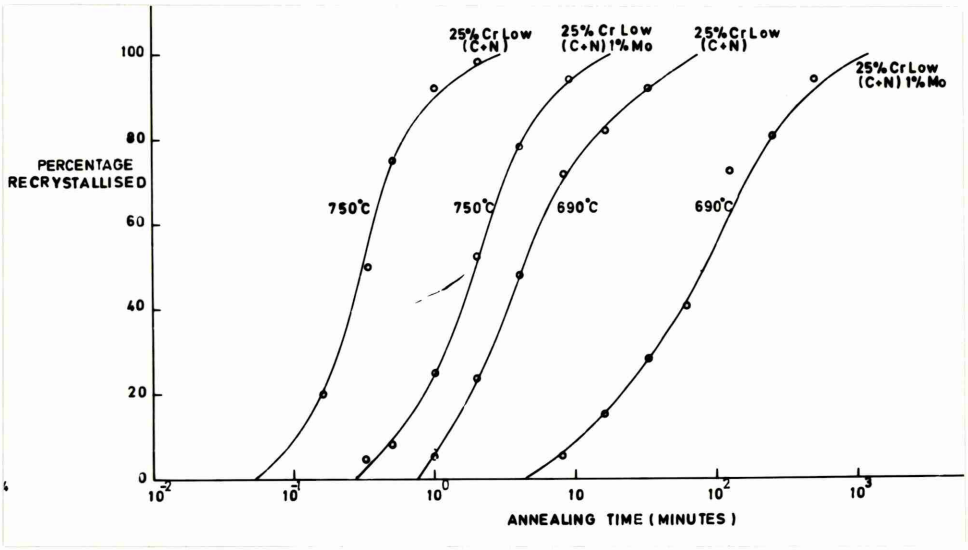
25% Cr Low (C+N)
25% Cr Low (C+N) 1% Mo
25% Cr Low (C+N)
25% Cr Low (C+N) 1% Mo
750°C
750°C
690°C
690°C
PERCENTAGE RECRYSTALLISED
ANNEALING TIME (MINUTES)

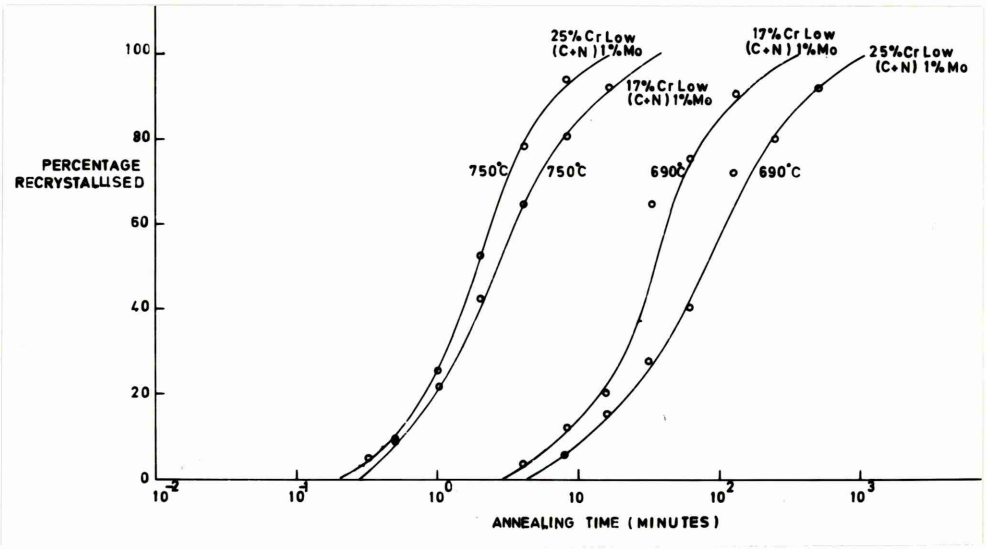
25% Cr Low (C+N) 1% Mo
17% Cr Low (C+N) 1% Mo
17% Cr Low (C+N) 1% Mo
25% Cr Low (C+N) 1% Mo
750°C
750°C
690°C
690°C
PERCENTAGE RECRYSTALLISED
ANNEALING TIME (MINUTES)

Fig (53)

The effect of molybdenum on recrystallisation in a 17%Cr high interstitial content steel

Fig (54)

The effect of interstitial content on recrystallisation in 17%Cr molybdenum steels

Fig (55)

The effect of titanium on recrystallisation in a 17%Cr low interstitial content steel

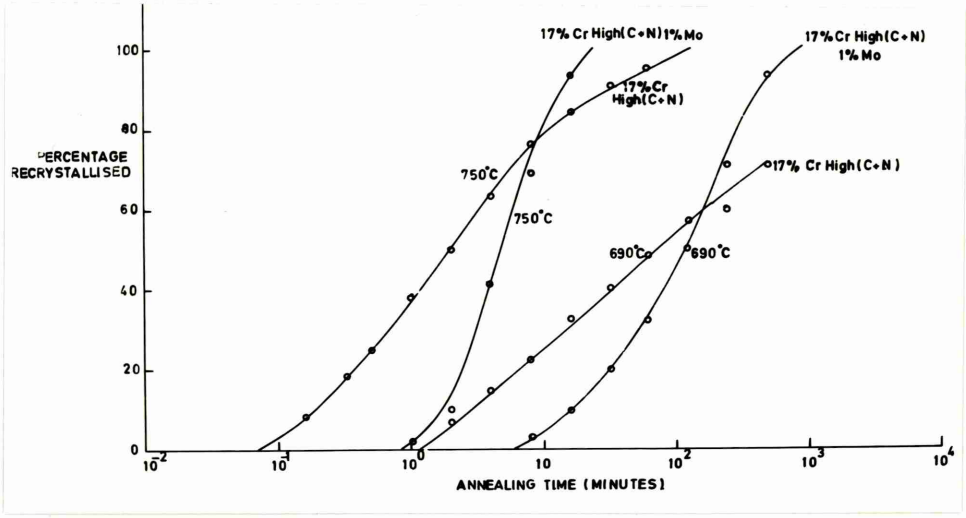
17% Cr High(C+N)1%Mo
17% Cr High(C+N)
1% Mo
17% Cr High(C+N)
17% Cr High(C+N)
750°C
750°C
690°C
690°C
PERCENTAGE RECRYSTALLISED
ANNEALING TIME (MINUTES)

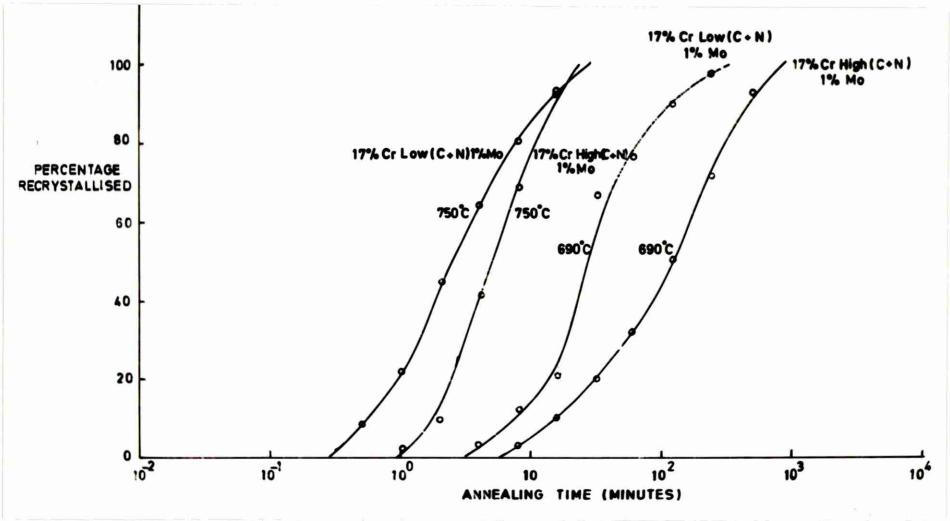
17% Cr Low(C+N)
1% Mo
17% Cr High(C+N)
1% Mo
17% Cr Low(C+N)1%Mo
17% Cr High(C+N)
1% Mo
750°C
750°C
690°C
690°C
PERCENTAGE RECRYSTALLISED
ANNEALING TIME (MINUTES)

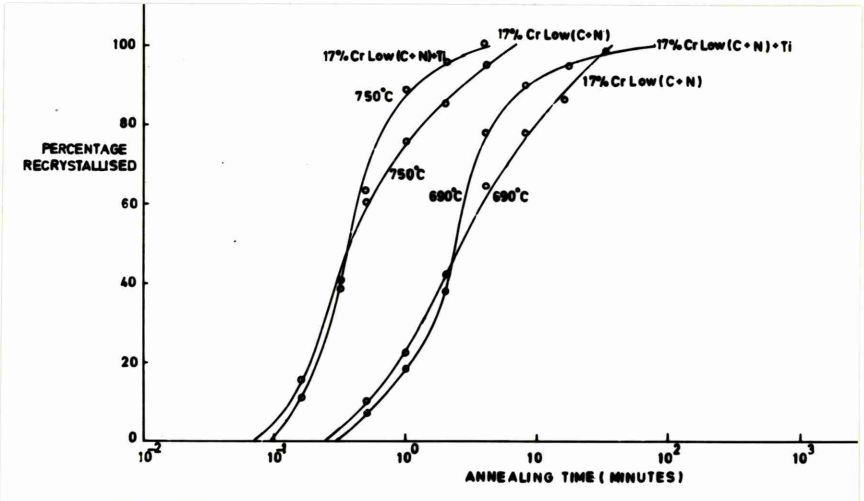
17% Cr Low(C+N)
17% Cr Low(C+N)+Ti
17% Cr Low(C+N)+Ti
17% Cr Low(C+N)
750°C
750°C
690°C
690°C
PERCENTAGE RECRYSTALLISED
ANNEALING TIME (MINUTES)

Fig (56)

The effect of niobium on recrystallisation in a 17%Cr low interstitial content steel

Fig (57)

The comparison between the effects of niobium and molybdenum on recrystallisation in 17%Cr low interstitial content steels

Fig (58)

The effect of niobium on recrystallisation in a 17%Cr high interstitial content steel

Fig (59)

The effect of interstitial content on recrystallisation in 17%Cr niobium steels

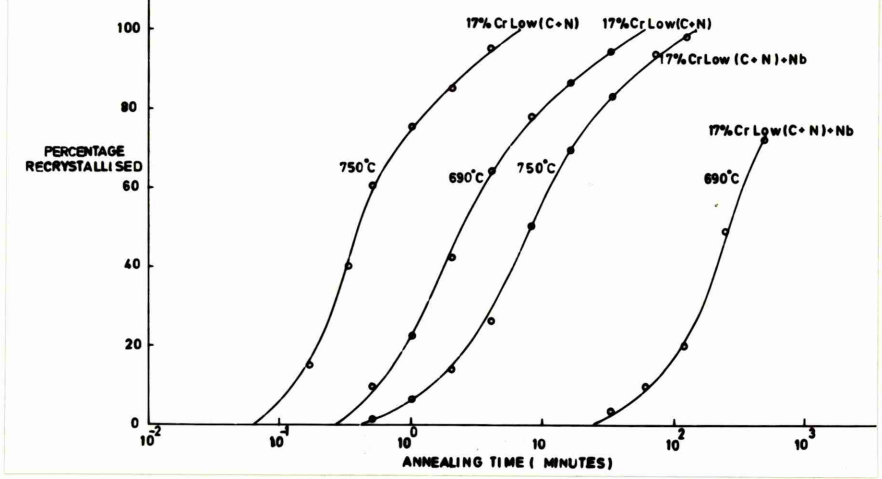
17% Cr Low (C+N)
17% Cr Low (C+N)
17% Cr Low (C+N)+Nb
17% Cr Low (C+N)+Nb
750°C
690°C
750°C
690°C
PERCENTAGE RECRYSTALLISED
ANNEALING TIME (MINUTES)

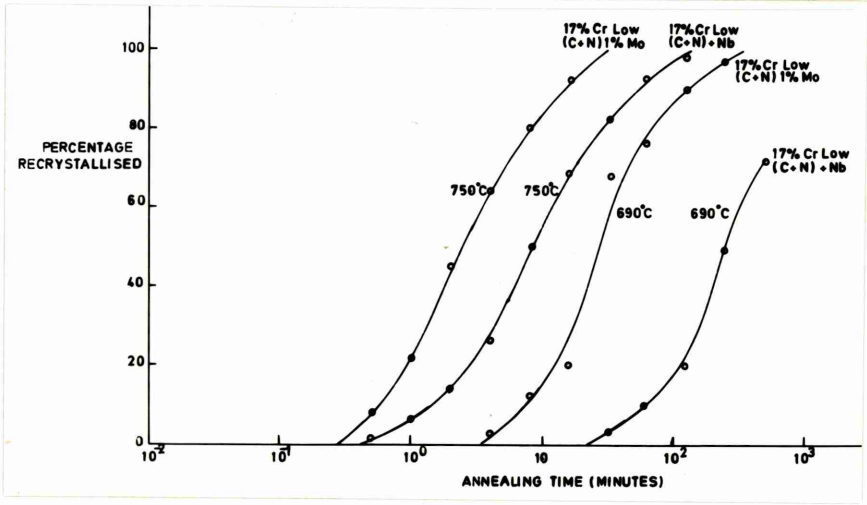
17% Cr Low (C+N) 1% Mo
17% Cr Low (C+N)+Nb
17% Cr Low (C+N) 1% Mo
17% Cr Low (C+N)+Nb
750°C
750°C
690°C
690°C
PERCENTAGE RECRYSTALLISED
ANNEALING TIME (MINUTES)

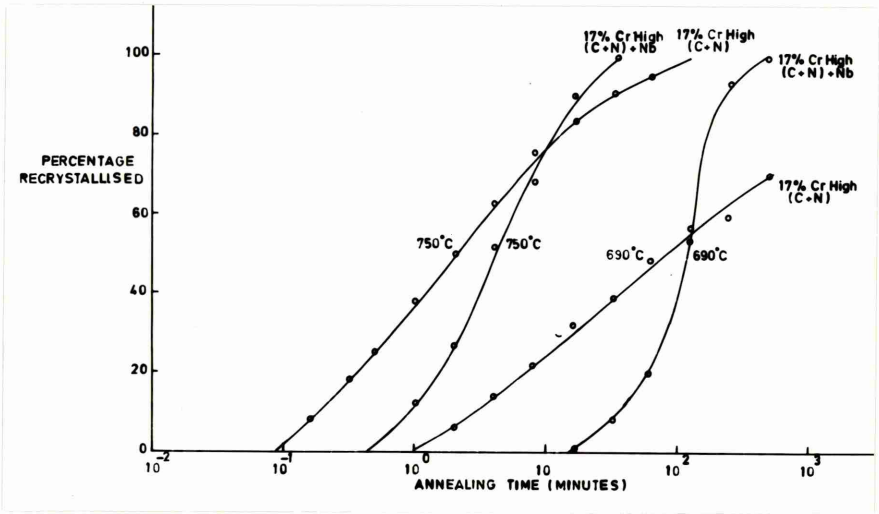
17% Cr High (C+N)+Nb
17% Cr High (C+N)
17% Cr High (C+N)+Nb
17% Cr High (C+N)
750°C
750°C
690°C
690°C
PERCENTAGE RECRYSTALLISED
ANNEALING TIME (MINUTES)

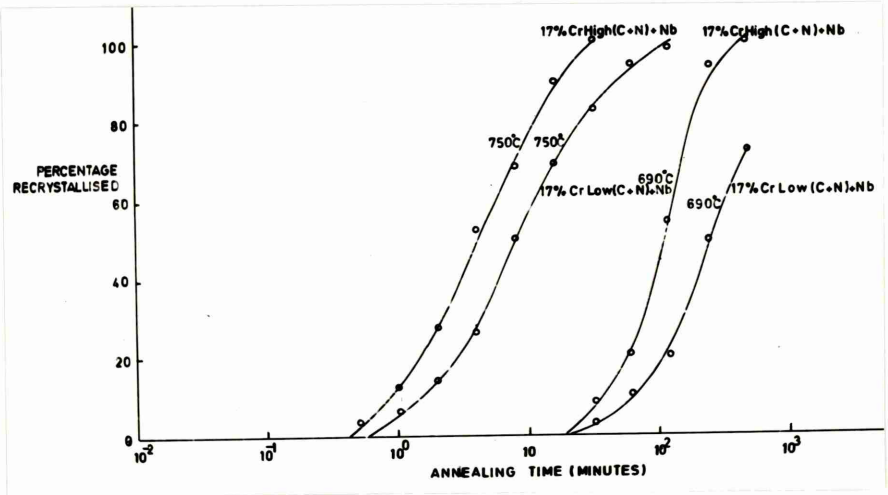
17% Cr High (C+N)+Nb
17% Cr High (C+N)+Nb
750°C
750°C
690°C
690°C
17% Cr Low (C+N)+Nb
17% Cr Low (C+N)+Nb
PERCENTAGE RECRYSTALLISED
ANNEALING TIME (MINUTES)

Fig (60a)

The effect of cold work on grain size and aspect ratio for 17%Cr low(C+N), 17%Cr low(C+N) 1%Mo, 17%Cr high(C+N) and 17%Cr high(C+N)1%Mo steels in the fully recrystallised condition

Fig (60b)

The effect of cold work on grain size and aspect ratio for 17%Cr low(C+N), 17%Cr low(C+N) + Nb, 17%Cr low(C+N) + Ti, 17%Cr high(C+N), and 17%Cr high(C+N) + Nb steels in the fully recrystallised condition

Fig (60c)

The effect of cold work on grain size and aspect ratio for 17%Cr low(C+N), 25%Cr low(C+N) and 25%Cr low(C+N) 1%Mo steels in the fully recrystallised condition

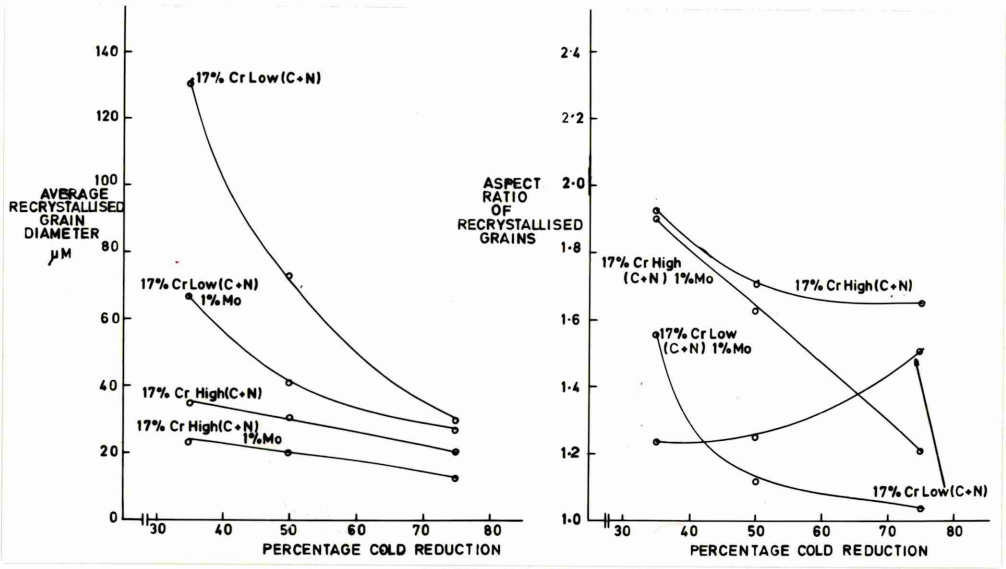
AVERAGE RECRYSTALLISED GRAIN DIAMETER μM
17% Cr Low(C+N)
17% Cr Low(C+N) 1%Mo
17% Cr High(C+N)
17% Cr High(C+N) 1%Mo
PERCENTAGE COLD REDUCTION
ASPECT RATIO OF RECRYSTALLISED GRAINS
17% Cr High (C+N) 1%Mo
17% Cr High(C+N)
17% Cr Low (C+N) 1%Mo
17% Cr Low(C+N)
PERCENTAGE COLD REDUCTION

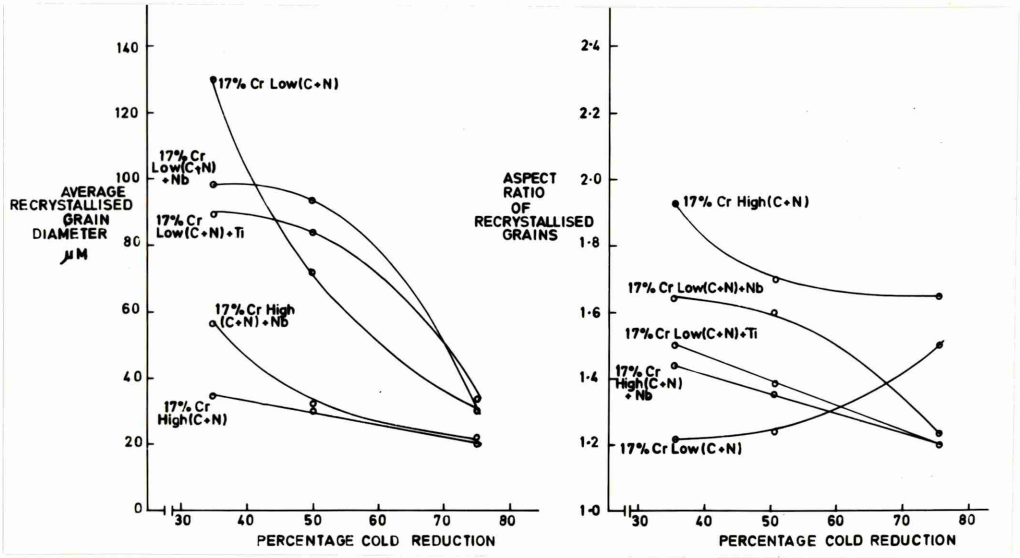
AVERAGE RECRYSTALLISED GRAIN DIAMETER μM
17% Cr Low(C+N)
17% Cr Low(C+N) +Nb
17% Cr Low(C+N)+Ti
17% Cr High (C+N) +Nb
17% Cr High(C+N)
PERCENTAGE COLD REDUCTION
ASPECT RATIO OF RECRYSTALLISED GRAINS
17% Cr High(C+N)
17% Cr Low(C+N)+Nb
17% Cr Low(C+N)+Ti
17% Cr High(C+N) +Nb
17% Cr Low(C+N)
PERCENTAGE COLD REDUCTION

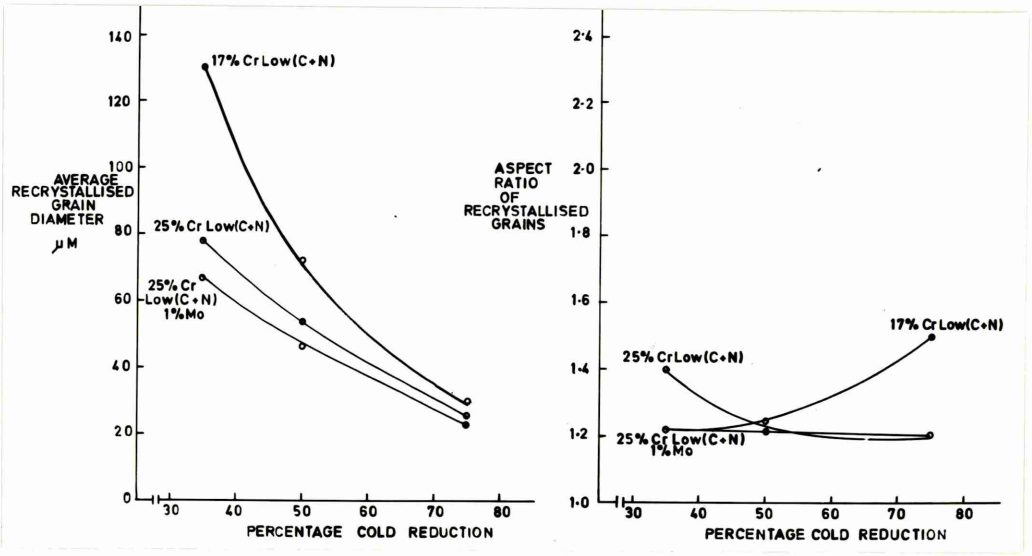
AVERAGE RECRYSTALLISED GRAIN DIAMETER μM
17% Cr Low(C+N)
25% Cr Low(C+N)
25% Cr Low(C+N) 1%Mo
PERCENTAGE COLD REDUCTION
ASPECT RATIO OF RECRYSTALLISED GRAINS
17% Cr Low(C+N)
25% Cr Low(C+N)
25% Cr Low(C+N) 1%Mo
PERCENTAGE COLD REDUCTION

Fig (61a)

The effect of annealing temperature on the recrystallised grain size for 17%Cr low(C+N), 17%Cr low(C+N) + Ti and 25%Cr low(C+N) steels

Fig (61b)

The effect of annealing temperature on the recrystallised grain size for 17%Cr low(C+N) 1%Mo, 17%Cr high(C+N) 1%Mo, 17%Cr high(C+N) + Nb, and 25%Cr low(C+N) 1%Mo steels

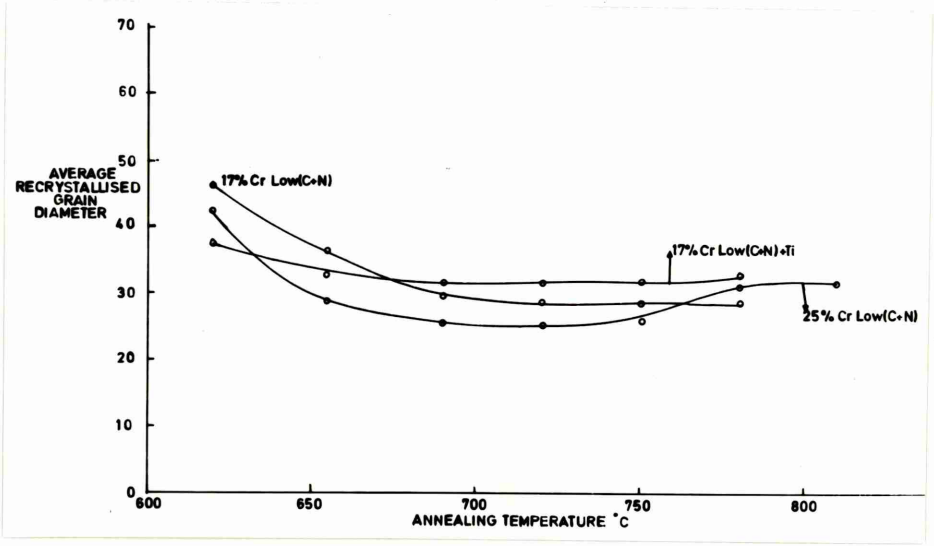
AVERAGE RECRYSTALLISED GRAIN DIAMETER
70
60
50
40
30
20
10
0
600
650
700
750
800
ANNEALING TEMPERATURE °C
17% Cr Low(C+N)
17% Cr Low(C+N)+Ti
25% Cr Low(C+N)

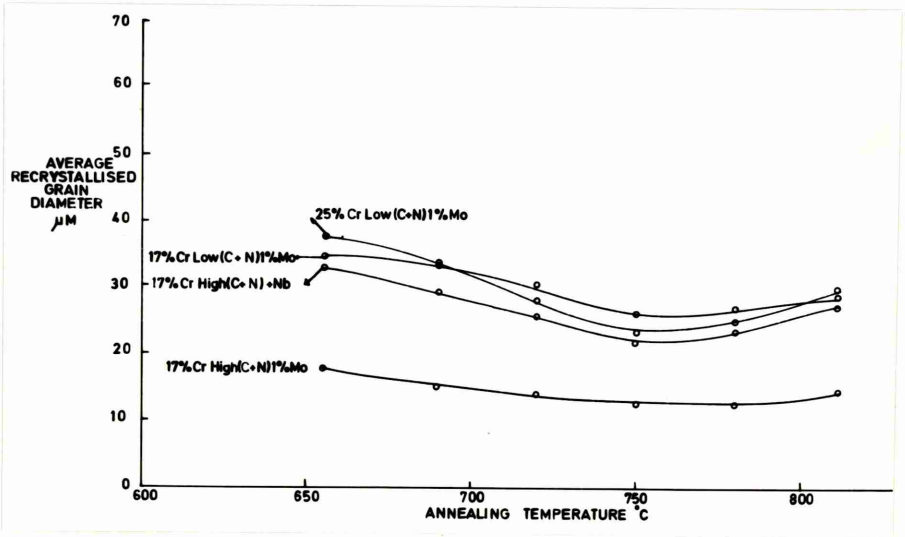
AVERAGE RECRYSTALLISED GRAIN DIAMETER μM
70
60
50
40
30
20
10
0
600
650
700
750
800
ANNEALING TEMPERATURE °C
25% Cr Low (C+N) 1% Mo
17% Cr Low (C+N) 1% Mo
17% Cr High (C+N) +Nb
17% Cr High (C+N) 1% Mo

Fig (62)

The effect of annealing temperature on recrystallisation for 17%Cr low(C+N) and 25%Cr low(C+N) steels after 35% and 75% reduction

Fig (63)

The effect of annealing temperature on recrystallisation for 17%Cr low(C+N) and 17%Cr high(C+N) steels after 75% reduction

Fig (64)

The effect of annealing temperature on recrystallisation for 17%Cr low(C+N), 17%Cr low(C+N) 1%Mo, 25%Cr low(C+N) steels after 75% reduction and for a 25%Cr low(C+N) 1%Mo steel after 35% and 75% reduction

Fig (65)

The effect of annealing temperature on recrystallisation for 17%Cr high(C+N) 1%Mo, 17%Cr low(C+N) + Nb and 17%Cr high(C+N) + Nb steelsafter 75% reduction

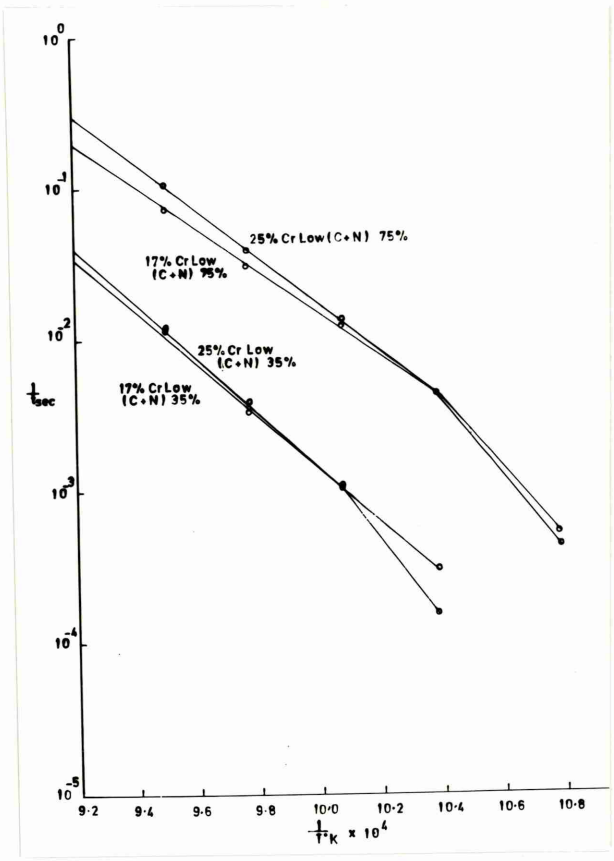
25% Cr Low (C+N) 75%
17% Cr Low (C+N) 75%
25% Cr Low (C+N) 35%
17% Cr Low (C+N) 35%
t sec
1/T°K x 10⁴

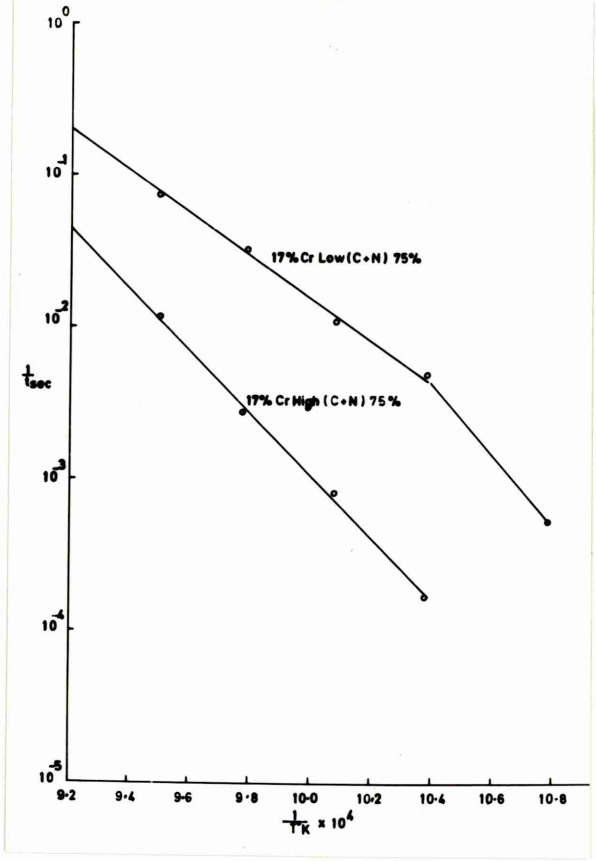
17% Cr Low (C+N) 75%
17% Cr High (C+N) 75%
t sec
1/T°K x 10⁴

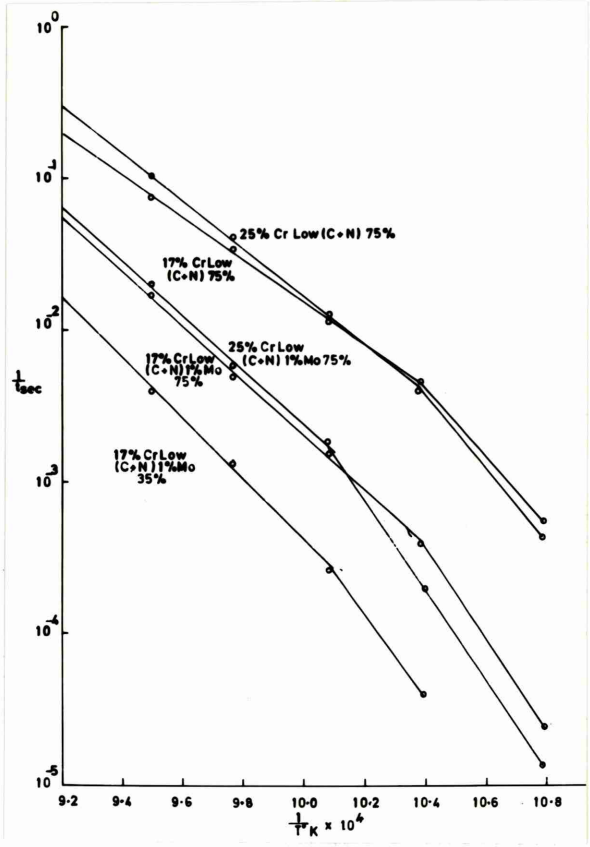
25% Cr Low (C+N) 75%
17% Cr Low (C+N) 75%
25% Cr Low (C+N) 1% Mo 75%
17% Cr Low (C+N) 1% Mo 75%
17% Cr Low (C+N) 1% Mo 35%
t sec
1/T°K x 10⁴

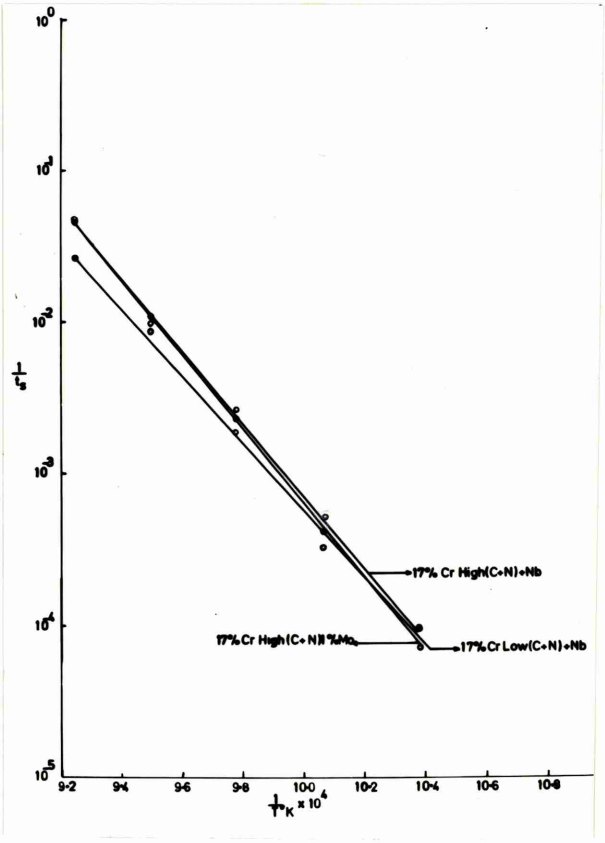
17% Cr High (C+N)+Nb
17% Cr High (C+N) 1% Mo
17% Cr Low (C+N)+Nb
1/T°K x 10⁴

Fig (66)

An inverse pole figure for a
17%Cr high(C+N) 1%Mo steel
in the hot rolled and
annealed condition

Fig (67)

An inverse pole figure for a
17%Cr low(C+N) + Nb steel
in the hot rolled and
annealed condition

Fig (68)

An inverse pole figure for a
17%Cr high(C+N) steel
in the hot rolled and
annealed condition

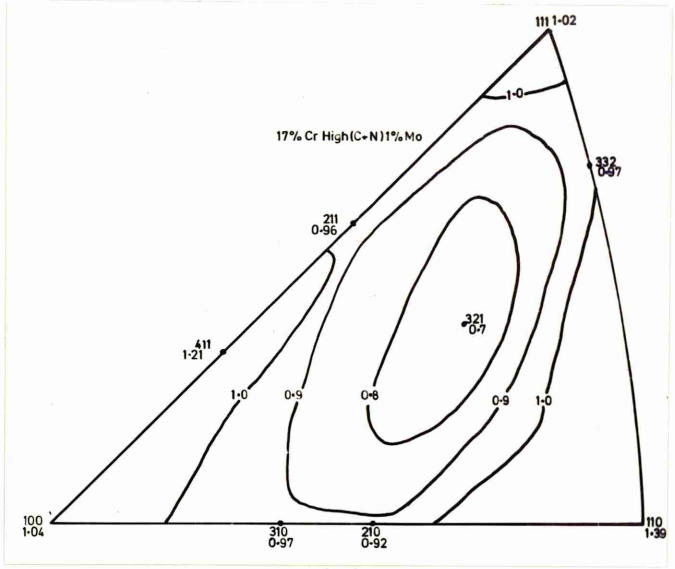
17% Cr High (C+N) 1% Mo
111 1·02
1·0
332
0·97
211
0·96
321
0·7
411
1·21
1·0
0·9
0·8
0·9
1·0
100
1·04
310
0·97
210
0·92
110
1·39

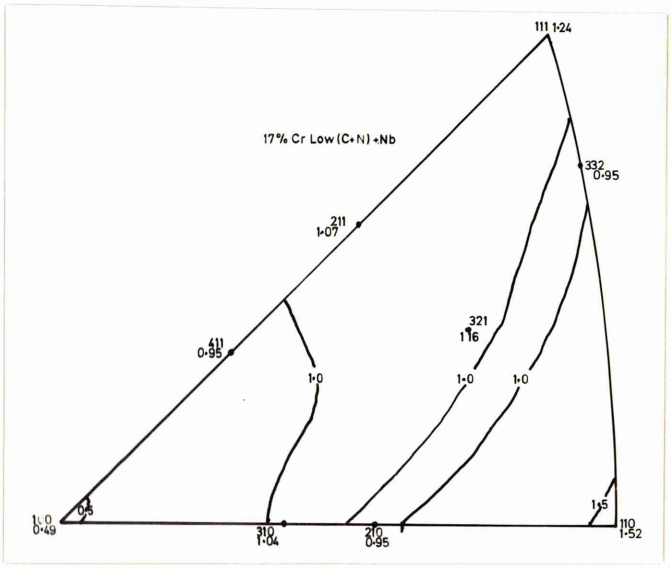
17% Cr Low (C+N) +Nb
111 1·24
332
0·95
211
1·07
321
1·16
411
0·95
1·0
1·0
1·0
1·0
0·5
1·5
110
1·52
310
1·04
210
0·95

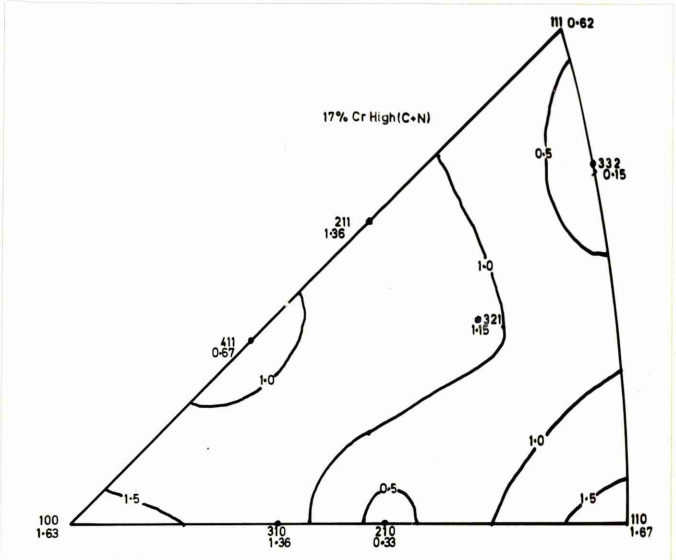
17% Cr High (C+N)
111 0·62
0·5
332
0·15
211
1·36
1·0
321
1·15
411
0·67
1·0
1·0
1·5
0·5
1·5
100
1·63
310
1·36
210
0·33
110
1·67

Fig (69)

An inverse pole figure for a
17%Cr low(C+N) + Ti steel
in the hot rolled and
annealed condition

Fig (70)

The effect of cold work on the
texture development in a
17%Cr low(C+N) steel

Fig (71)

The effect of cold work on the
texture development in a
17%Cr high(C+N) steel

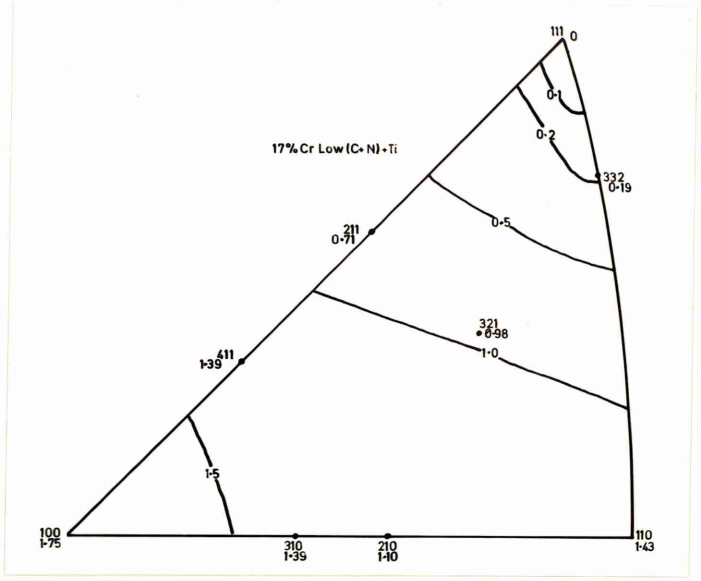
17% Cr Low (C+N)+Ti
111
0
0·1
0·2
332
0·19
0·5
211
0·71
321
0·98
1·0
411
1·39
1·5
100
1·75
310
1·39
210
1·10
110
1·43

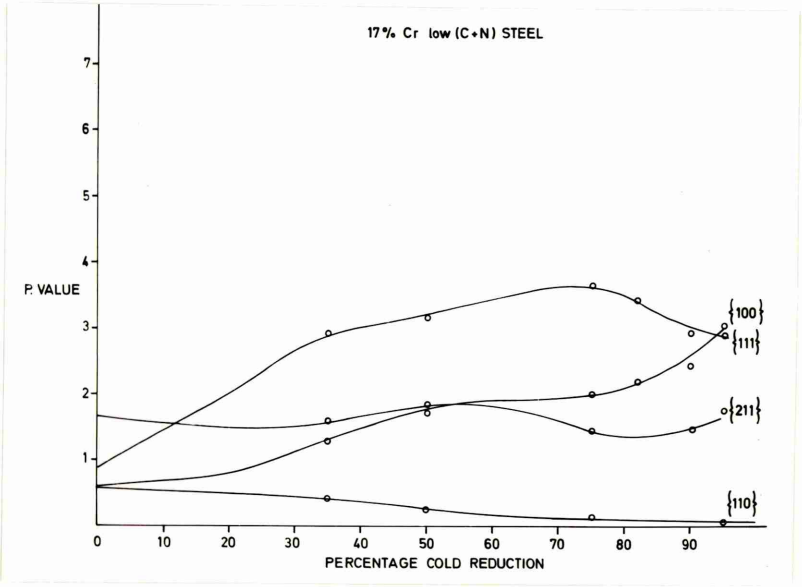
17% Cr low (C+N) STEEL
P. VALUE
PERCENTAGE COLD REDUCTION
{100}
{111}
{211}
{110}

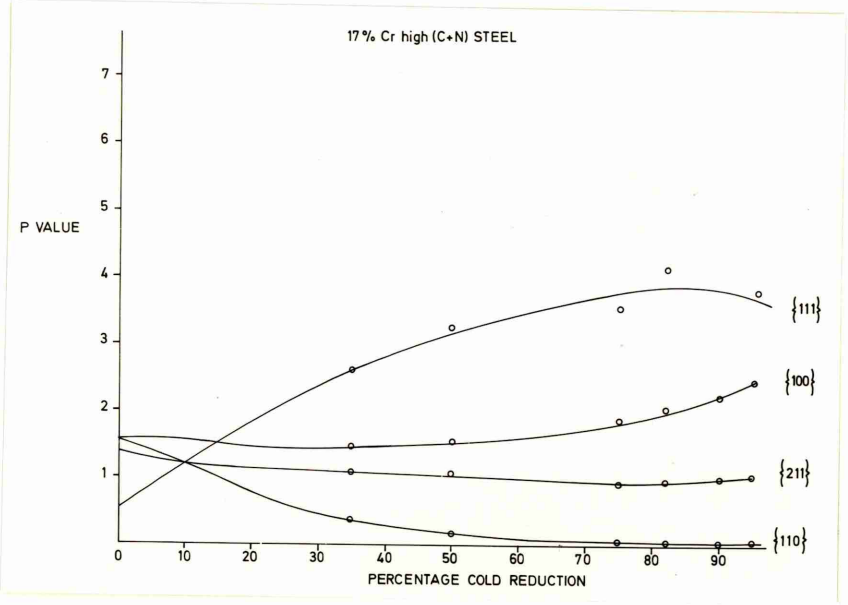
17% Cr high (C+N) STEEL
P VALUE
PERCENTAGE COLD REDUCTION
{111}
{100}
{211}
{110}

Fig (72)

The effect of cold work on the texture development in a 17%Cr low(C+N) + Ti steel

Fig (73)

The effect of cold work on the texture development in a 17%Cr low(C+N) + Nb steel

Fig (74)

The effect of cold work on the texture development in a 17%Cr high(C+N) + Nb steel

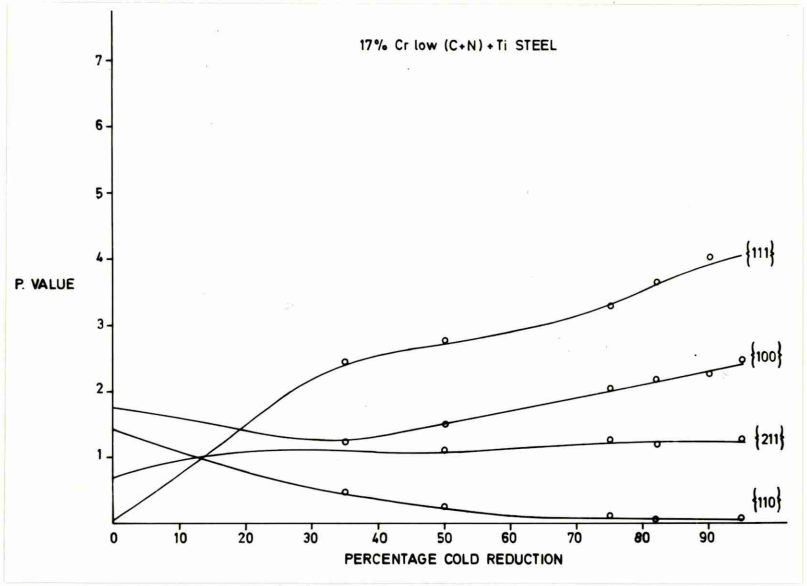
17% Cr low (C+N) + Ti STEEL
P. VALUE
PERCENTAGE COLD REDUCTION
{111}
{100}
{211}
{110}

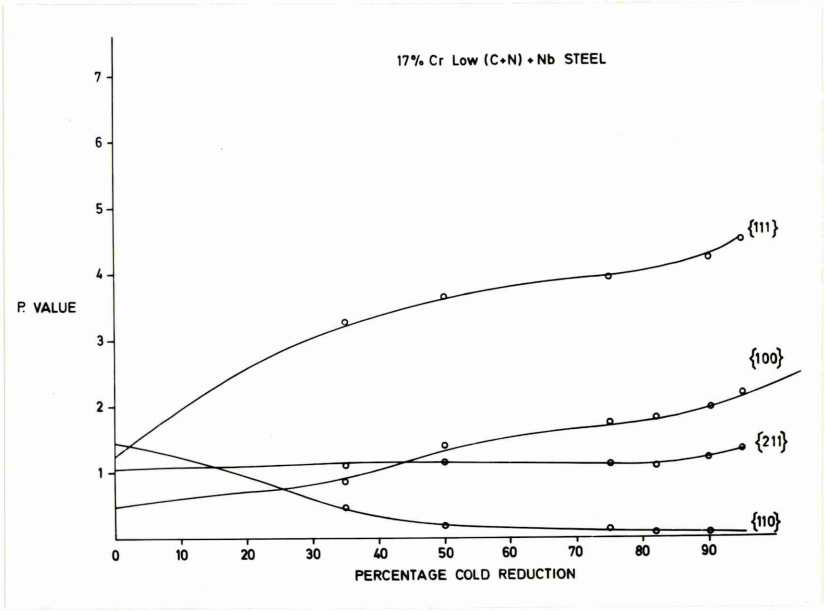
17% Cr Low (C+N) + Nb STEEL
P. VALUE
PERCENTAGE COLD REDUCTION
{111}
{100}
{211}
{110}

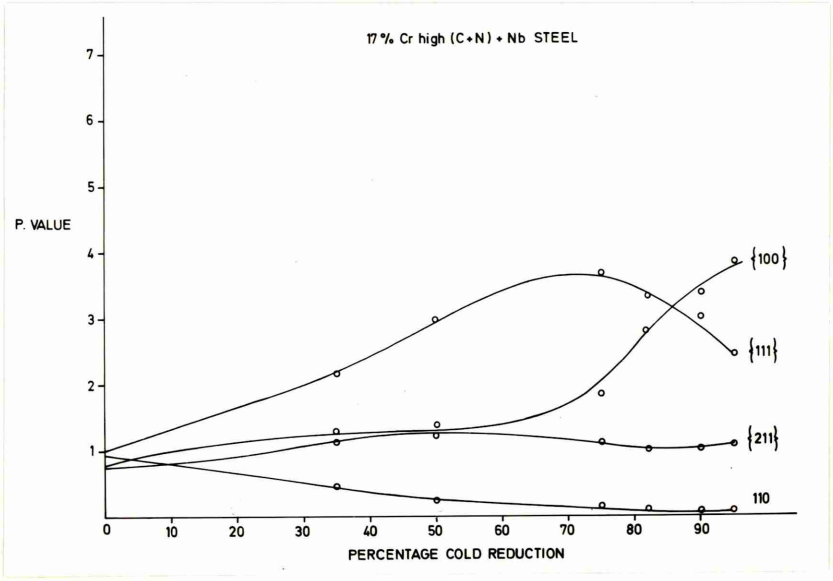
17% Cr high (C+N) + Nb STEEL
P. VALUE
PERCENTAGE COLD REDUCTION
{100}
{111}
{211}
110

Fig (75)

The effect of cold work on the texture development in a 17%Cr low(C+N) 1%Mo steel

Fig (76)

The effect of cold work on the texture development in a 17%Cr high(C+N) 1%Mo steel

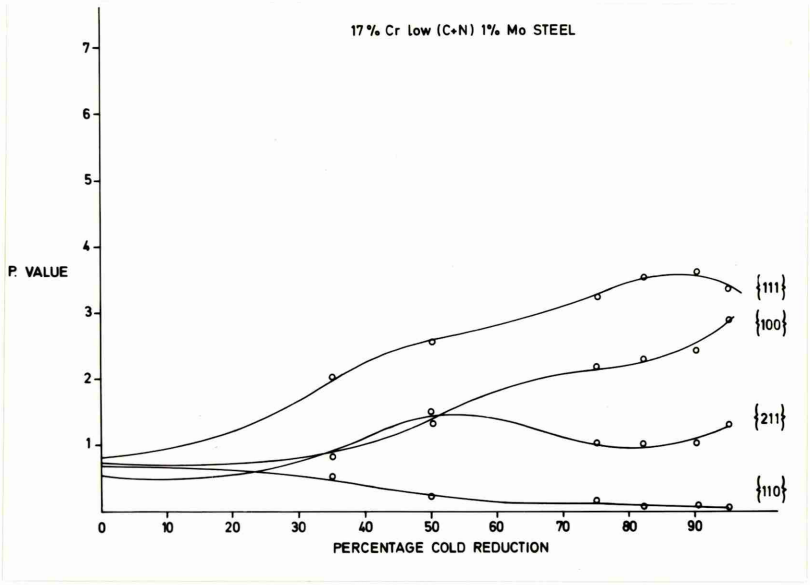
17 % Cr low (C+N) 1% Mo STEEL
P. VALUE
PERCENTAGE COLD REDUCTION
{111}
{100}
{211}
{110}

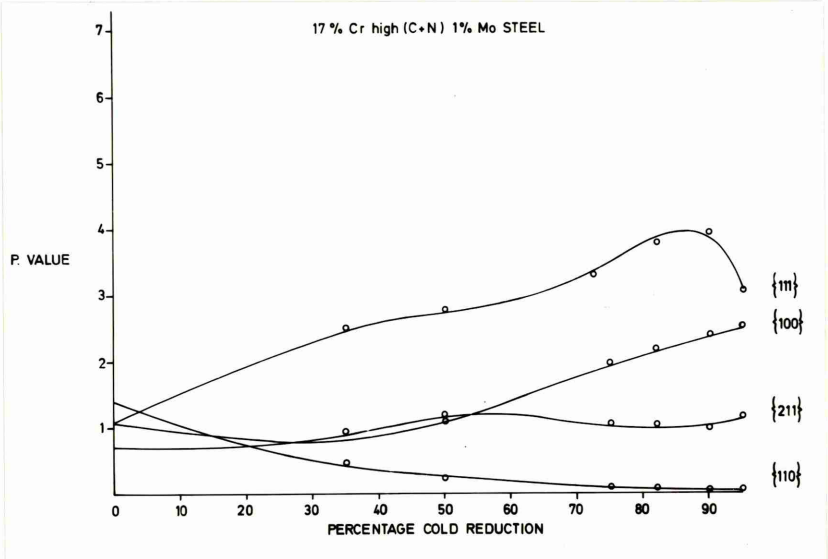
17 % Cr high (C+N) 1% Mo STEEL
P. VALUE
PERCENTAGE COLD REDUCTION
{111}
{100}
{211}
{110}

Fig (77)

The effect of cold work on the texture development in a 25%Cr low(C+N) steel

Fig (78)

The effect of cold work on the texture development in a 25%Cr low(C+N) 1%Mo steel

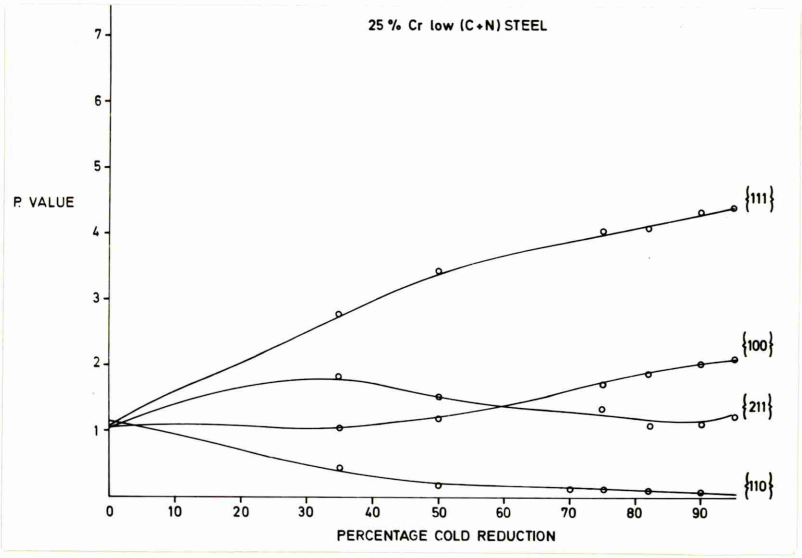
25 % Cr low (C+N) STEEL
P. VALUE
7
6
5
4
3
2
1
0
10
20
30
40
50
60
70
80
90
PERCENTAGE COLD REDUCTION
{111}
{100}
{211}
{110}

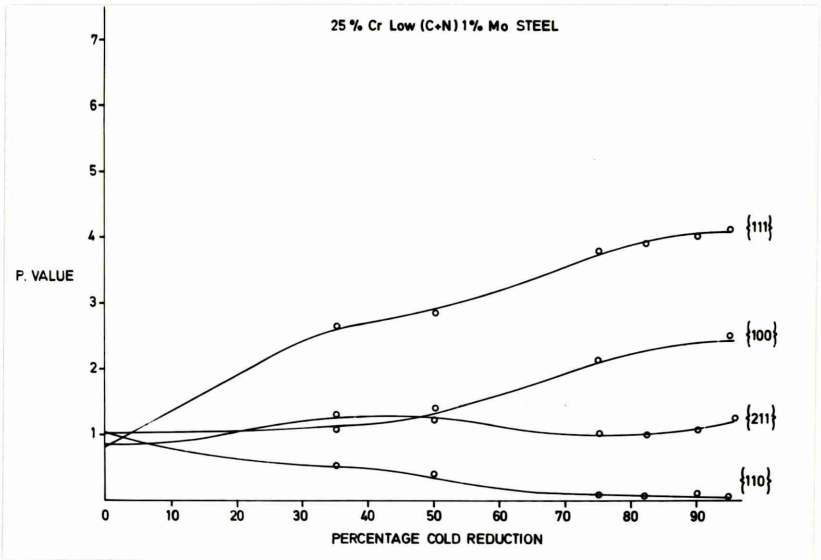
25 % Cr Low (C+N) 1% Mo STEEL
P. VALUE
7
6
5
4
3
2
1
0
10
20
30
40
50
60
70
80
90
PERCENTAGE COLD REDUCTION
{111}
{100}
{211}
{110}

Fig (79a)

A full pole figure of
a 17%Cr high(C+N) steel
after 35% reduction

Fig (79b)

A full pole figure of
a 17%Cr high(C+N) steel
after 50% reduction

Fig (79c)

A full pole figure of
a 17%Cr high(C+N) steel
after 75% reduction

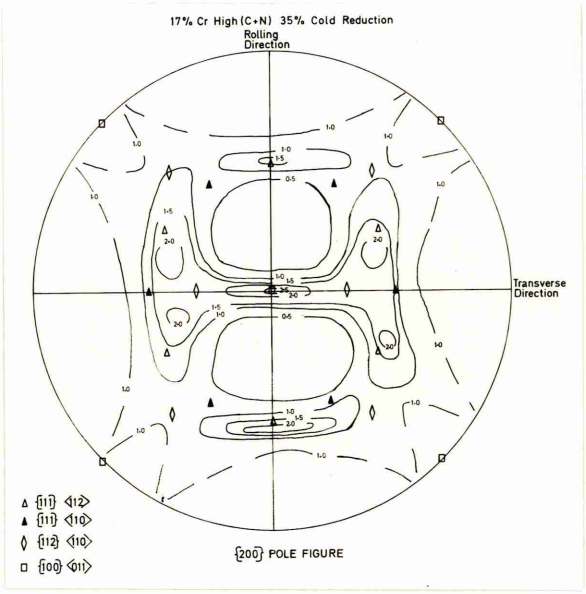
17% Cr High (C+N) 35% Cold Reduction
Rolling Direction
Transverse Direction
△ {111} ⟨112⟩
▲ {111} ⟨110⟩
◊ {112} ⟨110⟩
□ {100} ⟨011⟩
{200} POLE FIGURE

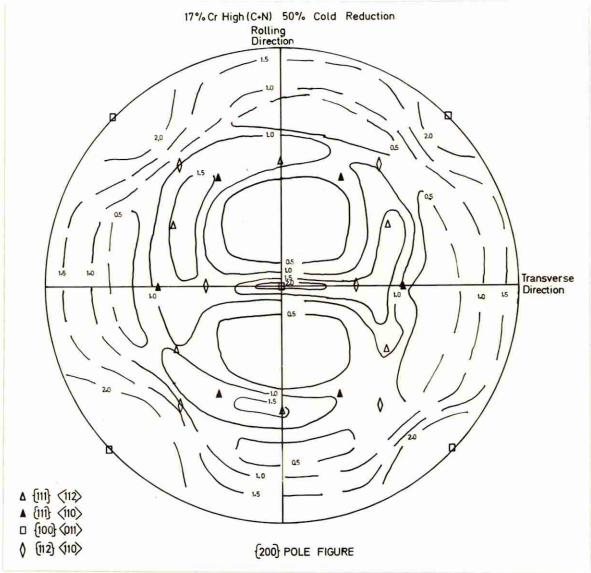
17% Cr High (C+N) 50% Cold Reduction
Rolling Direction
Transverse Direction
△ {111} ⟨112⟩
▲ {111} ⟨110⟩
□ {100} ⟨011⟩
◊ {112} ⟨110⟩
{200} POLE FIGURE

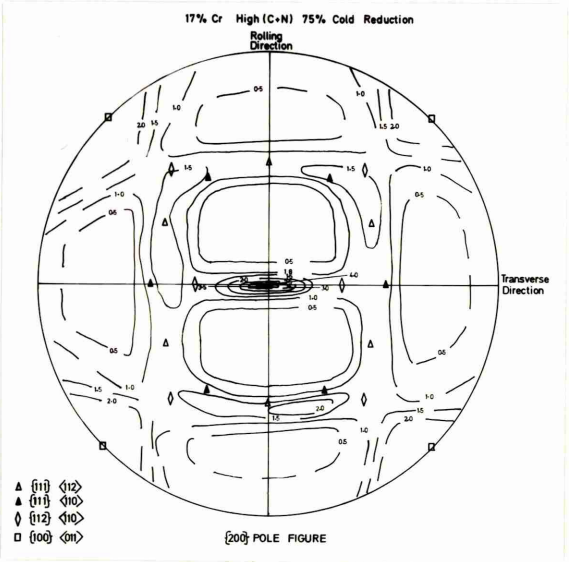
17% Cr High (C+N) 75% Cold Reduction
Rolling Direction
Transverse Direction
△ {111} ⟨112⟩
▲ {111} ⟨110⟩
◊ {112} ⟨110⟩
□ {100} ⟨011⟩
{200} POLE FIGURE

Fig (80a)

A full pole figure of
a 17%Cr low(C+N) steel
after 35% reduction

Fig (80b)

A full pole figure of
a 17%Cr low(C+N) steel
after 75% reduction

Fig (80c)

A full pole figure of
a 17%Cr low(C+N) steel
after 95% reduction

Fig (81)

A full pole figure of
a 17%Cr low(C+N) steel
after 95% reduction

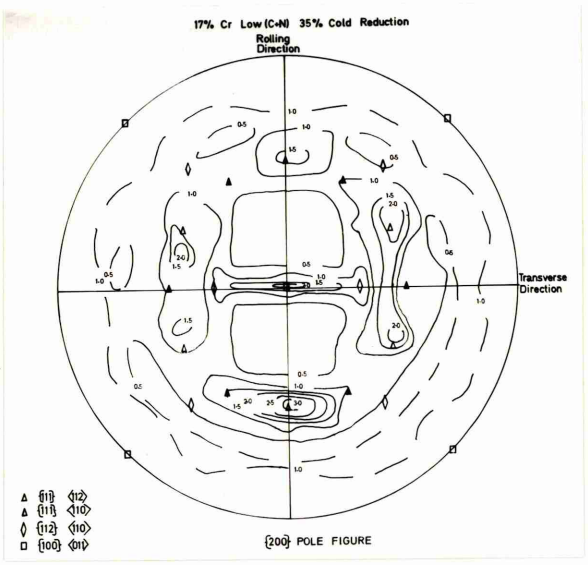
17% Cr Low (C+N) 35% Cold Reduction
Rolling Direction
Transverse Direction
△ {111} ⟨112⟩
▲ {111} ⟨110⟩
◊ {112} ⟨110⟩
□ {100} ⟨011⟩
{200} POLE FIGURE

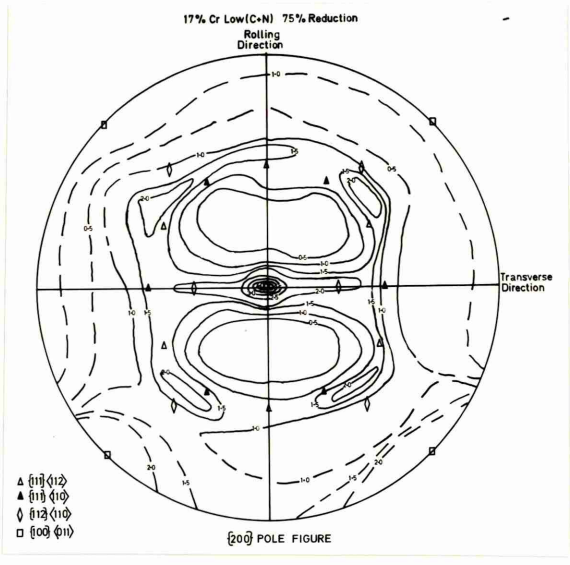
17% Cr Low (C+N) 75% Reduction
Rolling Direction
Transverse Direction
△ {111} ⟨112⟩
▲ {111} ⟨110⟩
◊ {112} ⟨110⟩
□ {100} ⟨011⟩
{200} POLE FIGURE

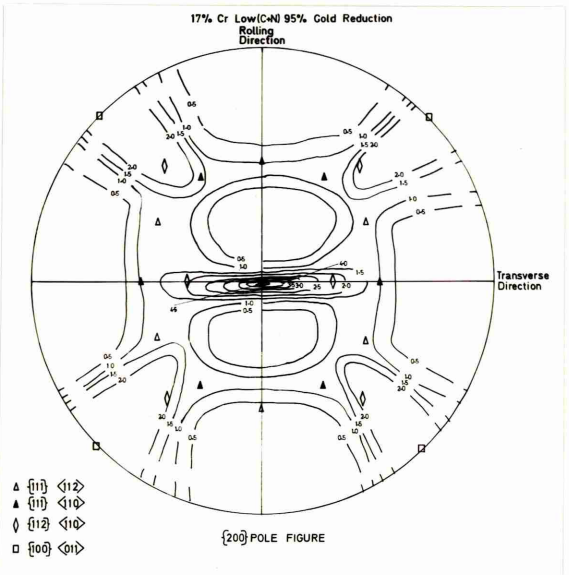
17% Cr Low (C+N) 95% Cold Reduction
Rolling Direction
Transverse Direction
△ {111} ⟨112⟩
▲ {111} ⟨110⟩
◊ {112} ⟨110⟩
□ {100} ⟨011⟩
{200} POLE FIGURE

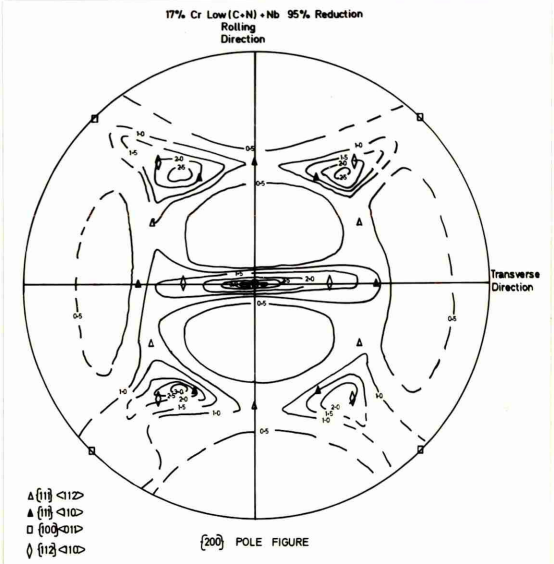
17% Cr Low (C+N) + Nb 95% Reduction
Rolling Direction
Transverse Direction
△ {111} ⟨112⟩
▲ {111} ⟨110⟩
□ {100} ⟨011⟩
◊ {112} ⟨110⟩
{200} POLE FIGURE

Fig (82)

The effect of cold reduction on the recrystallisation textures developed in a 17%Cr low(C+N) steel after annealing at 800°C

Fig (83)

The effect of cold reduction on the recrystallisation textures developed in a 17%Cr high(C+N) steel after annealing at 800°C

Fig (84)

The effect of cold reduction on the recrystallisation textures developed in a 17%Cr low(C+N) + Nb steel after annealing at 990°C

Fig (85)

The effect of cold reduction on the recrystallisation textures developed in a 17%Cr high(C+N) + Nb steel after annealing at 990°C

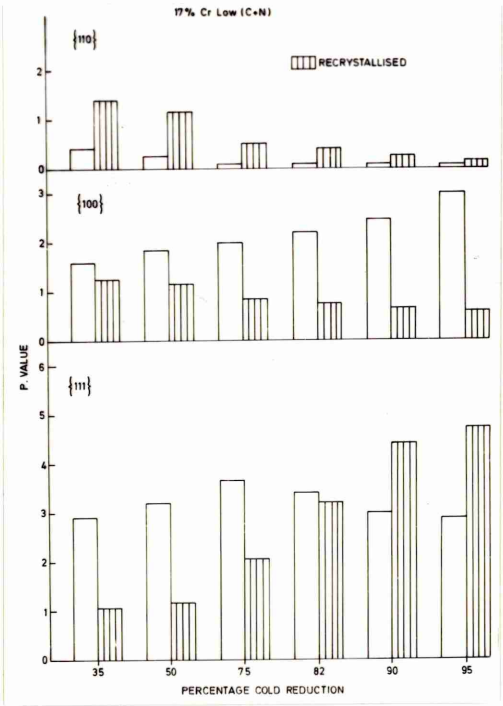
17% Cr Low (C+N)
{110}
RECRYSTALLISED
{100}
{111}
P. VALUE
PERCENTAGE COLD REDUCTION
35
50
75
82
90
95

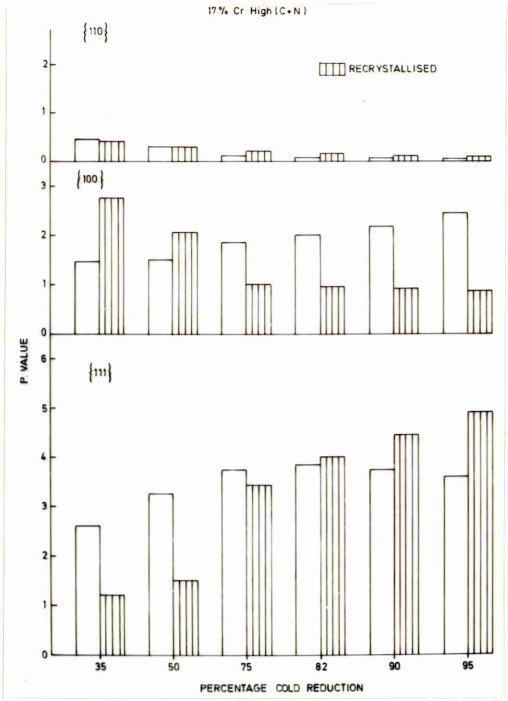
17% Cr High (C+N)
{110}
RECRYSTALLISED
{100}
{111}
P. VALUE
PERCENTAGE COLD REDUCTION
35
50
75
82
90
95

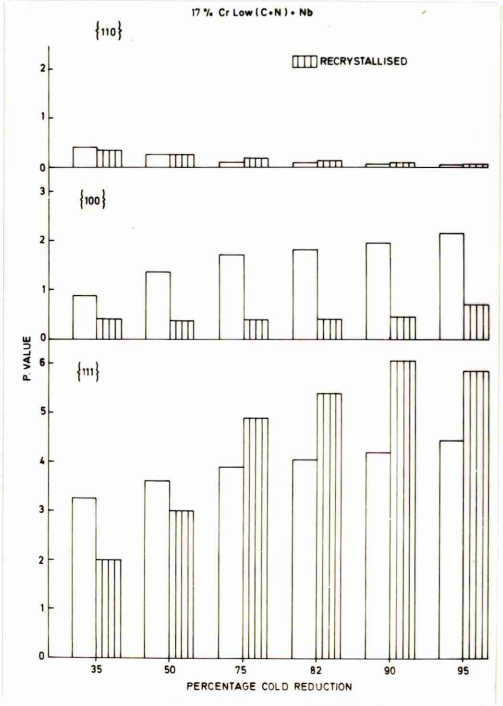
17% Cr Low (C+N) + Nb
{110}
RECRYSTALLISED
{100}
{111}
P. VALUE
PERCENTAGE COLD REDUCTION
35
50
75
82
90
95

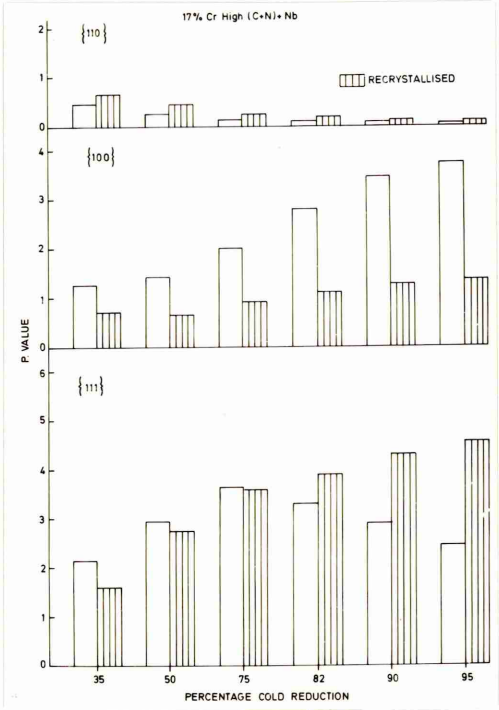
17% Cr High (C+N) + Nb
{110}
RECRYSTALLISED
{100}
{111}
P. VALUE
PERCENTAGE COLD REDUCTION
35
50
75
82
90
95

Fig 86

The effect of cold reduction on the recrystallisation textures developed in a 17% Cr low (C+N) + Ti steel after annealing at 800°C

Fig (87)

The effect of cold reduction on the recrystallisation textures developed in a 17%Cr low (C+N) 1% Mo steel, after annealing at 850°C

Fig (88)

The effect of cold reduction on the recrystallisation textures developed in a 17%Cr high(C+N) steel after annealing at 850°C

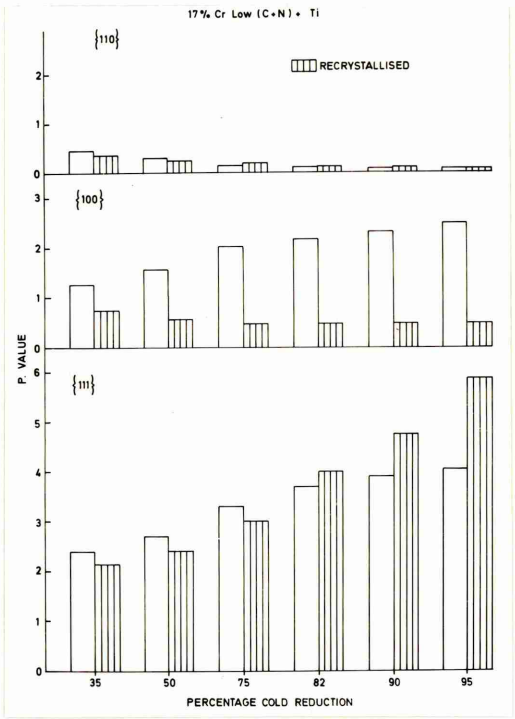
17 % Cr Low (C+N) + Ti
{110}
RECRYSTALLISED
{100}
{111}
P. VALUE
0
1
2
3
4
5
6
35
50
75
82
90
95
PERCENTAGE COLD REDUCTION

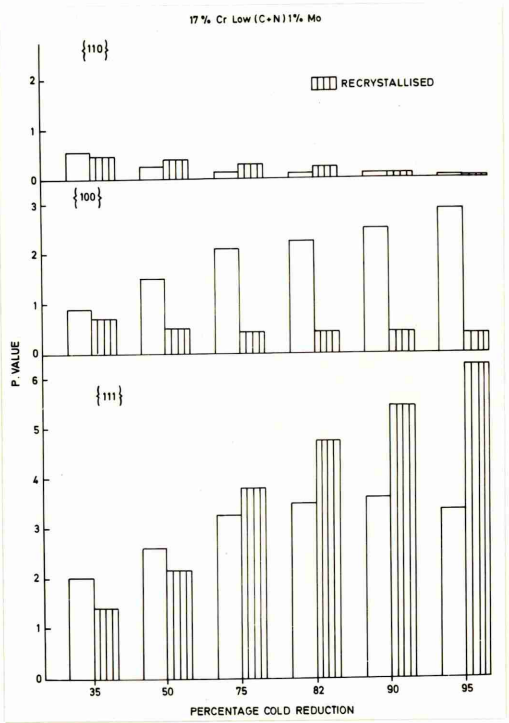
17 % Cr Low (C+N) 1% Mo
{110}
RECRYSTALLISED
{100}
{111}
P. VALUE
0
1
2
3
4
5
6
35
50
75
82
90
95
PERCENTAGE COLD REDUCTION

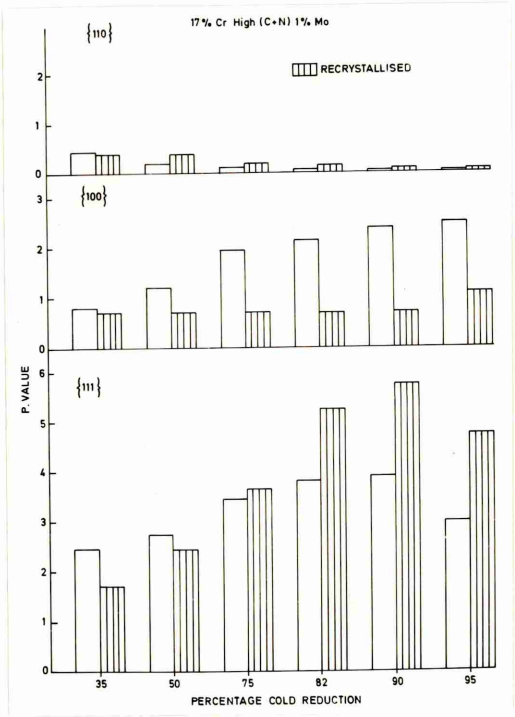
17 % Cr High (C+N) 1% Mo
{110}
RECRYSTALLISED
{100}
{111}
P. VALUE
0
1
2
3
4
5
6
35
50
75
82
90
95
PERCENTAGE COLD REDUCTION

Fig (89)

The effect of cold reduction on the recrystallisation textures developed in a 25%Cr low(C+N) steel after annealing at 800°C

Fig (90)

The effect of cold reduction on the recrystallisation textures developed in a 25%Cr low(C+N) steel after annealing at 850°C

Fig (91a)

Full pole figure for a 17%Cr low(C+N) steel showing the recrystallisation textures after 35% cold reduction and annealing at 800°C

Fig (91b)

Full pole figure for a 17%Cr low(C+N) steel showing the recrystallisation textures after 50% cold reduction and annealing at 800°C

Fig (91c)

Full pole figure for a 17%Cr low(C+N) steel showing the recrystallisation textures after 75% cold reduction and annealing at 800°C

Fig (91d)

Full pole figure for a 17%Cr low(C+N) steel showing the recrystallisation textures after 95% cold reduction and annealing at 800°C

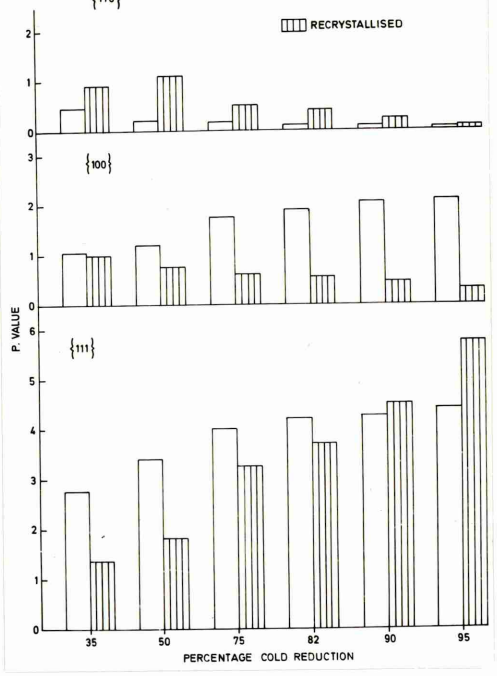
RECRYSTALLISED
{100}
{111}
P. VALUE
PERCENTAGE COLD REDUCTION
35
50
75
82
90
95

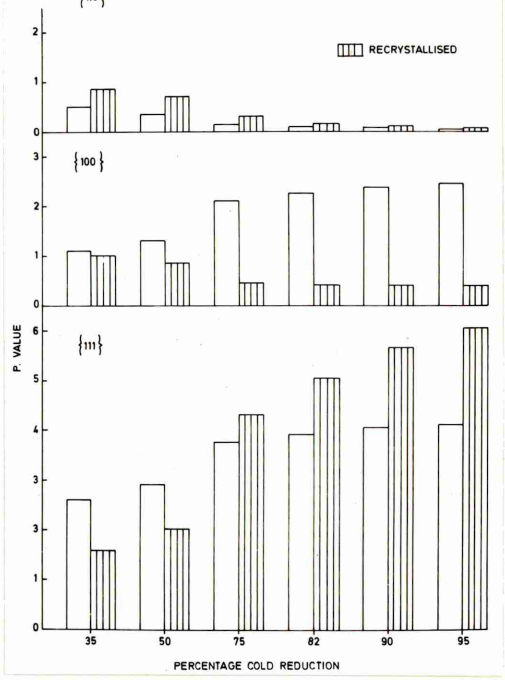
RECRYSTALLISED
{100}
{111}
P. VALUE
PERCENTAGE COLD REDUCTION
35
50
75
82
90
95

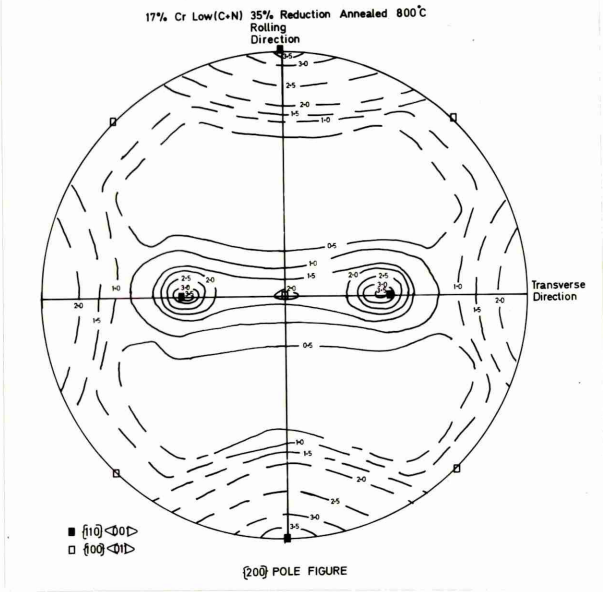
17% Cr Low(C+N) 35% Reduction Annealed 800°C
Rolling Direction
Transverse Direction
{110}<001>
{100}<011>
{200} POLE FIGURE

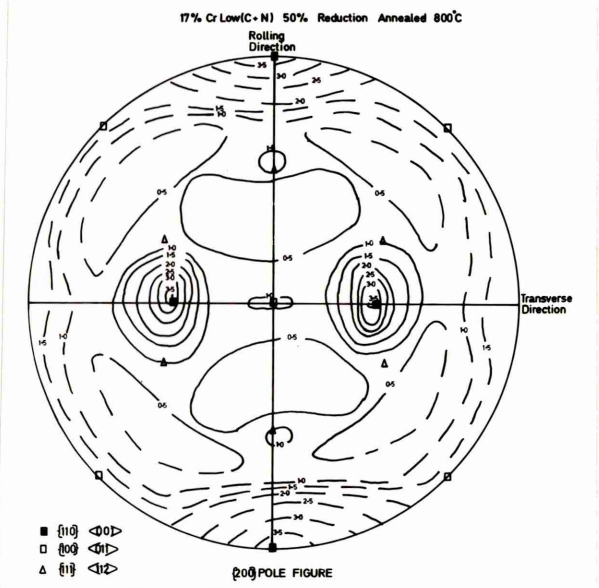
17% Cr Low(C+N) 50% Reduction Annealed 800°C
Rolling Direction
Transverse Direction
{110} <001>
{100} <011>
{111} <112>
{200} POLE FIGURE

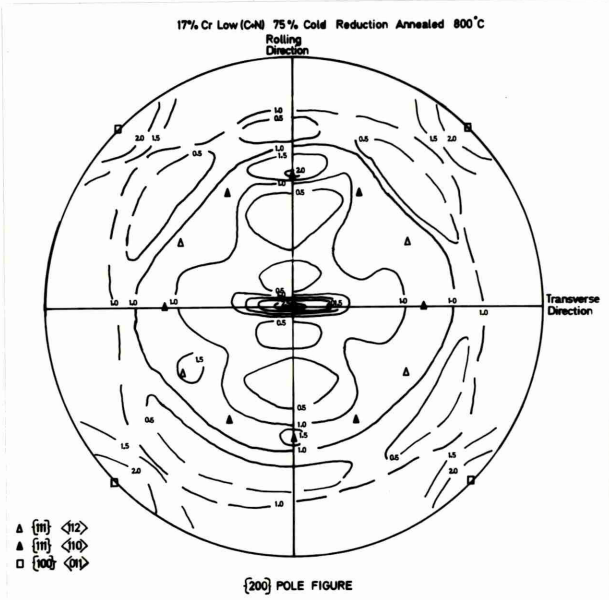
17% Cr Low (C+N) 75% Cold Reduction Annealed 800°C
Rolling Direction
Transverse Direction
{111} <112>
{111} <110>
{100} <011>
{200} POLE FIGURE

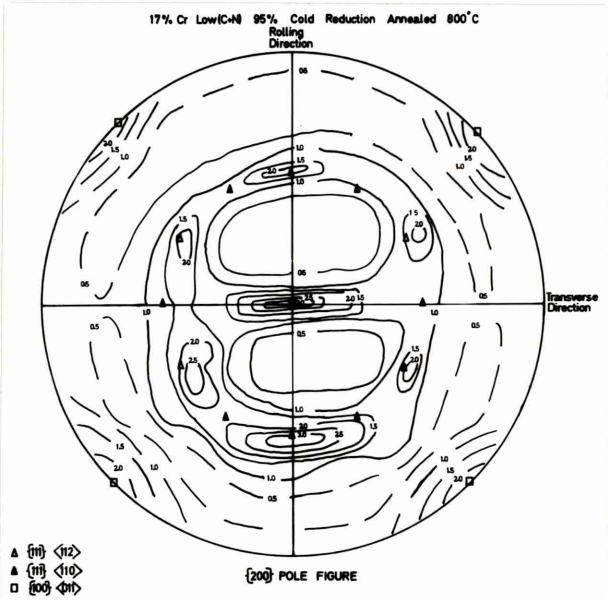
17% Cr Low(C+N) 95% Cold Reduction Annealed 800°C
Rolling Direction
Transverse Direction
{111} <112>
{111} <110>
{100} <011>
{200} POLE FIGURE

Fig (92a)

A full pole figure showing the recrystallisation textures developed in a 17%Cr high(C+N) steel after 35% reduction and annealing at 800°C

Fig (92b)

A full pole figure showing the recrystallisation textures developed in a 17%Cr high(C+N) steel after 50% reduction and annealing at 800°C

Fig (92c)

A full pole figure showing the recrystallisation textures developed in a 17%Cr high(C+N) steel after 75% reduction and annealing at 800°C

Fig (93a)

A full pole figure showing the recrystallisation textures developed in a 17%Cr low(C+N) + Nb steel after 35% reduction and annealing at 990°C

Fig (93b)

A full pole figure showing the recrystallisation textures developed in a 17%Cr low(C+N) + Nb steel after 50% reduction and annealing at 990°C

Fig (93c)

A full pole figure showing the recrystallisation textures developed in a 17%Cr low(C+N) + Nb steel after 75% reduction and annealing at 990°C

17% Cr High(C+N) 35% Cold Reduction Annealed 800°C

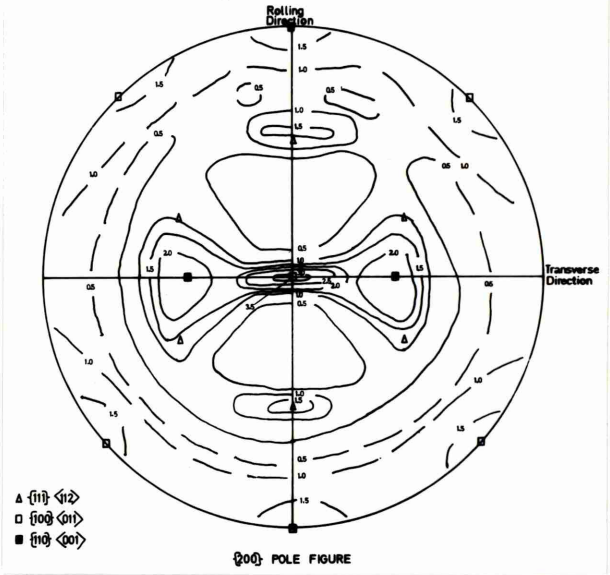

{200} POLE FIGURE

17% Cr High(C+N) 50% Cold Reduction Annealed 800°C

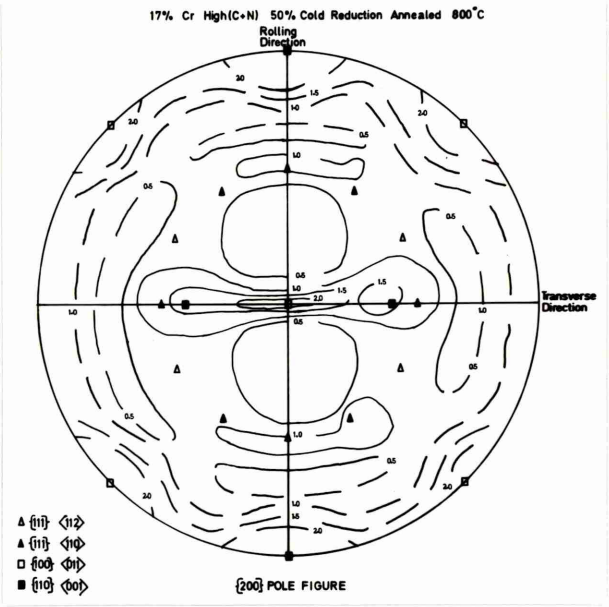

{200} POLE FIGURE

17% Cr High(C+N) 75% Cold Reduction Annealed 800°C

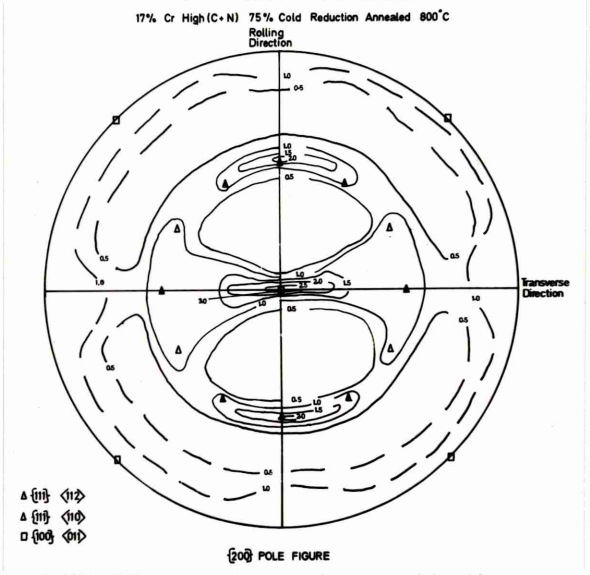

{200} POLE FIGURE

17% Cr Low(C+N)+Nb 35% Cold Reduction Annealed 990°C

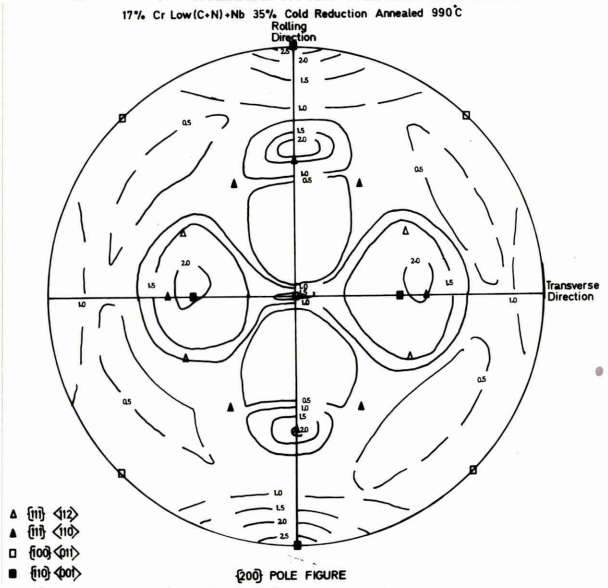

{200} POLE FIGURE

17% Cr Low(C+N)+Nb 50% Cold Reduction Annealed 990°C

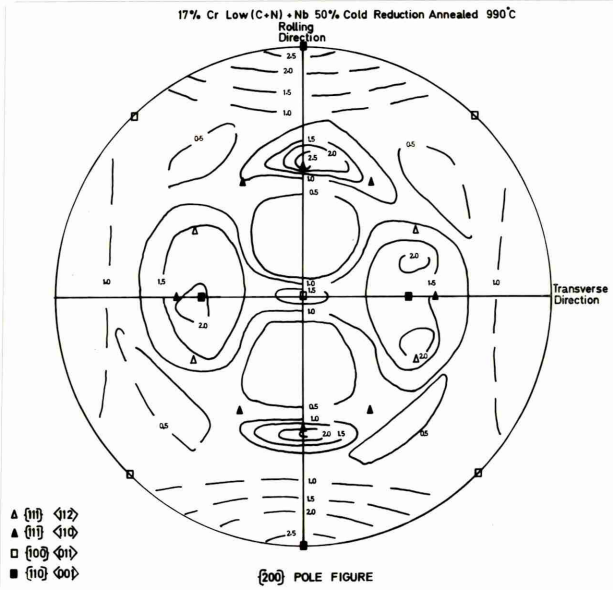

{200} POLE FIGURE

17% Cr Low(C+N)+Nb 75% Cold Reduction Annealed 990°C

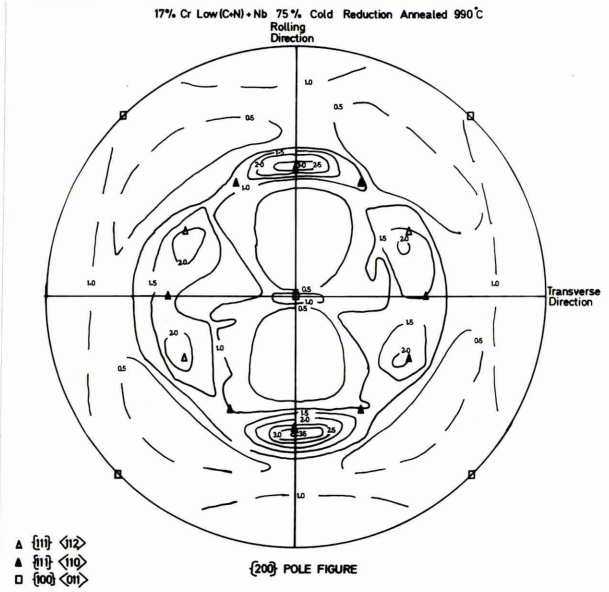

{200} POLE FIGURE

Fig (94)

A full pole figure showing the recrystallisation textures developed in a 17%Cr low(C+N) + Ti steel after 75% reduction and annealing at 800°C

Fig (95)

A full pole figure showing the recrystallisation textures developed in a 17%Cr high(C+N) + Nb steel after 75% reduction and annealing at 990°C

Fig (96)

A full pole figure showing the recrystallisation textures developed in a 17%Cr low(C+N) 1%Mo steel after 75% reduction and annealing at 850°C

Fig (97)

A full pole figure showing the recrystallisation textures developed in a 17%Cr high(C+N) 1%Mo steel after 75% reduction and annealing at 850°C

Fig (98)

A full pole figure showing the recrystallisation textures developed in a 25%Cr low(C+N) steel after 75% reduction and annealing at 800°C

Fig (99)

A full pole figure showing the recrystallisation textures developed in a 25%Cr low(C+N) 1%Mo steel after 75% reduction and annealing at 850°C

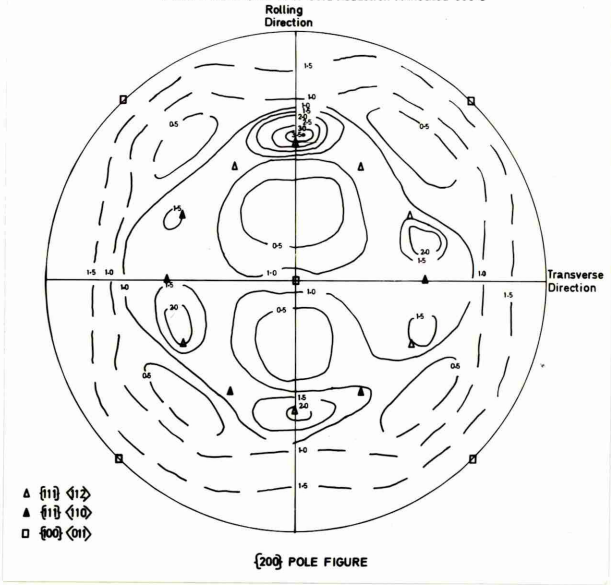

{200} POLE FIGURE

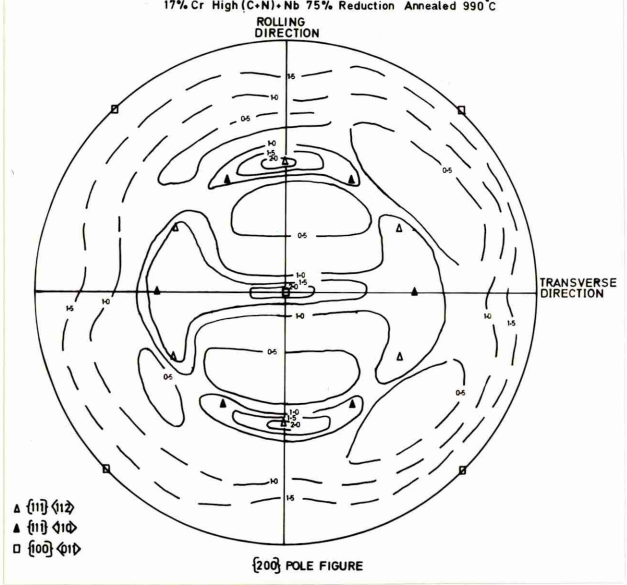

{200} POLE FIGURE

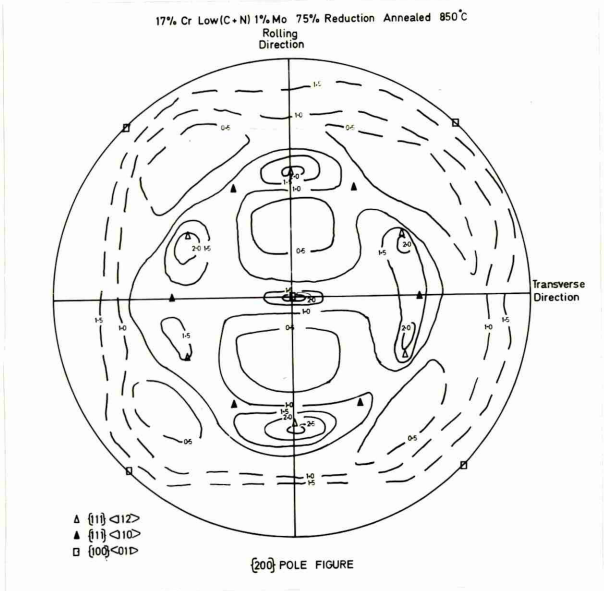

{200} POLE FIGURE

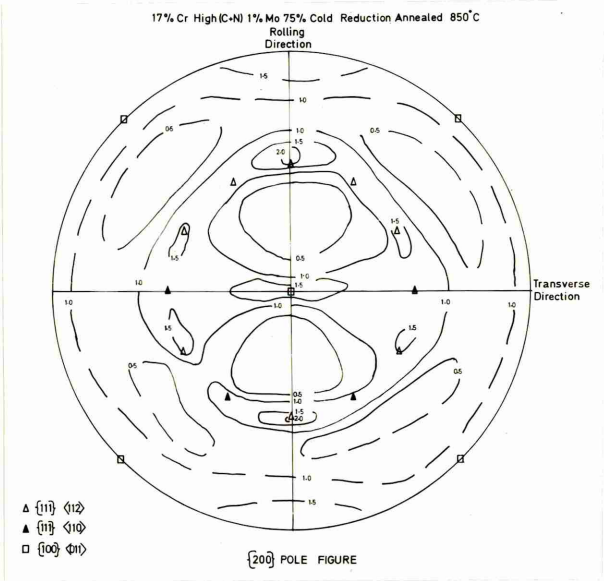

{200} POLE FIGURE

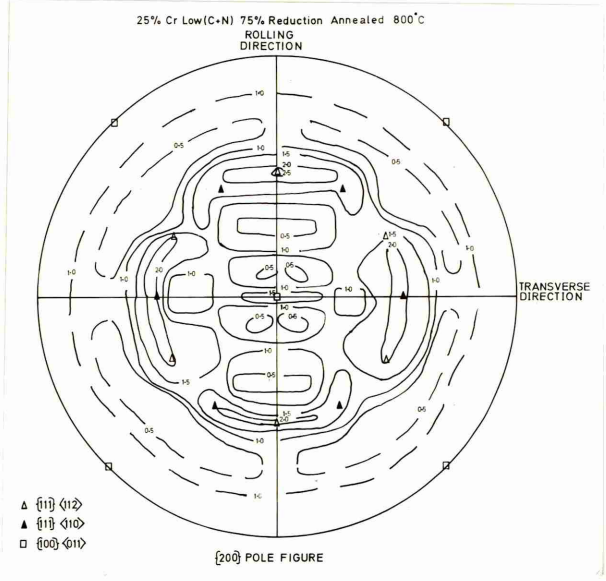

{200} POLE FIGURE

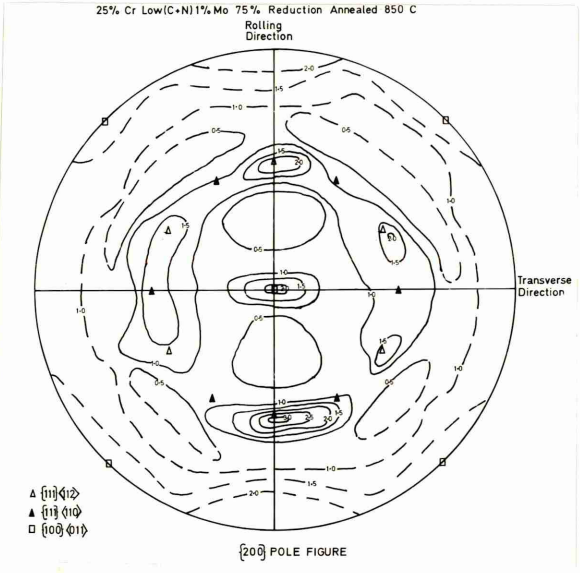

{200} POLE FIGURE

Fig (100a)

Optical micrograph
17%Cr low(C+N) steel
after 35% cold reduction

Magnification X 160

Fig (100b) (1)

As Fig (100a) but
specimen examined under
polarised light

Magnification X 160

Fig (100b) (2)

As Fig (100b) (1) but
analyser rotated by 90^{o}

Magnification X 160

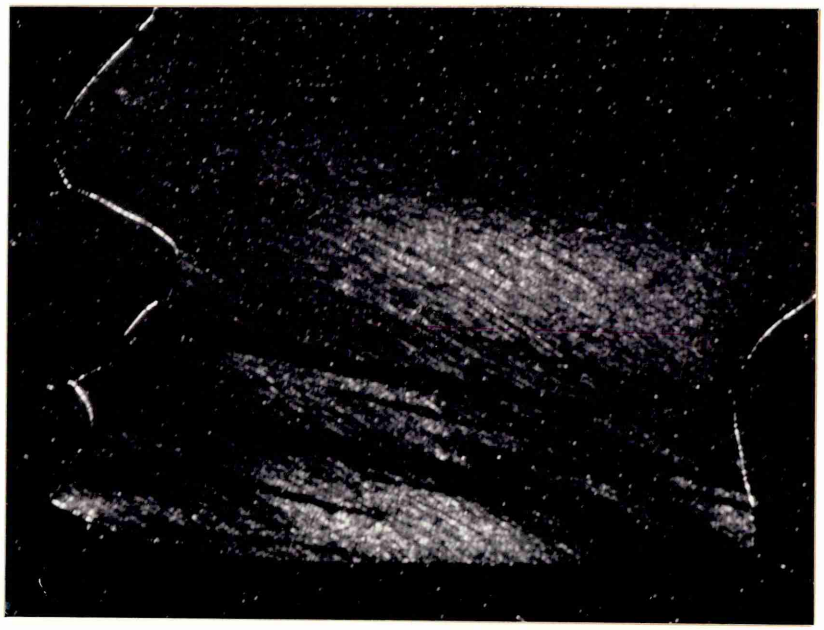

Fig (100c)

Optical micrograph
17%Cr low(C+N) steel
after 75% cold reduction

Magnification X 700

Fig (100d)

Thin foil electronmicrograph
17%Cr high(C+N) 1%Mo steel
after 75% cold reduction

Magnification X 25,000

Fig (100e)

Thin foil electronmicrograph
17%Cr low(C+N) steel after
50% cold reduction

Magnification X 25,000

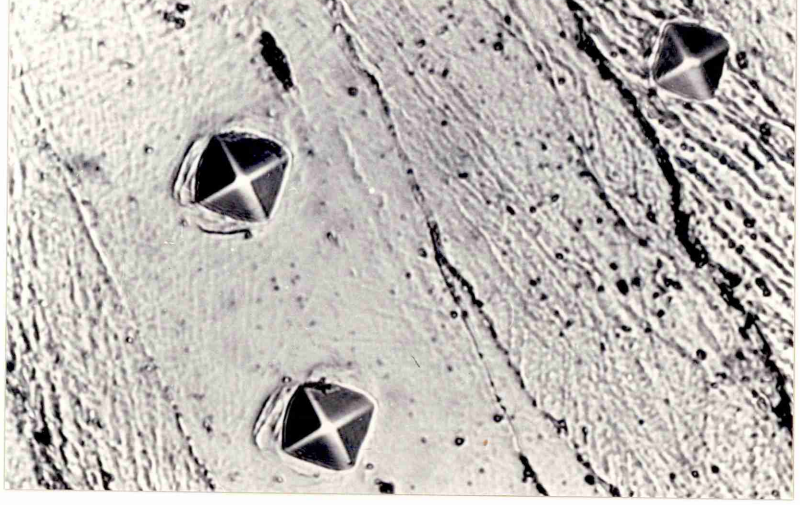

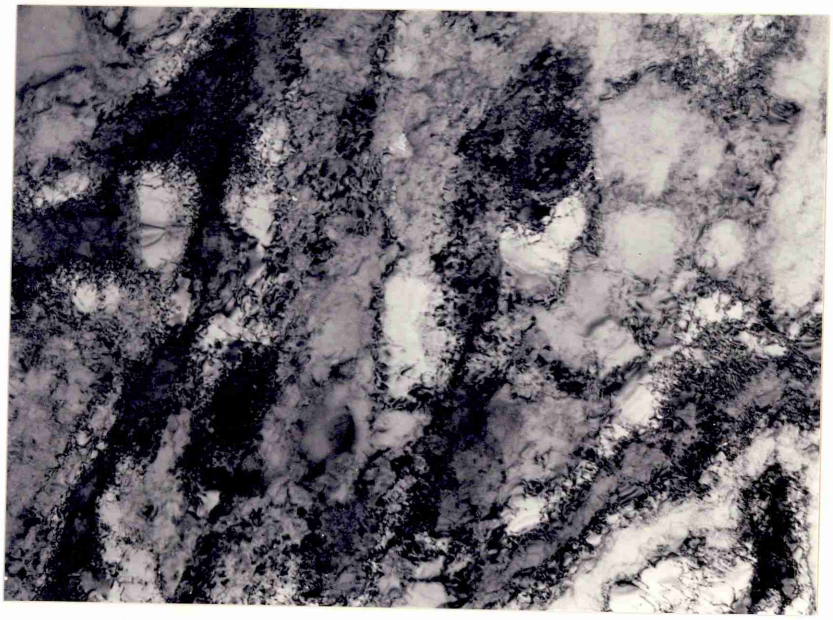

Fig (101)

Curves showing different rates of recovery between matrix grains containing deformation bands and those without deformation bands

Fig (102a)

Thin foil electronmicrograph 25%Cr low(C+N) steel after 75% cold reduction annealed for 30 seconds at 690°C

Magnification X 10,000

Fig (102b)

Thin foil electronmicrograph 25%Cr low(C+N) steel after 75% cold reduction annealed for 2 minutes at 690°C

Magnification X 4,000

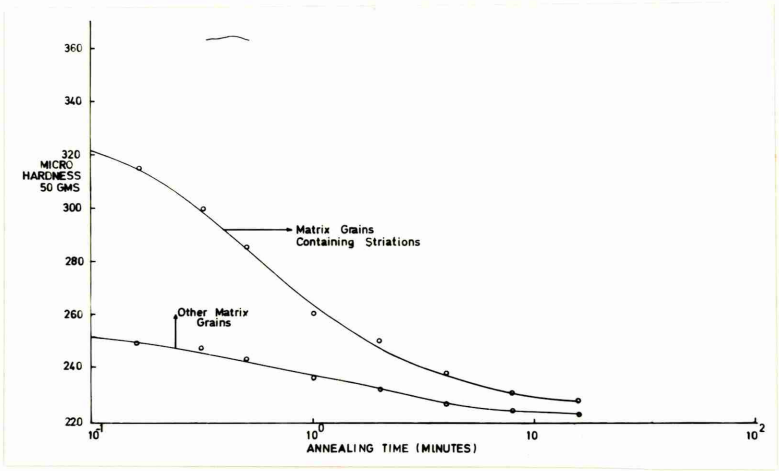
360
340
320
MICRO HARDNESS 50 GMS
300
280
260
240
220
Matrix Grains Containing Striations
Other Matrix Grains
10^{-1}
10^{0}
10
10^{2}
ANNEALING TIME (MINUTES)

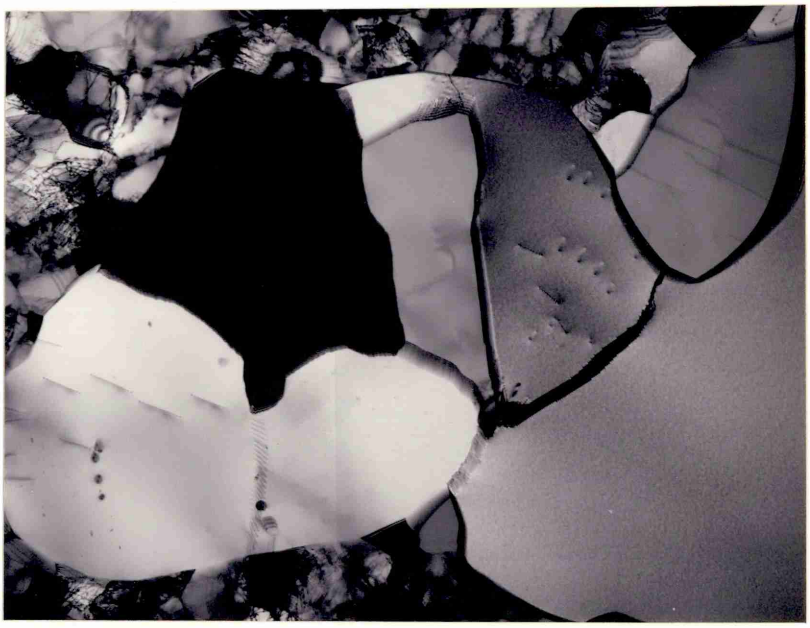

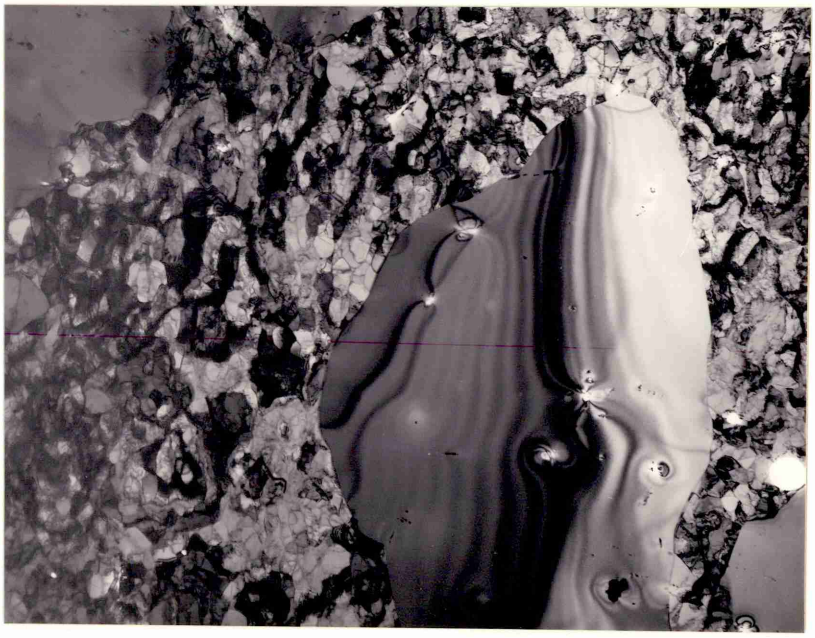

Fig (103a)

Thin foil electronmicrograph
17%Cr low(C+N) steel after
75% cold reduction and
annealed for 30 seconds at
655°C

Magnification X 75,000

Fig (103b)

Thin foil electronmicrograph
17%Cr low(C+N) steel after
75% cold reduction and
annealed for 2 minutes at
690°C

Magnification X 12,000

Fig (103c)

Optical micrograph
17%Cr low(C+N) steel after
35% cold reduction and
annealed for 2 minutes at
720°C

Magnification X 240

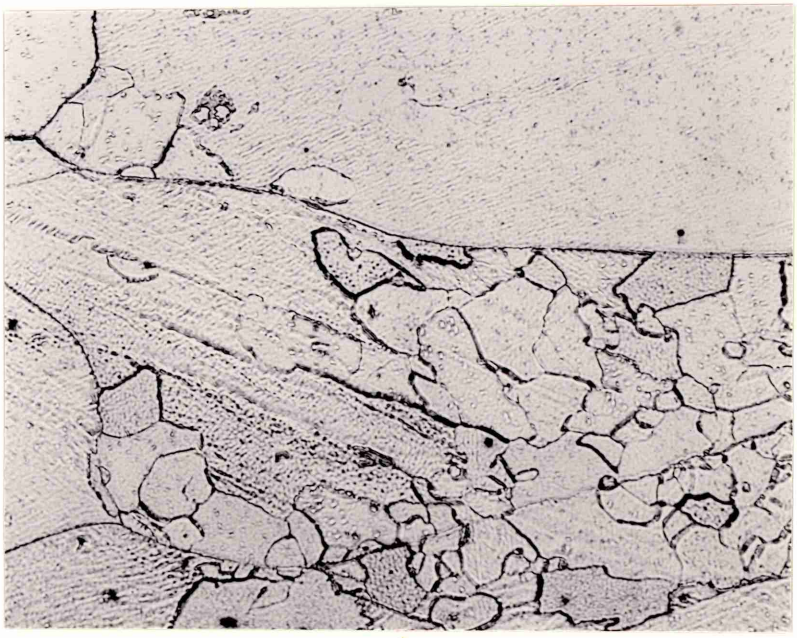

Fig (103d)

Thin foil electronmicrograph
17%Cr low(C+N) steel after
35% cold reduction and
annealed for 1 minute at
750^{o}C

Magnification X 20,000

Diffraction pattern of
recrystallised grain A and
matrix grain B

Interpretation of diffraction
pattern


A
B

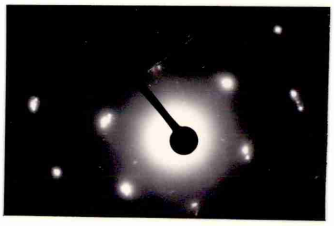

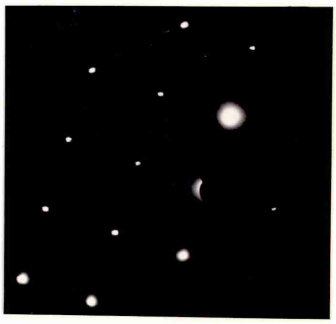

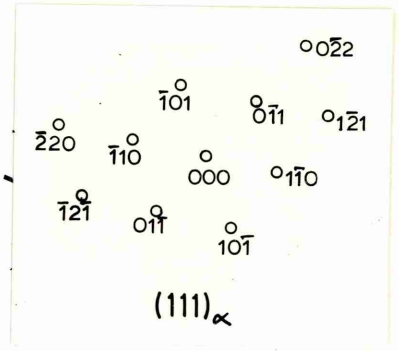
$0\bar{2}2$
$\bar{1}01$
$01\bar{1}$
$1\bar{2}1$
$\bar{2}20$
$\bar{1}10$
000
$1\bar{1}0$
$\bar{1}2\bar{1}$
$01\bar{1}$
$10\bar{1}$
$(111)_\alpha$

B

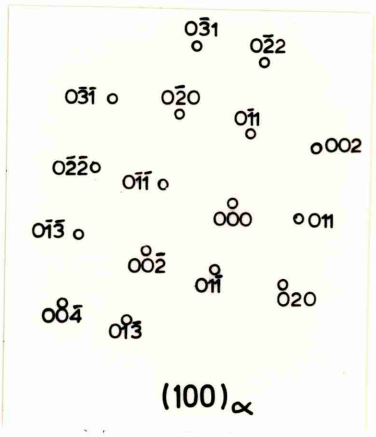
$0\bar{3}1$
$0\bar{2}2$
$03\bar{1}$
$0\bar{2}0$
$0\bar{1}1$
002
$02\bar{2}$
$01\bar{1}$
000
011
$01\bar{3}$
$00\bar{2}$
$0\bar{1}1$
020
$00\bar{4}$
$01\bar{3}$
$(100)_\alpha$

A

Fig (103e)

Optical micrograph
17%Cr low(C+N) steel after
35% cold reduction and
annealed for 2 hours at
800°C

Magnification X 160

Fig (103f)

Optical micrograph
17%Cr low(C+N) steel after
75% cold reduction and
annealed for 20 seconds at
720°C

Magnification X 160

Fig (103g)

Optical micrograph
17%Cr low(C+N) steel after
75% cold reduction and
annealed for 1 minute at
720°C

Magnification X 160

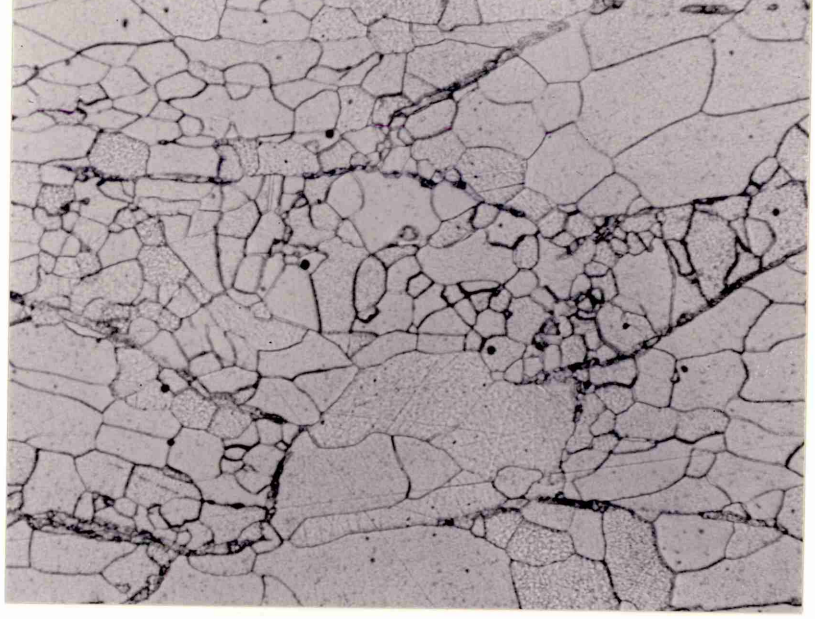

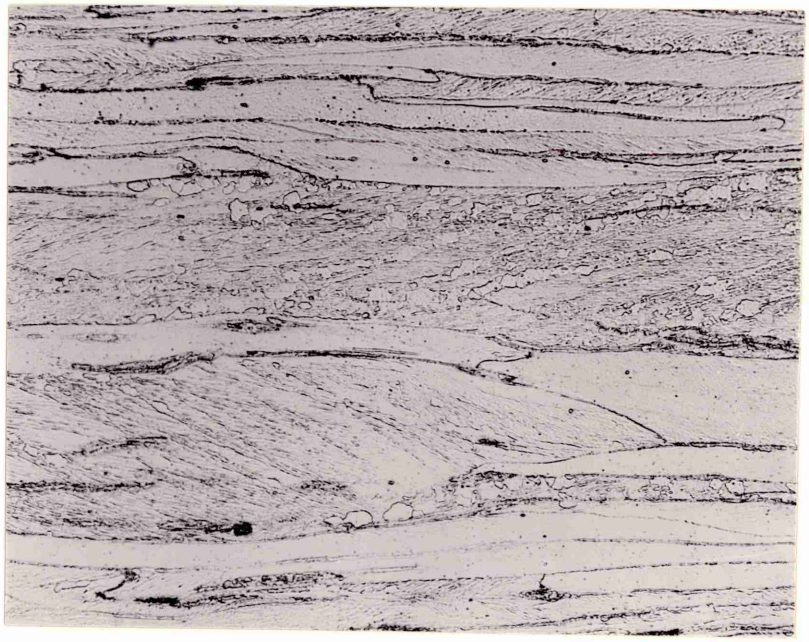

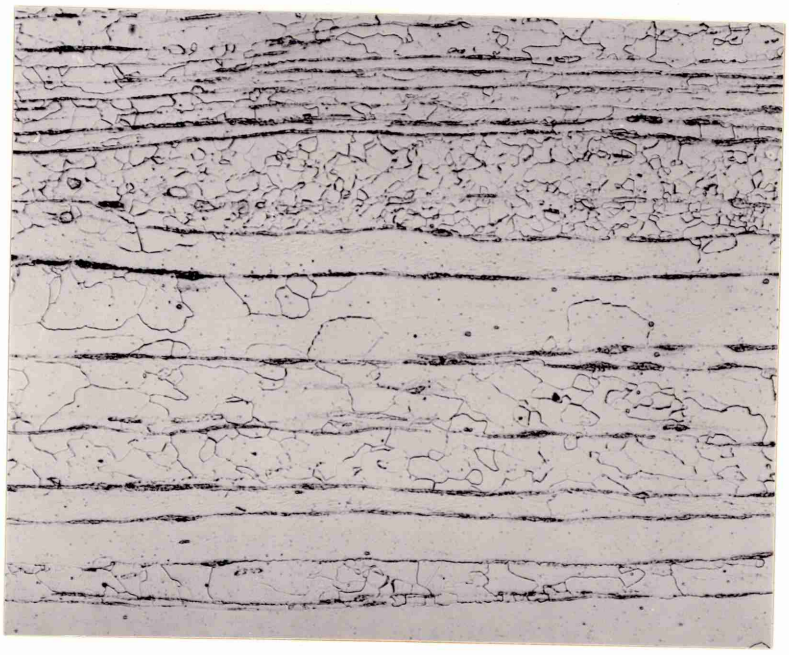

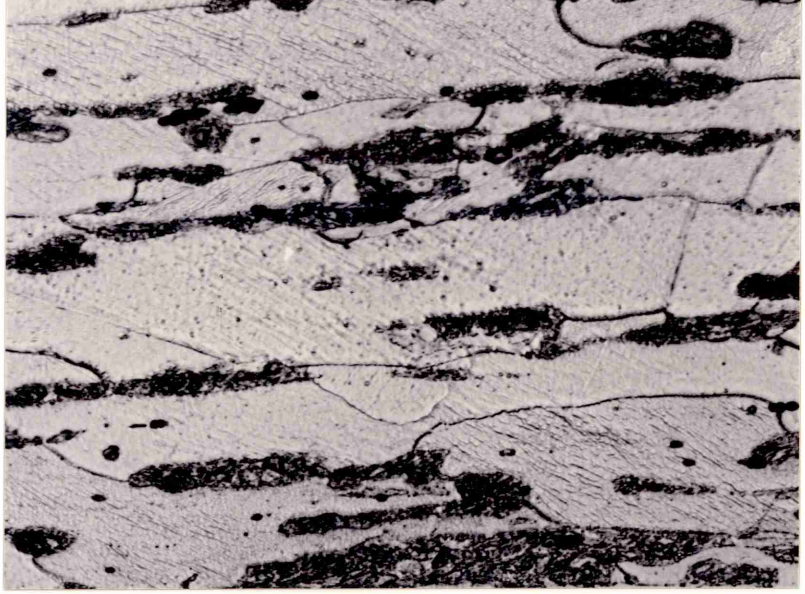

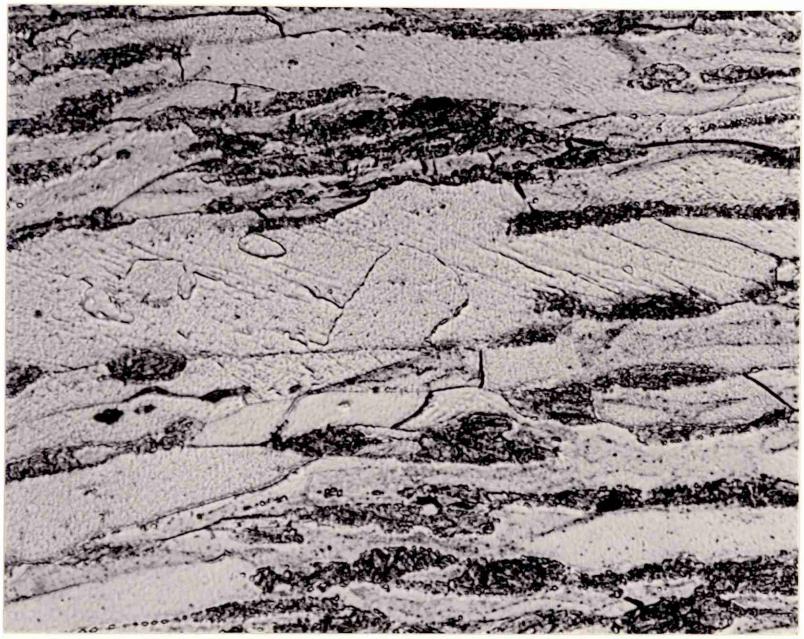

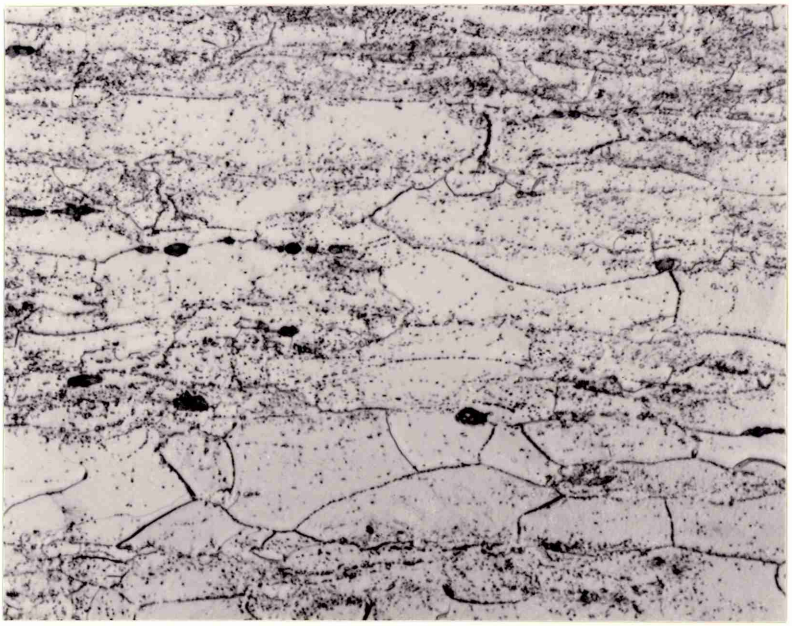

Fig (105a)

Thin foil electronmicrograph
17%Cr high(C+N) steel, after
75% cold reduction and annealed
for 10 seconds at 720°C

Magnification X 20,000

Fig (105b)

Thin foil electronmicrograph
17%Cr low(C+N) steel,
75% cold reduction and annealed
for 10 seconds at 720°C

Magnification X 20,000

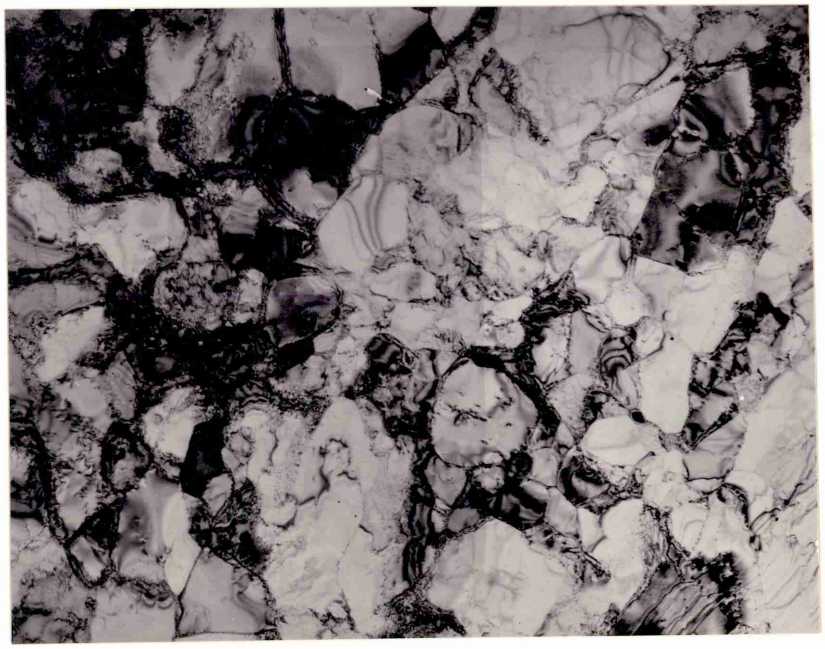

Fig (105c)

Thin foil electronmicrograph
17%Cr high(C+N) steel, after
75% cold reduction and annealed
for 20 seconds at 720°C

Magnification X 20,000

Diffraction patterns of
recrystallised grains A and B

Interpretation of diffraction
patterns

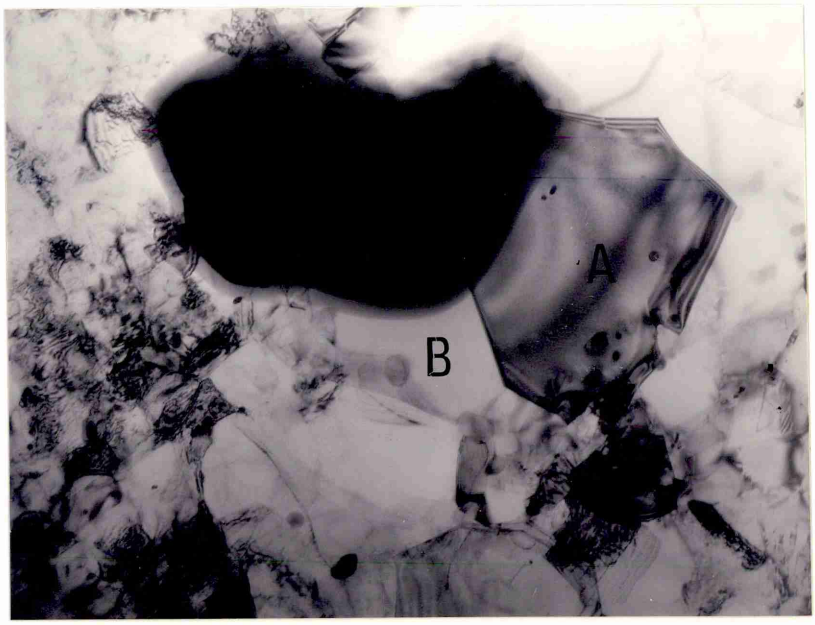
A
B

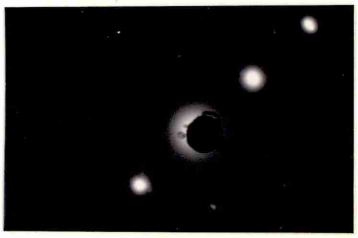

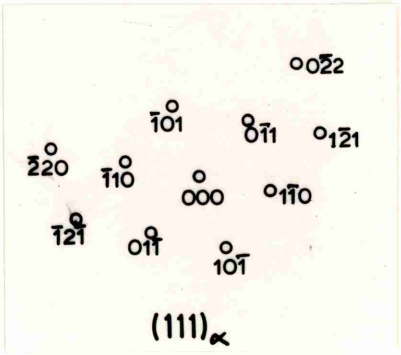
$00\bar{2}2$
$\bar{1}01$
$0\bar{1}1$
$1\bar{2}21$
$\bar{2}20$
$\bar{1}10$
000
$1\bar{1}0$
$\bar{1}2\bar{1}$
$01\bar{1}$
$10\bar{1}$
$(111)_\alpha$

A

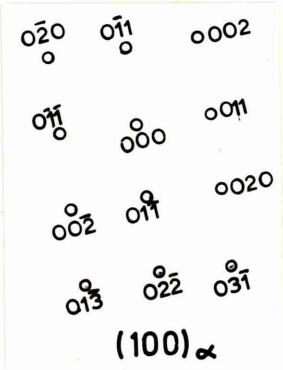
$0\bar{2}0$
$0\bar{1}1$
0002
$01\bar{1}$
000
011
0020
$00\bar{2}$
$01\bar{1}$
$01\bar{3}$
$02\bar{2}$
$03\bar{1}$
$(100)_\alpha$

B

Fig (105d)

Thin foil electronmicrograph
17%Cr high(C+N) steel, after
75% cold reduction and
annealed for 125 hours at
620°C

Magnification X 20,000

Fig (105e)

Thin foil electronmicrograph
17%Cr high(C+N) steel, after
75% cold reduction and
annealed for 32 minutes at
690°C

Magnification X 20,000

Fig (105f)

Thin foil electronmicrograph
17%Cr high(C+N) steel, after
75% cold reduction and
annealed for 1 hour at
690°C

Magnification X 20,000

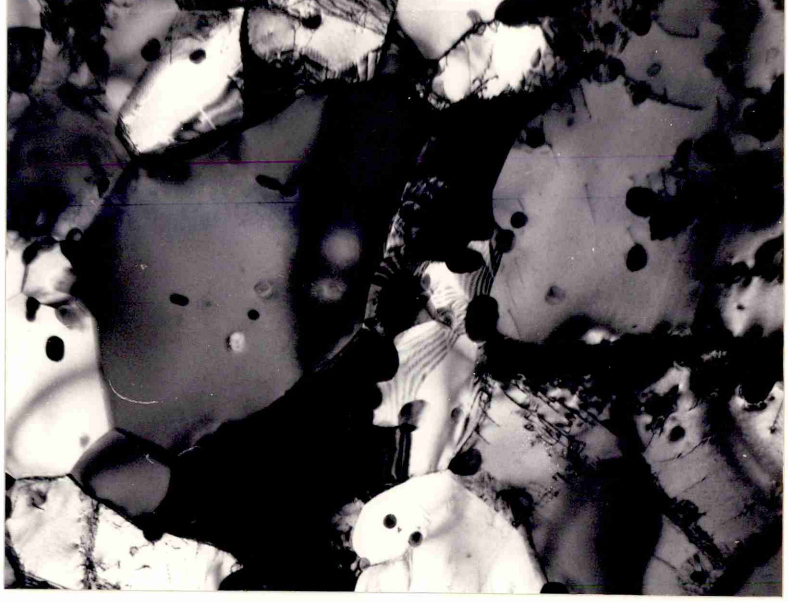

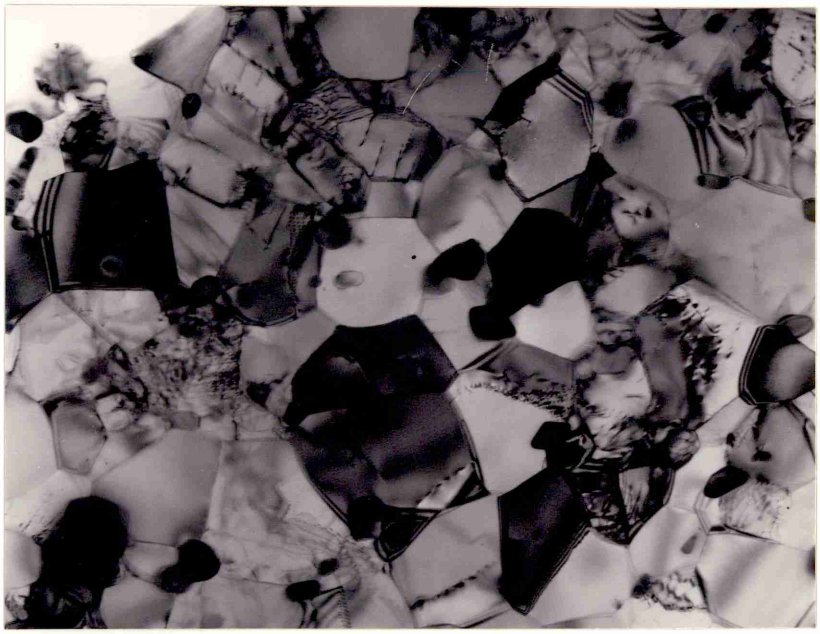

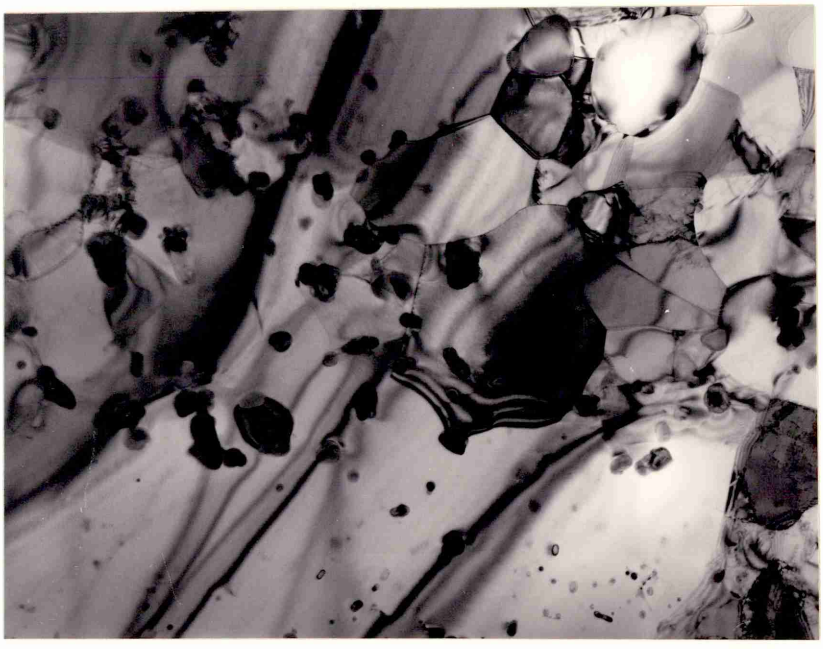

Fig (1059)

Thin foil electronmicrograph
17%Cr high(C+N) steel, after
50% cold reduction and
annealed for 2 minutes at
720°C

Magnification X 12,000

Diffraction patterns of
recrystallised grain A
and matrix grain B

Interpretation of diffraction
patterns

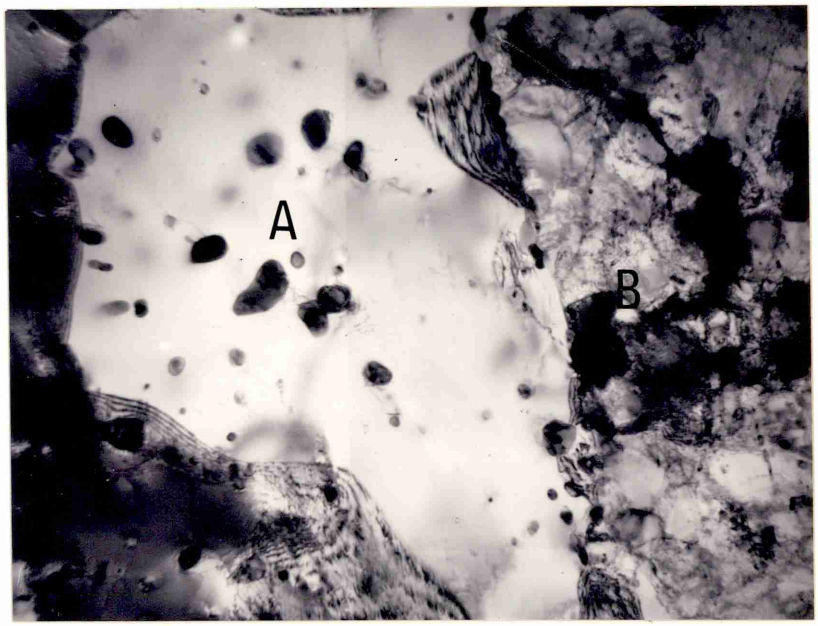
A
B

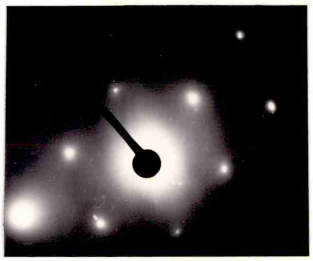

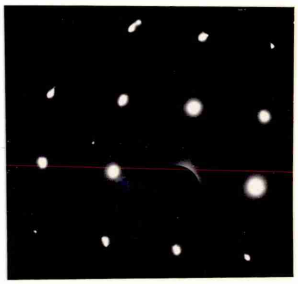


$0\bar{0}\bar{2}2$
$\bar{1}01$
$0\bar{1}1$
$1\bar{2}1$
$\bar{1}10$
000
$1\bar{1}0$
$\bar{1}2\bar{1}$
$01\bar{1}$
$10\bar{1}$
$(111)_\alpha$

B

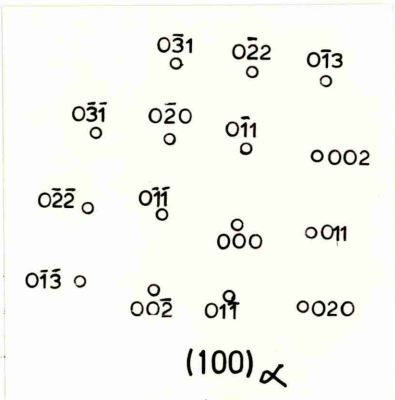
$0\bar{3}1$
$0\bar{2}2$
$0\bar{1}3$
$0\bar{3}\bar{1}$
$0\bar{2}0$
$01\bar{1}$
0002
$0\bar{2}\bar{2}$
$0\bar{1}\bar{1}$
000
011
$0\bar{1}\bar{3}$
$00\bar{2}$
$01\bar{1}$
0020
$(100)_\alpha$

A

Fig (105h)

Thin foil electronmicrograph 17%Cr high(C+N) steel, after 75% cold reduction and annealed for 125 hours at 620°C

Magnification X 25,000

Fig (106a)

Thin foil electronmicrograph 17%Cr low(C+N) + Ti steel, after 35% cold reduction and annealed for 10 seconds at 720°C

Magnification X 15,000

Fig (106b)

Thin foil electronmicrograph 17%Cr low(C+N) steel, after 35% cold reduction and annealed for 10 seconds at 720°C

Magnification X 15,000

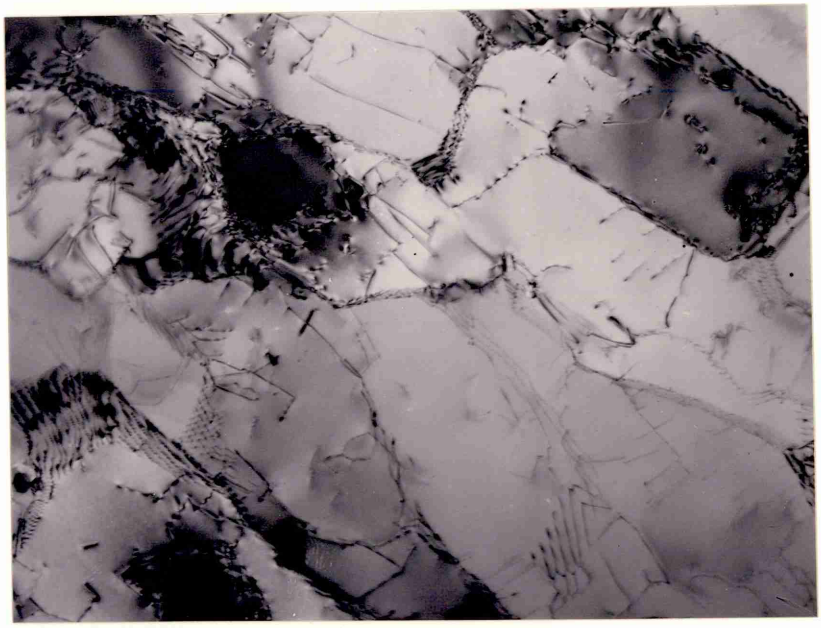

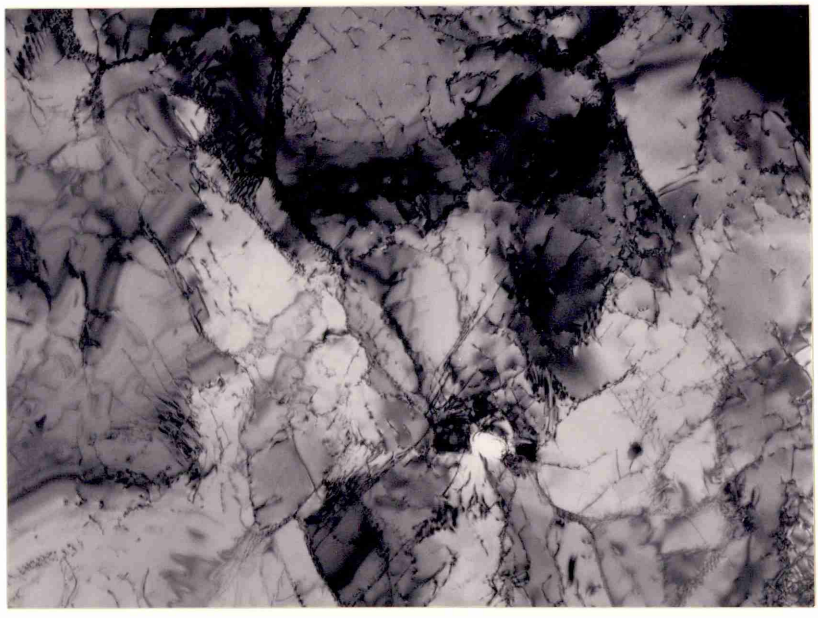

Fig (107a)

Optical micrograph
17%Cr low(C+N) + Ti steel,
after 50% cold reduction
and annealed for 30 seconds
at 750°C

Magnification X 2,000

Fig (107b)

Thin foil electronmicrograph
17%Cr low(C+N) + Ti steel,
after 75% cold reduction and
annealed for 30 seconds at
620°C

Magnification X 10,000

Fig (107c)

Optical micrograph
17%Cr low(C+N) + Ti steel,
after 50% cold reduction and
annealed for 30 seconds at
750°C

Magnification X 400

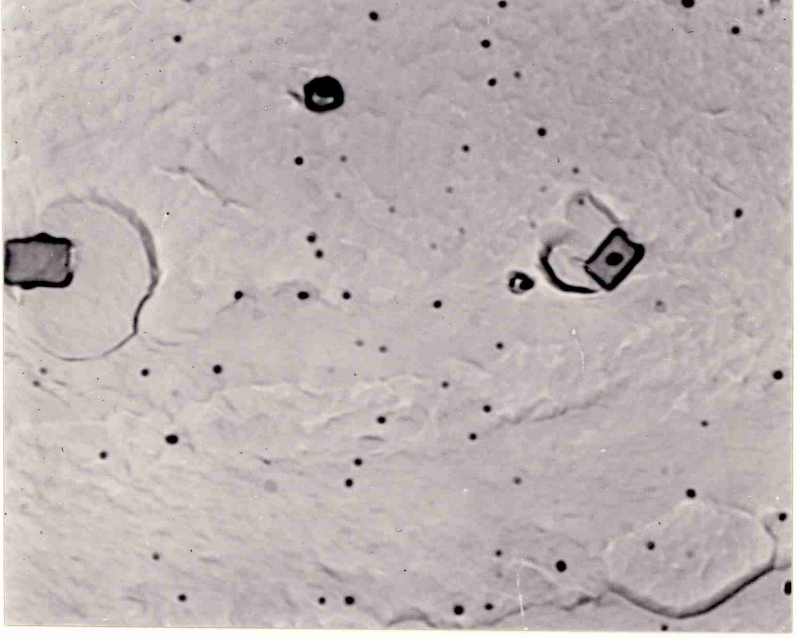

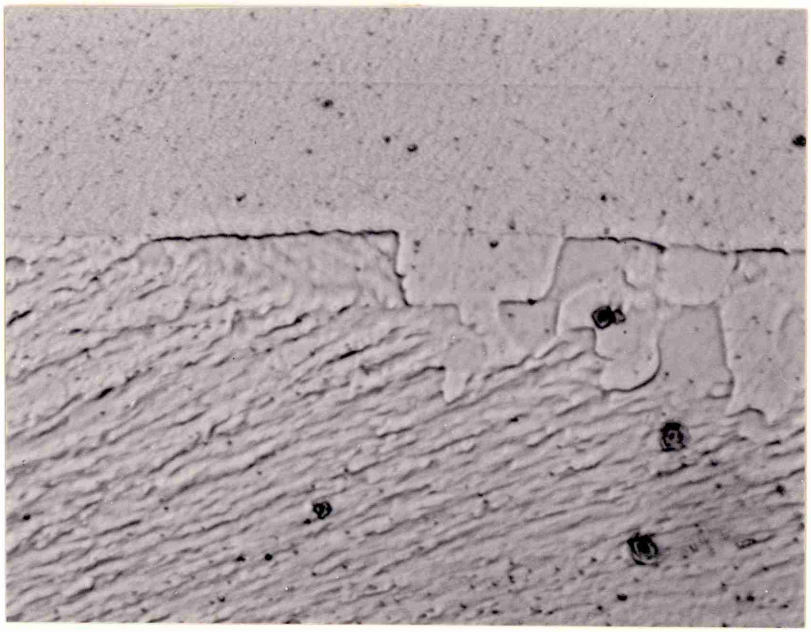

Fig (107d)

Thin foil electronmicrograph
17%Cr low(C+N) + Ti steel,
after 75% cold reduction and
annealed for 10 seconds at
750°C

Magnification X 40,000

Fig (108a)

Optical micrograph
17%Cr high(C+N) + Nb steel,
after 35% cold reduction and
annealed for 2 minutes at
750°C

Magnification X 1,000

Fig (108b)

Optical micrograph
17%Cr low(C+N) + Nb steel,
after 75% cold reduction and
annealed for 2 minutes at
750°C

Magnification X 15,000


1
2
A
B

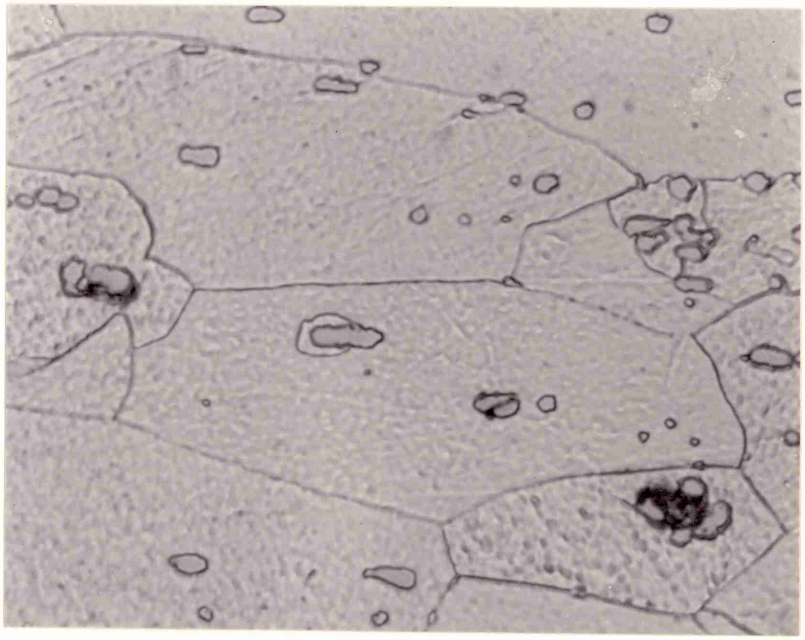

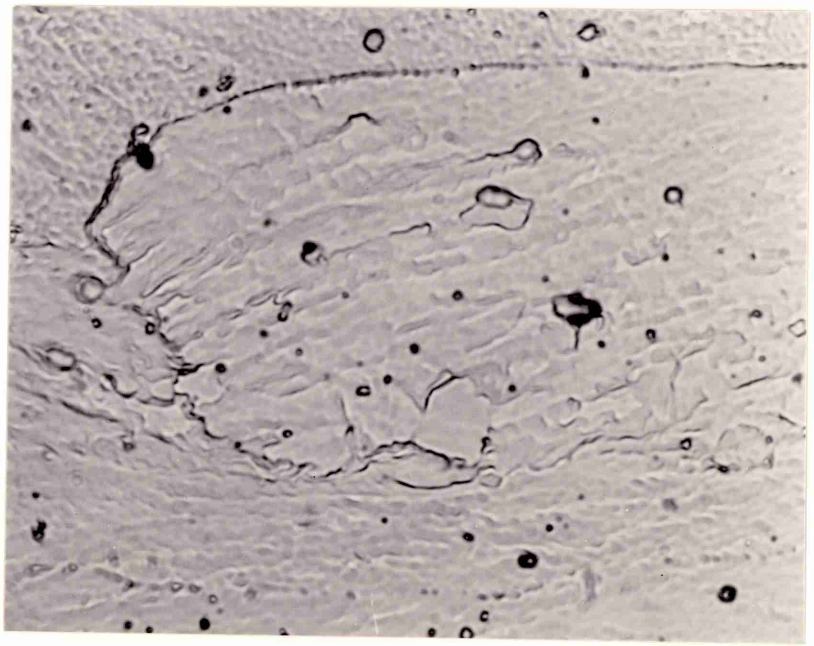

Fig (108c)

Thin foil electronmicrograph
17%Cr high(C+N) + Nb steel,
after 75% cold reduction and
annealed for 20 seconds at
750°C

Magnification X 16,000

Diffraction pattern
of grain adjacent
to particle

Interpretation of
diffraction pattern

Fig (108d)

Optical micrograph
17%Cr high(C+N) + Nb steel,
after 75% cold reduction and
annealed for 4 minutes at
750°C

Magnification X 600

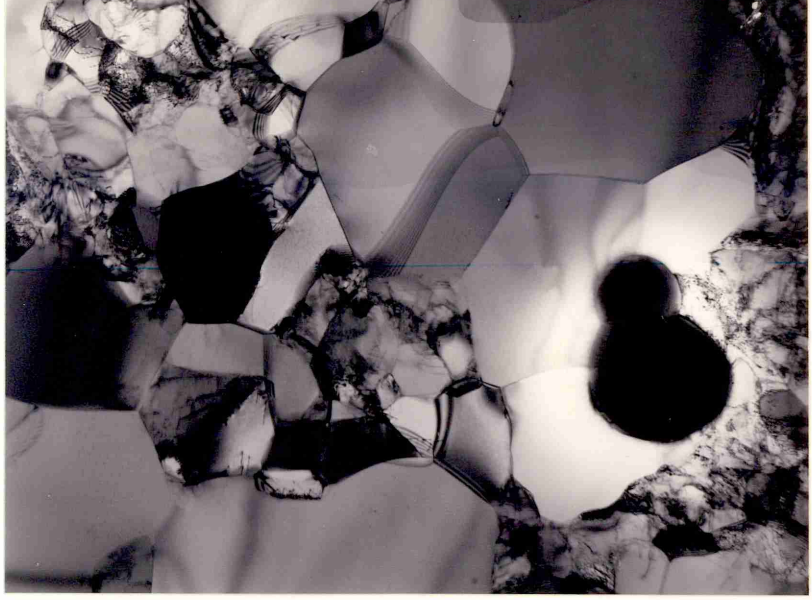

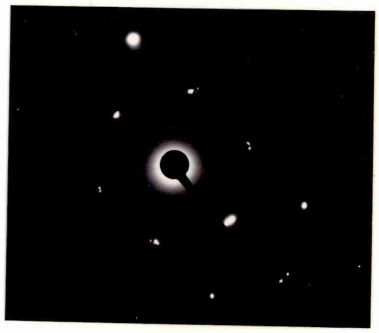

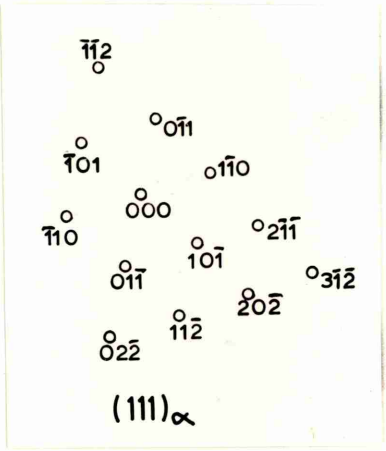
$\bar{1}\bar{1}2$
$0\bar{1}1$
$\bar{1}01$
$1\bar{1}0$
000
$\bar{1}10$
$2\bar{1}\bar{1}$
$10\bar{1}$
$01\bar{1}$
$3\bar{1}\bar{2}$
$20\bar{2}$
$11\bar{2}$
$02\bar{2}$
$(111)_\alpha$

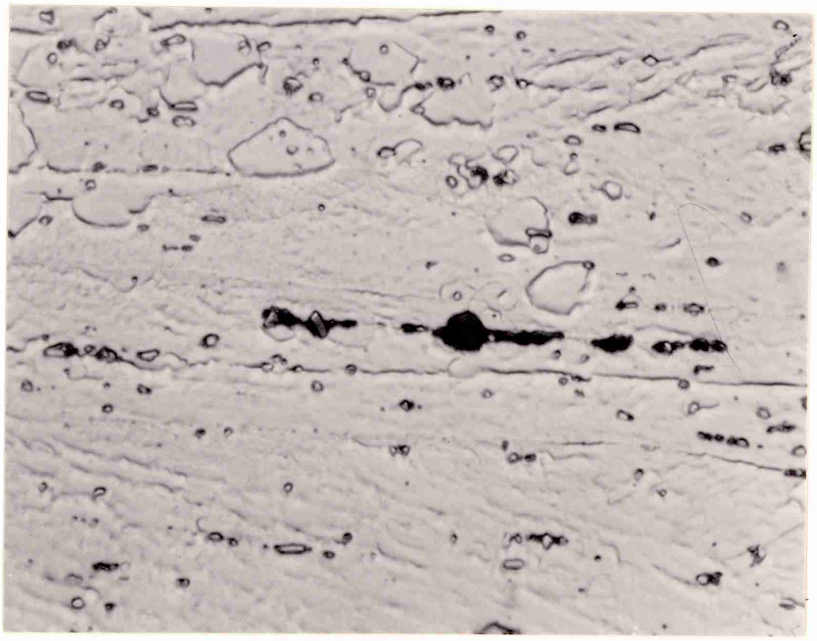

Fig (108e)

Thin foil electronmicrograph
17%Cr low(C+N) + Nb steel, after
50% cold reduction and annealed
for 30 seconds at 750°C

Magnification X 35,000

Fig (109a)

Thin foil electronmicrograph
17%Cr low(C+N) 1% Mo steel,
after 35% cold reduction and
annealed for 30 seconds at
690°C

Magnification X 25,000

Fig (109b)

Thin foil electronmicrograph
17%Cr low(C+N) 1% Mo steel,
after 35% cold reduction and
annealed for 2 minutes at
690°C

Magnification X 25,000

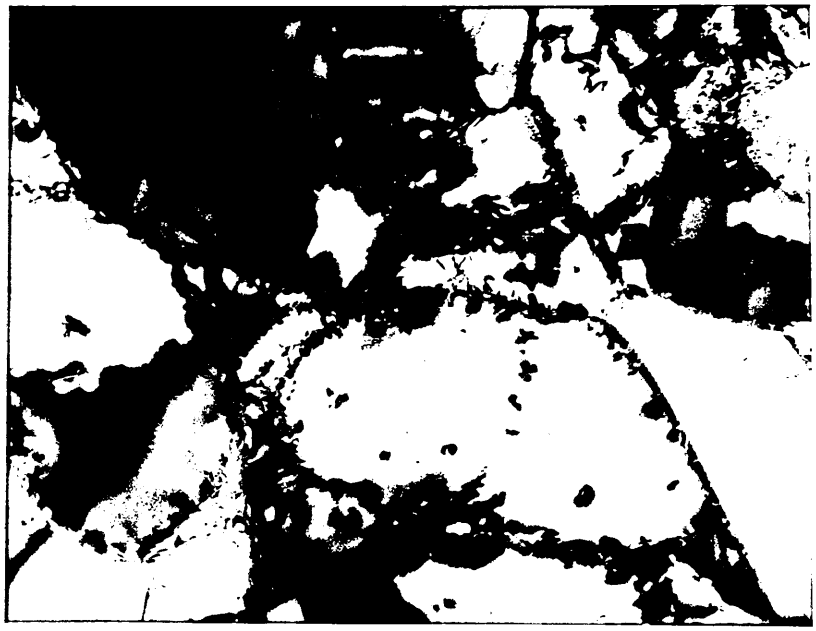

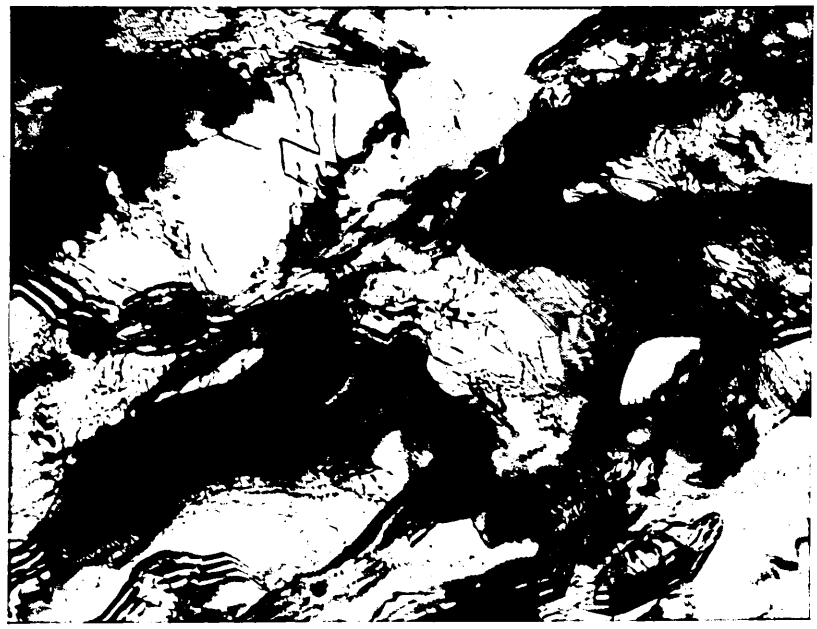

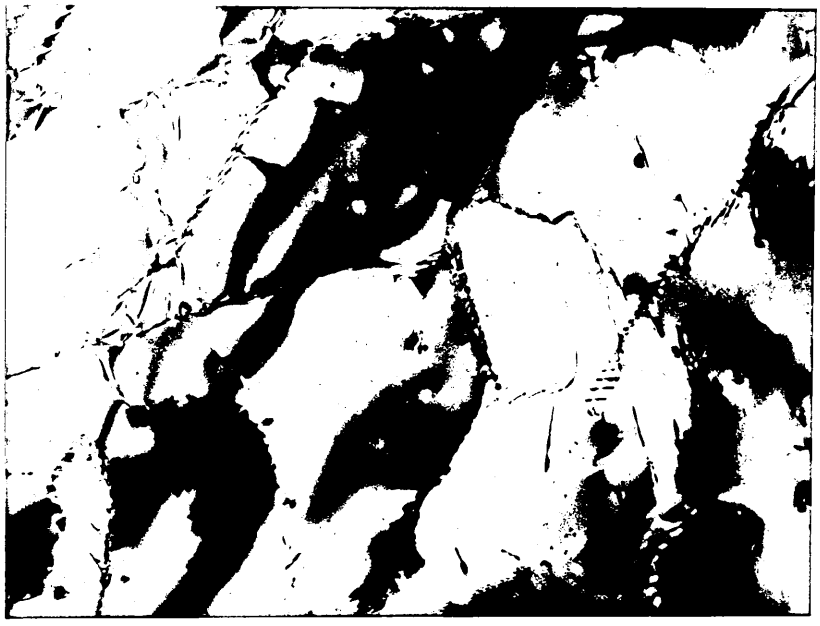

Fig (109c)

Thin foil electronmicrograph 17%Cr low(C+N) 1% Mo steel, after 35% cold reduction and annealed for 2 minutes at 690°C

Magnification X 50,000

Fig (109d)

Thin foil electronmicrograph 17%Cr low(C+N) 1% Mo steel, after 75% cold reduction and annealed for 1 minute at 690°C

Magnification X 35,000

Fig (109e)

Thin foil electronmicrograph 17%Cr low(C+N) 1% Mo steel, after 75% cold reduction and annealed for 1 minute at 690°C

Magnification X 12,000

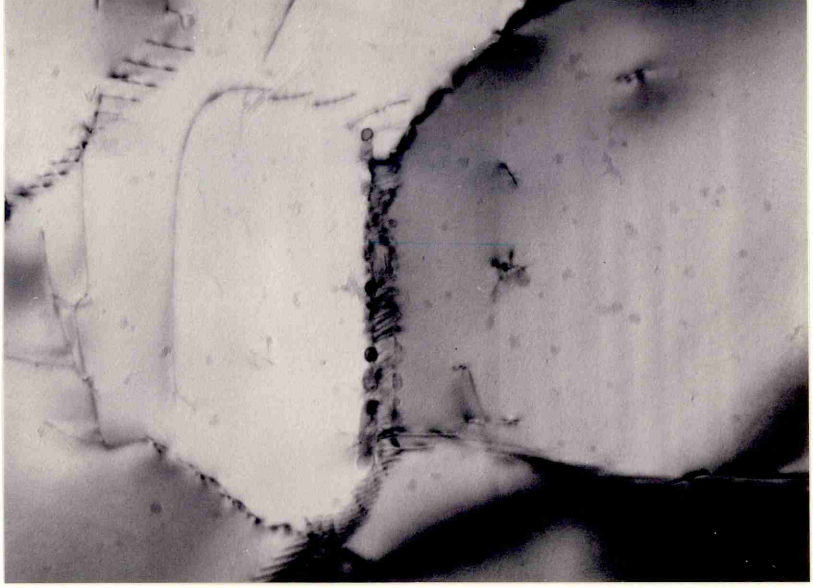

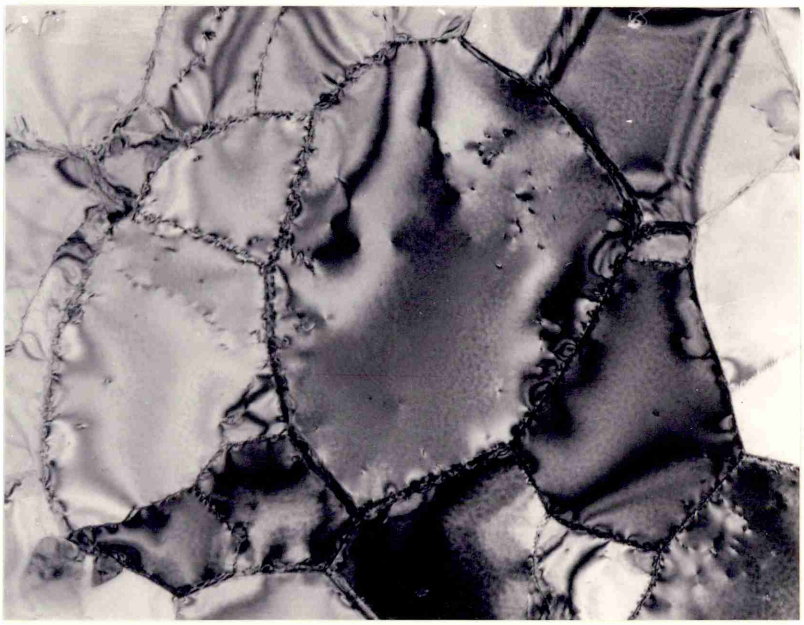

Fig (109f)

Optical micrograph
17%Cr low(C+N) 1% Mo steel,
after 50% cold reduction
and annealed for 2 minutes
at 750°C

Magnfication X 600

Fig (109g)

Thin foil electronmicrograph
17%Cr low(C+N) 1% Mo steel, after
50% cold reduction and
annealed for 2 minutes at
720°C

Magnification X 50,000

Fig (110a)

Thin foil electronmicrograph
17%Cr high(C+N) 1% Mo steel,
after 35% cold reduction

Magnification X 25,000

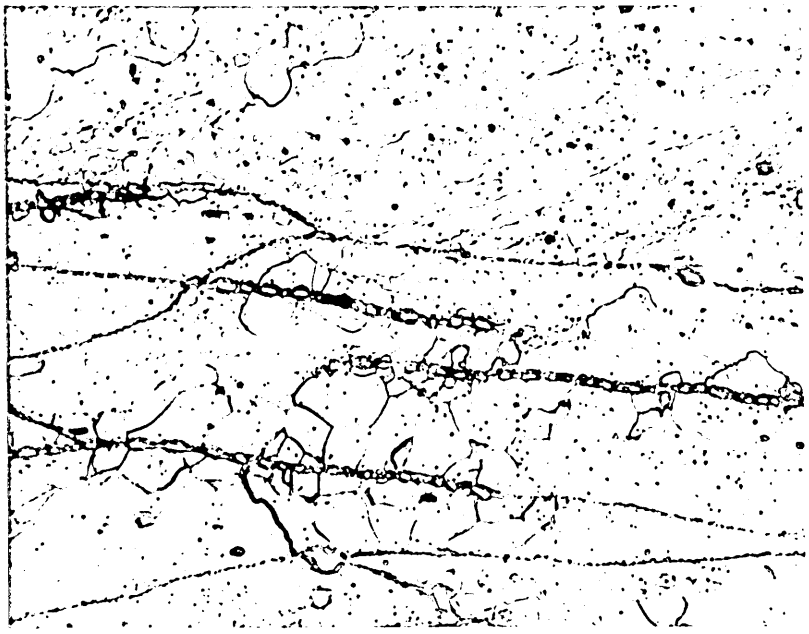

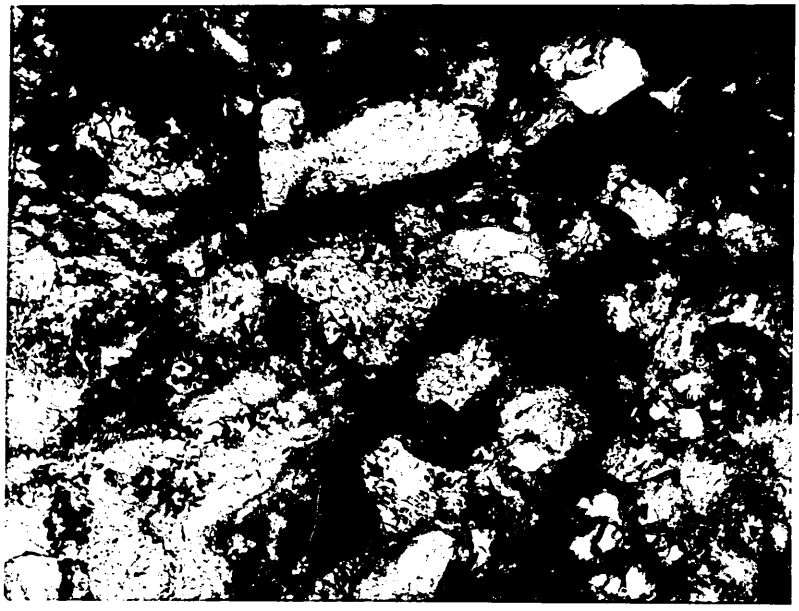

Fig (110b)

Thin foil electronmicrograph 17%Cr high(C+N) 1% Mo steel, after 35% cold reduction and annealed for 30 seconds at 690°C

Magnification X 25,000

Fig (110c)

Thin foil electronmicrograph 17%Cr high(C+N) 1% Mo steel, after 35% cold reduction and annealed for 2 minutes at 690°C

Magnification X 25,000

Fig (110d)

Thin foil electronmicrograph 17%Cr high(C+N) 1% Mo steel, after 35% cold reduction and annealed for 8 minutes at 690°C

Magnification X 25,000

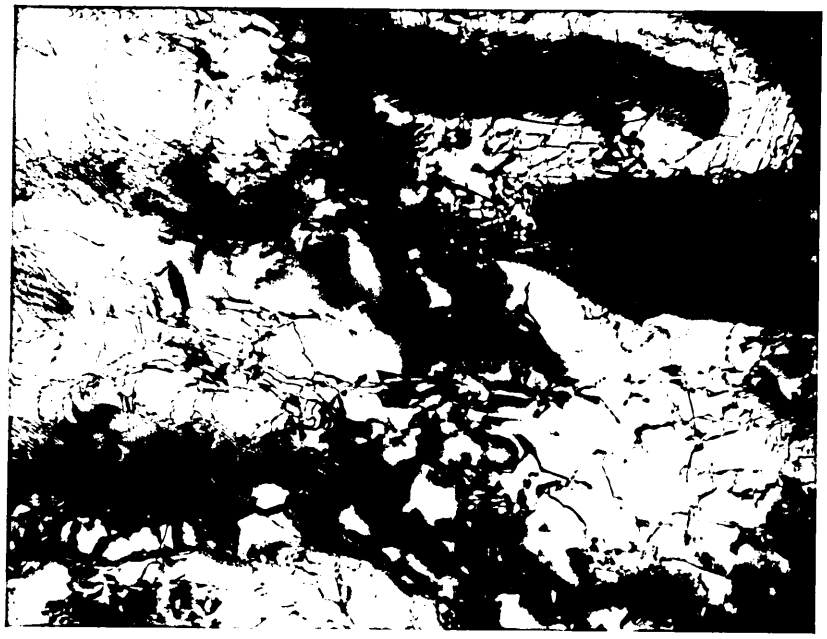

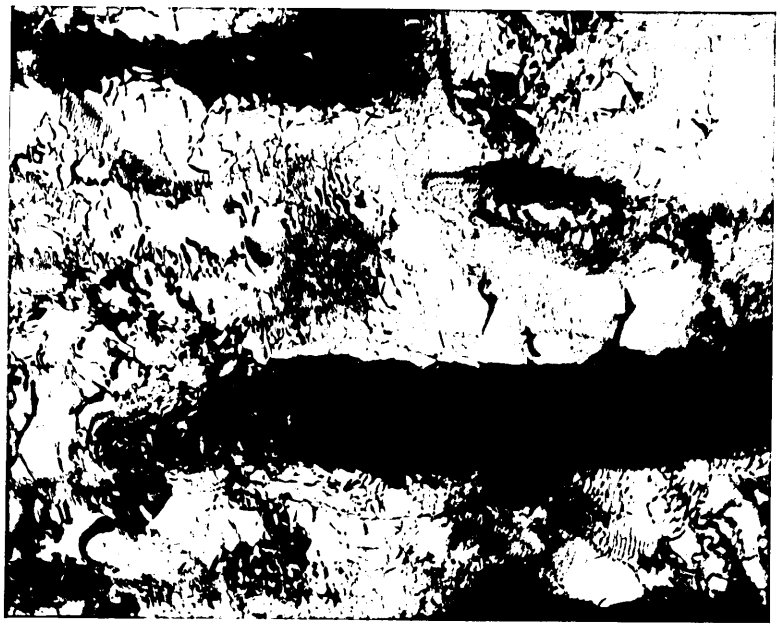

Fig (111a)

Optical micrograph
17%Cr high(C+N) 1% Mo steel,
after 35% cold reduction and
annealed for 8 minutes at
690°C

Magnification X 400

Fig (111b)

Optical micrograph
17%Cr high(C+N) 1% Mo steel,
after 35% cold reduction and
annealed for32 minutes at
690°C

Magnification X 400

Fig (111c)

Thin foil electronmicrograph
17%Cr high(C+N) 1% Mo steel,
after 75% cold reduction and
annealed for 4 minutes at
690°C

Magnification X 12,000

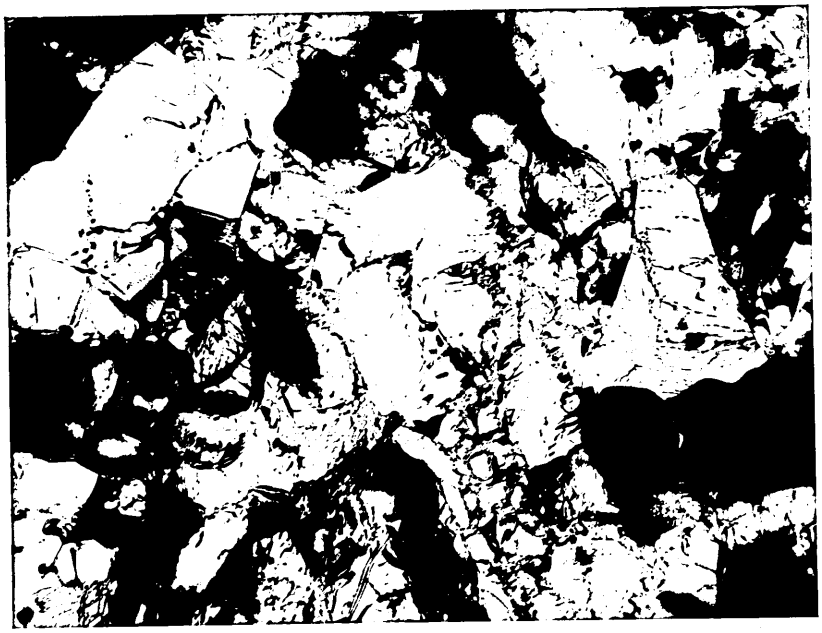

Fig (111d)

Thin foil electronmicrograph
17%Cr high(C+N) 1% Mo steel,
after 75% cold reduction and
annealed for 8 minutes at
690°C

Magnification X 50,000

Fig (112a)

Optical micrograph
25%Cr low(C+N) steel after
35% cold reduction and
annealed for 4 minutes at
720°C

Magnification X 400

Fig (112b)

Thin foil electronmicrograph
25%Cr low(C+N) steel, after
75% cold reduction and
annealed for 30 seconds at
690°C

Magnification X 35,000

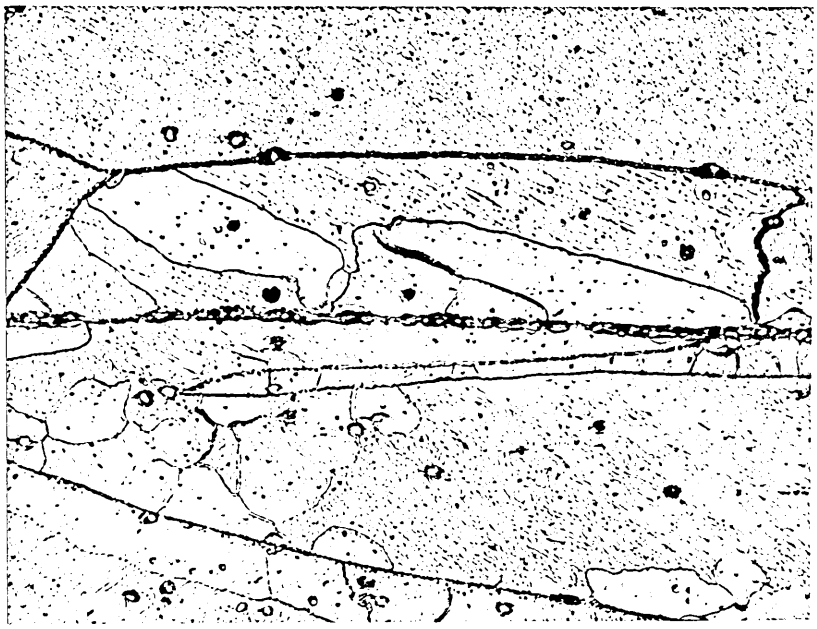

Fig (113a)

Thin foil electronmicrograph
25%Cr low(C+N) 1% Mo steel,
after 35% cold reduction and
annealed for 30 seconds at
690°C

Fig (113b)

Thin foil electronmicrograph
25%Cr low(C+N) 1% Mo steel,
after 35% cold reduction and
annealed for 2 minutes at
690°C

Magnification X 25,000

Fig (113c)

Optical micrograph
25%Cr low(C+N) 1% Mo steel,
after 50% cold reduction and
annealed for 2 minutes at
750°C

Magnification X 400

Fig (113d)

Thin foil electronmicrograph
25%Cr low(C+N) 1% Mo steel,
after 75% cold reduction and
annealed for 1 minute at
690°C

Magnification X 35,000

Fig (114a)

Fig (114)

The effect of percentage cold reduction on r_o, r_{45}, r_{90} and $\bar{r}$

Fig (114b)

Fig (114c)

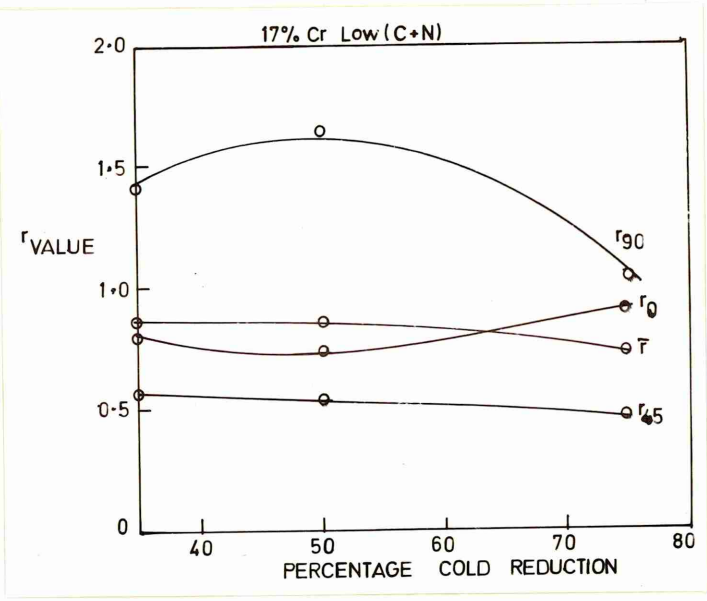
17% Cr Low (C+N)
2·0
1·5
1·0
0·5
0
r VALUE
r90
r0
r̄
r45
40
50
60
70
80
PERCENTAGE COLD REDUCTION

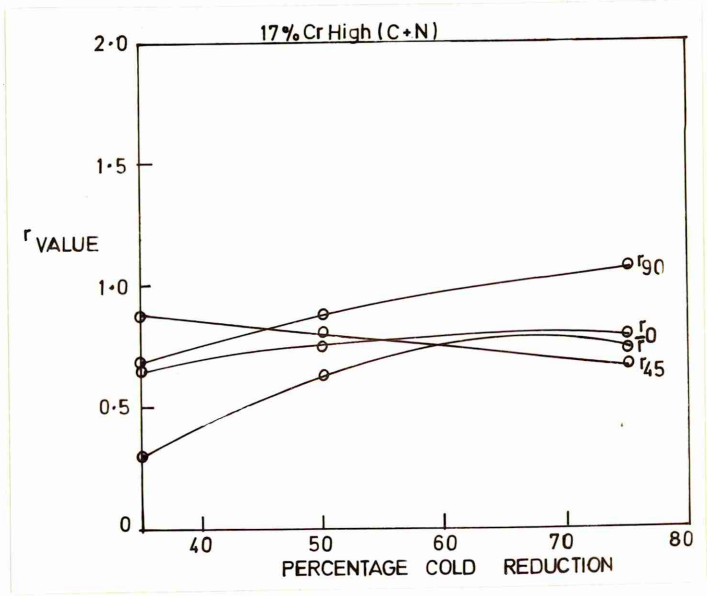
17% Cr High (C+N)
2·0
1·5
1·0
0·5
0
r VALUE
r90
r0
r̄
r45
40
50
60
70
80
PERCENTAGE COLD REDUCTION

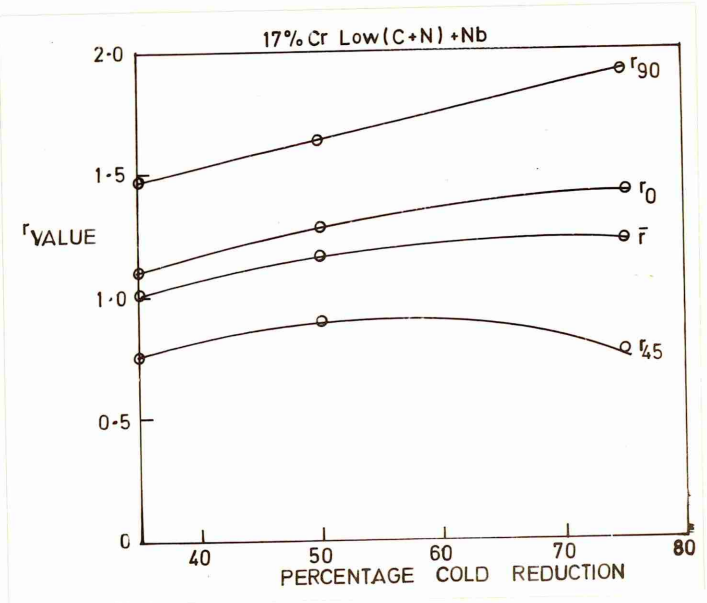
17% Cr Low (C+N) +Nb
2·0
1·5
1·0
0·5
0
r VALUE
r90
r0
r̄
r45
40
50
60
70
80
PERCENTAGE COLD REDUCTION

Fig (114d)

Fig (114)

The effect of percentage cold reduction on r_0, r_{45}, r_{90} and $\bar{r}$

Fig (114e)

Fig (114f)

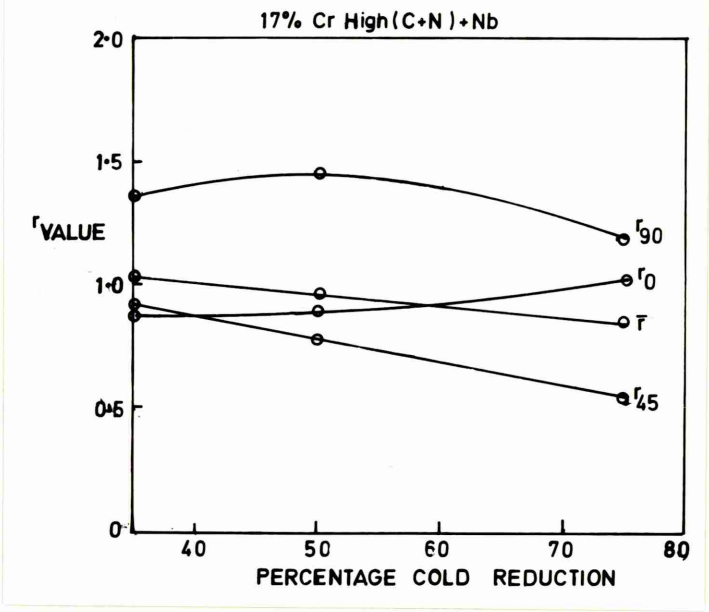
17% Cr High (C+N) + Nb
2·0
1·5
1·0
0·5
0
r VALUE
r90
r0
r̄
r45
40
50
60
70
80
PERCENTAGE COLD REDUCTION

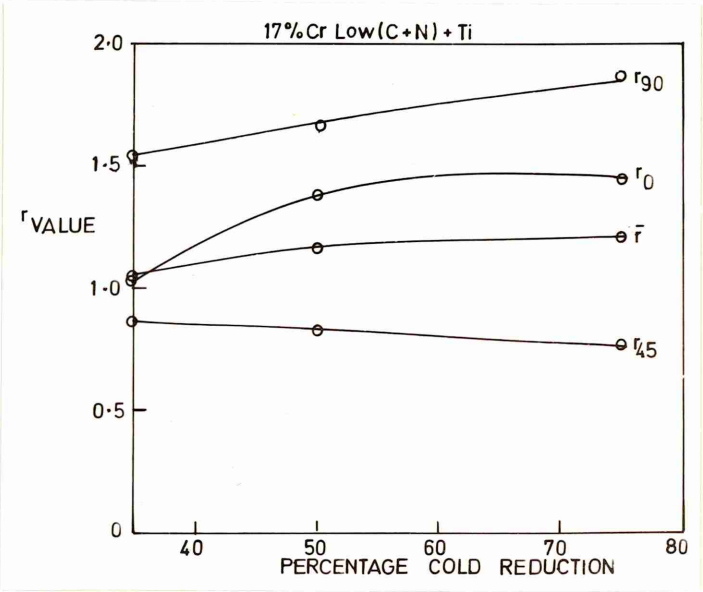
17% Cr Low (C+N) + Ti
2·0
1·5
1·0
0·5
0
r VALUE
r90
r0
r̄
r45
40
50
60
70
80
PERCENTAGE COLD REDUCTION

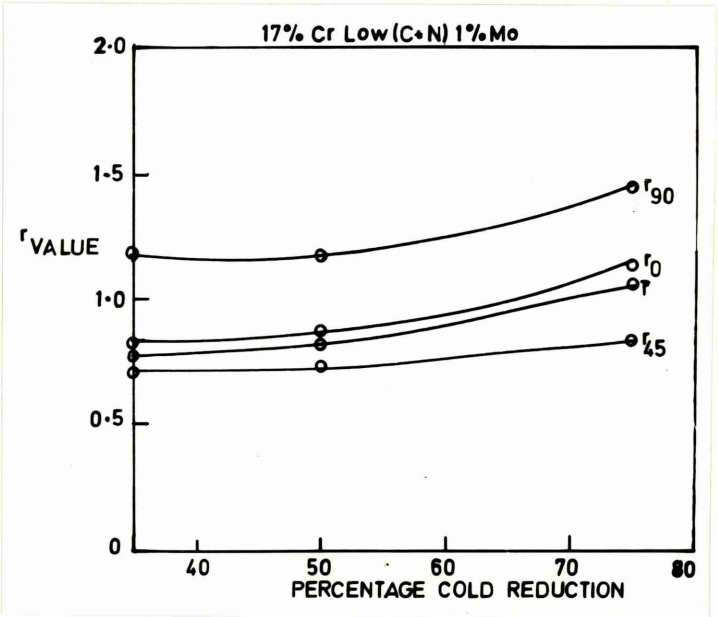
17% Cr Low (C+N) 1% Mo
2·0
1·5
1·0
0·5
0
r VALUE
r90
r0
r̄
r45
40
50
60
70
80
PERCENTAGE COLD REDUCTION

Fig (114g)

Fig (114)

The effect of percentage cold reduction on r_o, r_{45}, r_{90} and $\bar{r}$

Fig (114h)

Fig (114j)

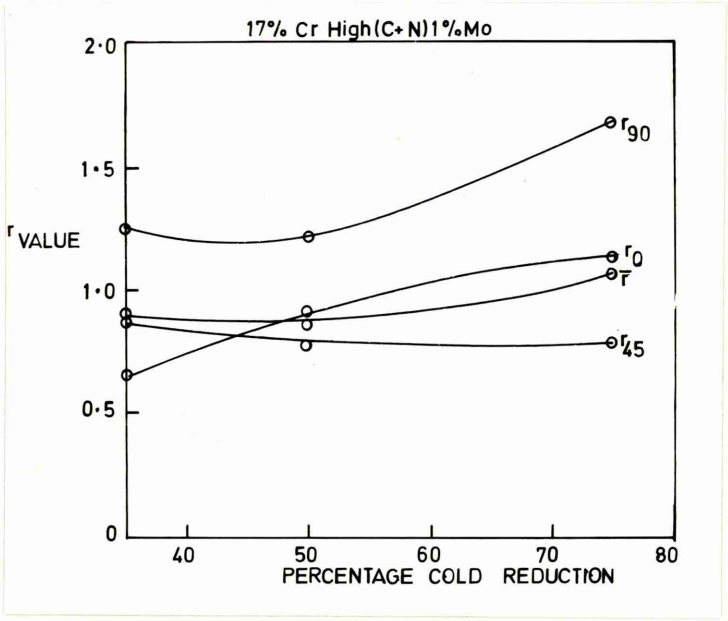
17% Cr High (C+N) 1% Mo
2·0
1·5
1·0
0·5
0
r VALUE
r_{90}
r_0
$\bar{r}$
r_{45}
40
50
60
70
80
PERCENTAGE COLD REDUCTION

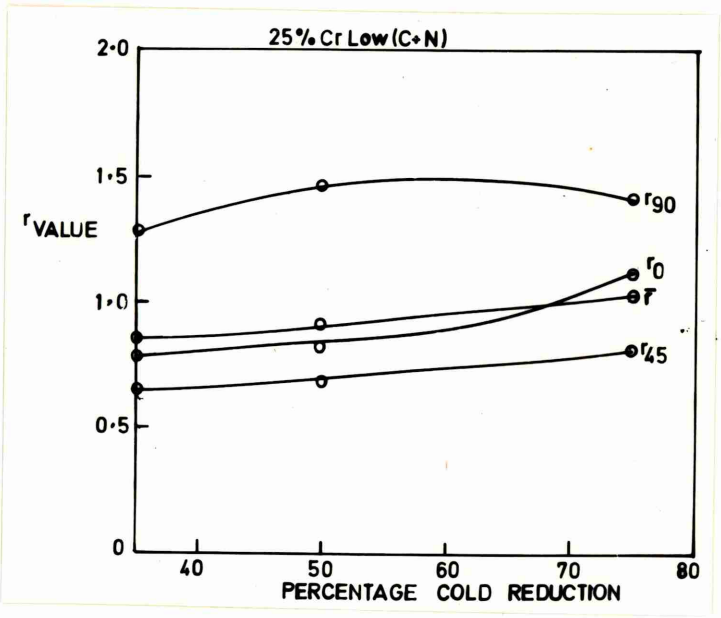
25% Cr Low (C+N)
2·0
1·5
1·0
0·5
0
r VALUE
r_{90}
r_0
$\bar{r}$
r_{45}
40
50
60
70
80
PERCENTAGE COLD REDUCTION

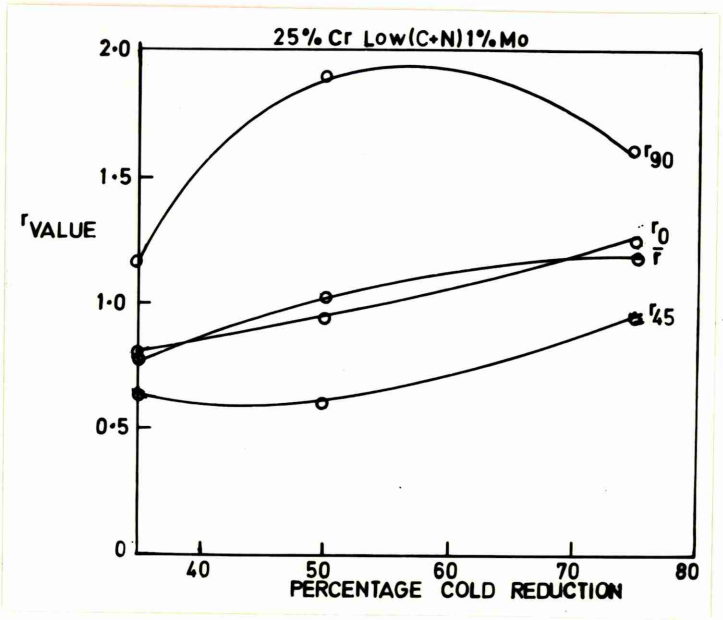
25% Cr Low (C+N) 1% Mo
2·0
1·5
1·0
0·5
0
r VALUE
r_{90}
r_0
$\bar{r}$
r_{45}
40
50
60
70
80
PERCENTAGE COLD REDUCTION

Fig (115)

A graph of $\bar{r}$ versus $\log_{10} \frac{I(111)}{I(100)}$

Fig (116)

True stress - true strain and work hardening curves showing the effect of increasing interstitial and chromium contents after 75% cold reduction in the fully recrystallised condition

Fig (117)

True stress - true strain and work hardening curves showing the effect of molybdenum in a 25%Cr low interstitial content steel after 75% cold reduction in the fully recrystallised condition

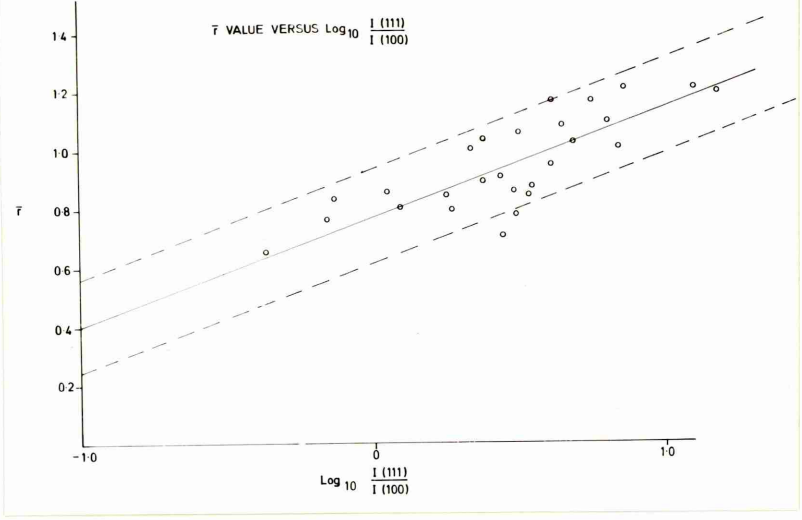
$\bar{r}$ VALUE VERSUS Log$_{10}$ $\frac{I\,(111)}{I\,(100)}$
1·4
1·2
1·0
0·8
0·6
0·4
0·2
$\bar{r}$
−1·0
0
1·0
Log$_{10}$ $\frac{I\,(111)}{I\,(100)}$

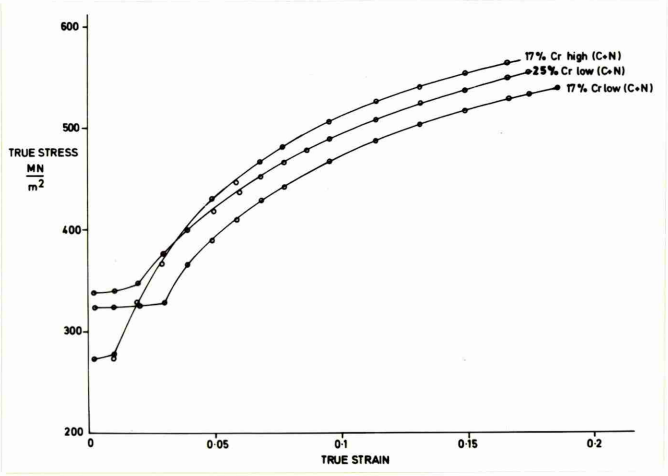
600
500
400
300
200
TRUE STRESS
$\frac{MN}{m^2}$
17% Cr high (C+N)
25% Cr low (C+N)
17% Cr low (C+N)
0
0·05
0·1
0·15
0·2
TRUE STRAIN

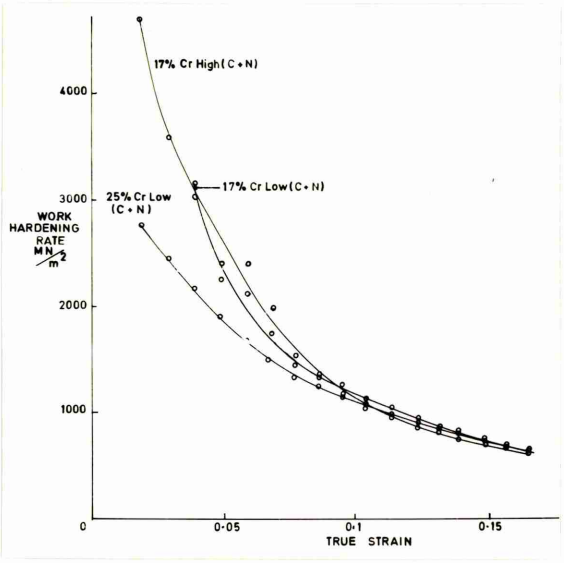
4000
3000
2000
1000
0
WORK HARDENING RATE
$\frac{MN}{m^2}$
17% Cr High (C+N)
17% Cr Low (C+N)
25% Cr Low (C+N)
0·05
0·1
0·15
TRUE STRAIN

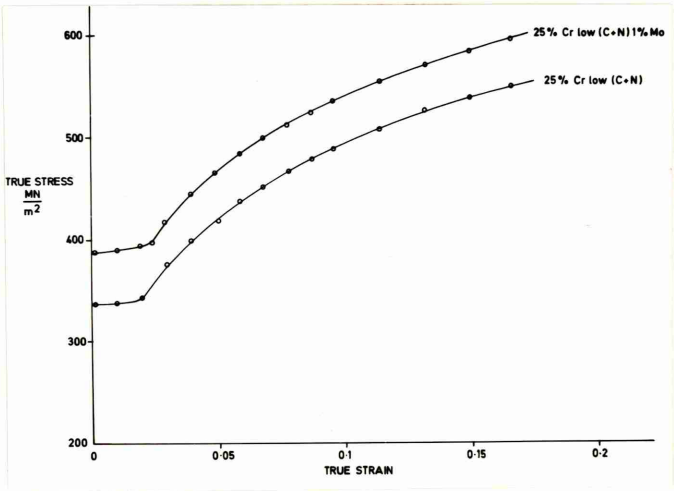
600
500
400
300
200
TRUE STRESS
$\frac{MN}{m^2}$
25% Cr low (C+N) 1% Mo
25% Cr low (C+N)
0
0·05
0·1
0·15
0·2
TRUE STRAIN

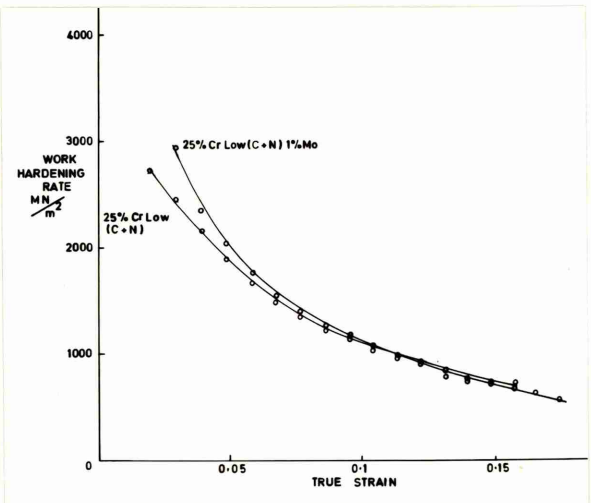
4000
3000
2000
1000
0
WORK HARDENING RATE
$\frac{MN}{m^2}$
25% Cr Low (C+N) 1% Mo
25% Cr Low (C+N)
0·05
0·1
0·15
TRUE STRAIN

Fig (118)

True stress - true strain and work hardening curves showing the effect of molybdenum at both interstitial levels in 17%Cr steels after 75% cold reduction in the fully recrystallised condition

Fig (119)

True stress - true strain and work hardening curves showing the effect of titanium and niobium in a 17%Cr low interstitial content steel after 75% reduction in the fully recrystallised condition

Fig (120)

True stress - true strain and work hardening curves showing the effect of niobium in a 17%Cr high interstitial content steel after 75% cold reduction in the fully recrystallised condition

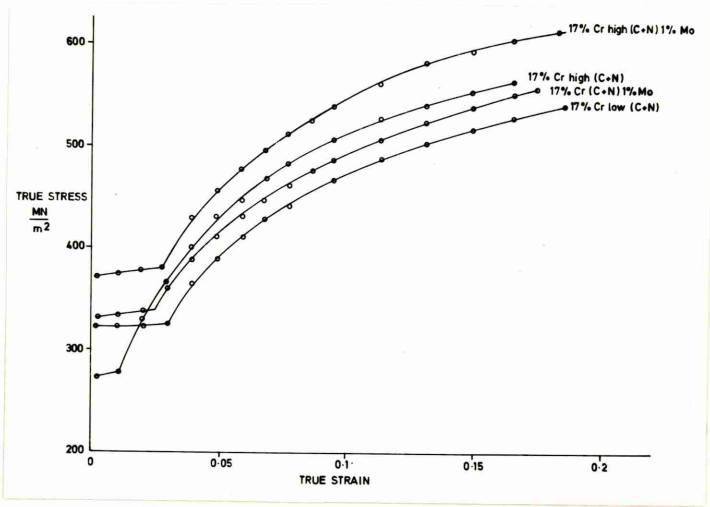
17% Cr high (C+N) 1% Mo
17% Cr high (C+N)
17% Cr (C+N) 1% Mo
17% Cr low (C+N)
TRUE STRESS
MN/m²
TRUE STRAIN
600
500
400
300
200
0
0·05
0·1
0·15
0·2

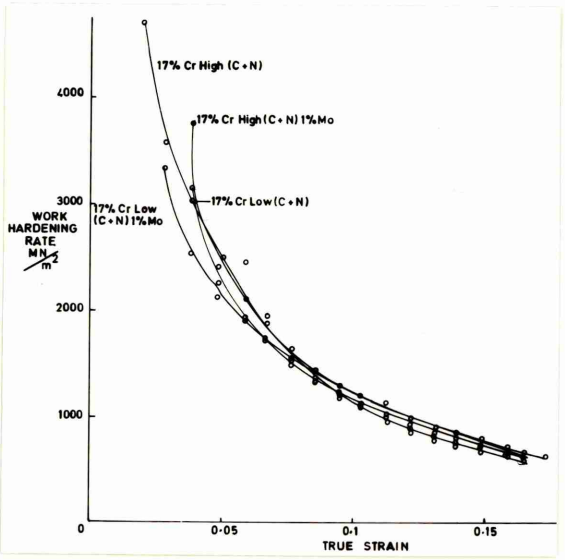
17% Cr High (C+N)
17% Cr High (C+N) 1% Mo
17% Cr Low (C+N)
17% Cr Low (C+N) 1% Mo
WORK HARDENING RATE
MN/m²
TRUE STRAIN
4000
3000
2000
1000
0
0·05
0·1
0·15

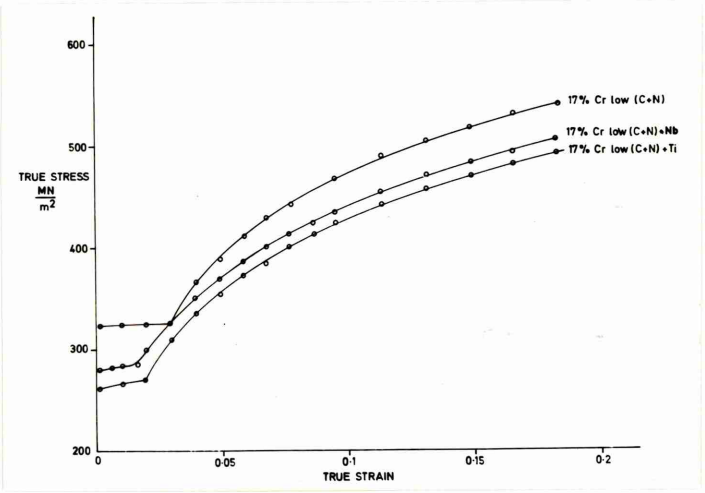
17% Cr Low (C+N)
17% Cr low (C+N)+Nb
17% Cr low (C+N)+Ti
TRUE STRESS
MN/m²
TRUE STRAIN
600
500
400
300
200
0
0·05
0·1
0·15
0·2

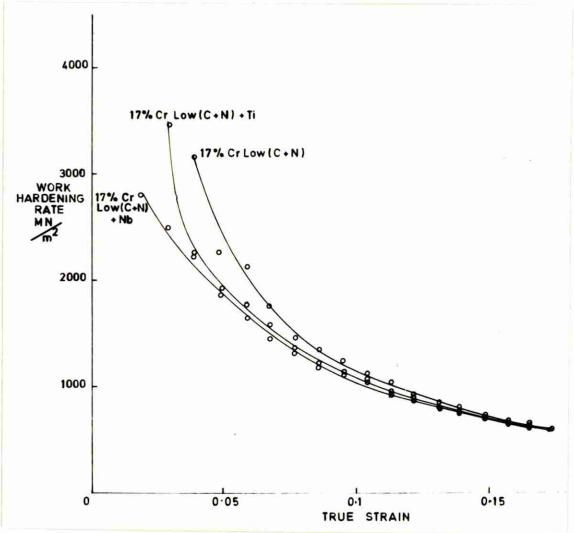
17% Cr Low (C+N)+Ti
17% Cr Low (C+N)
17% Cr Low (C+N)+Nb
WORK HARDENING RATE
MN/m²
TRUE STRAIN
4000
3000
2000
1000
0
0·05
0·1
0·15

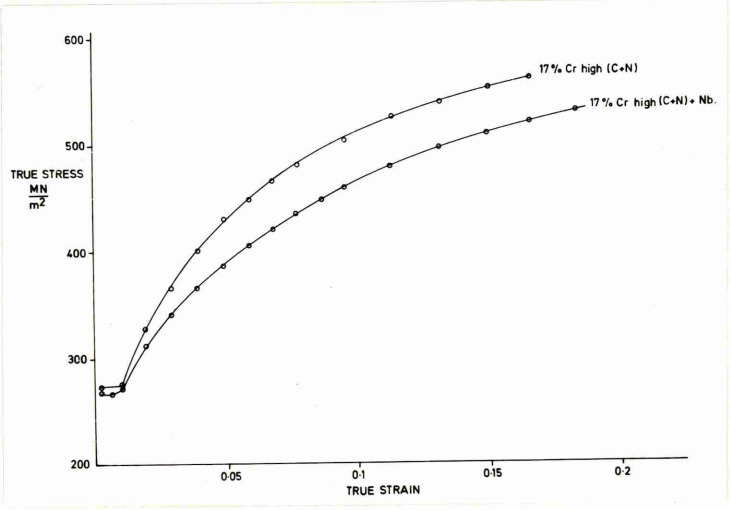
17% Cr high (C+N)
17% Cr high (C+N)+Nb.
TRUE STRESS
MN/m²
TRUE STRAIN
600
500
400
300
200
0·05
0·1
0·15
0·2

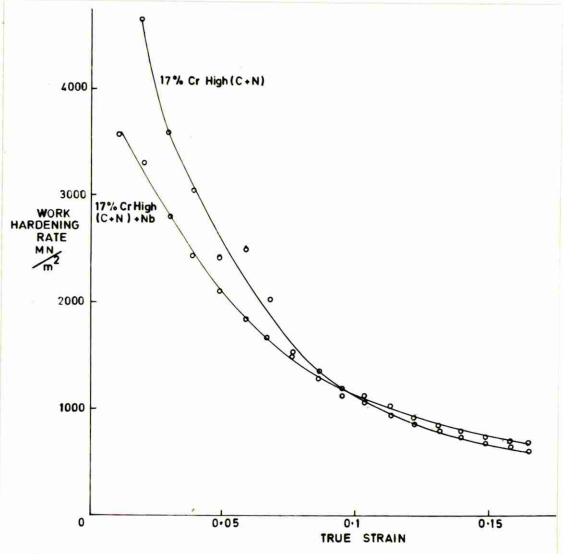
17% Cr High (C+N)
17% Cr High (C+N)+Nb
WORK HARDENING RATE
MN/m²
TRUE STRAIN
4000
3000
2000
1000
0
0·05
0·1
0·15

Fig (121)

True stress - true strain curves showing the effect of cold reduction on tensile properties

Fig (122a-c)

The effect of composition and cold work on the limiting drawing ratio

Fig (123)

A graph of LDR versus $\bar{r}$ value

Fig (124)

A graph of LDR versus $\log_{10} \frac{I(111)}{I(100)}$

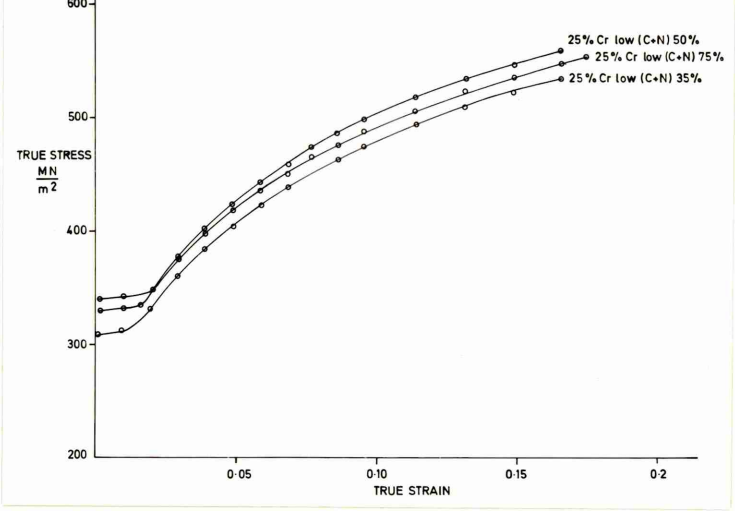
25% Cr low (C+N) 50%
25% Cr low (C+N) 75%
25% Cr low (C+N) 35%
TRUE STRESS
MN/m²
600
500
400
300
200
0·05
0·10
0·15
0·2
TRUE STRAIN

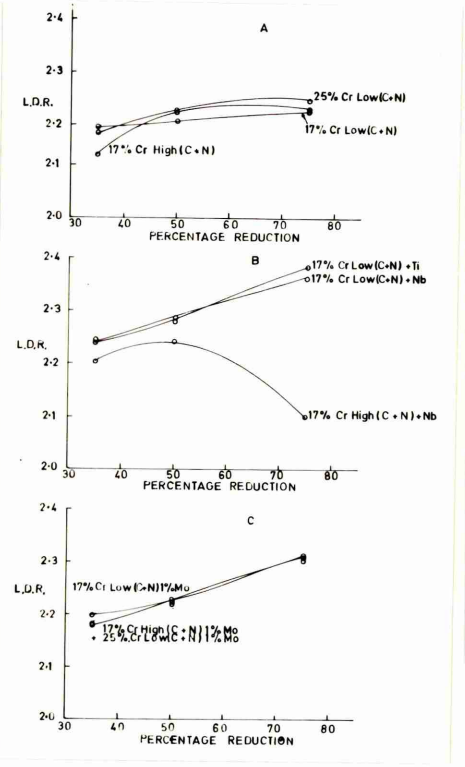
A
L.D.R.
25% Cr Low(C+N)
17% Cr Low(C+N)
17% Cr High(C+N)
PERCENTAGE REDUCTION
B
17% Cr Low(C+N) +Ti
17% Cr Low(C+N) +Nb
17% Cr High(C+N)+Nb
C
17% Cr Low(C+N)1%Mo
17% Cr High(C+N)1% Mo
+ 25% Cr Low(C+N)1% Mo

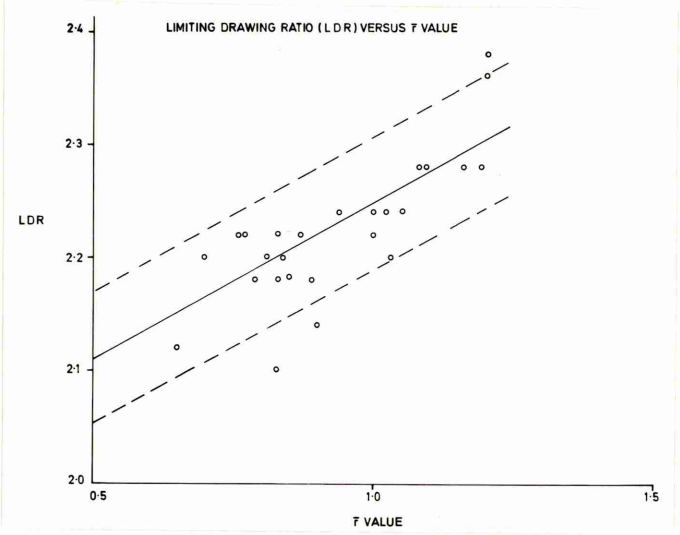
LIMITING DRAWING RATIO (LDR) VERSUS r̄ VALUE
LDR
r̄ VALUE

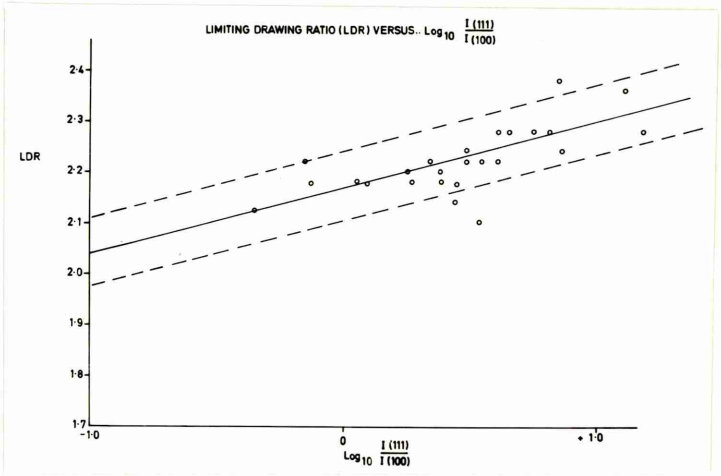
LIMITING DRAWING RATIO (LDR) VERSUS.. Log10 I(111)/I(100)
LDR
Log10 I(111)/I(100)

Fig (125)

The effect of cold reduction and composition on Δr and percentage earing.

Fig (126)

A graph of percentage earing versus Δr (degree of planar-anisotropy)

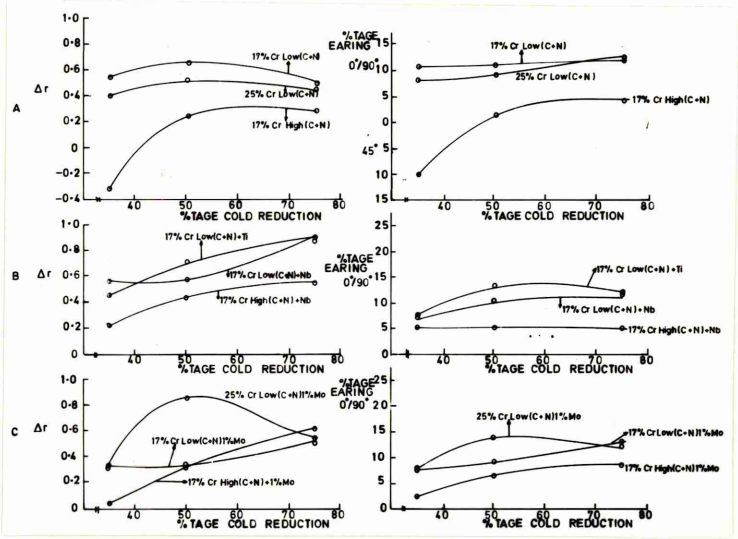
A
B
C
Δr
%TAGE EARING 0°/90°
%TAGE COLD REDUCTION
17% Cr Low(C+N)
25% Cr Low(C+N)
17% Cr High(C+N)
17% Cr Low(C+N)+Ti
17% Cr Low(C+N)+Nb
17% Cr High(C+N)+Nb
25% Cr Low(C+N)1%Mo
17% Cr Low(C+N)1%Mo
17% Cr High(C+N)+1%Mo

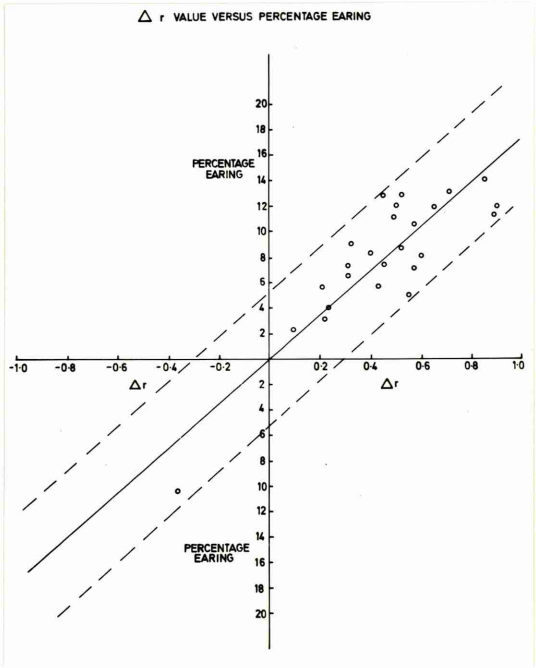
Δ r VALUE VERSUS PERCENTAGE EARING
PERCENTAGE EARING
Δr
PERCENTAGE EARING

Fig (127)

Photographs showing the effect
of composition and cold work
on the earing mode

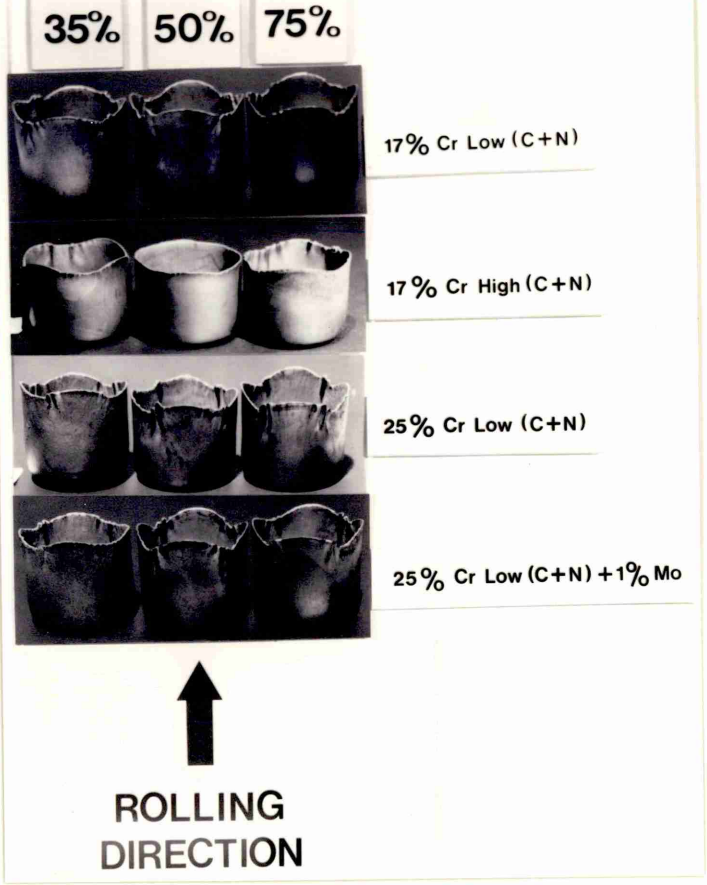
35%
50%
75%
17% Cr Low (C+N)
17% Cr High (C+N)
25% Cr Low (C+N)
25% Cr Low (C+N) +1% Mo
ROLLING DIRECTION

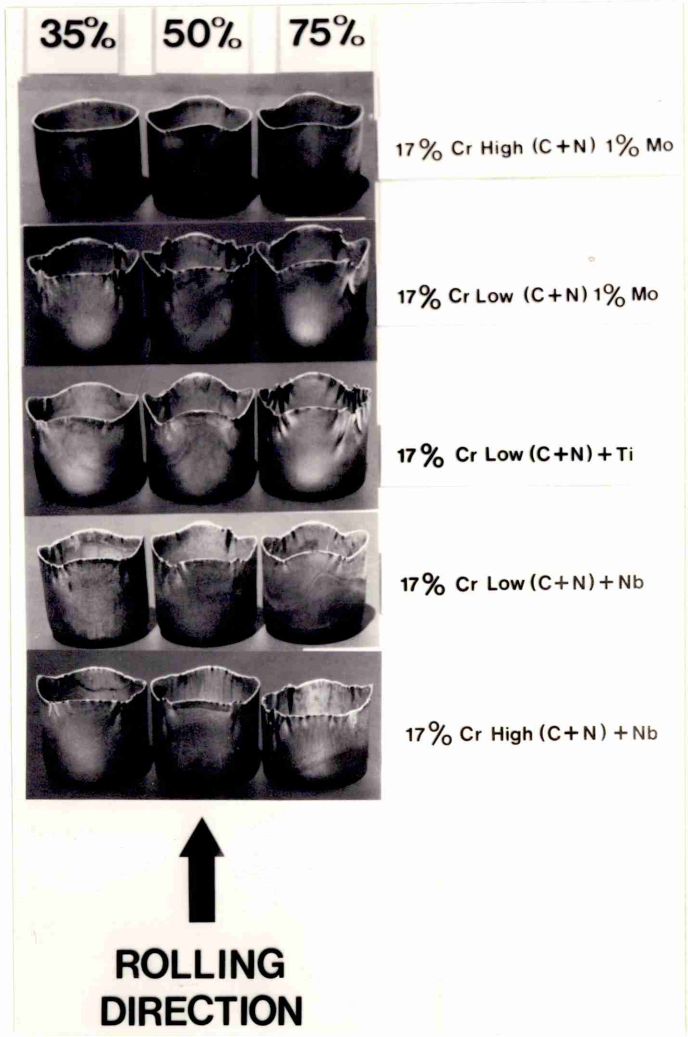
35%
50%
75%
17% Cr High (C+N) 1% Mo
17% Cr Low (C+N) 1% Mo
17% Cr Low (C+N) + Ti
17% Cr Low (C+N) + Nb
17% Cr High (C+N) + Nb
ROLLING DIRECTION

Fig (128)

Photographs showing the effect
of composition and cold reduction
on the degree of orange peel and
direction of fracture

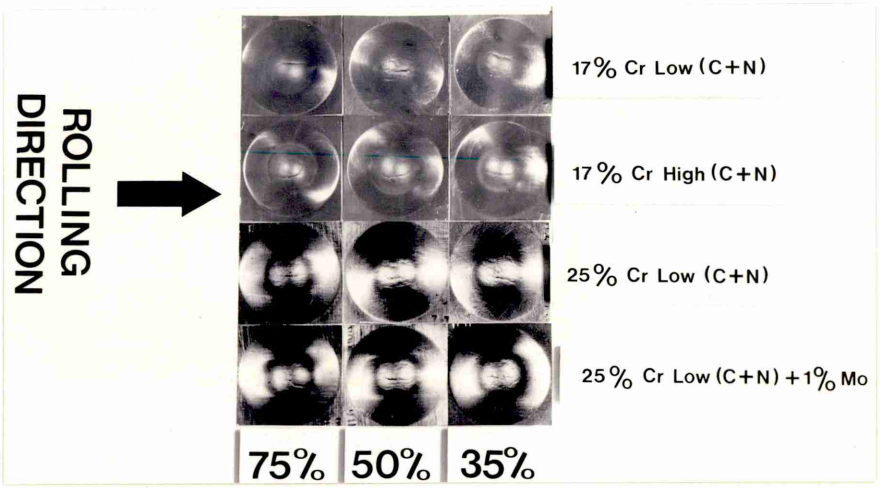
ROLLING DIRECTION
17% Cr Low (C+N)
17% Cr High (C+N)
25% Cr Low (C+N)
25% Cr Low (C+N) +1% Mo
75%
50%
35%

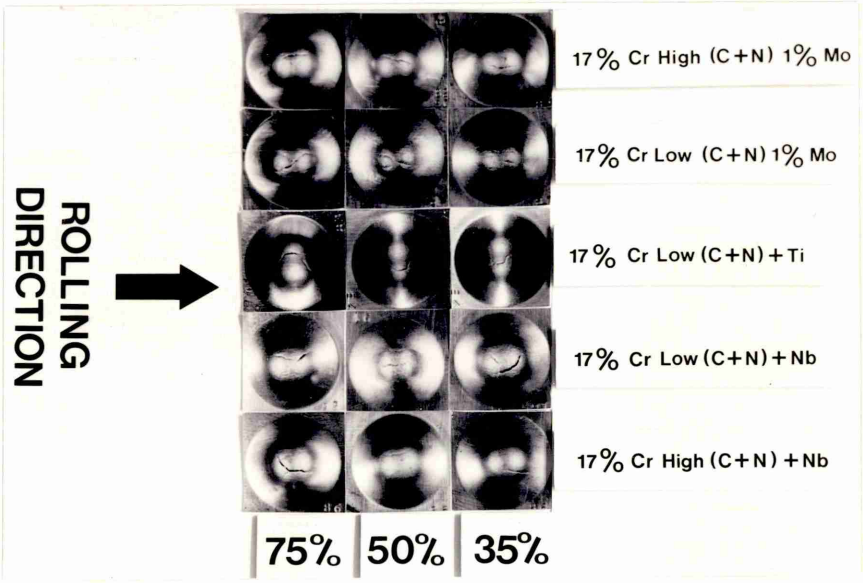
ROLLING DIRECTION
17% Cr High (C+N) 1% Mo
17% Cr Low (C+N) 1% Mo
17% Cr Low (C+N) + Ti
17% Cr Low (C+N) + Nb
17% Cr High (C+N) + Nb
75%
50%
35%

Fig (129)

Photograph showing the
failure zone in deep
drawn cups

Fig (130)

Scanning electronmicrograph
17%Cr high(C+N) + Nb steel,
fracture surface (the Swift
cupping test)

Magnification X 400

Fig (131)

Scanning electronmicrograph
17%Cr low(C+N) steel,
fracture surface (Erichsen test)

Magnification X 600

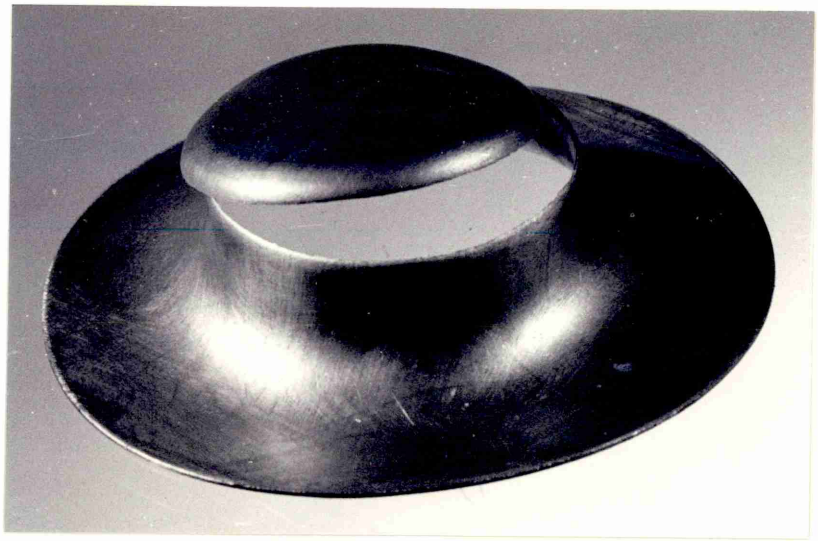

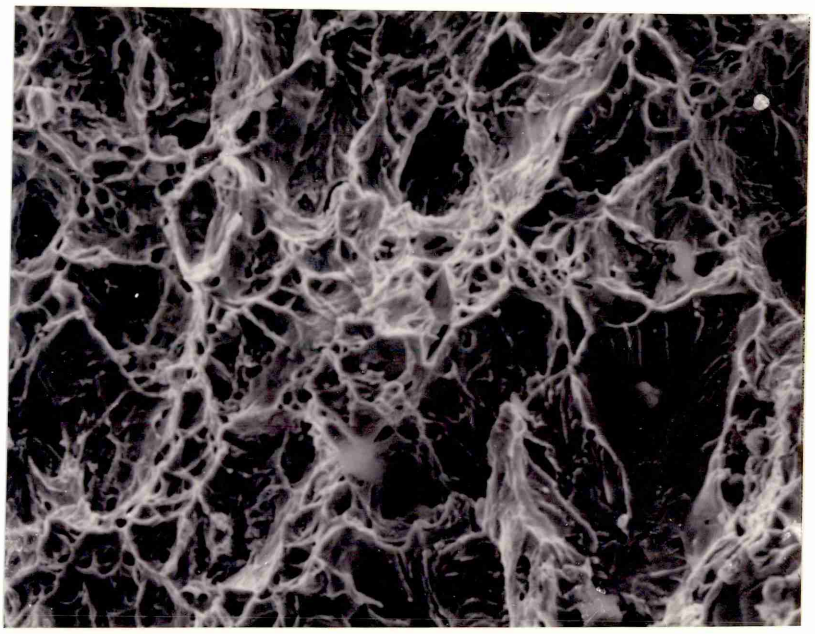

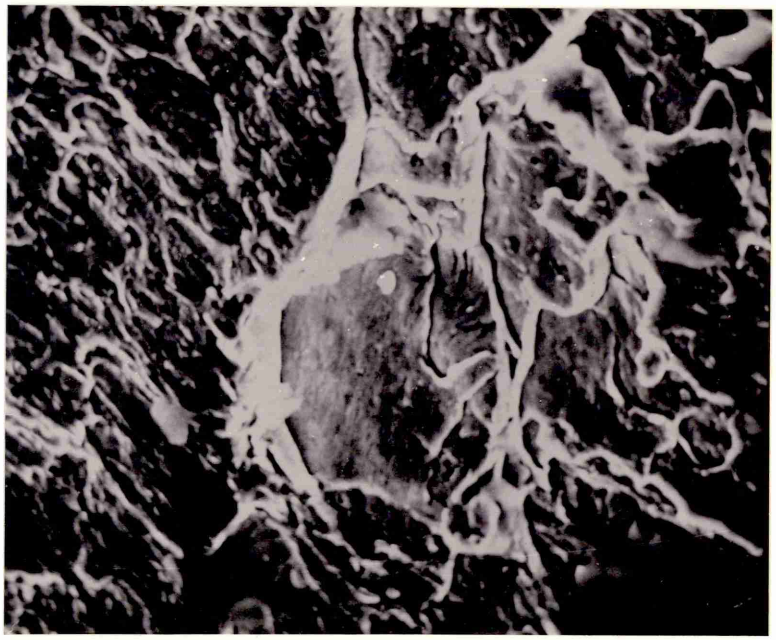

Fig (132)

Scanning electronmicrograph
17%Cr high(C+N) steel, fracture
surface (Erichsen test)

Magnification X 1,000

Fig (133a)

Scanning electronmicrograph
25%Cr low(C+N) steel, fracture
surface (Erichsen test)

Magnification X 900

Fig (133b)

As (133a) but higher magnification

Magnification X 4,500

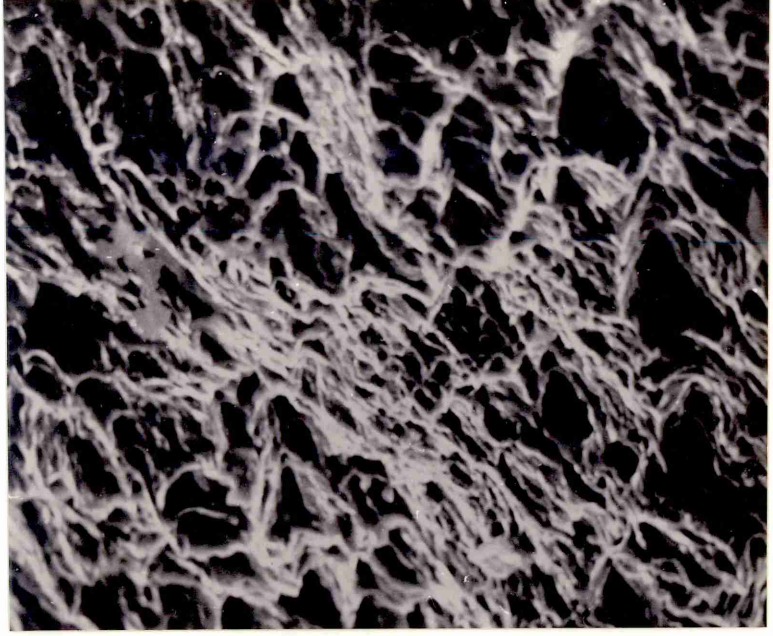

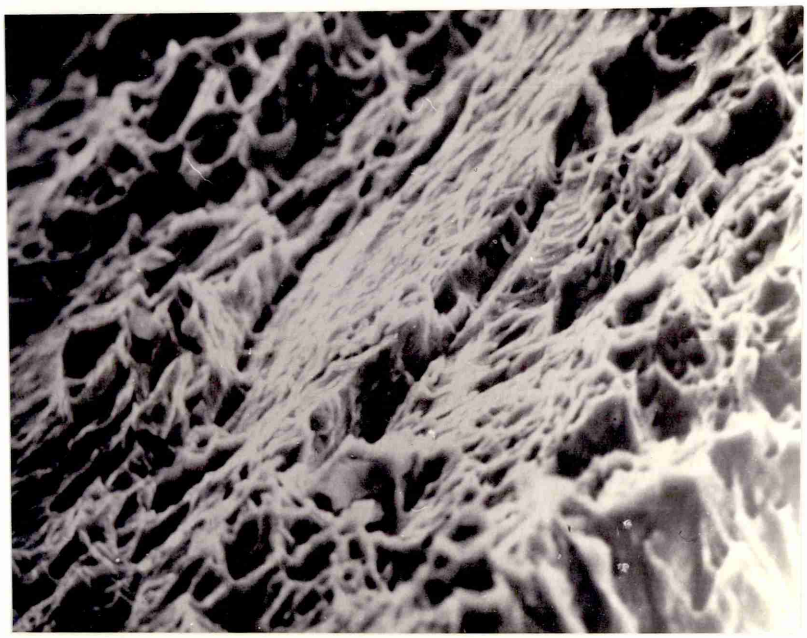

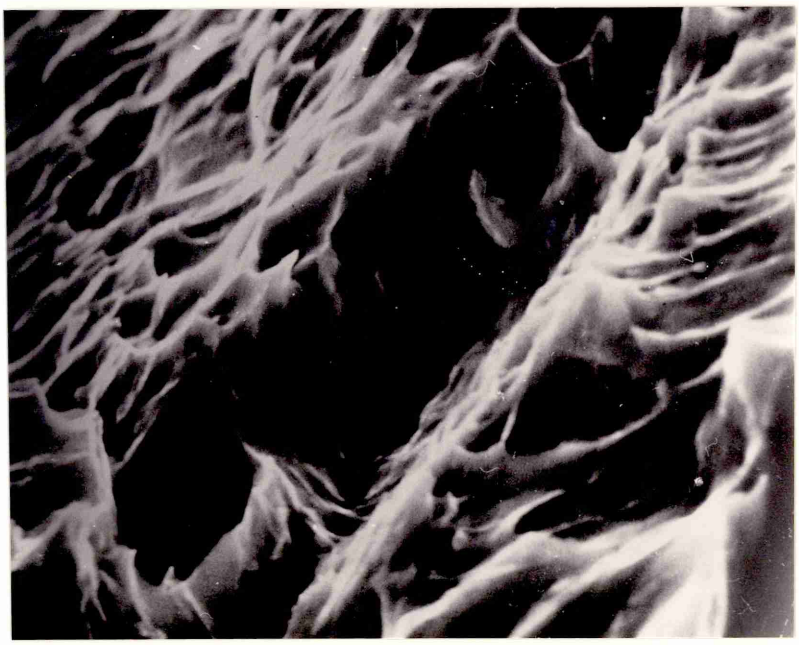

Fig (134)

Scanning electronmicrograph
17%Cr low(C+N) + Nb steel,
fracture surface (Erichsen
test)

Magnification X 1,800

Fig (135)

Scanning electronmicrograph
17%Cr high(C+N) + Nb steel,
fracture surface (Erichsen
test)

Magnification X 1,000

Fig (136a)

Scanning electronmicrograph
17%Cr high(C+N) + Nb steel,
fracture surface (Erichsen
test)

Magnification X 1,100

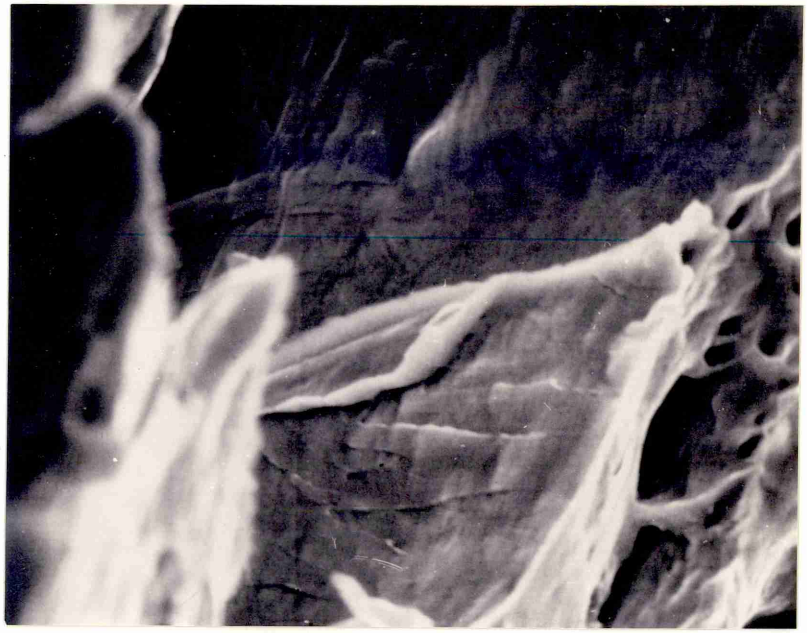

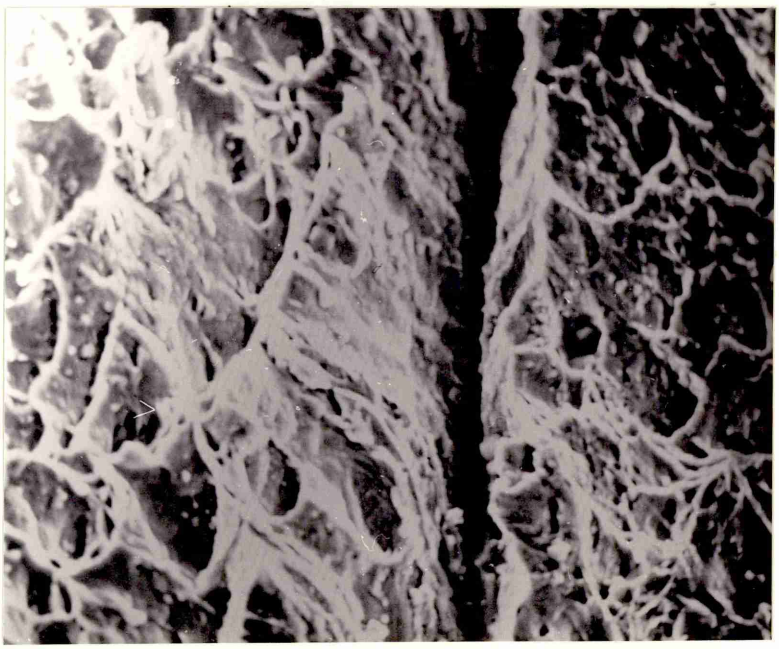

Fig (136b)

As (136a) but higher magnification

Magnification X 4,500

Fig (136c)

An optical micrograph of a 17%Cr high(C+N) + Nb steel. A section taken through the fracture from the failure zone of an Erichsen test

Magnification X 400

Fig (137a)

Scanning electronmicrograph 17%Cr low(C+N) 1% Mo steel, fracture surface (Erichsen test)

Magnification X 200

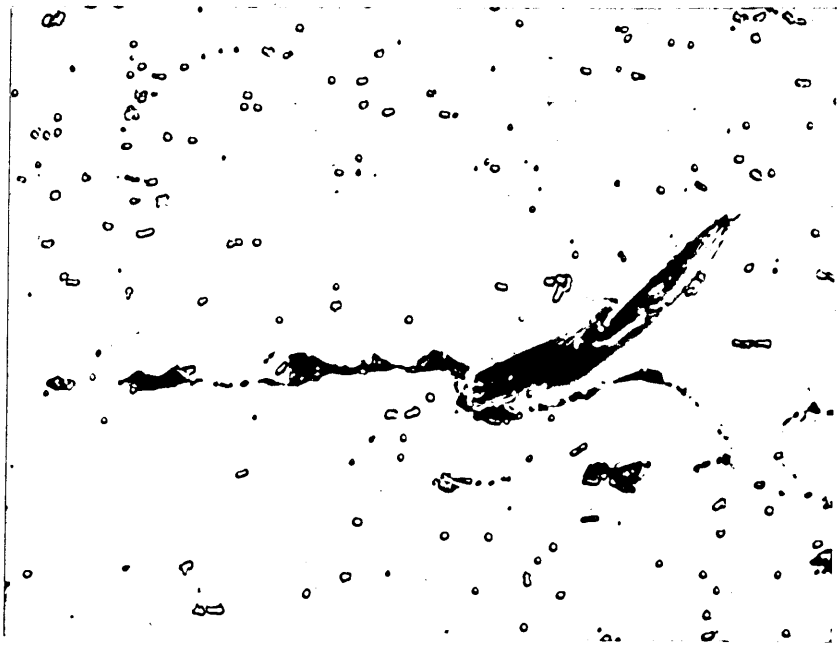

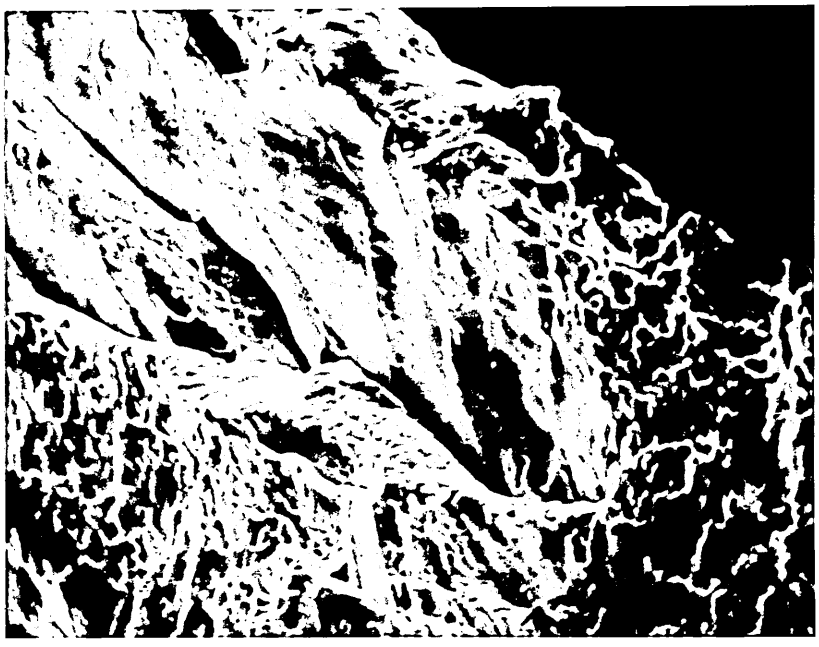

Fig (137b)

As (137a) but a higher magnification

Magnification X 2,000

Fig (138a)

Scanning electronmicrograph
25%Cr low(C+N) 1% Mo steel,
fracture surface (Erichsen
test)

Magnification X 500

Fig (138b)

As (137a) but a higher magnification

Magnification X 2,000

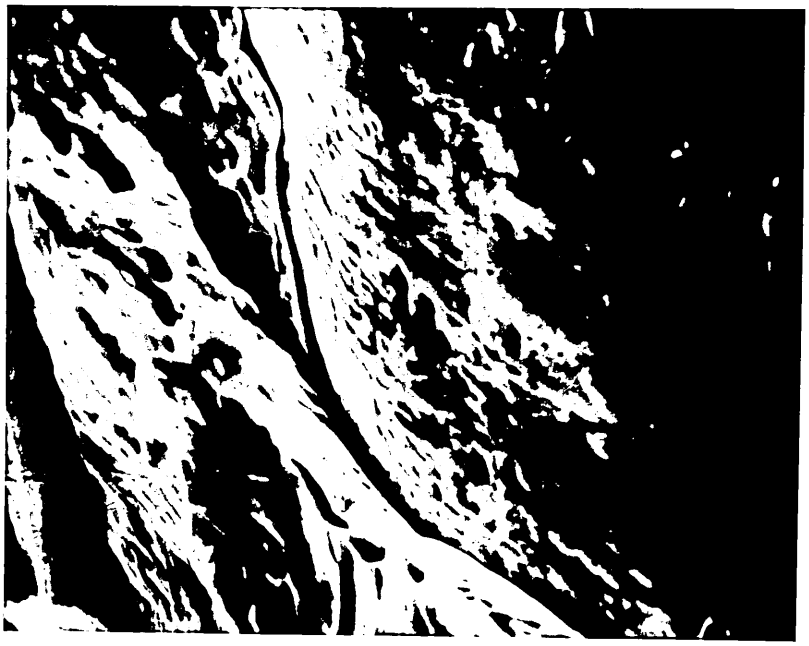

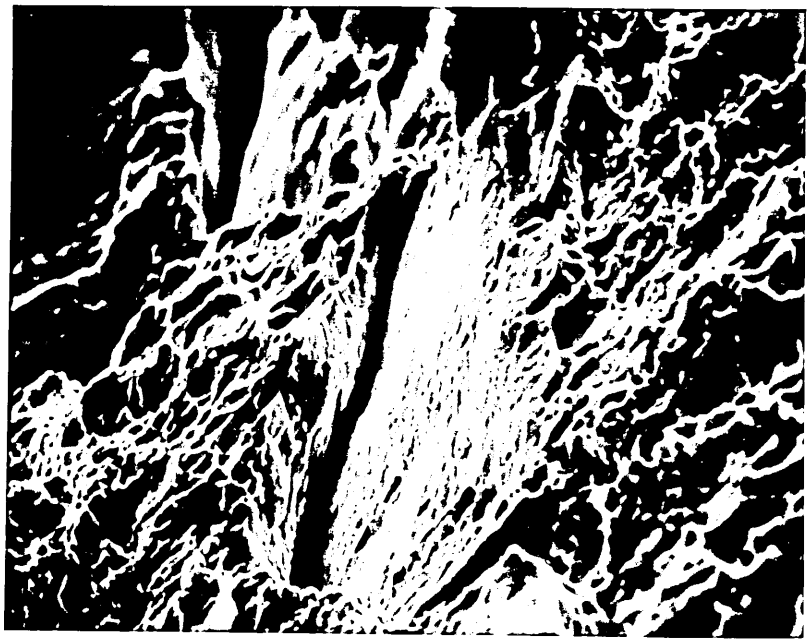

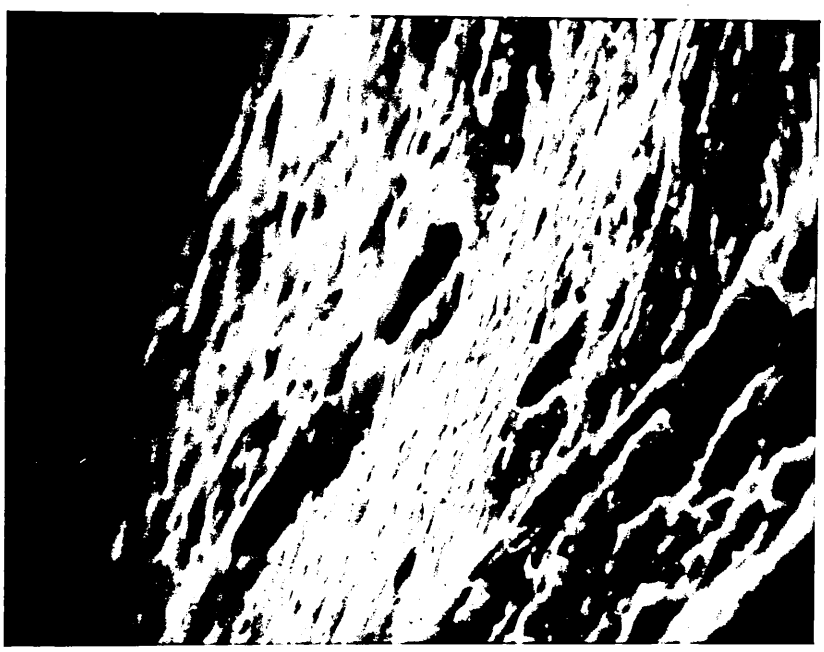

Fig (139)

Schematic solubility curves
for Nb (CN)

Fig (140)

Curves relating the critical
particle diameter for the unpinning
of subgrain boundaries to the
volume fraction of precipitates
for different subgrain sizes
(orientations)

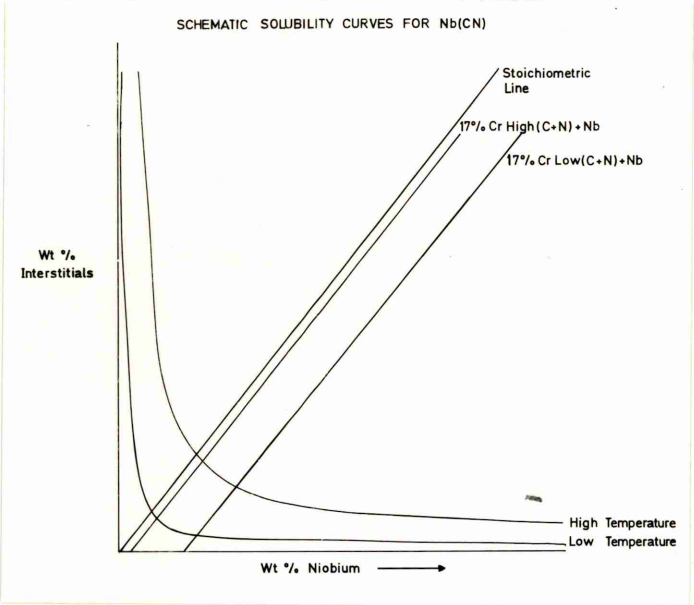
SCHEMATIC SOLUBILITY CURVES FOR Nb(CN)
Stoichiometric Line
17% Cr High (C+N) + Nb
17% Cr Low (C+N) + Nb
Wt % Interstitials
High Temperature
Low Temperature
Wt % Niobium

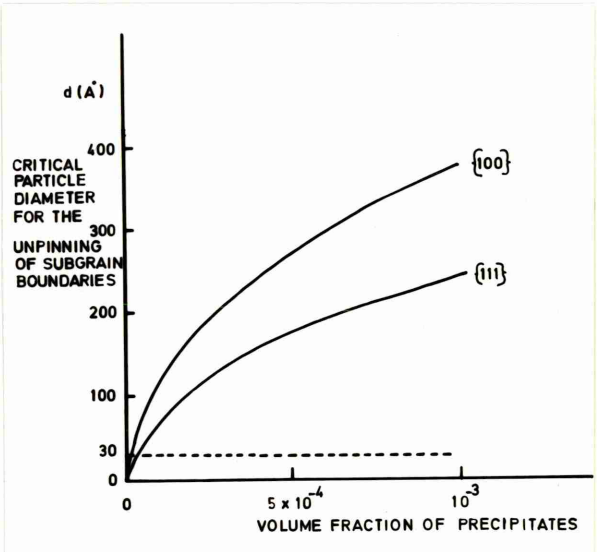
d (Å)
CRITICAL PARTICLE DIAMETER FOR THE UNPINNING OF SUBGRAIN BOUNDARIES
400
300
200
100
30
0
{100}
{111}
0
5 x 10^-4
10^-3
VOLUME FRACTION OF PRECIPITATES